



Provided by the author(s) and University of Galway in accordance with publisher policies. Please cite the published version when available.

Title	Noise in nonsmooth dynamical systems
Author(s)	Staunton, Eoghan J.
Publication Date	2020-01-24
Publisher	NUI Galway
Item record	<a href="http://hdl.handle.net/10379/15739">http://hdl.handle.net/10379/15739</a>

Downloaded 2024-04-25T11:06:48Z

Some rights reserved. For more information, please see the item record link above.





**NUI Galway**  
**OÉ Gaillimh**

# Noise in Nonsmooth Dynamical Systems

Thesis submitted in fulfilment  
of the requirements for the  
degree of Doctor of Philosophy.

## PhD Thesis

**Candidate:** Eoghan J. Staunton

**Supervisor:** Dr Petri T. Piiroinen

**Head of School:** Dr Rachel Quinlan

**Head of Discipline:** Dr Martin Meere

**Date:** September 2019



School of Mathematics,  
Statistics and  
Applied Mathematics



# Declaration

I hereby certify that this material, which I now submit for assessment on the programme of study leading to the award of PhD is entirely my own work and has not been taken from the work of others save and to the extent that such work has been cited and acknowledged within the text of my work. I have not obtained a degree in this University, or elsewhere, on the basis of this work.

School of Mathematics, Statistics and Applied Mathematics,  
National University of Ireland, Galway  
September 2019

---

Eoghan J. Staunton

# Acknowledgements

I would like to thank my supervisor Dr Petri Piironen for his tremendous help, encouragement and guidance throughout my time as a postgraduate student. I would like to express my appreciation to the administrative staff, Mary, Noelle and Collette who were amazingly supportive in helping me get through the day-to-day practicalities involved in completing a PhD in NUI Galway. I would also like to thank the other research staff for their support and input along the way especially my graduate research committee members, Dr Niall Madden, Dr Ray Ryan, Dr Michael Tuite and Dr Aisling McCluskey.

I am grateful to have been blessed with a friendly and helpful group of fellow postgraduates who created a great atmosphere to study in the School of Mathematics, Statistics and Applied Mathematics. In particular I would like to thank the members of the NUI Galway Modelling Research group, who provided helpful input and productive critiques during our weekly meetings, and the NUI Galway SIAM Student Chapter who made my time as a research student so enjoyable. I would also like to thank my family and friends for their unwavering support throughout the past four years without which this thesis would not have been possible.

Finally, I am grateful to the Irish Research Council for funding this PhD project.

# Abstract

This *article-based thesis* comprises a collection of four articles, each of which constitutes a chapter, written and formatted in pre-print manuscript form. The general aim underlying these articles is to understand how noise affects the dynamics of nonsmooth dynamical systems. Nonsmooth dynamical systems arise naturally when modelling systems in engineering and applied sciences and are characterised by sudden changes in system properties. Examples of naturally arising nonsmooth systems include mechanical systems involving impacts or friction, economic or sociological systems with decision thresholds, switching electronic systems and climate systems with sharp ice-cap boundaries. The dynamical systems resulting from these models exhibit several unique behaviours including new types of bifurcations called discontinuity-induced bifurcations, which can be considered the hallmark of nonsmooth systems. A level of noise or randomness is also ubiquitous in real-world systems and has been shown to have significant nontrivial effects on smooth but nonlinear systems close to bifurcation points. As a result, it is both interesting and important to understand the effects of noise on the unique dynamics possible in nonsmooth systems.

**Keywords** – Dynamical Systems, Nonsmooth, Hybrid, Stochastic, Bifurcations

# Contents

<b>1</b>	<b>Introduction</b>	<b>1</b>
1.1	Outline of Thesis . . . . .	2
<b>2</b>	<b>Dynamical Systems</b>	<b>5</b>
2.1	Notation and Conventions . . . . .	8
2.2	Smooth Maps . . . . .	9
2.3	Smooth Flows . . . . .	10
2.4	Stability and Poincaré Maps . . . . .	11
2.5	Bifurcations . . . . .	15
2.6	Continuation . . . . .	19
<b>3</b>	<b>Nonsmooth Systems</b>	<b>23</b>
3.1	Nonsmooth Maps . . . . .	23
3.2	Piecewise-smooth Flows and Hybrid Systems . . . . .	25
3.3	Discontinuity Mappings . . . . .	27
3.4	The Square Root Map . . . . .	34
<b>4</b>	<b>Noise</b>	<b>39</b>
4.1	Probability and Stochastic Processes . . . . .	39
4.1.1	Elementary Measure Theory . . . . .	39
4.1.2	Probability Theory . . . . .	42
4.1.3	Stochastic Processes . . . . .	45
4.2	Noise in dynamical systems . . . . .	49
4.2.1	Noise in Smooth Dynamical Systems . . . . .	50
4.2.2	Noise in Nonsmooth Dynamical Systems . . . . .	54
<b>5</b>	<b>Discussion and Outlook</b>	<b>59</b>
<b>6</b>	<b>Summary of Papers and Author Contributions</b>	<b>63</b>
6.1	Paper 1 . . . . .	63
6.2	Paper 2 . . . . .	64
6.3	Paper 3 . . . . .	65
6.4	Paper 4 . . . . .	66

<b>7</b>	<b>Paper 1</b>	<b>79</b>
7.1	Introduction . . . . .	80
7.2	The Deterministic Square Root Map . . . . .	82
	7.2.1 The Map . . . . .	82
	7.2.2 Symbolic Dynamics . . . . .	82
	7.2.3 Bifurcations and Deterministic Structures . . . . .	83
7.3	Noise . . . . .	89
	7.3.1 The Square Root Map With Noise . . . . .	89
	7.3.2 Numerical Observations . . . . .	90
7.4	The Evolution of Deviations . . . . .	93
	7.4.1 Analysis . . . . .	94
	7.4.2 Comparison to Numerical Observations . . . . .	99
7.5	Deviation Distributions and Noise Thresholds . . . . .	100
	7.5.1 Significant Shifts in Behaviour . . . . .	103
	7.5.2 The Effective Destruction of Attractors . . . . .	107
	7.5.3 The Reversal of Relationships . . . . .	110
	7.5.4 Generalising to Higher Periods . . . . .	111
7.6	Scaling . . . . .	111
7.7	Discussion . . . . .	116
7.A	Appendix: A Linearisation Approach . . . . .	125
<b>8</b>	<b>Paper 2</b>	<b>127</b>
8.1	Introduction . . . . .	128
8.2	The Deterministic Square Root Map . . . . .	129
	8.2.1 The Map . . . . .	129
	8.2.2 Symbolic Dynamics . . . . .	130
	8.2.3 Bifurcations and Deterministic Structures . . . . .	130
8.3	The Addition of Noise . . . . .	133
	8.3.1 The Square Root Map With Noise . . . . .	133
	8.3.2 Numerical Observations . . . . .	134
	8.3.3 The Evolution of Deviations . . . . .	136
8.4	The Persistence of Unstable Behaviour Due to Noise . . . . .	139
	8.4.1 The Transition . . . . .	140
	8.4.2 Contraction and Expansion . . . . .	141
	8.4.3 Deviation Distributions Under Repeated Iteration on the Right . . . . .	149
	8.4.4 Examples . . . . .	151
8.5	Discussion . . . . .	153
<b>9</b>	<b>Paper 3</b>	<b>159</b>
9.1	Introduction . . . . .	161
9.2	Basic Analysis . . . . .	163
	9.2.1 Discontinuity Mappings and Saltation Matrices . . . . .	163
	9.2.2 Noisy Boundaries . . . . .	167

---

9.2.3	Derivation of the Noisy Saltation Matrix . . . . .	169
9.2.4	Poincaré Map . . . . .	173
9.2.5	Summary . . . . .	176
9.3	Introducing Noise . . . . .	177
9.3.1	A Zero-Mean Mean-Reverting Process . . . . .	177
9.3.2	The Distribution of $\Delta t_{\text{ref}}$ . . . . .	180
9.4	Examples . . . . .	181
9.4.1	A Two Region Piecewise Smooth System . . . . .	182
9.4.2	A Limit Cycle in a Piecewise-Linear System . . . . .	185
9.4.3	The Chua Circuit . . . . .	196
9.5	Summary and Discussion . . . . .	215
<b>10</b>	<b>Paper 4</b>	<b>223</b>
10.1	Introduction . . . . .	224
10.2	Deterministic Piecewise-smooth and Hybrid Dynamical Systems . . . . .	227
10.2.1	Transversal Crossings . . . . .	228
10.2.2	Grazing Interactions . . . . .	231
10.3	Stochastic Processes . . . . .	233
10.4	Hybrid Systems . . . . .	235
10.4.1	Stochastically Oscillating Boundaries . . . . .	235
10.4.2	Rugged Boundaries . . . . .	241
10.5	Systems with Higher-Order Discontinuities . . . . .	244
10.5.1	Stochastically Oscillating Boundaries . . . . .	249
10.5.2	Rugged Boundaries . . . . .	250
10.6	Grazing . . . . .	252
10.6.1	Stochastic Oscillations . . . . .	255
10.6.2	Rugged Boundaries . . . . .	258
10.7	Numerical Examples . . . . .	259
10.7.1	Hybrid Systems with Stochastically Oscillating Boundaries . . . . .	260
10.7.2	Hybrid Systems with Rugged Boundaries . . . . .	266
10.7.3	Continuous Systems . . . . .	268
10.7.4	Grazing . . . . .	274
10.8	Summary and Discussion . . . . .	278
10.A	Appendix: Generalised Ornstein-Uhlenbeck Processes . . . . .	286

# List of Figures

2.1	Intertwined basins of attraction in the Chua circuit. . . . .	7
2.2	Poincaré map schematic. . . . .	14
2.3	Bifurcations of fixed points of maps or equilibria of flows. . . . .	17
2.4	Homoclinic bifurcation diagram. . . . .	19
3.1	Nonsmooth fold bifurcation diagram. . . . .	24
3.2	Schematic of a reference trajectory intersecting a discontinuity boundary transversally in a hybrid system. . . . .	28
3.3	Deriving the zero-time discontinuity mapping for transversal boundary crossings. . . . .	30
3.4	Impacting and non-impacting trajectories in the neighbourhood of a reference grazing trajectory. . . . .	32
3.5	Deriving the zero-time discontinuity mapping for a grazing trajectory. . . . .	33
4.1	Sample paths of a standard Browian motion $B_t$ . . . . .	46
4.2	Sample paths of an Ornstein-Uhlenbeck Process . . . . .	48
4.3	Sample paths of generalised Ornstein-Uhlenbeck processes. . . . .	49
4.4	The transcritical bifurcation of the logistic map. . . . .	51
4.5	Bifurcation diagram of the logistic map with parametric noise. . . . .	52
7.1	Bifurcation diagrams for the deterministic square root map showing a period adding cascade of attractors. . . . .	84
7.2	Riddled basins of attraction in the square root map. . . . .	87
7.3	a) The primary basins of attraction of the square root map. b) The steady state distribution of iterates of the square root map. . . . .	89
7.4	The relationship between noise amplitude and proportion of time spent in $RL$ and $RLL$ behaviour for values of $\mu$ on the interval of multistability. . . . .	92
7.5	Comparing the numerically calculated distributions of deviations about the deterministic periodic orbits of the square root map to our semi-analytic prediction. . . . .	99
7.6	Example threshold values of the noise amplitude $\Delta$ for which the three effects described in Section 7.5 occur in the square root map. . . . .	102

7.7 Numerically calculated threshold noise amplitudes to:  
a) cause a significant shift in behaviour  
b) destroy periodic behaviour  
c) induce a reversal in the relationship. . . . . 104

7.8 The  $\varrho$  values associated with the threshold noise amplitudes to:  
a) cause a significant shift in behaviour  
b) destroy periodic behaviour  
c) induce a reversal in the relationship. . . . . 105

7.9 The relationship between noise amplitude and proportion of time spent in  $RL$  and  $RLL$  behaviour for  $\mu = 0.0063$  grouped by initial condition. . . . . 109

7.10 The relationship between noise amplitude and proportion of time spent in  $RL$  and  $RLL$  behaviour for  $\mu = 0.00642$  grouped by initial condition. . . . . 109

7.11 The relationship between noise amplitude and proportion of time spent in  $RL$  and  $RLL$  behaviour for  $\mu = 0.0068$  grouped by initial condition. . . . . 109

8.1 Bifurcation diagrams for the deterministic square root map showing a period adding cascade of attractors. . . . . 131

8.2 Bifurcation diagrams for the square root map with additive Gaussian white noise. . . . . 134

8.3 The changing proportion of time spent in  $RL$  &  $RLL$  behaviour and transition ( $RR$ ) for increasing amplitude of additive noise. . . . . 136

8.4 Comparing the numerically calculated distributions of deviations about the deterministic periodic orbits of the square root map to our semi-analytic prediction. . . . . 139

8.5 Graphical representation on a log scale of the sets  $A_{RL^{k-2}R}$ . . . . . 143

8.6 The evolution of the set  $A_{RR}$  under repeated application of the square root map. . . . . 147

8.7 a) The number of iterates required for orbits with a range of initial conditions to transition to  $RLL$  behaviour.  
b) The steady-state distribution of the last left iterate of the  $RLL$  orbit truncated to  $A_{RR}$ .  
c) The distribution shown in b) after undergoing repeated iterations on the right-hand side of the square root map. . . . . 150

8.8 a) An example of a noise-induced transition from settled  $RLL$  to persistent  $RL$  behaviour.  
b) An example of a noise-induced transition from settled  $RL^5$  to persistent  $RL^4$  behaviour. . . . . 151

8.9	a) The iterates $x_0, \dots, x_7$ associated with the eight underlined terms in the symbolic sequence (8.19) in the case of the transition shown in Figure 8.8a)	
	b) A close-up look at the persistent noise induced $RL$ behaviour shown in in Figure 8.8a) and the associated deterministic square root map dynamics. . . . .	152
9.1	Schematic of a reference trajectory starting at $\mathbf{x}_0^{\text{ref}}$ crossing a discontinuity boundary transversally in a hybrid dynamical system. . . . .	165
9.2	Deriving the zero-time discontinuity mapping. . . . .	166
9.3	Schematic showing the construction of $\mathbf{M}(\mathbf{x})$ :	
	a) in the absence of noise.	
	b) in the presence of noise. . . . .	175
9.4	Sample time series for $P(t)$ , the corresponding velocity process is shown in Figure 9.5. . . . .	179
9.5	Sample time series for $V(t)$ , the corresponding position process is shown in Figure 9.4. . . . .	179
9.6	Sample joint Distribution of $P(t)$ and $V(t)$ . . . . .	180
9.7	The image of the perimeter of the circle of radius 0.01 about $\hat{\mathbf{x}}_0^{\text{ref}}$ after time $T$ , compared to the linear approximation given by (9.88). . . . .	182
9.8	The distribution of the image of the perimeter of the circle of radius 0.01 about $\hat{\mathbf{x}}_0^{\text{ref}}$ after time $T$ , given by:	
	a) numerical simulation of the full nonlinear stochastic system,	
	b) the approximation (9.90). . . . .	184
9.9	Stable limit cycle in the system given by (9.92)-(9.96). . . . .	187
9.10	The characteristic multipliers and period of the limit cycle in the system given by (9.92)-(9.96). . . . .	188
9.11	The distribution of $\Delta t_1$ given by numerical simulation and linear approximation. . . . .	190
9.12	The sample path of the position process $P$ over one period of the stable limit cycle of the system (9.92)-(9.96). . . . .	191
9.13	The distribution of trajectories with starting point $\mathbf{x}_0^{\text{ref}}$ , after one deterministic period, given by:	
	a) numerical simulation.	
	b) approximated using (9.106). . . . .	192
9.14	The distribution of trajectories with starting point $\mathbf{x}_0^{\text{ref}}$ , on their first return to the Poincaré section $\mathcal{P}$ , given by:	
	a) numerical simulation.	
	b) approximated using (9.106). . . . .	193
9.15	The distribution of trajectories with starting point $\mathbf{x}_0^{\text{ref}}$ , on their 100 <sup>th</sup> return to the Poincaré section $\mathcal{P}$ , given by:	
	a) numerical simulation.	
	b) approximated using (9.106). . . . .	193

9.16	The proportion of trajectories with initial conditions $\mathbf{x}_0 = \mathbf{x}_{SM} + (\epsilon, 0)^T$ about the deterministic stable manifold of $\mathbf{x}_R^{eq}$ escaping the basin of attraction of the stable limit cycle, given by numerical simulation and approximated using (9.106). . . . .	194
9.17	The distribution of the $x$ -coordinates of the trajectories with starting point $\mathbf{x}_0$ such that $\mathbf{x}_{SM} - \mathbf{x}_0 = 10^{-6}$ , on their first return to the Poincaré section $\mathcal{P}$ , provided they have remained inside the deterministic basin of attraction. . . . .	195
9.18	Circuit diagram of the Chua circuit. . . . .	197
9.19	Typical $V$ - $I$ characteristic of the Chua diode. . . . .	197
9.20	Five coexisting attractors in the Chua circuit. . . . .	199
9.21	The basins of attraction of five coexisting attractors in the Chua circuit. . . . .	200
9.22	Distribution of the $x$ co-ordinates of 10,000 trajectories with initial conditions on $\mathbf{C}^-$ after one period in a system with a noisy boundary. . . . .	201
9.23	Bifurcation diagrams showing the saddle bifurcations of $\mathbf{C}^-$ as the magnitude of $\epsilon$ grows. . . . .	202
9.24	The distribution of trajectories with initial conditions on $\mathbf{C}^-$ after 20 periods in a system with a noisy boundary, on the Poincaré section $\{(x, y, z) : z = z_0^{ref}\}$ given by: a) numerical simulation of the whole system. b) first-order approximation. . . . .	202
9.25	a) Steady state distribution of orbit errors on the discontinuity boundary $\mathcal{D}^-$ for trajectories with initial condition on the periodic orbit $\mathbf{C}^-$ . b) Convergence of the standard deviation in the $z$ -direction, $\sigma_z$ , to its steady state value for the distribution shown in a). . . . .	204
9.26	Invariant ellipses with $R = 5$ and $R = 7$ corresponding to the invariant distributions associated with the two intersections a) $\hat{\mathbf{x}}_1$ and b) $\hat{\mathbf{x}}_2$ of $\mathbf{C}^-$ with $\mathcal{D}^-$ where $\Sigma = \sigma = 0.5875$ . . . . .	206
9.27	Invariant ellipses with $R = 5$ and $R = 7$ corresponding to the invariant distributions associated with the two intersections a) $\hat{\mathbf{x}}_1$ and b) $\hat{\mathbf{x}}_2$ of $\mathbf{C}^-$ with $\mathcal{D}^-$ where $\Sigma = \sigma = 0.7$ . . . . .	207
9.28	Approximation of the distribution of the positions of the trajectories simulated in Figure 9.22 using (9.118). . . . .	209
9.29	The distribution of $x$ co-ordinates of trajectories with initial conditions on $\mathbf{C}^-$ after one period in a system with a noisy boundary and $\epsilon = -6.21 \times 10^{-5}$ compared to: a) first-order approximation. b) second order approximation. . . . .	210
9.30	The distribution of $x$ co-ordinates of trajectories with initial conditions on $\mathbf{C}^-$ after one period in a system with a noisy boundary and $\epsilon = -5.589 \times 10^{-4}$ compared to: a) first-order approximation. b) second order approximation. . . . .	211

9.31	Three coexisting attractors in the Chua circuit. . . . .	211
9.32	The basins of attraction of three coexisting attractors in the Chua circuit. . . . .	212
9.33	Bifurcation diagram showing the pitchfork bifurcations of $\mathbf{C}^1$ and as $\mathbf{C}^2$ the magnitude of $\epsilon$ grows. . . . .	213
9.34	Invariant ellipses corresponding to the invariant linearised distributions associated with the intersections $\hat{\mathbf{x}}_4^1$ , and $\hat{\mathbf{x}}_2^2$ , of $\mathbf{C}^1$ and $\mathbf{C}^2$ with $\mathcal{D}^-$ , respectively.	
	a) We take $\epsilon \approx -0.20595$ and plot ellipses for $R = 5$ and $R = 7$ .	
	b) We take $\epsilon \approx -0.20800$ and plot ellipses for $R = 5$ . . . . .	214
10.1	Schematic of a reference trajectory intersecting a discontinuity boundary transversally in a hybrid system. . . . .	228
10.2	Deriving the zero-time discontinuity mapping for transversal boundary crossings. . . . .	229
10.3	A grazing trajectory in a hybrid dynamical system. . . . .	232
10.4	Deriving the zero-time discontinuity mapping for a grazing trajectory.	233
10.5	The dynamics of a bouncing ball in a stable periodic orbit with period $\frac{2n\pi}{\omega}$ with one impact per period for $n = 1, 2, 3$ . . . . .	262
10.6	The dynamics of a bouncing ball in a stable periodic orbit with period $\frac{6n\pi}{\omega}$ with three impacts per period for $n = 1, 2, 3$ . . . . .	262
10.7	a) The magnitude of the eigenvalues of the periodic orbits shown in Figure 10.5 as $\omega$ increases.	
	b) Representative figure of the positions of the eigenvalues of the periodic orbit in the complex plane for $n = 1$ . . . . .	264
10.8	The basins of attraction of the bouncing ball system (10.143)-(10.144) in $(v_{\text{out}}, \tau)$ -space. . . . .	265
10.9	The pdf of the maximum height attained by the bouncing ball between its 50 <sup>th</sup> and 51 <sup>st</sup> impacts given by	
	a) full simulation of the system.	
	b) linear approximation. . . . .	265
10.10	Heatmaps of the distribution of the maximum height attained by the bouncing ball and its corresponding horizontal position after one bounce on the rugged surface given by:	
	a) full simulation of the system.	
	b) linear approximation. . . . .	269
10.11	Circuit diagram of the Chua circuit. . . . .	269
10.12	Typical voltage-current response of the Chua diode. . . . .	270
10.13	Five coexisting attractors in the Chua circuit. . . . .	271

---

10.14	The distributions of trajectories with initial conditions on $\mathbf{C}^-$ on their first return to the Poincaré section given by:	
	a) full numerical-simulation.	
	b) approximations obtained by using the SZDM (10.94) in place of boundary interactions. . . . .	272
10.15	Schematic of a one-degree-of-freedom impact oscillator. . . . .	275
10.16	Grazing orbit in the system (10.175). . . . .	276
10.17	Histograms of the pdf of the maximum amplitude attained by the impact oscillator by full simulation of the system and by approximation using the SZDM (10.123). . . . .	277





# Chapter 1

## Introduction

Traditionally *smooth* and *deterministic dynamical systems* are used to model real-world phenomena. These models often present a simplified view of the world where, on one hand, the evolution of systems is always smooth and exhibits no interruptions such as impacts, switches, slides or jumps and, on the other hand, the future of any system is completely determined by its present state [1].

However, when modelling many real-world systems one or both of these simplifications may not hold. For example, in many cases, the modelling of real-world systems in engineering, natural or social sciences naturally gives rise to *nonsmooth dynamical systems*. These systems are characterised by having periods of smooth evolution interrupted by sudden changes in system properties. For example, the study of mechanical systems with impacts or friction [2, 3, 4, 5, 6], switching in electrical circuits [7, 8], and relay control systems [9] all naturally lead to nonsmooth systems. More complex systems such as climate, ecological, biological and financial systems have also been modelled using nonsmooth models [10, 11, 12, 13, 14, 15, 16]. Furthermore, real-world systems are also rarely entirely deterministic and it has been shown that a level of randomness or noise is ubiquitous in real-world systems [17]. Models known as *stochastic* models possess some inherent randomness, allowing us

to account for this noise.

Independently, both nonsmoothness and noise have been shown to be the drivers of significant changes in the qualitative behaviour of dynamical systems. Nonsmooth systems exhibit all of the behaviour of smooth systems. However, several unique phenomena also occur including new types of *bifurcations* called *discontinuity-induced bifurcations* (DIBs). Examples include *grazing* bifurcations, *border-collision/boundary-equilibrium* bifurcations, *sliding* bifurcations, *sticking* bifurcations and others [18, 19, 20, 21, 22]. These new bifurcations are often caused by the fact that nearby trajectories can undergo different sequences of events and so are topologically distinct.

In smooth nonlinear systems the addition of noise has been shown to have the greatest effect on the outcome of the system in the neighbourhood of bifurcation points, the hallmark of nonlinear dynamical systems. For example, noise has been shown to delay bifurcations, destroy attractors, induce stability [23, 24, 25, 26] and even drive behaviour that has no deterministic counterpart [27]. The study of the impact of noise on nonsmooth systems is a relatively new field. In-depth studies have been carried out into the effects of noise on piecewise-linear maps [28, 29], grazing bifurcations in impacting systems [30, 31] and on periodic orbits with sliding [32, 33]. The purpose of this thesis is to continue investigating the effects of noise on nonsmooth systems. In particular, since DIBs could be considered the hallmark of nonsmooth systems, we will focus on the effects of noise in their neighbourhood.

## 1.1 Outline of Thesis

The work presented here is intended to further our knowledge of the effects of noise on nonsmooth dynamical systems. We pay particular attention to the use of *discontinuity mappings* in a stochastic setting and analysing the impact of noise on the dynamics of the *square root map*.

The outline of the thesis is as follows. Chapter 2 introduces key tools and concepts

in dynamical systems. In Chapter 3 we discuss the specifics of nonsmooth systems including *piecewise-smooth flows*, *piecewise-smooth maps* and *hybrid dynamical systems*. Chapter 4 focuses on noise, introducing key concepts in probability and stochastic processes. In order to motivate our investigations we also report on some existing research into the significant effects of noise on both smooth and nonsmooth dynamical systems. A concluding discussion on the subject of the thesis is presented in Chapter 5, while the four papers that form the bulk of this thesis are summarised with a discussion of author contributions in Chapter 6, and these papers form the remaining four chapters of the thesis. Chapter 7 and Chapter 8 concern the effects of noise on multistability in the square root map, while in Chapters 9 and 10 we derive discontinuity mappings for nonsmooth dynamical systems with stochastic discontinuity boundaries.



# Chapter 2

## Dynamical Systems

In this chapter we give a brief overview of dynamical systems theory for general dynamical systems. We will also introduce discrete-time iterated *maps* and continuous-time systems governed by ordinary differential equations known as *flows* in the smooth case. We then present some tools useful for analysing the stability of *invariant sets* such as *equilibrium points* or *periodic orbits*, and methods used to locate attractors in smooth or nonsmooth dynamical systems. More in-depth treatment of these concepts and tools can be found in texts by Guckenheimer and Holmes [34], Kuznetsov [35], Wiggins [36] and others, for example [37, 38].

First, let us define the key concepts in general dynamical systems. Dynamical systems are rules describing systems that evolve in time. They can be written in terms of an  $n$ -dimensional state space  $\mathcal{S} \subset \mathbb{R}^n$  whose coordinates describe the state of the system at any point in time  $t \in \mathbb{T}$ , and a dynamical rule  $\phi : \mathcal{S} \times \mathbb{T} \rightarrow \mathcal{S}$  that gives the future values of all state-space variables, given only their present values where

$$\begin{aligned}\phi(\mathbf{x}, t + s) &= \phi(\phi(\mathbf{x}, t), s), \quad \mathbf{x} \in \mathcal{S}, \quad t, s \in \mathbb{T}, \\ \phi(\mathbf{x}, 0) &= \mathbf{x}, \quad \mathbf{x} \in \mathcal{S}.\end{aligned}\tag{2.1}$$

The time index set  $\mathbb{T}$  is taken to be  $\mathbb{T} = \mathbb{Z}$  for discrete-time systems and  $\mathbb{T} = \mathbb{R}$  for

continuous-time systems.

We call the set of points

$$\Gamma = \{\mathbf{y} \in \mathcal{S} : \mathbf{y} = \phi(\mathbf{x}, t), t \in \mathbb{T}\} \quad (2.2)$$

the trajectory through the point  $\mathbf{x}$ , while

$$\Gamma^+ = \{\mathbf{y} \in \mathcal{S} : \mathbf{y} = \phi(\mathbf{x}, t), t > 0\} \quad \text{and} \quad \Gamma^- = \{\mathbf{y} \in \mathcal{S} : \mathbf{y} = \phi(\mathbf{x}, t), t < 0\} \quad (2.3)$$

are called the forward and backward trajectories, respectively. Often, where there is no ambiguity, we will use the term trajectory to refer to the forward trajectory through a point  $\mathbf{x}$ .

An invariant set in a dynamical system is a subset  $\mathcal{I} \subset \mathcal{S}$  such that if  $\mathbf{x} \in \mathcal{I}$  then the forward trajectory  $\Gamma^+$  through  $\mathbf{x}$  is a subset of  $\mathcal{I}$ . In other words, trajectories that start in, or enter into  $\mathcal{I}$ , do not leave  $\mathcal{I}$ . A closed and bounded invariant set  $\mathcal{A}$  is called an attractor of a dynamical system if

- for any sufficiently small neighbourhood  $\mathcal{C}$  of  $\mathcal{A}$ , there exists another neighbourhood  $\mathcal{D}$  of  $\mathcal{A}$  such that all forward trajectories starting in  $\mathcal{C}$  are contained in  $\mathcal{D}$ , and
- for all  $\mathbf{x} \in \mathcal{C}$ ,  $\phi(\mathbf{x}, t) \rightarrow \mathcal{A}$  as  $t \rightarrow \infty$ .

We call the maximal set  $\mathcal{B}$  such that when  $\mathbf{x} \in \mathcal{B}$ ,  $\phi(\mathbf{x}, t) \rightarrow \mathcal{A}$  as  $t \rightarrow \infty$  the basin of attraction of  $\mathcal{A}$ . This means that an attractor is a set of states in the state-space towards which nearby states in the attractor's basin of attraction evolve over time. As a result, the set of attractors of a dynamical system generally describe the long-term behaviour of the system and so the modern theory of dynamical systems focuses on the existence and stability of recurrent motions and attractors. The complexity of a dynamical system, its behaviours and importantly its attractors depend on the system's dimensionality, nonlinearity and nonsmoothness. While low-dimensional

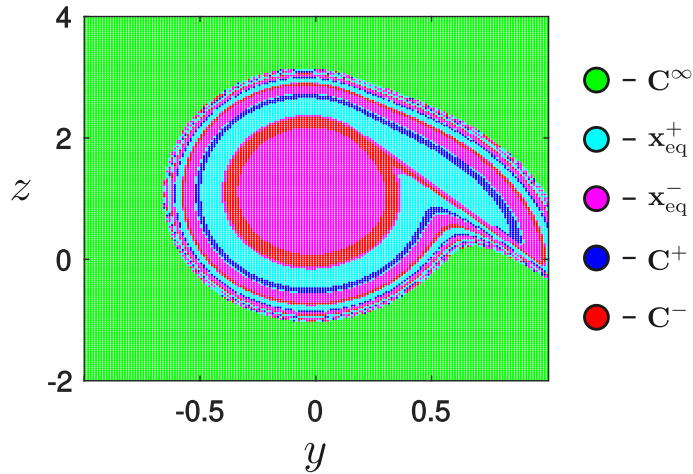


**Figure 2.1:** A 2-dimensional slice of the intertwined basins of attraction of five coexisting attractors in the Chua circuit. Each colour represents a different basin of attraction

smooth linear systems are easy to visualise, their dynamics and properties are limited compared to high-dimensional nonlinear and nonsmooth systems. Higher-dimensional nonlinear and nonsmooth dynamical systems can exhibit complex behaviours such as *multistability*, *quasi-periodicity* and *chaos*.

Later, when considering the effects of noise on nonsmooth dynamical systems, we will focus on the effects of noise on attractors. In particular, we will consider the effects of noise on systems with multiple attractors. In such multistable systems the size and structure of the basins of competing attractors will play key roles in determining the principal effects of noise on the system. We will see that, even in relatively simple nonsmooth systems, the structure of the systems' basins of attraction can have a very complicated structure. For example, Figure 2.1 shows the intertwined fractal structure of the basins of attraction of five coexisting attractors in the *Chua circuit* [39], a simple 3-dimensional piecewise-linear dynamical system that is discussed in detail in Chapter 9.

Before looking at some specifics for both discrete-time iterated maps and continuous-time flows in the smooth case, we will introduce some notation and conventions used throughout this thesis in our study and analysis of dynamical systems .

## 2.1 Notation and Conventions

Throughout this thesis we will take state-space vectors  $\mathbf{x} \in \mathbb{R}^n$ , and the value of their corresponding time derivatives or images under maps  $\mathbf{f}(\mathbf{x}) \in \mathbb{R}^n$ , to be column vectors.

We will use the *numerator layout* or the *Jacobian formulation* when calculating derivatives with respect to vectors [40]. Under this convention we lay out the derivative of a vector with respect to another vector according to the layout of the numerator and the transpose of the layout of the denominator. For example, this gives that, for a scalar function  $y : \mathbb{R}^n \rightarrow \mathbb{R}$ , a column vector  $\mathbf{x} \in \mathbb{R}^n$  and a scalar  $z \in \mathbb{R}$

$$\frac{\partial y}{\partial \mathbf{x}} = \left( \frac{\partial y}{\partial x_1} \quad \frac{\partial y}{\partial x_2} \quad \cdots \quad \frac{\partial y}{\partial x_n} \right) \in \mathbb{R}^{1 \times n}, \quad (2.4)$$

$$\frac{\partial \mathbf{x}}{\partial z} = \left( \frac{\partial x_1}{\partial z} \quad \frac{\partial x_2}{\partial z} \quad \cdots \quad \frac{\partial x_n}{\partial z} \right)^T \in \mathbb{R}^{n \times 1}, \quad (2.5)$$

while for column vectors  $\mathbf{y} \in \mathbb{R}^m$  and  $\mathbf{x} \in \mathbb{R}^n$

$$\frac{\partial \mathbf{y}}{\partial \mathbf{x}} = \begin{pmatrix} \frac{\partial y_1}{\partial x_1} & \frac{\partial y_1}{\partial x_2} & \cdots & \frac{\partial y_1}{\partial x_n} \\ \frac{\partial y_2}{\partial x_1} & \frac{\partial y_2}{\partial x_2} & \cdots & \frac{\partial y_2}{\partial x_n} \\ \vdots & & \ddots & \\ \frac{\partial y_m}{\partial x_1} & \frac{\partial y_m}{\partial x_2} & \cdots & \frac{\partial y_m}{\partial x_n} \end{pmatrix} \in \mathbb{R}^{m \times n}, \quad (2.6)$$

$$\frac{\partial \mathbf{x}}{\partial \mathbf{y}} = \begin{pmatrix} \frac{\partial x_1}{\partial y_1} & \frac{\partial x_1}{\partial y_2} & \cdots & \frac{\partial x_1}{\partial y_m} \\ \frac{\partial x_2}{\partial y_1} & \frac{\partial x_2}{\partial y_2} & \cdots & \frac{\partial x_2}{\partial y_m} \\ \vdots & & \ddots & \\ \frac{\partial x_n}{\partial y_1} & \frac{\partial x_n}{\partial y_2} & \cdots & \frac{\partial x_n}{\partial y_m} \end{pmatrix} \in \mathbb{R}^{n \times m}. \quad (2.7)$$

In addition, where there is no ambiguity, we will use subscript notation for derivatives, i.e.

$$y_{\mathbf{x}} = \frac{\partial y}{\partial \mathbf{x}}, \quad \mathbf{x}_z = \frac{\partial \mathbf{x}}{\partial z}, \quad \mathbf{y}_{\mathbf{x}} = \frac{\partial \mathbf{y}}{\partial \mathbf{x}}, \quad \mathbf{x}_{\mathbf{y}} = \frac{\partial \mathbf{x}}{\partial \mathbf{y}}. \quad (2.8)$$

## 2.2 Smooth Maps

In the discrete-time case, where  $t \in \mathbb{T} = \mathbb{Z}$ , we describe dynamical systems as iterated maps, that is

$$\mathbf{x}_{t+1} = \mathbf{f}(\mathbf{x}_t), \quad \mathbf{x}_0 \in \mathcal{S} \subset \mathbb{R}^n, \quad (2.9)$$

so that

$$\phi(\mathbf{x}_0, t) = \mathbf{x}_t = \mathbf{f}(\mathbf{x}_{t-1}) = \mathbf{f} \circ \mathbf{f} \circ \cdots \circ \mathbf{f}(\mathbf{x}_0) = \mathbf{f}^t(\mathbf{x}_0), \quad (2.10)$$

where  $\mathbf{x}_t \in \mathcal{S} \subset \mathbb{R}^n$  is the state at time  $t$ ,  $\mathbf{x}_0$  is the system's initial condition and  $\mathbf{f} : \mathcal{S} \rightarrow \mathcal{S}$ , which is  $C^k$  for some  $k \geq 1$ , is the corresponding mapping.

The simplest example of an invariant set of a map consists of a single point known as a fixed point, that is a point  $\mathbf{x}^*$  such that

$$\mathbf{x}^* = \mathbf{f}(\mathbf{x}^*) = \mathbf{f}^t(\mathbf{x}^*), \quad \forall t \in \mathbb{T}. \quad (2.11)$$

The next simplest example of an invariant set of a map is a periodic orbit of period  $p$ , that is a set of  $p$  points  $\Gamma_p = \{\mathbf{x}_1^*, \mathbf{x}_2^*, \dots, \mathbf{x}_p^*\}$  such that

$$\mathbf{x}_i^* = \mathbf{f}^p(\mathbf{x}_i^*) = \mathbf{f}^{pt}(\mathbf{x}_i^*), \quad i = 1, 2, \dots, p, \quad \forall t \in \mathbb{T} \quad (2.12)$$

and

$$\mathbf{x}_{(i+1) \bmod p}^* = \mathbf{f}(\mathbf{x}_i^*), \quad i = 1, 2, \dots, p. \quad (2.13)$$

We note that a period- $p$  point of a map  $\mathbf{f} : \mathcal{S} \rightarrow \mathcal{S}$  is simply a fixed point of the map  $\mathbf{f}^p : \mathcal{S} \rightarrow \mathcal{S}$ .

In Section 2.4 we will discuss when these invariant sets are attractors of the dynamical system and how they can be related to invariant sets in the continuous-time case. First, in Section 2.3 we will give a brief overview of continuous-time flows.

## 2.3 Smooth Flows

In the continuous-time case, where  $t \in \mathbb{T} = \mathbb{R}$ , we describe dynamical systems as systems of ordinary differential equations

$$\dot{\mathbf{x}} = \mathbf{f}(\mathbf{x}), \quad \mathbf{x} \in \mathcal{S} \subset \mathbb{R}^n, \quad (2.14)$$

so that the *flow function*  $\phi(\mathbf{x}, t)$  satisfies

$$\phi_t(\mathbf{x}, t) = \mathbf{f}(\phi(\mathbf{x}, t)), \quad \phi(\mathbf{x}, 0) = \mathbf{x}, \quad (2.15)$$

where  $\mathbf{x} \in \mathcal{S} \subset \mathbb{R}^n$  is the state,  $\dot{\mathbf{x}} \in \mathbb{R}^n$  is the time derivative of the state and  $\mathbf{f}$ , which is  $C^k$  for some  $k \geq 1$ , is the corresponding vector field. Given a  $C^k$  vector field the flow function  $\phi(\mathbf{x}, t)$ , and hence the dynamical system, is  $C^{k+1}$ .

Analogously to a fixed point in an iterated map, the simplest example of an invariant set of a flow consists of a single point known as an equilibrium point. An equilibrium point  $\mathbf{x}^*$  is a point such that

$$\mathbf{x}^* = \phi(\mathbf{x}^*, t), \quad \forall t \in \mathbb{T}. \quad (2.16)$$

or equivalently

$$\mathbf{f}(\mathbf{x}^*) = 0. \quad (2.17)$$

The next simplest example of an invariant set of a flow is a periodic orbit of period  $\tau$ , that is a state-space trajectory  $\Gamma_\tau$  that forms a closed curve with

$$\mathbf{x} = \phi(\mathbf{x}, \tau), \quad \forall \mathbf{x} \in \Gamma_\tau. \quad (2.18)$$

Other possible invariant sets include quasi-periodic orbits, which correspond to invariant topological circles of maps, and chaotic sets. However, we will restrict our

focus to the effects of noise on simpler dynamical behaviour and in the following section we will describe how we can determine the *stability* of such invariant sets.

## 2.4 Stability and Poincaré Maps

When we analyse dynamical systems, arising from models of real-world systems, *stable* behaviour is generally of most interest. The stability of a state-space trajectory in a dynamical system is a measure of its sensitivity to perturbations. Roughly speaking, we will call a reference trajectory *Lyapunov stable* if the forward trajectories of nearby trajectories always remain close to the reference forward trajectory. The reference trajectory is called *asymptotically stable* if nearby trajectories converge to the reference trajectory as  $t \rightarrow \infty$ . In this way an invariant set that is asymptotically stable can for our purposes be considered synonymous to the concept of an attractor.

More formally, a reference trajectory  $\phi(\mathbf{x}, t)$  in a dynamical system is called Lyapunov stable if  $\forall \epsilon > 0, \exists \delta > 0$  such that if  $\|\mathbf{x} - \mathbf{y}\| < \delta$  then  $\|\phi(\mathbf{x}, t) - \phi(\mathbf{y}, t)\| < \epsilon$  for  $t > 0$ . It is asymptotically stable if it is Lyapunov stable and  $\exists \delta^* > 0$  such that if  $\|\mathbf{x} - \mathbf{y}\| < \delta^*$ , then  $\phi(\mathbf{y}, t) \rightarrow \phi(\mathbf{x}, t)$  as  $t \rightarrow \infty$ .

In order to understand the stability of a given reference trajectory with initial condition  $\mathbf{x}_0^{\text{ref}}$  we need to understand the nature and behaviour of nearby trajectories. Such a local analysis can be achieved by a linear approximation about the reference trajectory. For a flow given by (2.14) we find that

$$\phi(\mathbf{x}, t) - \phi(\mathbf{x}_0^{\text{ref}}, t) \approx \phi_{\mathbf{x}}(\mathbf{x}_0^{\text{ref}}, t)(\mathbf{x} - \mathbf{x}_0^{\text{ref}}), \quad (2.19)$$

where the Jacobian  $\phi_{\mathbf{x}}(\mathbf{x}_0^{\text{ref}}, t)$ , which is sometimes referred to as the *fundamental matrix solution* of the trajectory, is the solution to

$$\dot{\Phi}(\mathbf{x}, t) = \mathbf{f}_{\mathbf{x}}(\phi(\mathbf{x}_0^{\text{ref}}, t))\Phi(\mathbf{x}, t), \quad \Phi(\mathbf{x}, 0) = \mathbf{I}, \quad (2.20)$$

with  $\Phi(\mathbf{x}, t) = \phi_{\mathbf{x}}(\mathbf{x}, t)$ , where the differential equation (2.20) is known as the *first variational equation* and  $\mathbf{I}$  is the identity matrix.

For simplicity, we will concentrate on the stability of equilibrium points of flows and fixed points of maps. Although the variational equation can be used in the stability analysis of periodic orbits of flows we will show later in this section that we can simply consider periodic orbits of flows as fixed points of maps by constructing *Poincaré maps*. We have also shown earlier that periodic orbits in iterated maps are simply fixed points of higher-order maps.

In the case where  $\mathbf{x}_0^{\text{ref}}$  is an equilibrium point we have that

$$\mathbf{f}_{\mathbf{x}}(\phi(\mathbf{x}_0^{\text{ref}}, t)) = \mathbf{f}_{\mathbf{x}}(\mathbf{x}_0^{\text{ref}}) \quad (2.21)$$

and so it follows directly that

$$\phi(\mathbf{x}, t) - \phi(\mathbf{x}_0^{\text{ref}}, t) \approx e^{\mathbf{f}_{\mathbf{x}}(\mathbf{x}_0^{\text{ref}})t}(\mathbf{x} - \mathbf{x}_0^{\text{ref}}). \quad (2.22)$$

This means that the equilibrium point  $\mathbf{x}_0^{\text{ref}}$  is asymptotically stable if the real parts of all of the eigenvalues of  $\mathbf{f}_{\mathbf{x}}(\mathbf{x}_0^{\text{ref}})$  are negative. Conversely, if any of the real parts of the eigenvalues is positive the equilibrium point is unstable. We refer to equilibrium points as *hyperbolic* if none of the eigenvalues lie on the imaginary axis and *non-hyperbolic* or *degenerate* otherwise.

Similarly, for an iterated map given by (2.9), linearisation about a fixed point  $\mathbf{x}_0^{\text{ref}}$  gives that

$$\phi(\mathbf{x}, t) - \phi(\mathbf{x}_0^{\text{ref}}, t) = \mathbf{f}^t(\mathbf{x}) - \mathbf{f}^t(\mathbf{x}_0^{\text{ref}}) \approx (\mathbf{f}_{\mathbf{x}}(\mathbf{x}_0^{\text{ref}}))^t (\mathbf{x} - \mathbf{x}_0^{\text{ref}}). \quad (2.23)$$

It follows that  $\mathbf{x}_0^{\text{ref}}$  is asymptotically stable if all the eigenvalues  $\lambda \in \mathbb{C}$  of  $\mathbf{f}_{\mathbf{x}}(\mathbf{x}_0^{\text{ref}})$  are less than unity in magnitude, and unstable if at least one eigenvalue lies outside the unit circle. We refer to the fixed point as hyperbolic if none of the eigenvalues lie on

the unit circle and non-hyperbolic or degenerate otherwise.

Let us now introduce the concept of a Poincaré map that allows us to treat a periodic solution of a continuous-time flow as a fixed point of a discrete-time map. First we construct a codimension-one surface  $\mathcal{P}$  in state space called a *Poincaré section*. We assume that  $\mathcal{P}$  can be described as the zeros of a real-valued function  $h_{\mathcal{P}}$ , i.e.

$$\mathcal{P} = \{\mathbf{x} \in \mathcal{S} : h_{\mathcal{P}}(\mathbf{x}) = 0\}. \quad (2.24)$$

In particular we choose  $\mathcal{P}$  such that the periodic orbit under study intersects the surface transversally at  $\mathbf{x}_{\mathcal{P}}$ , so that

$$h_{\mathcal{P},\mathbf{x}}(\mathbf{x}_{\mathcal{P}})\mathbf{f}(\mathbf{x}_{\mathcal{P}}) \neq 0. \quad (2.25)$$

We then define the Poincaré map  $\mathbf{M}_{\mathcal{P}} : \mathcal{P} \rightarrow \mathcal{P}$  local to  $\mathbf{x}_{\mathcal{P}}$  as the map that takes points near  $\mathbf{x}_{\mathcal{P}}$  to their next intersection with  $\mathcal{P}$  near  $\mathbf{x}_{\mathcal{P}}$  along their forward trajectory. In other words,

$$M_{\mathcal{P}}(\mathbf{x}) = \phi(\mathbf{x}, \tau_{\mathcal{P}}(\mathbf{x})), \quad (2.26)$$

where  $\tau_{\mathcal{P}}(\mathbf{x})$  is the time closest to the period of the periodic orbit  $\tau$ , such that

$$h_{\mathcal{P}}(\phi(\mathbf{x}, \tau_{\mathcal{P}}(\mathbf{x}))) = 0. \quad (2.27)$$

In particular, we note that  $\mathbf{x}_{\mathcal{P}}$  is a fixed point of the Poincaré map, and thus  $\mathbf{M}_{\mathcal{P}}(\mathbf{x}_{\mathcal{P}}) = \mathbf{x}_{\mathcal{P}}$ , and  $\tau_{\mathcal{P}}(\mathbf{x}_{\mathcal{P}}) = \tau$ .

Although it is generally impossible to find a closed formula for  $\mathbf{M}_{\mathcal{P}}$  we can find the stability of the periodic orbit by finding the stability of the fixed point  $\mathbf{x}_{\mathcal{P}}$  by linearising the map and examining the eigenvalues of  $\mathbf{M}_{\mathcal{P},\mathbf{x}}(\mathbf{x}_{\mathcal{P}})$  as described in (2.23).

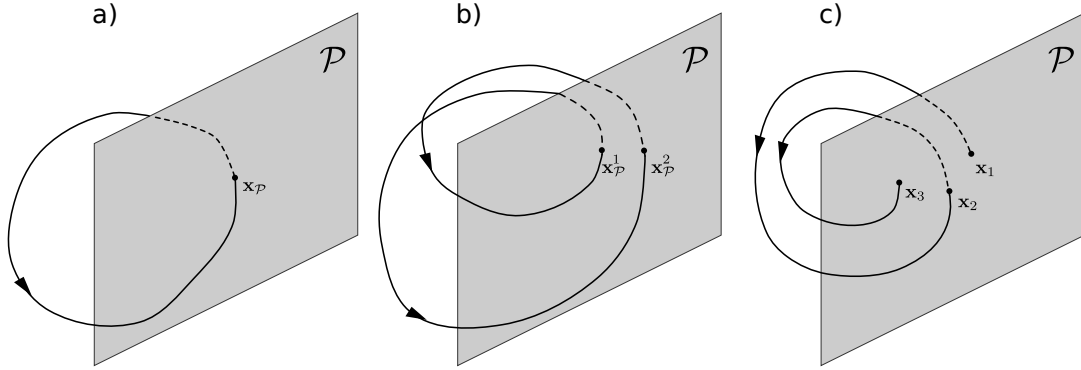


**Figure 2.2:** a) The fixed point  $\mathbf{x}_P$  of a Poincaré map corresponding to a period- $\tau$  periodic orbit in a flow. b) The periodic orbit  $\{\mathbf{x}_P^1, \mathbf{x}_P^2\}$  of a Poincaré map corresponding to a higher period periodic orbit in a flow. c) The first three iterates of a Poincaré mapping starting at  $\mathbf{x}_1$ .

It remains to find an expression for  $\mathbf{M}_{P,\mathbf{x}}(\mathbf{x}_P)$ . We find that

$$\mathbf{M}_{P,\mathbf{x}}(\mathbf{x}_P) = \phi_{\mathbf{x}}(\mathbf{x}_P, \tau) + \phi_t(\mathbf{x}_P, \tau)\tau_{P,\mathbf{x}}(\mathbf{x}_P), \quad (2.28)$$

and given (2.25) the Implicit Function Theorem (IFT) guarantees that  $\tau_P(\mathbf{x})$  has a locally unique differentiable solution near  $\mathbf{x} = \mathbf{x}_P$ . Implicit differentiation of (2.27) gives

$$\tau_{\mathbf{x}}(\mathbf{x}_P) = -\frac{h_{P,\mathbf{x}}(\mathbf{x}_P)\phi_{\mathbf{x}}(\mathbf{x}_P, \tau)}{h_{P,\mathbf{x}}(\mathbf{x}_P)\phi_t(\mathbf{x}_P, \tau)}, \quad (2.29)$$

hence

$$\begin{aligned} \mathbf{M}_{P,\mathbf{x}}(\mathbf{x}_P) &= \left( \mathbf{I} - \frac{\phi_t(\mathbf{x}_P, \tau)h_{P,\mathbf{x}}(\mathbf{x}_P)}{h_{P,\mathbf{x}}(\mathbf{x}_P)\phi_t(\mathbf{x}_P, \tau)} \right) \phi_{\mathbf{x}}(\mathbf{x}_P, \tau) \\ &= \left( \mathbf{I} - \frac{\mathbf{f}(\mathbf{x}_P)h_{P,\mathbf{x}}(\mathbf{x}_P)}{h_{P,\mathbf{x}}(\mathbf{x}_P)\mathbf{f}(\mathbf{x}_P)} \right) \phi_{\mathbf{x}}(\mathbf{x}_P, \tau). \end{aligned} \quad (2.30)$$

We note that multiplying a vector by  $\mathbf{M}_{P,\mathbf{x}}(\mathbf{x}_P)$  is simply a projection of the result of multiplying by the *monodromy matrix* or fixed time mapping  $\phi_{\mathbf{x}}(\mathbf{x}_P, \tau)$  associated with the periodic orbit, onto  $\mathcal{P}$ . This makes sense since we also have that  $\mathbf{M}_P(\mathbf{x})$

can be written as

$$M_{\mathcal{P}}(\mathbf{x}) = \phi(\mathbf{x}, \tau_{\mathcal{P}}(\mathbf{x})) = \phi(\phi(\mathbf{x}, \tau), \tau_{\mathcal{P}}(\mathbf{x}) - \tau), \quad (2.31)$$

where  $\tau_{\mathcal{P}}(\mathbf{x}) - \tau \lll 1$  for  $\mathbf{x}$  close to  $\mathbf{x}_{\mathcal{P}}$ . At least one eigenvalue of  $\phi_{\mathbf{x}}(\mathbf{x}_{\mathcal{P}}, \tau)$  is equal to one, and this eigenvalue corresponds to the eigenvector  $\mathbf{f}(\mathbf{x}_{\mathcal{P}})$ , i.e. deviations tangential to the periodic orbit. This eigenvalue also corresponds to a zero eigenvalue of  $\mathbf{M}_{\mathcal{P}, \mathbf{x}}(\mathbf{x}_{\mathcal{P}})$ . Apart from this trivial eigenvalue the eigenvalues of the monodromy matrix and the Poincaré map are the same. We will sometimes call these eigenvalues *Floquet multipliers* or simply *multipliers*. Based on our arguments for fixed points of iterated maps earlier, we say that a periodic orbit is stable if the multipliers of its Poincaré map are less than unity in magnitude and unstable if at least one of the multipliers lies outside the unit circle in the complex plane.

## 2.5 Bifurcations

Nonlinear dynamical systems arising from models of real-world systems tend to have several parameters that affect their behaviour. A *bifurcation* may be defined as a qualitative change in the structural behaviour of a dynamical system under parameter variation. By qualitative changes in the structural behaviour of a dynamical system we mean changes in the number or stability properties of attractors. Bifurcations are of particular interest to us as it has been shown that noise tends to have its largest effects close to bifurcation points.

Bifurcations can be split into two main categories, *local bifurcations* and *global bifurcations*. Local bifurcations are bifurcations that can be detected by changes in local stability as parameters change. Bifurcations that can not be found in this way are called global bifurcations. Bifurcations can also be categorised by their *codimension*, the number of independent conditions that need to be satisfied for the bifurcation to occur. In this thesis we restrict our attention to codimension-one

bifurcations.

Here we give a brief overview of the types of bifurcations that are most relevant to this thesis. In particular, we will focus on local bifurcations of fixed points of maps. Through Poincaré and higher-order maps these bifurcations will also allow us to understand local bifurcations of periodic orbits of flows and maps. We will also discuss the associated bifurcations of equilibrium points of flows.

A local codimension-1 bifurcation of a periodic orbit of a flow or a fixed point of an iterated map corresponds to one of the eigenvalues of the linearised map crossing through the unit circle in the complex plane. The nature of the bifurcation depends on how this crossing is achieved. Similarly, a local bifurcation of an equilibrium point of flow corresponds to an eigenvalue passing through the imaginary axis. Figure 2.3 summarises some of these codimension-1 bifurcations that appear in systems considered in this thesis. Local bifurcations of equilibria and fixed points have been extensively studied and classified, see for example the work of Guckenheimer and Holmes [34], Kuznetsov [35] or Wiggins [36]. All these bifurcations, which are called *steady bifurcations* of equilibria of flows, have direct analogs for maps. They occur in a map when one of the eigenvalues of the corresponding Jacobian passes through  $+1$  and in a flow when one of the eigenvalues passes through  $0$  as the bifurcation parameter  $\mu$  is varied.

Figure 2.3 a) shows a *saddle-node* or *fold* bifurcation. A saddle-node bifurcation involves the collision and subsequent annihilation of two fixed points or equilibria or the sudden appearance of two fixed points or equilibria. In one-dimensional systems the two fixed points or equilibria have opposite stability, however this is not guaranteed in higher-dimensional systems. In the context of a Poincaré map this bifurcation involves the collision and disappearance of two periodic orbits as one of the Floquet multipliers passes through  $+1$ .

Figure 2.3 b) shows a *transcritical bifurcation*. In this bifurcation two branches of fixed points or equilibrium points cross transversally and exchange stability properties. In

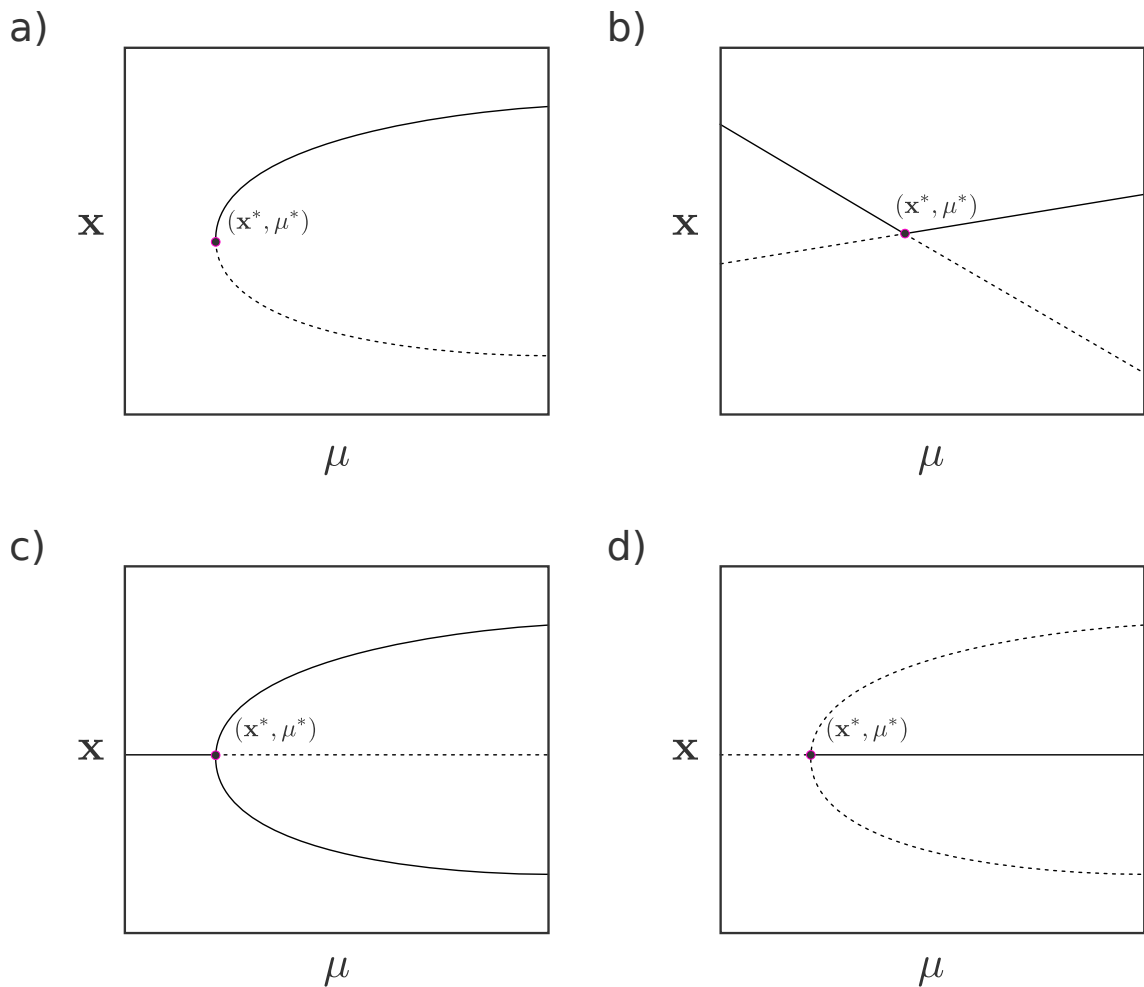


**Figure 2.3:** Bifurcation diagrams for the main local bifurcations of fixed points of maps or equilibria of flows which appear in this thesis. In all four bifurcation diagrams the bifurcation point  $(\mathbf{x}^*, \mu^*)$  is indicated by a circle, solid lines correspond to stable branches and dashed lines correspond to unstable branches. a) Saddle-node or fold bifurcation. b) Transcritical bifurcation. c) Supercritical pitchfork bifurcation. d) Subcritical pitchfork bifurcation.

the context of a Poincaré map of a two-dimensional flow this bifurcation corresponds to a stable and unstable periodic-orbit existing locally on each side of the bifurcation point.

Figure 2.3 c) and d) show *pitchfork bifurcations*. In a pitchfork bifurcation there is a single branch of fixed points that change stability in the bifurcation and two additional branches of fixed points are born with the opposite stability to that of the single branch. Pitchfork bifurcations are sometimes called *symmetry breaking bifurcations* as, for systems with  $\mathbf{Z}_2$  symmetry, the original branch of solutions are invariant under the action of the symmetry group but the bifurcating branches are not. In the *supercritical* case a stable fixed point becomes unstable and two stable fixed points are born while in the *subcritical* case an unstable fixed point becomes stable and two unstable fixed points are born. In a Poincaré map this bifurcation corresponds to a periodic orbit splitting into two periodic orbits of the same stability as the original periodic orbit separated by a periodic orbit of the opposite stability.

Other local bifurcations of maps and flows also exist, but we do not encounter them in this thesis. For example, *period-doubling* bifurcations of maps occur when one of the eigenvalues passes through  $-1$ . In such bifurcations a fixed point switches stability and a period-2 orbit of the same stability as the original stability of the fixed point is born. There is no direct analog of this for equilibrium points of flows. In 2 or higher-dimensional flows a *Hopf* bifurcation involves the birth of a limit cycle and occurs when a complex-conjugate pair of eigenvalues cross the imaginary axis, the analog form maps is the *Neimark-Sacker* bifurcation where a complex conjugate pair of eigenvalues cross the unit circle and an invariant circle is born. In the context of a Poincaré map the Neimark-Sacker bifurcation corresponds to the birth of an invariant torus.

Although we deal mainly with local bifurcations in this thesis we do encounter one global bifurcation in Chapter 9. As we have mentioned before, global bifurcations cannot be detected by examining the eigenvalues of the linearised system, instead

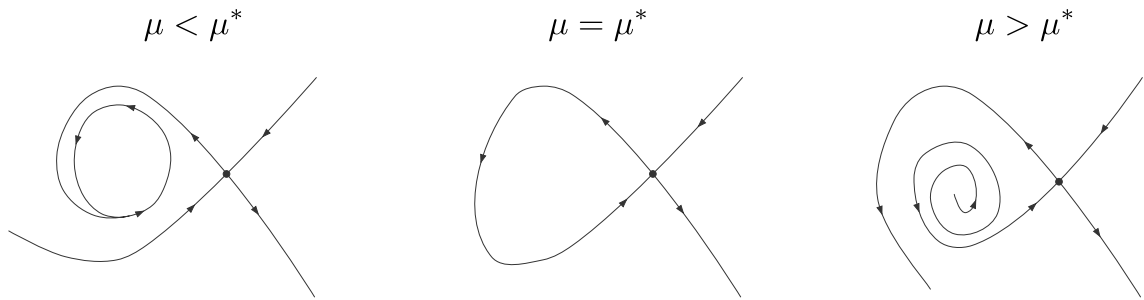


**Figure 2.4:** Schematic showing the destruction of a stable periodic orbit in a homoclinic connection at  $\mu = \mu^*$ .

global bifurcations tend to occur when the topology of stable and unstable manifolds change. The example of a global bifurcation we encounter in Chapter 9 is a *homoclinic bifurcation*. In this bifurcation, which is shown in Figure 2.4, the stable and unstable manifold of the same invariant set intersect for some value of the bifurcation parameter  $\mu$ . In our case this causes the destruction of a stable periodic orbit. Other global bifurcations include *heteroclinic bifurcations* where the stable and unstable manifolds of two or more different invariant sets coincide for some value of  $\mu$ . Heteroclinic bifurcations can also result in the annihilation of periodic attractors or other more complex phenomena.

## 2.6 Continuation

So far we have discussed the stability and bifurcations of periodic-orbits in flows, but we have not described any methodology for locating such orbits. In this section we will briefly outline a method for locating stable or unstable periodic solutions and a *continuation* or *path-following* algorithm for following those periodic solutions under parameter variation. The method we describe here that is used throughout the thesis is known as the *shooting method*. A more in-depth treatment and more complex methods such as the pseudo-arclength method can be found in texts such as [41, 42, 43, 44]. Many software packages are also freely available such as AUTO [45] and the MATLAB package MATCONT [46].

Suppose that the periodic orbit of period  $\tau$  we wish to locate intersects the Poincaré section  $\mathcal{P} = \{\mathbf{x} : h_{\mathcal{P}}(\mathbf{x}) = 0\}$  transversally, at some point  $\mathbf{x}_{\mathcal{P}}$ , where both  $\mathbf{x}_{\mathcal{P}}$  and  $\tau$  are unknown. We then have a system of  $n + 1$  equations in  $n + 1$  unknowns given by

$$h_{\mathcal{P}}(\mathbf{x}_{\mathcal{P}}) = 0 \tag{2.32}$$

and

$$\phi(\mathbf{x}_{\mathcal{P}}, \tau) = \mathbf{x}_{\mathcal{P}}. \tag{2.33}$$

With good initial guesses  $\mathbf{x}_0 \approx \mathbf{x}_{\mathcal{P}}$  and  $\tau_0 \approx \tau$  we can now use Newton's method to solve for  $\mathbf{x}_{\mathcal{P}}$  and  $\tau$

$$\begin{pmatrix} \mathbf{x}_{k+1} \\ \tau_{k+1} \end{pmatrix} = \begin{pmatrix} \mathbf{x}_k \\ \tau_k \end{pmatrix} - \mathbf{N}^{-1} \begin{pmatrix} \phi(\mathbf{x}_k, \tau_k) - \mathbf{x}_k \\ h_{\mathcal{P}}(\mathbf{x}_k) \end{pmatrix}, \tag{2.34}$$

where

$$\mathbf{N} = \begin{pmatrix} \phi_{\mathbf{x}}(\mathbf{x}_k, \tau_k) - \mathbf{I} & \phi_t(\mathbf{x}_k, \tau_k) \\ h_{\mathcal{P},\mathbf{x}}(\mathbf{x}_k) & 0 \end{pmatrix}. \tag{2.35}$$

Given sufficiently good initial guesses the iterates of (2.34) will converge to the correct values quadratically in the error so that

$$\begin{pmatrix} \mathbf{x}_k \\ \tau_k \end{pmatrix} \rightarrow \begin{pmatrix} \mathbf{x}_{\mathcal{P}} \\ \tau \end{pmatrix} \quad \text{as } k \rightarrow \infty. \tag{2.36}$$

In practice, initial guesses often arise from direct numerical simulation of the system.

Now, suppose a hyperbolic periodic orbit transversal to  $\mathcal{P}$  has been found using the method outlined above or otherwise. We will employ a continuation or path following algorithm to follow the periodic solution as we change the parameter values. Under small parameter variation this periodic orbit is guaranteed to persist and so we will try to locate the point it crosses the Poincaré section  $\mathbf{x}'_{\mathcal{P}}$  and its period  $\tau'$  using (2.34). We use our knowledge of the actual values of  $\mathbf{x}_{\mathcal{P}}$  and  $\tau$  previously found to

inform our initial guesses for  $\mathbf{x}'_{\mathcal{P}}$  and  $\tau'$ . Once the periodic solution has been located for more than one set of parameter values we can use extrapolation techniques to produce good initial guesses for the Newton scheme. The most simple extrapolation method to use is linear extrapolation where we take our initial guesses to be

$$\begin{pmatrix} \mathbf{x}_0 \\ \tau_0 \end{pmatrix} = \begin{pmatrix} 2\mathbf{x}_{\mathcal{P}}^2 - \mathbf{x}_{\mathcal{P}}^1 \\ 2\tau^2 - \tau^1 \end{pmatrix}, \quad (2.37)$$

where  $\mathbf{x}_{\mathcal{P}}^1$ ,  $\mathbf{x}_{\mathcal{P}}^2$ ,  $\tau^1$  and  $\tau^2$  are the two previously found intersections with  $\mathcal{P}$  and periods, respectively. More complex extrapolation methods can also be used depending on the situation, for example quadratic extrapolation close to saddle-node bifurcations. This method was used when locating unstable periodic orbits close to bifurcation in the Chua circuit in Chapter 9.



# Chapter 3

## Nonsmooth Systems

We now introduce the types of dynamical systems that we are most interested in, namely, nonsmooth dynamical systems. In this chapter we will briefly introduce three types of nonsmooth dynamical systems: *piecewise-smooth maps*, *piecewise-smooth flows* and *hybrid systems*. For our purposes, the terms nonsmooth and piecewise-smooth can be treated as synonymous, and like much of the literature we will use them interchangeably. We will also introduce the concept of a *discontinuity mapping* and present a derivation of the *square root map*, topics which are central to the papers that comprise the bulk of this thesis. For more information on nonsmooth dynamical systems one can consult the foundational book of di Bernardo *et al.* [22], or the review papers [1, 18, 47].

### 3.1 Nonsmooth Maps

Recall from Chapter 2 that a smooth map is described by

$$\mathbf{x}_{t+1} = \mathbf{f}(\mathbf{x}_t), \quad \mathbf{x}_0 \in \mathcal{S} \subset \mathbb{R}^n, \quad (3.1)$$

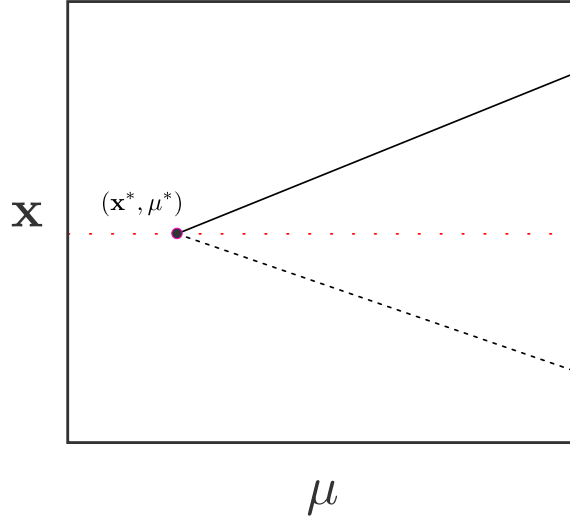


**Figure 3.1:** Bifurcation diagram of a nonsmooth fold at  $(\mathbf{x}^*, \mu^*)$ . Here the dotted red line represents the discontinuity boundary. Solid black lines correspond to stable branches and dashed lines correspond to unstable branches of equilibria.

where  $\mathbf{x}_t \in \mathcal{S} \subset \mathbb{R}^n$  is the state at time  $t \in \mathbb{T} = \mathbb{Z}$  and  $\mathbf{f} : \mathcal{S} \rightarrow \mathcal{S}$ , which is  $C^k$  is the corresponding mapping. A nonsmooth or piecewise-smooth map is a map defined by a finite set of smooth maps

$$\begin{aligned} \mathbf{x}_{k+1} &= \mathbf{f}_i(\mathbf{x}_k), \quad \mathbf{x}_k \in \mathcal{S}_i, \\ \mathbf{x}_0 &\in \mathcal{S} \subset \mathbb{R}^n, \end{aligned} \tag{3.2}$$

where  $\cup_i \mathcal{S}_i = \mathcal{S} \subset \mathbb{R}^n$  and each  $\mathcal{S}_i$  has a nonempty interior. The intersection  $\Sigma_{ij} = \mathcal{S}_i \cap \mathcal{S}_j$  is either the empty set or an  $(n-1)$ -dimensional manifold which is the boundary between  $\mathcal{S}_i$  and  $\mathcal{S}_j$ .

As we have discussed previously, nonsmooth maps display phenomena not seen in smooth maps. One example of this is a simple discontinuity-induced bifurcation known as a *border-collision* bifurcation. A border-collision bifurcation occurs when a branch of fixed points in one region of the map  $\mathcal{S}_i$  crosses a boundary  $\Sigma_{ij}$ , under parameter variation. There are many possible outcomes of a border-collision bifurcation, here we will mention one of the simplest which is known as a *nonsmooth*

*fold* and is shown in Figure 3.1. Nonsmooth folds are crucial in the creation of the period-adding cascade of the *square root map*, which we study under the influence of additive noise in Chapters 7 and 8. In a nonsmooth fold, a branch of equilibria in  $\mathcal{S}_i$  and a separate branch of equilibria in  $\mathcal{S}_j$  collide with the boundary for some value of the bifurcation parameter  $\mu^*$ . Beyond this value both branches of equilibria are virtual, i.e. the branch of fixed points given by the map  $\mathbf{f}_i$  lies in  $\mathcal{S}_j$  and vice-versa.

## 3.2 Piecewise-smooth Flows and Hybrid Systems

As stated in Chapter 2, smooth continuous time dynamical systems can be described as initial value problems (IVPs) given by

$$\dot{\mathbf{x}} = \mathbf{f}(\mathbf{x}), \quad \mathbf{x}(0) = \mathbf{x}_0, \quad (3.3)$$

where  $\mathbf{x} \in \mathcal{S} \subset \mathbb{R}^n$  is the state,  $\dot{\mathbf{x}} \in \mathbb{R}^n$  the time derivative of the state and  $\mathbf{f}$ , which is  $C^k$  (with  $k \geq 1$ ), the corresponding vector field. We also define the flow function  $\phi(\mathbf{x}, t)$ , which is  $C^k$  in its arguments, as the collection of trajectories given by  $\mathbf{f}$ , such that the unique solution to (3.3) can be written

$$\mathbf{x}(t) = \phi(\mathbf{x}_0, t). \quad (3.4)$$

Piecewise-smooth flows can be described as IVPs given by

$$\begin{aligned} \dot{\mathbf{x}} &= \mathbf{f}_i(\mathbf{x}), \quad \mathbf{x} \in \mathcal{S}_i, \\ \mathbf{x}(0) &= \mathbf{x}_0, \end{aligned} \quad (3.5)$$

where  $\cup_i \mathcal{S}_i = \mathcal{S} \subset \mathbb{R}^n$  and each  $\mathcal{S}_i$  has a nonempty interior. The indices  $i$  range over some finite indexing set and the intersection  $\Sigma_{ij} = \mathcal{S}_i \cap \mathcal{S}_j$  is either the empty set or an  $(n - 1)$ -dimensional manifold which is the boundary between  $\mathcal{S}_i$  and  $\mathcal{S}_j$ . In *Filippov systems*, i.e. systems where  $\mathbf{f}_i \neq \mathbf{f}_j$  on the boundary  $\Sigma_{ij}$ , we note that there

is a possibility of *sliding motion*. Suppose that  $\Sigma_{ij}$  is defined by the function  $h_{ij}$ , so that

$$\Sigma_{ij} = \{\mathbf{x} \in \mathcal{S} : h_{ij}(\mathbf{x}) = 0\}. \quad (3.6)$$

We call the region

$$\Sigma_{ij}^s = \{\mathbf{x} \in \Sigma_{ij} : (h_{ij,\mathbf{x}}(\mathbf{x})\mathbf{f}_i(\mathbf{x}))(h_{ij,\mathbf{x}}(\mathbf{x})\mathbf{f}_j(\mathbf{x})) < 0\}, \quad (3.7)$$

where the component of  $\mathbf{f}_i$  normal to the boundary has the opposite sign to the component of  $\mathbf{f}_j$  normal to the boundary, the *sliding region*. In this region the boundary is either simultaneously attracting or repelling with respect to both vector fields. Thus, it is important to be able to define the *sliding vector field*  $\mathbf{f}_{ij}^s$  on the boundary for these regions. One method for defining this vector field is *Filippov's convex method* [48], where we take a convex combination of  $\mathbf{f}_i$  and  $\mathbf{f}_j$ , so that

$$\mathbf{f}_{ij}^s = \left(1 - \frac{h_{ij,\mathbf{x}}\mathbf{f}_i}{h_{ij,\mathbf{x}}(\mathbf{f}_i - \mathbf{f}_j)}\right)\mathbf{f}_i + \left(\frac{h_{ij,\mathbf{x}}\mathbf{f}_i}{h_{ij,\mathbf{x}}(\mathbf{f}_i - \mathbf{f}_j)}\right)\mathbf{f}_j. \quad (3.8)$$

Another method for constructing the sliding vector field which can produce subtly different results is *Utkin's equivalent control method* [49]. More recently Jeffrey has generalised Filippov's method to introduce nonlinear sliding modes, revealing the potential for *hidden dynamics* on the boundary and other complex phenomena [50, 51].

A *hybrid system* is a generalisation of a piecewise-smooth dynamical system where a non-identity mapping  $\mathbf{j}_{ij}$  is applied on the boundary  $\Sigma_{ij}$ . In other words, a hybrid system is a dynamical system defined by the IVP

$$\begin{aligned} \dot{\mathbf{x}} &= \mathbf{f}_i(\mathbf{x}), & \mathbf{x} &\in \mathcal{S}_i, \\ \mathbf{x}(0) &= \mathbf{x}_0, \end{aligned} \quad (3.9)$$

with the addition of the set of jump maps

$$\mathbf{x} \rightarrow \mathbf{j}_{ij}(\mathbf{x}), \quad \mathbf{x} \in \Sigma_{ij}. \quad (3.10)$$

Provided  $\mathbf{j}_{ij}$  is not the identity mapping (in which case the system is simply a piecewise-smooth vector field) the hybrid system undergoes state jumps, unlike Filippov systems or piecewise-smooth flows that only undergo jumps in the vector field or its time derivatives.

### 3.3 Discontinuity Mappings

Suppose now that we wish to calculate the local mapping of a trajectory in a piecewise-smooth flow or hybrid system that interacts with at least one of the system discontinuity boundaries  $\Sigma_{ij}$ . For example, we may want to calculate the Poincaré mapping of a periodic orbit. This will require us to define a *discontinuity mapping* (DM) associated with each boundary interaction, local to the point of intersection of the trajectory with the boundary. In the literature two types of DMs are considered; *Poincaré discontinuity mappings* (PDMs) that are defined with respect to a local Poincaré section transverse to the discontinuity boundary and *zero-time discontinuity mappings* (ZDMs) that, as the name suggests, take place in zero time. In this thesis we focus on ZDMs although the construction of a PDM is similar.

When constructing a DM, ignoring the case of a trajectory crossing the discontinuity boundary at a point of co-dimension 2 or higher (where two or more discontinuity boundaries intersect), locally we can consider a piecewise-smooth or hybrid system with two regions separated by a single discontinuity boundary. In other words, appropriately relabelling  $\mathbf{f}_i, \mathbf{f}_j, \mathcal{S}_i, \mathcal{S}_j$  and  $\Sigma_{ij}$  locally, we can consider the system

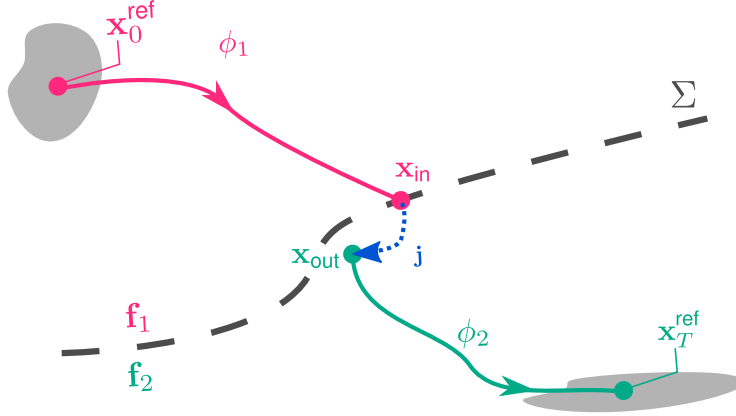


**Figure 3.2:** Schematic of a reference trajectory intersecting a discontinuity boundary transversally in a hybrid system.

defined by

$$\begin{aligned} \dot{\mathbf{x}} &= \begin{cases} \mathbf{f}_1(\mathbf{x}) & \mathbf{x} \in \mathcal{S}_-, \\ \mathbf{f}_2(\mathbf{x}) & \mathbf{x} \in \mathcal{S}_+, \end{cases} \\ \mathbf{x} &\rightarrow \mathbf{j}(\mathbf{x}), \quad \mathbf{x} \in \Sigma, \end{aligned} \quad (3.11)$$

where the discontinuity boundary

$$\Sigma = \{\mathbf{x} : h(\mathbf{x}, t) = 0\} \quad (3.12)$$

is defined by the zeros of a real-valued function  $h$  that separates the state space into the two regions

$$\mathcal{S}_- = \{\mathbf{x} : h(\mathbf{x}, t) < 0\} \quad \text{and} \quad \mathcal{S}_+ = \{\mathbf{x} : h(\mathbf{x}, t) > 0\}. \quad (3.13)$$

Here we assume a reference trajectory, with initial point  $\mathbf{x}_0^{\text{ref}}$ , intersects the discontinuity boundary transversally at time  $t_{\text{ref}}$  as shown in Figure 3.2, i.e.

$$h(\phi_1(\mathbf{x}_0^{\text{ref}}, t_{\text{ref}})) = 0 \quad (3.14)$$

with

$$h_{\mathbf{x}}(\phi_1(\mathbf{x}_0^{\text{ref}}, t_{\text{ref}}))\mathbf{f}_1(\phi_1(\mathbf{x}_0^{\text{ref}}, t_{\text{ref}})) \neq 0, \quad (3.15)$$

where  $\phi_1$  is the flow function prior to reaching  $\Sigma$  with corresponding vector field  $\mathbf{f}_1$ . After the discontinuity the flow function is given by  $\phi_2$  with corresponding vector field  $\mathbf{f}_2$ , and so after a time  $T > t_{\text{ref}}$  the trajectory reaches the point

$$\mathbf{x}_T^{\text{ref}} = \phi_2(\mathbf{j}(\phi_1(\mathbf{x}_0^{\text{ref}}, t_{\text{ref}})), T - t_{\text{ref}}). \quad (3.16)$$

We further assume that the vector fields  $\mathbf{f}_1$  and  $\mathbf{f}_2$ , and their corresponding flows, are smoothly extendible in a neighbourhood of  $\mathbf{x}_{\text{in}} = \phi_1(\mathbf{x}_0^{\text{ref}}, t_{\text{ref}})$  and  $\mathbf{x}_{\text{out}} = \mathbf{j}(\mathbf{x}_{\text{in}})$ , respectively. Since we are interested in a representation of the flow of the overall system for trajectories with initial conditions  $\mathbf{x}_0 \approx \mathbf{x}_0^{\text{ref}}$  and total time  $T$  we study the mapping

$$\phi(\mathbf{x}_0, T) = \phi_2(\mathbf{j}(\phi_1(\mathbf{x}_0, t)), T - t), \quad (3.17)$$

where  $t = t(\mathbf{x}_0)$  is the time of flight to reach the discontinuity boundary. Note that

$$t(\mathbf{x}_0) = t_{\text{ref}} + t(\phi_1(\mathbf{x}_0, t_{\text{ref}})), \quad (3.18)$$

where  $t(\phi_1(\mathbf{x}_0, t_{\text{ref}}))$  is possibly negative. Since  $t(\mathbf{x}_0) \neq t_{\text{ref}}$  a trajectory starting at  $\mathbf{x}_0$  is topologically distinct from the reference trajectory. In order to account for this we want to construct a ZDM  $\mathbf{D}(\mathbf{x})$  for  $\mathbf{x}$  in a neighbourhood of  $\mathbf{x}_{\text{in}}$  such that

$$\phi(\mathbf{x}_0, T) = \phi_2(\mathbf{D}(\phi_1(\mathbf{x}_0, t_{\text{ref}})), T - t_{\text{ref}}). \quad (3.19)$$

Referring to (3.18) we find that the appropriate ZDM  $\mathbf{D}(\mathbf{x})$  is given by

$$\mathbf{D}(\mathbf{x}) = \phi_2(\mathbf{j}(\phi_1(\mathbf{x}, t(\mathbf{x}))), -t(\mathbf{x})). \quad (3.20)$$

The map  $\mathbf{D}$  takes a point in a neighbourhood of  $\mathbf{x}_{\text{in}}$  and maps it to a point in a



where  $\mathbf{f}_{\text{in}} = \mathbf{f}_1(\mathbf{x}_{\text{in}})$  and  $\mathbf{f}_{\text{out}} = \mathbf{f}_2(\mathbf{x}_{\text{out}})$ . Given the transversality condition (3.15), by the IFT we have that  $t(\mathbf{x})$  is a uniquely defined differentiable function in a neighbourhood of  $\mathbf{x}_{\text{in}}$  with derivative

$$t_{\mathbf{x}}(\mathbf{x}_{\text{in}}) = -\frac{h_{\mathbf{x}}(\mathbf{x}_{\text{in}})}{h_{\mathbf{x}}(\mathbf{x}_{\text{in}})\mathbf{f}_{\text{in}}}, \quad (3.23)$$

and so we can write

$$\mathbf{D}_{\mathbf{x}}(\mathbf{x}_{\text{in}}) = \mathbf{j}_{\mathbf{x}}(\mathbf{x}_{\text{in}}) + \frac{(\mathbf{f}_{\text{out}} - \mathbf{j}_{\mathbf{x}}(\mathbf{x}_{\text{in}})\mathbf{f}_{\text{in}})h_{\mathbf{x}}(\mathbf{x}_{\text{in}})}{h_{\mathbf{x}}(\mathbf{x}_{\text{in}})\mathbf{f}_{\text{in}}}. \quad (3.24)$$

This expression for the saltation matrix was first given by Aizerman and Gantmacher in 1958 [52].

Not all boundary crossings in nonsmooth systems are transversal. An example of a non-transversal *grazing* interaction is shown in Figure 3.4. Here we assume that the reference trajectory, with initial point  $\mathbf{x}_0^{\text{ref}}$ , grazes the discontinuity boundary  $\Sigma$  at  $\mathbf{x}^*$  at time  $t_1$ , i.e.

$$h(\phi(\mathbf{x}_0^{\text{ref}}, t_{\text{ref}})) = h(\mathbf{x}^*) = 0, \quad (3.25)$$

$$h_{\mathbf{x}}(\mathbf{x}^*)\mathbf{f}(\mathbf{x}^*) = v^* = 0, \quad (3.26)$$

$$(h_{\mathbf{xx}}(\mathbf{x}^*)\mathbf{f}(\mathbf{x}^*) + h_{\mathbf{x}}(\mathbf{x}^*)\mathbf{f}_{\mathbf{x}}(\mathbf{x}^*))\mathbf{f}(\mathbf{x}^*) = a^* > 0. \quad (3.27)$$

After a time  $T = t_1 + t_2$  the trajectory reaches the point

$$\mathbf{x}_T^{\text{ref}} = \phi(\mathbf{j}(\phi(\mathbf{x}_0^{\text{ref}}, t_1)), t_2) = \phi(\phi(\mathbf{x}_0^{\text{ref}}, t_1), t_2), \quad (3.28)$$

where  $\mathbf{j}(\mathbf{x}^*) = \mathbf{x}^*$  for grazing points.

Next we will give a brief overview of how the ZDM associated with such a grazing trajectory can be constructed in the deterministic case. We consider a hybrid system such that all dynamics take place in  $\mathcal{S}^+ \cup \Sigma$  with the smooth evolution of the system

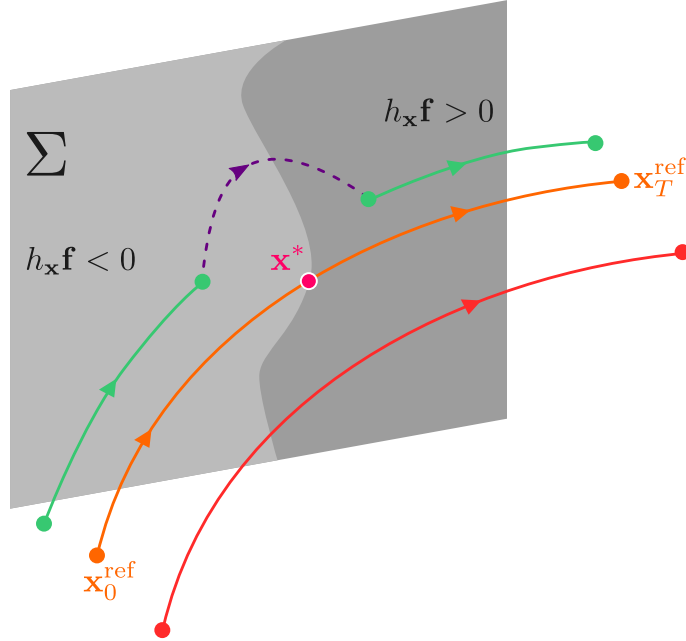


**Figure 3.4:** Schematic of a reference trajectory (orange) which grazes the discontinuity boundary  $\Sigma$  at  $\mathbf{x}^*$  and two nearby trajectories, one which does not impact  $\Sigma$  (red) and one which impacts  $\Sigma$  at low normal velocity (green).

governed by

$$\dot{\mathbf{x}} = \mathbf{f}(\mathbf{x}), \quad \mathbf{x} \in \mathcal{S}^+, \quad (3.29)$$

which is smoothly extendible into  $\mathcal{S}^-$ . Points on  $\Sigma$  are grouped into incoming trajectories, where  $h_{\mathbf{x}}(\mathbf{x})\mathbf{f}(\mathbf{x}) < 0$ , grazing trajectories, where  $h_{\mathbf{x}}(\mathbf{x})\mathbf{f}(\mathbf{x}) = 0$ , and outgoing trajectories, where  $h_{\mathbf{x}}(\mathbf{x})\mathbf{f}(\mathbf{x}) > 0$ . The jump map

$$\mathbf{j} : \Sigma \rightarrow \Sigma \quad (3.30)$$

maps points on incoming trajectories to points on outgoing trajectories and is the identity for grazing trajectories.

Consider a grazing reference trajectory such as the one shown in Figure 3.4. Taking points  $\mathbf{x}_0$  in a neighbourhood of  $\mathbf{x}_0^{\text{ref}}$  and evolving for time  $T = t_1 + t_2$  we note that trajectories will either intersect  $\Sigma$  in a neighbourhood of  $\mathbf{x}^*$  at a time close to  $t_1$  or not intersect  $\Sigma$  at all. We want to construct a ZDM  $\mathbf{D}(\mathbf{x})$  defined in a neighbourhood

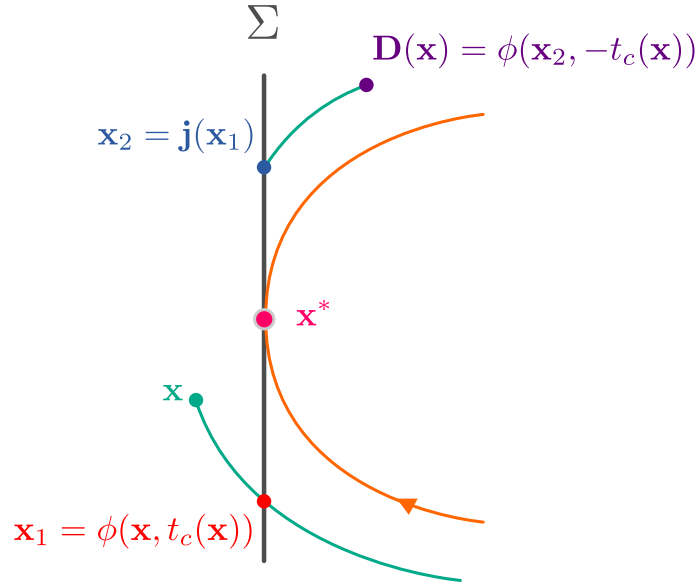


**Figure 3.5:** Deriving the zero-time discontinuity mapping  $\mathbf{D}(\mathbf{x})$  for a grazing trajectory.  $\mathbf{D}$  takes a point  $\mathbf{x}$ , on an impacting trajectory in the neighbourhood of  $\mathbf{x}^*$ , to the point  $\mathbf{x}_1$  on the boundary by flowing for a time  $t_c(\mathbf{x})$ , applies the jump mapping  $\mathbf{j}$  to arrive at  $\mathbf{x}_2$  and finally corrects for zero time by flowing for a time  $-t_c(\mathbf{x})$  to arrive at  $\mathbf{D}(\mathbf{x})$ .

of  $\mathbf{x}^*$  such that the local mapping from a neighbourhood of  $\mathbf{x}_0^{\text{ref}}$  to a neighbourhood of  $\mathbf{x}_T^{\text{ref}}$  is given by

$$\phi(\mathbf{D}(\phi(\mathbf{x}, t_1)), t_2). \quad (3.31)$$

In the case of trajectories that do not intersect the boundary and grazing points, then  $\mathbf{D}$  is trivially the identity. In the case of intersecting trajectories we construct  $\mathbf{D}$  in the manner shown in Figure 3.5. For intersecting points  $\mathbf{x}_0$  in a neighbourhood of  $\mathbf{x}_0^{\text{ref}}$ ,  $\mathbf{x} = \phi(\mathbf{x}_0, t_1)$  is in a neighbourhood of  $\mathbf{x}^*$ . We let  $t_c(\mathbf{x})$  be the (possibly negative) time of flight from  $\mathbf{x}$  to  $\Sigma$ . The appropriate ZDM can then be constructed in the following manner. First, take an intersecting point  $\mathbf{x}$  in a neighbourhood of  $\mathbf{x}^*$  to the boundary at  $\mathbf{x}_1 = \phi(\mathbf{x}, t_c(\mathbf{x}))$ . Next, apply the jump map sending  $\mathbf{x}_1$  to  $\mathbf{x}_2 = \mathbf{j}(\mathbf{x}_1)$  and finally correct to zero time by sending  $\mathbf{x}_2$  to  $\mathbf{D}(\mathbf{x}) = \phi(\mathbf{x}_2, -t_c(\mathbf{x}))$ . In other words,  $\mathbf{D}(\mathbf{x})$  is given by

$$\mathbf{D}(\mathbf{x}) = \phi(\mathbf{j}(\phi(\mathbf{x}, t_c(\mathbf{x}))), -t_c(\mathbf{x})), \quad (3.32)$$

which has a very similar form to (3.20). In this case, however, since the boundary intersection is not transversal we cannot find  $\mathbf{D}_{\mathbf{x}}(\mathbf{x}^*)$  in the same way as before. Instead, we must use higher-order approximations of  $t_c(\mathbf{x})$ . More details on this can be found in Section 3.4, Chapter 10 and [53], for example.

### 3.4 The Square Root Map

Many nonsmooth maps are derived as local mappings of continuous time nonsmooth systems, constructed using discontinuity mappings. One example is that of the square root map, which we have analysed in the first two papers that comprise Chapters 7 and 8 of this thesis. The square root map is derived as the local mapping for a model of an impact oscillator close to grazing impacts. It was first derived by Nordmark for a single degree-of-freedom system [54] and then generalised by Fredriksson and Nordmark to  $n$  degrees of freedom [55]. The map and similar maps involving square-root singularities have since been analysed by many others [5, 56, 57, 58]. In this section we will give a brief overview of the square root map and its derivation referring to Figure 3.5. We will closely follow the presentations of Fredriksson & Nordmark [55] and di Bernardo *et al.* [22].

We consider the local mapping associated with a grazing periodic orbit in a general hybrid system given by (3.29)-(3.30). The ZDM associated with the point  $\mathbf{x}^*$ , where the periodic orbit grazes the discontinuity boundary  $\Sigma$ , which satisfies the conditions (3.25), is given by (3.32) for nearby impacting points and the identity for non-impacting points. We assume that  $h$  is well defined at the grazing point, i.e.

$$h(\mathbf{x}^*) = 0, \quad h_{\mathbf{x}}(\mathbf{x}^*) \neq 0. \quad (3.33)$$

We then separate impacting points from non-impacting points by considering the

local minimum of the function

$$H(\mathbf{x}, t) = h(\phi(\mathbf{x}, t)), \quad (3.34)$$

with the smallest magnitude of  $t$ , which we will denote  $\zeta(\mathbf{x})$ . We divide the neighbourhood of  $\mathbf{x}^*$  into the three sets

$$\mathcal{X}_{\text{impacting}} = \{\mathbf{x} : \zeta(\mathbf{x}) < 0\}, \quad (3.35)$$

$$\mathcal{X}_{\text{grazing}} = \{\mathbf{x} : \zeta(\mathbf{x}) = 0\}, \quad (3.36)$$

$$\mathcal{X}_{\text{non-impacting}} = \{\mathbf{x} : \zeta(\mathbf{x}) > 0\}, \quad (3.37)$$

of impacting, non-impacting and grazing points, respectively. Let  $\mathbf{x} \in \mathcal{X}_{\text{impacting}}$  be an impacting point in neighbourhood of the grazing point  $\mathbf{x}^*$ . Suppose  $\tau$  is the time of flight from  $\mathbf{x}$  to the point  $\mathbf{x}_0$  where  $H(\mathbf{x}, t)$  reaches its local minimum, then expanding about  $\mathbf{x}^*$  to leading order we find that

$$\mathbf{x}_0 = \mathbf{x} + \mathbf{f}(\mathbf{x}^*)\tau. \quad (3.38)$$

Expanding about  $t = 0$  along the flow starting at  $\mathbf{x}_1$  we find that

$$H(\mathbf{x}_0, t) = H(\mathbf{x}_0, 0) + \frac{\partial}{\partial t}H(\mathbf{x}_0, 0)t + \frac{\partial^2}{\partial t^2}H(\mathbf{x}_0, 0)\frac{t^2}{2} + \mathcal{O}(t^3) = \zeta(\mathbf{x}) + \frac{a^*}{2}t^2 + \mathcal{O}(t^3), \quad (3.39)$$

where  $a^* = \frac{\partial^2}{\partial t^2}H(\mathbf{x}_0, 0)$ . Setting (3.39) equal to zero we find that the time of flight from  $\mathbf{x}$  to the boundary  $t_c(\mathbf{x})$  is given by

$$t_c(\mathbf{x}) = \tau - \sqrt{-\frac{2}{a^*}\zeta(\mathbf{x}) + \mathcal{O}(\zeta(\mathbf{x}))}, \quad (3.40)$$

and so expanding the flow in  $t$  about the grazing point we find that the point

$\mathbf{x}_1 = \phi(\mathbf{x}, t_c(\mathbf{x}))$  is given by

$$\mathbf{x}_1 = \mathbf{x} + f(\mathbf{x}^*) \left( \tau - \sqrt{-\frac{2}{a^*} \zeta(\mathbf{x})} \right) + \mathcal{O}(\zeta(\mathbf{x})). \quad (3.41)$$

The point  $\mathbf{x}_2 = \mathbf{j}(\mathbf{x}_1)$  is given by a reset map based on the normal velocity at impact so that

$$\mathbf{j}(\mathbf{x}_1) = \mathbf{x}_1 + \gamma(\mathbf{x}_1) h_{\mathbf{x}}(\mathbf{x}_1) \mathbf{f}(\mathbf{x}_1). \quad (3.42)$$

Here  $\gamma$  is an appropriate smooth function such that  $\mathbf{j}$  leaves the positional coordinates unchanged. Expanding the normal velocity at  $\mathbf{x}_1$  in a Taylor series about  $\mathbf{x}_0$  we find that

$$\begin{aligned} h_{\mathbf{x}}(\mathbf{x}_1) \mathbf{f}(\mathbf{x}_1) &= h_{\mathbf{x}}(\mathbf{x}_0) \mathbf{f}(\mathbf{x}_0) - a^* \sqrt{-\frac{2}{a^*} \zeta(\mathbf{x})} + \mathcal{O}(\zeta(\mathbf{x})) \\ &= -a^* \sqrt{-\frac{2}{a^*} \zeta(\mathbf{x})} + \mathcal{O}(\zeta(\mathbf{x})). \end{aligned} \quad (3.43)$$

We can now write

$$\begin{aligned} \mathbf{x}_2 = \mathbf{j}(\mathbf{x}_1) &= \mathbf{x}_1 - \gamma(\mathbf{x}_1) \left( a^* \sqrt{-\frac{2}{a^*} \zeta(\mathbf{x})} + \mathcal{O}(\zeta(\mathbf{x})) \right), \\ &= \mathbf{x} + f(\mathbf{x}^*) \left( \tau - \sqrt{-\frac{2}{a^*} \zeta(\mathbf{x})} \right) - \gamma(\mathbf{x}^*) \sqrt{-2a^* \zeta(\mathbf{x})} + \mathcal{O}(\zeta(\mathbf{x})). \end{aligned} \quad (3.44)$$

The final step in the zero-time discontinuity mapping is to flow from  $\mathbf{x}_2$  for the time  $-t_c(\mathbf{x})$  to reach  $\mathbf{D}(\mathbf{x})$  and so to leading order we find

$$\begin{aligned} \mathbf{D}(\mathbf{x}) &= \mathbf{x}_2 - t_c(\mathbf{x}) f(\mathbf{x}^*) \\ &= \mathbf{x} + t_c(\mathbf{x}) f(\mathbf{x}^*) - \gamma(\mathbf{x}^*) \sqrt{-2a^* \zeta(\mathbf{x})} - t_c(\mathbf{x}) f(\mathbf{x}^*) \\ &= \mathbf{x} - \gamma(\mathbf{x}^*) \sqrt{-2a^* \zeta(\mathbf{x})}, \end{aligned} \quad (3.45)$$

for  $\mathbf{x} \in \mathcal{X}_{\text{impacting}}$  and

$$\mathbf{D}(\mathbf{x}) = \mathbf{x}, \quad (3.46)$$

for  $\mathbf{x} \in \mathcal{X}_{\text{grazing}} \cup \mathcal{X}_{\text{non-impacting}}$ .

Let us now consider the local fixed-time mapping  $\mathbf{M}_S(\mathbf{y})$ , where  $\mathbf{y} = \mathbf{x} - \mathbf{x}^*$ , associated with the grazing periodic orbit  $\mathcal{G}$  that has period  $T$ , i.e.  $\phi(\mathbf{x}^*, T) = \mathbf{x}^*$ . Let  $\mathbf{J} = \phi_{\mathbf{x}}(\mathbf{x}^*, T)$  be the linearisation about the periodic orbit disregarding impacts. Then, by linearising  $\zeta(\mathbf{x})$  about  $\mathbf{x}^*$ , to leading order we find that

$$\mathbf{M}_S(\mathbf{y}) = \begin{cases} \mathbf{J}\mathbf{y} - \sqrt{-2a^*h_{\mathbf{x}}(\mathbf{x}^*)}\mathbf{y}\mathbf{J}\gamma(\mathbf{x}^*), & h_{\mathbf{x}}(\mathbf{x}^*)\mathbf{y} < 0, \\ \mathbf{J}\mathbf{y}, & h_{\mathbf{x}}(\mathbf{x}^*)\mathbf{y} \geq 0. \end{cases} \quad (3.47)$$

The corresponding Poincaré mapping can then be found by a simple projection. Introducing a bifurcation parameter  $\mu \in \mathbb{R}$  and a coordinate transform such that the periodic orbit  $\mathcal{G}(\mu)$  undergoes grazing at  $(\mathbf{x}^*, \mu^*) = (\mathbf{0}, 0)$  we find the normal form map  $\mathbf{S}$  at a grazing bifurcation is the square root map (for details consult [22])

$$\mathbf{x}_{n+1} = \mathbf{S}(\mathbf{x}_n, \mu) = \begin{cases} \mathbf{L}\mathbf{x}_n + \mathbf{M}\mu + \mathbf{N}\sqrt{-y(\mathbf{x}_n, \mu)}, & y(\mathbf{x}_n, \mu) < 0, \\ \mathbf{L}\mathbf{x}_n + \mathbf{M}\mu, & y(\mathbf{x}_n, \mu) \geq 0, \end{cases} \quad (3.48)$$

where

$$y(\mathbf{x}, \mu) = h_{\mathbf{x}}(\mathbf{0})\mathbf{L}\mathbf{x} + (h_{\mathbf{x}}(\mathbf{0})\mathbf{M} + h_{\mu}(\mathbf{0}))\mu, \quad (3.49)$$

for some  $\mathbf{L} \in \mathbb{R}^{n \times n}$ ,  $\mathbf{M} \in \mathbb{R}^{n \times 1}$  and  $\mathbf{N} \in \mathbb{R}^{n \times 1}$ .

In Chapters 7 and 8 we consider a one-dimensional square root map. It has been shown by Nordmark [59] that the one-dimensional square root map is the limit mapping of more general  $n$ -dimensional square root maps that arise in the unfolding of grazing bifurcations. In other words, in the limit of a small bifurcation parameter the results obtained by analysing the one-dimensional square root map are valid for higher-dimensional systems.

In this thesis we write the one-dimensional square root map as

$$x_{n+1} = S(x_n, \mu) = \begin{cases} \mu + bx_n, & x < 0, \\ \mu - a\sqrt{x_n}, & x \geq 0, \end{cases} \quad (3.50)$$

where  $a \in \mathbb{R}$  is a positive parameter and  $0 < b < 1$ . For  $\mu < 0$  (3.50) has a stable fixed point, but for  $\mu > 0$  we can summarise the system's possible behaviours as follows:

**Strongly stable case:** If  $0 < b < \frac{1}{4}$  there is a period-adding cascade of stable periodic orbits. That is, there are values of  $\mu > 0$  for which a stable periodic orbit of period  $k$  for each  $k \in \mathbb{N}$  with  $k \rightarrow \infty$  as  $\mu \rightarrow 0$ . Moreover, adjacent periodic windows overlap, creating intervals of bistability.

**Intermediate case:** If  $\frac{1}{4} < b < \frac{2}{3}$  there is again a period-adding cascade of stable periodic orbits accumulating on  $\mu = 0$  as  $k \rightarrow \infty$ . However, between period- $k$  and period- $(k + 1)$  windows we now see chaotic attractors.

**Weakly stable case:** If  $\frac{2}{3} < b < 1$  as  $\mu$  decreases towards zero there are a finite number of period-addings followed by a chaotic attractor on an interval of  $\mu$  values that extends to  $\mu = 0$ . The chaotic attractor's size is proportional to  $\sqrt{\mu}$ .

The dynamics of the  $n$ -dimensional square root map (3.48) are directly analagous when the leading eigenvalue  $\lambda$  of the matrix  $\mathbf{L}$  is real, positive and less than one [22, 59]. In this case the map has a stable node when

$$\tilde{\mu} = -(h_{\mathbf{x}}(\mathbf{0})(\mathbf{I} - \mathbf{L})^{-1}\mathbf{M} + h_{\mu}(\mathbf{0}))\mu < 0. \quad (3.51)$$

When  $\tilde{\mu} > 0$ , replacing  $b$  with  $\lambda$  and  $\mu$  with  $\tilde{\mu}$ , we once again observe the strongly stable, intermediate and weakly stable cases described for the one-dimensional map above.

# Chapter 4

## Noise

Now that we have introduced the reader to dynamical systems, in this chapter we briefly introduce some basic concepts in probability and stochastic processes. More detail can be found in texts such as Øksendal's monograph [60]. We also briefly discuss some previous studies into the effects of noise on dynamical systems in both smooth and nonsmooth settings, drawing on examples from [24, 25, 31, 32].

### 4.1 Probability and Stochastic Processes

The foundations of *probability theory* can be taken directly from *measure theory*. Here we will introduce the key concepts in measure theory and show how they can be extended to probability theory and used when considering *stochastic processes*.

#### 4.1.1 Elementary Measure Theory

A *measure space* is a triple  $(S, \mathcal{A}, \mu)$  where  $S$  is a set,  $\mathcal{A}$  is a  $\sigma$ -algebra and  $\mu$  is a *measure*. First, let us define a  $\sigma$ -algebra. A  $\sigma$ -algebra  $\mathcal{A}$  of  $S$  is a collection of subsets of  $S$  such that:

- $\emptyset \in \mathcal{A}$ .

- If  $A \in \mathcal{A}$  then  $A^c \in \mathcal{A}$ .
- If  $\{A_i\} \subset \mathcal{A}$  then  $\bigcup_{i \in I} A_i \in \mathcal{A}$  for a countable indexing set  $I$ .

The pair  $(S, \mathcal{A})$  is called a *measurable space* while the elements of  $\mathcal{A}$  are known as *measurable sets*. Furthermore a function from one measurable space to another  $f : (S, \mathcal{A}) \rightarrow (R, \mathcal{B})$  is called a *measurable function* if

$$\forall B \in \mathcal{B} : f^{-1}(B) = \{s \in S : f(s) \in B\} \in \mathcal{A}. \quad (4.1)$$

In general, it can be hard to explicitly describe a given  $\sigma$ -algebra concisely. Two simple  $\sigma$ -algebras on a given set  $S$  are the power set of  $S$ ,  $2^S$ , and the trivial  $\sigma$ -algebra,  $\{S, \emptyset\}$ . More complicated  $\sigma$ -algebras are usually described by *generating* them from a smaller collection of sets that can be explicitly described. The  $\sigma$ -algebra generated by the collection of sets  $\mathcal{E}$  is the  $\sigma$ -algebra given by the intersection of all  $\sigma$ -algebras containing  $\mathcal{E}$ , in other words, it is the smallest such  $\sigma$ -algebra. We can also generate  $\sigma$ -algebras from collections of functions. The  $\sigma$ -algebra generated by the collection of functions  $\mathcal{G}$  is the smallest  $\sigma$ -algebra for which all of the functions in  $\mathcal{G}$  are measurable.

An important example of such a  $\sigma$ -algebra is the *Borel  $\sigma$ -algebra* on a metric space  $M$ . The Borel  $\sigma$ -algebra on  $M$ , denoted  $\mathcal{B}_M$ , is the smallest  $\sigma$ -algebra containing all open subsets of  $M$ . For example, the Borel  $\sigma$ -algebra on  $\mathbb{R}$ , with the usual metric, is generated by the collection of intervals

$$\{(a, b) : a, b \in \mathbb{R}, a < b\}. \quad (4.2)$$

We note that if  $(S, \mathcal{B}_S)$  is a metric space with its Borel  $\sigma$ -algebra every continuous function  $f : S \rightarrow \mathbb{R}$  is measurable.

We will now define the final element of a measure space. A *measure*  $\mu$  on a measurable space  $(S, \mathcal{A})$  is a function  $\mu : \mathcal{A} \rightarrow [0, \infty]$  such that

- $\mu(\emptyset) = 0$ .
- If  $\forall i \neq j : A_i \cap A_j = \emptyset$ , then  $\mu\left(\bigcup_i A_i\right) = \sum_i \mu(A_i)$ .

We call a measure finite if  $\forall A \in \mathcal{A} : \mu(A) < \infty$  or equivalently if  $\mu(S) < \infty$ . A *probability measure* is a finite measure  $P$  on  $S$  such that  $P(S) = 1$ . An example of an important measure on the Borel  $\sigma$ -algebra of the real line  $\mathcal{B}_{\mathbb{R}}$  is the *Lebesgue measure*  $\mu_{\mathcal{L}}$ . This measure has the property that the measure of an interval is its length.

We can now define integration on measure spaces with respect to a measure which we will later extend to probability spaces. Suppose  $f : (S, \mathcal{A}, \mu) \rightarrow (\mathbb{R}, \mathcal{B}_{\mathbb{R}}, \nu)$  is a measurable function. We will define the *Lebesgue integral*  $\int f d\mu$  by starting with simple cases for which the integral can be explicitly written. First, let  $f$  take on finitely many non-negative values  $\alpha_i \in [0, \infty)$ . Let  $A_i = \{s \in S : f(s) = \alpha_i\}$  then we can define  $f$  as

$$f(s) = \sum_i \alpha_i \mathbf{1}_{A_i}(s), \quad (4.3)$$

where  $\mathbf{1}_{A_i}$  is the indicator function of the set  $A_i$ . We call  $f$  a non-negative *simple function*. The integral of  $f$  with respect to the measure  $\mu$  is then well defined as

$$\int f d\mu = \sum_i \alpha_i \mu(A_i). \quad (4.4)$$

Now let  $f : S \rightarrow [0, \infty]$  be a measurable non-negative valued function. Then we define

$$\int f d\mu = \sup \left\{ \int g d\mu : 0 \leq g \leq f \right\}, \quad (4.5)$$

where  $g$  is a non-negative simple function. Finally, if  $f$  is a general measurable function  $f : S \rightarrow \mathbb{R}$  we define

$$\int f d\mu = \int f^+ d\mu - \int f^- d\mu, \quad (4.6)$$

where  $f^+$  and  $f^-$  are non-negative measurable functions such that  $f^+ - f^- = f$  and  $f^+ + f^- = |f|$ . Sometimes, we may wish to integrate over a specific subset  $A$  of  $S$ , which we write as

$$\int_A f d\mu = \int_S f \mathbf{1}_A d\mu = \int f \mathbf{1}_A d\mu. \quad (4.7)$$

When a function  $f$  is *Riemann integrable* on an interval  $[a, b]$  its Riemann integral coincides with its Lebesgue integral with respect to the Lebesgue measure  $\mu_{\mathcal{L}}$ , i.e.

$$\int_a^b f(x) dx = \int_{[a,b]} f d\mu_{\mathcal{L}}. \quad (4.8)$$

### 4.1.2 Probability Theory

A probability space  $(\Omega, \mathcal{F}, P)$  is a measure space where  $P$  is a probability measure, i.e.  $P(\Omega) = 1$ . We usually refer to  $\Omega$  as the *sample space*, elements  $\omega \in \Omega$  as *outcomes*, and measurable sets  $F \in \mathcal{F}$  as *events* which occur with probability  $P(F)$ . A *random variable* is a measurable function  $X : \Omega \rightarrow S$ , where  $S$  is usually  $\mathbb{R}$ . If  $S = \mathbb{R}^n$  with  $n > 1$  we sometimes call  $X$  a *random vector* and if  $S = \mathbb{R}^{m \times n}$  with  $m, n > 1$  we sometimes call  $X$  a *random matrix* to emphasise its structure.

A random variable  $X$  induces a *probability distribution*  $\mu_X$  on  $\mathbb{R}^n$  given by

$$\mu_X(B) = P(\{\omega \in \Omega : X(\omega) \in B\}) = P(X^{-1}(B)). \quad (4.9)$$

The *expectation* or *expected value* of  $X$  is given by

$$E(X) = \int_{\Omega} X dP = \int_{\mathbb{R}^n} x d\mu_X. \quad (4.10)$$

More generally, if  $g : \mathbb{R}^n \rightarrow \mathbb{R}^n$  is a Borel measurable function then

$$E(g(X)) = \int_{\Omega} g(X) dP = \int_{\mathbb{R}^n} g(x) d\mu_X. \quad (4.11)$$

The *cumulative distribution function* (CDF)  $F_X$  of a random variable  $X$  is given by

$$F_X(x) = P(\{\omega \in \Omega : X(\omega) \leq x\}). \quad (4.12)$$

The *probability density function* (PDF)  $f_X$  of  $X$  is given by the derivative of its distribution with respect to Lebesgue measure

$$f_X = \frac{d\mu_X}{dx}. \quad (4.13)$$

When  $f_X$  exists  $F_X$  is differentiable *almost everywhere*<sup>1</sup> with

$$f_X = \frac{dF_X}{dx}, \quad (4.14)$$

which allows us to express the expected value of  $g(X)$  as the Riemann integral

$$E(g(X)) = \int_{\mathbb{R}^n} g(x) f_X(x) dx. \quad (4.15)$$

The *variance* of a one-dimensional random variable  $X$  is given by

$$\text{Var}(X) = E((X - E(X))^2), \quad (4.16)$$

while the *covariance matrix*  $\Sigma(X)$  of a random vector  $X$  has entries

$$\Sigma_{ij} = E((X_i - E(X_i))(X_j - E(X_j))) = \begin{cases} \text{Cov}(X_i, X_j) & i \neq j, \\ \text{Var}(X_i) & i = j. \end{cases} \quad (4.17)$$

In probability theory,  $\sigma$ -algebras represent information. The  $\sigma$ -algebra  $\mathcal{F}$  represents all the information, known and unknown, about the experiment, whereas sub- $\sigma$ -algebras  $\mathcal{A}$  of  $\mathcal{F}$  represent partial information. Knowing the  $\sigma$ -algebra  $\mathcal{A}$  means knowing for each event  $A \in \mathcal{A}$  whether  $A$  happened or not. Sub- $\sigma$ -algebras generated

<sup>1</sup>This means that the set of values of  $x$  where  $F_X$  is not differentiable has measure 0.

by random variables allow us to define the notion of independence. Two events  $A, B \in \mathcal{F}$  are called independent if

$$P(A \cap B) = P(A)P(B) \quad (4.18)$$

and a collection of sub- $\sigma$ -algebras  $\mathcal{A}_1, \mathcal{A}_2, \dots, \mathcal{A}_k$  are independent if, for every choice of events  $A_1 \in \mathcal{A}_1, A_2 \in \mathcal{A}_2, \dots, A_k \in \mathcal{A}_k$ ,

$$P(A_1 \cap A_2 \cap \dots \cap A_k) = P(A_1)P(A_2) \dots P(A_k). \quad (4.19)$$

Finally a collection of random variables  $X_1, X_2, \dots, X_k$  are independent if the collection of sub- $\sigma$ -algebras they generate is independent.

In this thesis we will focus mostly on *Gaussian* or *normal* random variables. A random variable  $X : \Omega \rightarrow \mathbb{R}^n$  is called a Gaussian random variable if the distribution of  $X$  has a density  $f_X$  of the form

$$f_X(x) = \frac{1}{(2\pi)^{n/2} \sqrt{\det(\Sigma)}} \exp\left(-\frac{1}{2}(x - \nu)^T \Sigma^{-1}(x - \nu)\right), \quad (4.20)$$

where  $\Sigma = \Sigma(X)$  is the covariance matrix of  $X$  and  $\nu = E(X)$  is the expected value of  $X$ . We say that  $X$  is distributed as Gaussian with mean  $\nu$  and covariance matrix  $\Sigma$  and write

$$X \sim N(\nu, \Sigma). \quad (4.21)$$

Gaussian random variables have many nice properties. For example, they are symmetrically distributed about their mean  $\nu$  and the sum of two independently distributed Gaussian random variables is also Gaussian.

### 4.1.3 Stochastic Processes

Noise is most often included in dynamical systems by way of a *stochastic process*. A stochastic process is a collection of random variables

$$\{X_i : i \in \mathcal{I}\}, \quad (4.22)$$

where  $\mathcal{I}$  is some arbitrary index set. We will usually consider stochastic processes indexed by the set  $[0, \infty)$  representing continuous forward time

$$\{X_t : t \in [0, \infty)\}. \quad (4.23)$$

Stochastic processes can have *filtrations* associated with them. A filtration on a probability space  $(\Omega, \mathcal{F}, P)$  is a collection of  $\sigma$ -algebras  $\{\mathcal{F}_t : [0, \infty)\}$  such that

$$\mathcal{F}_s \subseteq \mathcal{F}_t \subseteq \mathcal{F} \quad 0 \leq s \leq t. \quad (4.24)$$

A process  $X = \{X_t\}$  is *adapted* to the filtration  $\{\mathcal{F}_t\}$  if  $X_t$  is measurable with respect to  $\mathcal{F}_t$  for all  $t$ . A stochastic process also generates a filtration. The filtration  $\{\mathcal{F}_t^X\}$  generated by  $\{X_t\}$  is the smallest filtration to which  $\{X_t\}$  is adapted.

Perhaps the most famous example of a continuous time stochastic process is *Brownian motion*. This process can be used to describe the irregular motion of grains of pollen suspended in liquid as observed by Scottish botanist Robert Brown in 1828. We plot sample paths of a one-dimensional Brownian motion  $B_t$  in Figure 4.1. The process can be considered as continuous-time random walk and is defined as follows:

Let  $(\Omega, \mathcal{F}, P)$  be a probability space and  $\{B_t\}$  be a  $\mathbb{R}^n$ -valued stochastic process adapted to the filtration  $\{\mathcal{F}_t\}$ . The stochastic process  $\{B_t\}$  is an  $n$ -dimensional Brownian motion if

- Its paths are almost everywhere continuous;

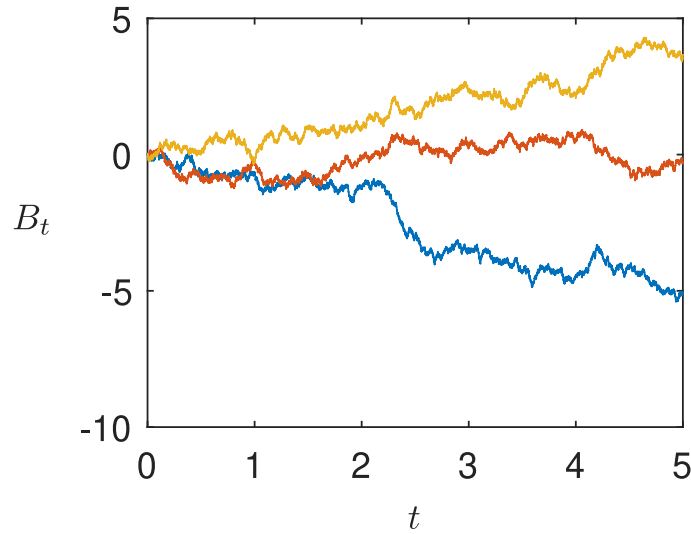


**Figure 4.1:** Sample paths of a standard Brownian motion  $B_t$ .

- For  $0 \leq s < t$ , the difference  $B_t - B_s$  is independent of  $\mathcal{F}_s$  and has a Gaussian distribution with mean 0 and covariance matrix  $(t - s)\mathbf{I}$ , where  $\mathbf{I}$  is the  $n \times n$  identity matrix.

If  $B_0 = 0$  we call the stochastic process a *standard Brownian motion*. It turns out that standard Brownian motion is the only process indexed by  $[0, \infty)$ , with mean zero, continuous paths and stationary, Gaussian, and independent increments. It was formulated mathematically by Norbert Wiener in 1923 [61] and is sometimes called a *Wiener process* and denoted  $W_t$  in his honour. Brownian motion is an example of a *Gaussian process*, i.e. a process  $\{X_t\}$  such that for a finite set of indices  $\{t_1, t_2, \dots, t_n\}$  the vector  $(X_{t_1}, X_{t_2}, \dots, X_{t_n})$  has a Gaussian distribution.

Let  $\mathcal{V}$  be the class of functions

$$f(t, \omega) : [0, \infty) \times \Omega \rightarrow \mathbb{R}, \quad (4.25)$$

such that  $f(t, \omega)$  is  $\mathcal{B}_{[0, \infty)} \times \mathcal{F}$  measurable,  $\mathcal{F}_t$ -adapted and  $E(\int_S^T f(t, \omega)^2 dt) < \infty$ .

We call a function  $g \in \mathcal{V}$  *elementary* if it can be written in the form

$$g(t, \omega) = \sum_j \beta_j(\omega) \mathbf{1}_{[t_j, t_{j+1})}(t). \quad (4.26)$$

For elementary functions we define the *Itô integral* with respect to one-dimensional Brownian motion as

$$\int_S^T g(t, \omega) dB_t(\omega) = \sum_j \beta_j(\omega) (B_{t_{j+1}}(\omega) - B_{t_j}(\omega)). \quad (4.27)$$

For  $f \in \mathcal{V}$  we define the *Itô integral* as

$$\int_S^T f(t, \omega) dB_t = \lim_{n \rightarrow \infty} \int_S^T g_n(t, \omega) dB_t, \quad (4.28)$$

where  $\{g_n\}$  is a sequence of elementary functions in  $\mathcal{V}$  such that

$$\lim_{n \rightarrow \infty} E \left( \int_S^T (f(t, \omega) - g_n(t, \omega))^2 dt \right) = 0. \quad (4.29)$$

An important corollary of this definition is the *Itô isometry*

$$\forall f \in \mathcal{V} : E \left[ \left( \int_S^T f(t, \omega) dB_t \right)^2 \right] = E \left[ \int_S^T f^2(t, \omega) dt \right], \quad (4.30)$$

which is extremely useful when calculating the variance of a stochastic process.

An important Itô process that appears in Chapters 9 and 10 is the *Ornstein-Uhlenbeck* process [60]. Since Brownian motion is not differentiable with respect to time the Ornstein-Uhlenbeck process was introduced as an attempt to model the velocity of a particle undergoing Brownian motion directly. The time integral of an Ornstein-Uhlenbeck process then gives a smooth approximation of Brownian motion.

An Ornstein-Uhlenbeck Itô process is a mean reverting process. In particular, we

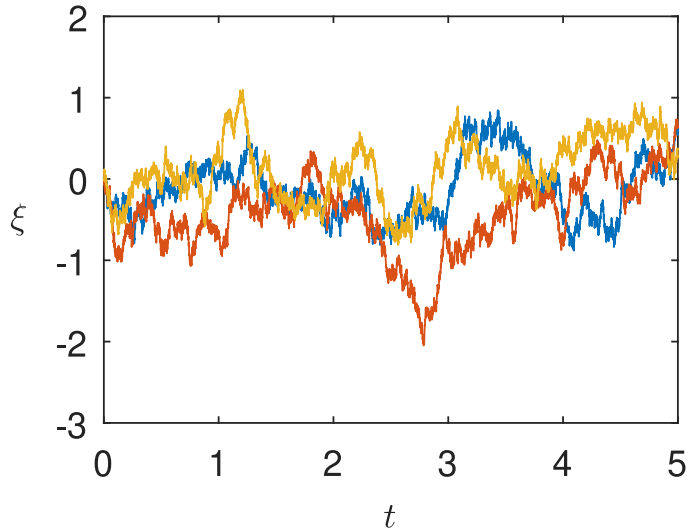


**Figure 4.2:** Sample paths of an Ornstein-Uhlenbeck Process (4.33) with  $\sigma = 1$  and  $\theta = 5$ .

will consider the mean-reverting process  $\xi(t)$  with mean zero, given by

$$d\xi(t) = -\theta\xi(t)dt + \sigma dB_t, \quad \xi(0) = \xi_0. \quad (4.31)$$

By using the integrating factor  $e^{\theta t}$  we find that

$$d(e^{\theta t}\xi(t)) = \sigma e^{\theta t}dB_t \quad (4.32)$$

and hence

$$\xi(t) = e^{-\theta t}\xi_0 + \sigma \int_0^t e^{\theta(s-t)}dB_s \sim N\left(e^{-\theta t}\xi_0, \frac{\sigma^2(1 - e^{-2\theta t})}{2\theta}\right). \quad (4.33)$$

We plot three sample paths of an Ornstein-Uhlenbeck process with  $\sigma = 1$  and  $\theta = 5$  in Figure 4.2 and note their oscillation about the mean compared to the sample paths of a standard Brownian motion shown in Figure 4.1. This makes an Ornstein-Uhlenbeck process a more suitable choice when one wants the process to fluctuate about some fixed mean rather than allowing for the possibility of a long-term drift.

In Chapters 9 and 10 we construct generalised Ornstein-Uhlenbeck processes  $P_n(t)$

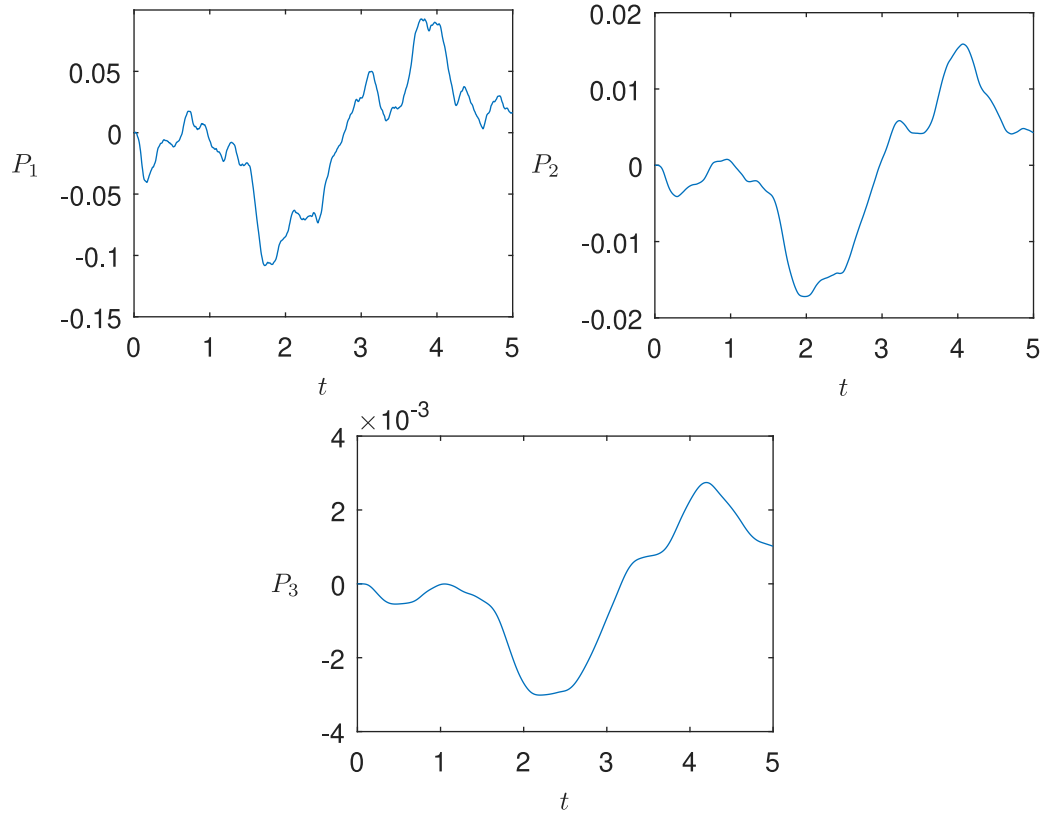


**Figure 4.3:** Sample paths of generalised Ornstein-Uhlenbeck processes (4.34) with  $\sigma = 1$  and  $\theta = 5$  for  $n = 1, 2, 3$ .

that are  $n$  times differentiable. These are constructed iteratively from a base Ornstein-Uhlenbeck process such that

$$\dot{P}_n(t) = -\theta P_n(t) + \sigma P_{n-1}(t), \quad P_0(t) = \xi(t). \quad (4.34)$$

Each  $P_n(t)$  is a mean-reverting Gaussian process with mean zero. Sample paths for  $P_i(t)$  for  $i = 1, 2, 3$  can be seen in Figure 4.3.

## 4.2 Noise in dynamical systems

The effects of noise on dynamical systems is an important and active area of research as all real-world systems are subjected to some level of uncertainty. Noise can enter dynamical systems through measurement noise or through a high number of unknown

degrees of freedom. Brownian motion, for example, occurs as a result of a pollen grain's interaction with a huge number of water molecules whose complicated motion is required by the molecular-kinetic theory of heat. The noisy signal received by the brain is thought to be the result of receiving synaptic inputs from tens of thousands of other cells at once [25]. In electronic systems *shot noise* refers to noise caused by the discrete nature of electronic charges modelled by a *Poisson process*, while *Johnson-Nyquist noise* refers to fluctuations due to thermal agitation that are present in any system due to its temperature being higher than absolute zero [17]. In this section we will present some short illustrative examples of previous research into the effects of noise on both smooth and nonsmooth dynamical systems.

### 4.2.1 Noise in Smooth Dynamical Systems

In smooth dynamical systems noise can drastically alter dynamics especially in the vicinity of bifurcations, the hallmark of nonlinear systems. Noise can stabilise unstable behaviours or destabilise attractors-shifting bifurcations [25, 26], or induce behaviors that have no counterpart in the corresponding deterministic system, through noise-induced transitions [27]. In this section we will present two examples of the significant effects noise can have on smooth dynamical systems. The first example will examine the effect of noise on a transcritical bifurcation in the discrete-time logistic map. The second will be the continuous-time example of a two-dimensional supercritical pitchfork bifurcation in a model of a parametrically driven damped anharmonic oscillator.

In [24] Linz and Lücke investigated the effects of both additive and multiplicative noise on the first two bifurcations of the logistic map as the control parameter  $r$  is increased from 0. Here we will briefly summarise their results relating to the effects of multiplicative or parametric noise on the first bifurcation, a transcritical bifurcation.

The logistic map is a one-dimensional map that is a discrete-time analogue to the Verhulst model of population growth [62, 63]. In the deterministic case the logistic

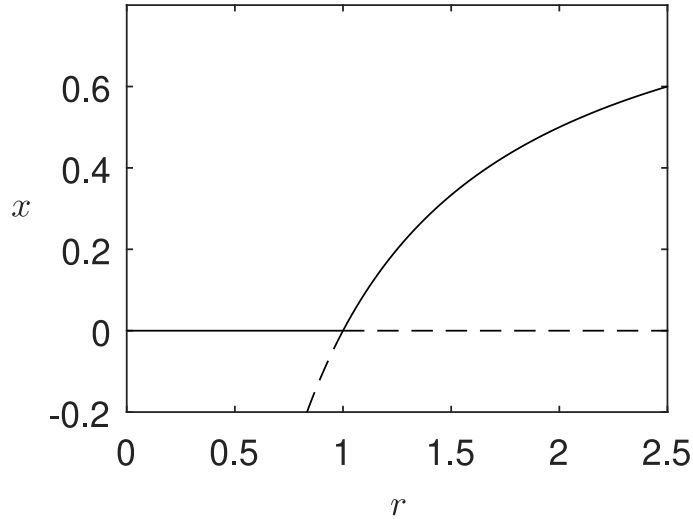


**Figure 4.4:** The transcritical bifurcation that occurs at  $r^c = 1$  in the deterministic logistic map. Solid black lines correspond to stable branches and dashed lines correspond to unstable branches of equilibria.

map is given by

$$x_{t+1} = rx_t(1 - x_t), \quad (4.35)$$

where the control parameter  $r \in [0, \infty)$ . The map has fixed points at  $x^0 = 0$  and  $x^1 = 1 - 1/r$ . These fixed points exchange stability in a transcritical bifurcation at  $r^c = 1$ , as shown in Figure 4.4. The fixed point  $x^0$  is stable for  $r < r^c$  while the fixed point  $x^1$  is stable for  $r > r^c$ .

We introduce parametric noise to the logistic map replacing the constant control parameter  $r$  with a stochastic time-varying control parameter

$$r_t = r(1 + \sigma\xi_t), \quad (4.36)$$

where  $\xi_t$  is a random variable and  $0 < \sigma \ll 1$  is a measure of the noise amplitude. In particular, we take the distribution of  $\xi_t$  to be such that  $E(\xi_t) = 0$  and  $E(\xi_t^2) = 1$ . Let us now consider the effect of noise on the transcritical bifurcation of the deterministic system at  $r^c = 1$ . In the noisy case, with noise amplitude  $\sigma$ , the fixed point  $x^0$  is

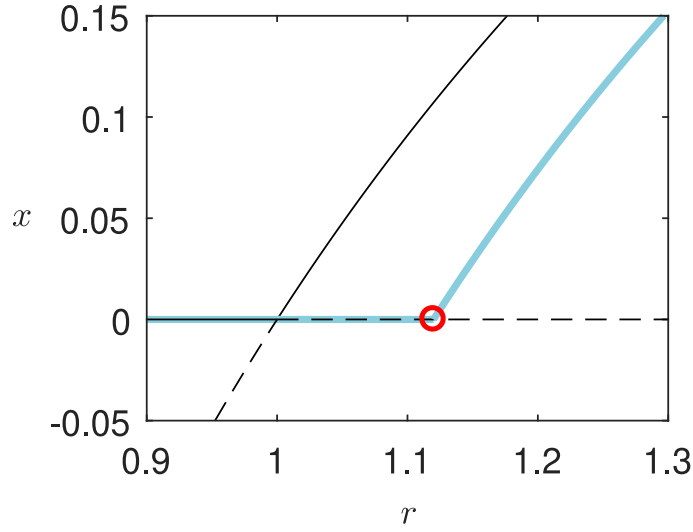


**Figure 4.5:** Representative bifurcation diagram of the logistic map with small parametric noise. The expectation of the stationary distribution  $E(x)$  is shown with thick blue lines, the corresponding deterministic bifurcation diagram is shown with thin black lines. The critical value of the control parameter  $r^c(\sigma)$  is highlighted with a red circle.

stable for  $r$  such that

$$\lim_{n \rightarrow \infty} \left| \frac{\partial x_n}{\partial x_0} \right|_{x_0=0} = \lim_{n \rightarrow \infty} \prod_{t=0}^{n-1} r |1 + \sigma \xi_t| \leq 1. \quad (4.37)$$

The fixed-point therefore becomes unstable for  $r > r^c(\sigma)$ , where  $r^c$  is the value of  $r$  which solves

$$\lim_{n \rightarrow \infty} \left( \prod_{t=0}^{n-1} r^c |1 + \sigma \xi_t| \right)^{\frac{1}{n}} = 1 \quad (4.38)$$

or equivalently

$$r^c(\sigma) = \exp(-E(\ln |1 + \sigma \xi|)), \quad (4.39)$$

where  $\xi$  is the stationary distribution of the noise terms  $\xi_t$ .

Expanding (4.39) about  $\sigma = 0$  we find that

$$r^c(\sigma) = 1 + \frac{\sigma^2}{2} + \mathcal{O}(\sigma^4) > 1, \quad (4.40)$$

regardless of the specific distribution of  $\xi_t$ . In other words, parametric noise stabilises the fixed point  $x^0 = 0$ , beyond the transcritical bifurcation that takes place at  $r^c(0) = 1$  in the deterministic system. Linz and Lücke also showed in numerical tests [24] that for low noise amplitudes  $\sigma$  and small  $r$  above  $r^c(\sigma)$  the system displays small low-amplitude fluctuations about a mean which grows with  $r$ , similar to how the deterministic fixed point  $x^1$  grows beyond  $r = 1$  as shown in Figure 4.5. In other words, they found that parametric noise effectively delays the first bifurcation of the logistic map.

Next we consider an example in continuous time. In [64] Lücke and Schank considered the effects of stochastic forcing on a nonlinear oscillator. Nonlinear oscillators are used to model a wide range of real-world processes including mechanical oscillators, biological systems and electronic circuits. In [64] the oscillator considered is a parametrically driven, damped anharmonic oscillator given by

$$m\ddot{x} + m\gamma\dot{x} = (r + \sigma\xi(t))x - x^3, \quad (4.41)$$

where the forcing  $\xi(t)$  is a stationary stochastic process with mean zero and  $\sigma$  is the noise amplitude.

In the deterministic case, where  $\sigma = 0$ , the system undergoes a supercritical pitchfork bifurcation. The fixed point at  $x_0 = 0$  becomes unstable and two stable fixed points at  $x_{1,2} = \pm\sqrt{r}$  are born when the bifurcation parameter  $r$  increases through the critical value  $r_c = 0$ . Similar to the logistic map case where Linz and Lücke [24] showed that small parametric noise delays a transcritical bifurcation, Lücke and Schank [64] showed that the pitchfork bifurcation at  $r_c = 0$  is delayed by the presence of small parametric noise with amplitude  $0 < \sigma \ll 1$ . In particular, they showed that the critical value of  $r$  for which  $x_0$  loses stability in the noisy case is given by

$$r_c(\sigma) = \sigma^2 \frac{1}{m} \int_0^\infty \frac{D(\omega)}{\omega^2 + \gamma^2} \frac{d\omega}{\pi} + \mathcal{O}(\sigma^4), \quad (4.42)$$

where  $D(\omega)$  is the spectrum

$$D(\omega) = \int_{-\infty}^{\infty} e^{i\omega t} E(\xi(t)\xi(0))dt. \quad (4.43)$$

In the language of Arnold [26], the phenomena described in both the logistic map and the anharmonic oscillator examples are *p-bifurcations*. A *p-bifurcation* or *phenomenological bifurcation* is a stochastic bifurcation characterised by a qualitative change in the stationary distribution of a noisy dynamical system, for example from unimodal to bimodal. In [26] Arnold also defined stochastic bifurcations known as *d-bifurcations*. A *d-bifurcation* or *dynamical bifurcation* is different to a *p-bifurcation* and corresponds to the separation of dynamics into state space regions between which no transitions are possible. Dynamical bifurcations are characterised by bifurcations of invariant measures and their definition reduces to the deterministic definition of bifurcation in the absence of noise.

## 4.2.2 Noise in Nonsmooth Dynamical Systems

The effects of noise on nonsmooth systems has seen limited research compared to smooth dynamical systems and is the subject of this thesis. Much of the existing work focuses on piecewise-linear maps [28, 29, 65], switched control systems [32, 33, 66, 67], vibro-impacting systems [30, 31, 68, 69, 70] and noise-induced oscillations in systems such as the piecewise-linear FitzHugh-Nagumo model [71]. Here we will present two examples of recent research in the area highlighting the significant effects noise can have on the behaviour of nonsmooth systems. The first example will be a discrete-time example from Griffin and Hogan [28] and the second a continuous-time example from Simpson and Kuske [32, 33, 72].

The first example we consider is a one-dimensional piecewise-linear map studied by Griffin and Hogan [28] in the presence of additive noise. The precise map they

studied is given by

$$x_{t+1} = \begin{cases} \alpha x_t - \mu + \sigma \xi_t, & x_t \geq 0, \\ \beta x_t - \mu - \gamma + \sigma \xi_t, & x_t < 0, \end{cases} \quad (4.44)$$

where  $\alpha$ ,  $\mu$ ,  $\beta$  and  $\gamma$  are real parameters,  $\sigma$  is the noise amplitude and the noise terms  $\xi_t$  are independently distributed Gaussian random variables with mean zero and unit variance, i.e.  $\xi_t \stackrel{\text{i.i.d.}}{\sim} N(0, 1)$ .

Griffin and Hogan [28] consider the map with  $\gamma = -1, 0, +1$ , but here we will focus on presenting the results in the  $\gamma = -1$  case. In this case the deterministic map ( $\sigma = 0$ ) with  $\alpha = 1/2$  and  $\beta = -1/2$  undergoes a bifurcation at  $\mu = 0$ . For  $\mu < 0$  a stable fixed point exists at  $x_1 = \frac{\mu}{\alpha-1}$ , this fixed point undergoes a border-collision bifurcation at  $\mu = 0$  and beyond this point the dynamics of the map are more complicated with higher-order solutions existing. Griffin and Hogan showed that the invariant distribution associated with (4.44) in the presence of noise undergoes qualitative changes as the noise amplitude  $\sigma$  is increased, in other words, it undergoes a  $p$ -bifurcation. Increasing  $\sigma$  from zero the invariant distribution for  $\mu < 0$  close to the bifurcation point is initially unimodal, centred on the fixed point at  $x_1$ . As the noise amplitude is increased further the distribution becomes trimodal with two smaller modes created close to the higher order solutions for  $\mu > 0$  due to the advance of the deterministic bifurcation. Increasing  $\sigma$  once more the two smaller modes and the larger mode eventually merge.

The map (4.44) with  $\sigma = 0$  is the Poincaré map, associated with the Poincaré section

$$\mathcal{P} = \{(x, y) : x = 0, y > 0\}, \quad (4.45)$$

of the two-dimensional piecewise-smooth ODE given by

$$\dot{x} = y, \quad (4.46)$$

$$\dot{y} = 2p(j)y - 1 + p^2(j)x, \quad (4.47)$$

where  $p(j)$  is a piecewise-smooth function. The authors also showed that including noise in (4.46), by writing the system as the SDE

$$dx = ydt + \frac{\sigma}{\sqrt{2\pi}}dB_t^1, \quad (4.48)$$

$$dy = (2p(j)y - 1 + p^2(j)x)dt + \frac{\sigma}{\sqrt{2\pi}}dB_t^2, \quad (4.49)$$

where  $\mathbf{B}_t = (B_t^1, B_t^2)^T$  is a standard two-dimensional Brownian process, produces identical  $p$ -bifurcations to those observed in the map when  $\gamma = -1$ .

The second example we consider is a continuous-time example studied by Simpson and Kuske. In [32, 33, 72] the authors investigated the effects of noise on sliding periodic orbits in piecewise-smooth vector fields. In particular, they considered a relay control model given by

$$\dot{\mathbf{x}} = A\mathbf{x} - \text{sgn}(c^T \mathbf{x})b, \quad (4.50)$$

where  $\mathbf{x} \in \mathbb{R}^3$  is the state of the system,  $-\text{sgn}(c^T \mathbf{x})$  is the control response,

$$A = \begin{pmatrix} -5.05 & 1 & 0 \\ -25.25 & 0 & 1 \\ 1.25 & 0 & 0 \end{pmatrix}, \quad b = \begin{pmatrix} 1 \\ -2 \\ 1 \end{pmatrix} \quad \text{and} \quad c = \begin{pmatrix} 1 \\ 0 \\ 0 \end{pmatrix}. \quad (4.51)$$

This system has a symmetric periodic attractor  $\Gamma$  with two sliding segments along the discontinuity boundary  $\Sigma = \{\mathbf{x} : c^T \mathbf{x} = 0\}$ . We will denote the period of  $\Gamma$  as  $\tau_\Gamma$ . Periodic sliding attractors exist in this system for a large range of parameter values and the results that we describe in what follows also hold for other values of  $A$ ,  $b$

and  $c$ .

From the viewpoint of control, it is important to understand the robustness of the periodic attractor  $\Gamma$  to the presence of noise. In this context the authors considered the system (4.50) with small white noise added to the control response such that

$$d\mathbf{x} = (A\mathbf{x} - \text{sgn}(c^T \mathbf{x})b)dt + \sigma b d\mathbf{B}_t, \quad (4.52)$$

where  $\mathbf{B}_t$  is a standard three-dimensional Brownian process and  $0 < \sigma \lll 1$ . In particular, they investigated how the period of the sliding periodic orbit  $\tau_\Gamma$  is affected by the addition of noise. They described a change in the oscillation time of  $\Gamma$  as significant if the square of the difference

$$\text{Diff}(\tilde{\tau}_\Gamma(\sigma))^2 = (E(\tilde{\tau}_\Gamma(\sigma)) - \tau_\Gamma)^2 \quad (4.53)$$

is comparable to, or larger than,  $\text{Var}(\tilde{\tau}_\Gamma(\sigma))$ , where  $\tilde{\tau}_\Gamma(\sigma)$  is the oscillation time of the periodic behaviour in the presence of noise.

Using both Monte-Carlo simulations and analytic arguments, the authors showed that the addition of small white noise caused a significant decrease in oscillation time. They argued that this significant decrease was caused by four separate phenomena associated with the geometry of the deterministic system:

1. The deterministic periodic orbit  $\Gamma$  slowly approaches the discontinuity boundary at a sharp angle. As a result, small additive noise tends to push solutions onto the discontinuity boundary early, reducing  $E(\tilde{\tau}_\Gamma(\sigma))$ .
2. Small noise pushes solutions slightly off the discontinuity boundary while they would be sliding in the deterministic system. This allows the vector field away from the discontinuity boundary to influence dynamics, further reducing  $E(\tilde{\tau}_\Gamma(\sigma))$ .
3. Away from the discontinuity boundary solutions rapidly contract onto a slow

manifold. This inhibits the possibility of large deviations in  $\tilde{\tau}_\Gamma(\sigma)$ , reducing  $Var(\tilde{\tau}_\Gamma(\sigma))$ .

4. In (4.52) noise is purely added to the control response. The authors showed that this causes the leading-order contribution of noise during stochastically perturbed sliding to vanish, further reducing  $Var(\tilde{\tau}_\Gamma(\sigma))$ .

For systems with different geometries and sliding periodic orbits the opposite is also possible, i.e. noise can result in a significant increase in the oscillation time of a sliding periodic orbit.

In general we see that noise can have a large and unexpected influence on the dynamics of both smooth and nonsmooth systems. Given the limited amount of research in the area of nonsmooth systems there is much to explore. Chapters 7-10 aim to contribute to our understanding of this area.

# Chapter 5

## Discussion and Outlook

This thesis, and principally the four papers collected in Chapters 7-10, aims to further our knowledge of stochastic nonsmooth dynamical systems, an area which has so far seen limited research. We believe that our findings have the potential to have far reaching applications and to motivate important future work. This is as a result of the fact that systems that are both stochastic and nonsmooth arise naturally when constructing mathematical models in a wide range of contexts, from engineering and control theory, to economics and sociology, to biology and ecology.

The papers contained in this thesis can be split into two pairs in a very natural manner. The first two papers, contained in Chapters 7 and 8, focus on a illustrative example of a noisy nonsmooth system. These chapters highlight the complex and non-trivial effects noise can have on even the simplest nonsmooth systems. The papers that form Chapters 9 and 10, on the other hand, concern the development and validation of new tools in analysing and efficiently simulating general nonsmooth dynamical systems with stochastic discontinuity boundaries.

The example considered in Chapters 7 and 8 is that of the square root map, a piecewise smooth map that arises in the study of impacting mechanical systems. In particular, the one-dimensional version of the map that we studied has been shown

by Nordmark [59] to be a universal limit for higher-dimensional square root mappings arising from the study of impact oscillators near zero-velocity *grazing* impacts. We considered the system under the influence of additive white noise and found that the effects of noise on the dynamics of the system are highly non-trivial. We showed that multistability could be both destroyed and induced by the addition of noise and that, in general, there is a non-monotonic relationship between noise amplitude and the behaviour of the square root map. The non-trivial results of this work should motivate the analysis of the effects of noise on other more complicated nonsmooth systems.

Chapters 9 and 10 focus on the development of stochastic zero-time discontinuity mappings. In a deterministic context zero-time discontinuity mappings, and discontinuity mappings in general, facilitate the analysis of the dynamics of nonsmooth systems and their bifurcations by correcting for the effects of trajectories crossing discontinuity boundaries. In these papers we developed a variety stochastic of zero-time discontinuity mappings for the analysis of different phenomena in continuous-time nonsmooth systems with stochastic discontinuity boundaries. We also briefly showed how these mappings can be used to determine the effects of noise on bifurcations in these systems. We believe that the methods derived in these papers have the potential to facilitate further analysis of the effects of noise on nonsmooth systems and their bifurcations. These methods are also useful for efficient numerical simulation of piecewise-smooth and hybrid dynamical systems with noisy discontinuity boundaries.

While there is a huge amount of work still to be done, we hope that we have contributed in some way to both motivate and facilitate further research into stochastic nonsmooth dynamical systems. Looking to the future, we believe that there is a clear need for, and obvious benefits to be gained from, a deeper understanding of the effects of noise on nonsmooth dynamical systems. In recent years we have seen nonsmooth dynamical models being applied to an increasingly wide variety of problems including human sleep [73], bipedal walking [74], climate change [12], mitosis

[14], economic cooperation [75], seasonality in electricity markets [76], electrostatic energy harvesting [77], superconductors [78] and more [1, 79]. Understanding the effects of noise on such systems and the sensitivity to noise of more traditionally studied examples of nonsmooth dynamical systems such as impact oscillators [5, 54], drills [80], brakes [81], electronic converters [7, 8], control systems [82] and neuronal models [83] has the potential for interesting and impactful results.

Noise enters nonsmooth systems such as those described above in a variety of ways. For example, noisy decision thresholds that fluctuate randomly in time about some expected threshold in economic or sociological models could be modelled as noisy discontinuity boundaries. Similarly, the uncertain time of the onset of winter or summer in seasonal models and noisy switches in electrical and control models also constitute stochastic discontinuity boundaries. In other models the largest source of noise can be in the continuous evolution of the system away from discrete events, in such cases the noise must be applied to the vector field. Examples of this include impact oscillators where noise enters the system through the external periodic forcing, noisy integrate and fire neuronal models, and noise in the input to a superconducting resonator. In some cases significant noise could be present in both the discontinuity boundary and the system's smooth evolution away from boundaries.

A particular area of future research that would naturally extend the work contained in this thesis is the development of stochastic discontinuity mappings for systems where the noise is applied to the vector field, rather than the position of the discontinuity boundary. Combining the results of this potential research with our work on discontinuity mappings for systems with noisy boundaries would allow us to perform local analysis on the vast majority of noisy nonsmooth systems.



# Chapter 6

## Summary of Papers and Author Contributions

### 6.1 Paper 1

*Noise and Multistability in the Square Root Map* [84]

Eoghan J. Staunton and Petri T. Piiroinen

In this paper we describe the complex structure of the basins of attraction of stable periodic orbits of the one-dimensional square root map and how this produces sensitivity to the addition of small amplitude noise. In particular we focus on how noise of varying amplitudes affects the system in parameter regions of attractor coexistence and also how trajectories jump between different periodic behaviours. We show that there is a non-monotonic relationship between the noise amplitude and the proportion of time spent in each periodic behaviour. These relationships will be explained by examining approximations of steady-state distributions of trajectory deviations due to noise and the complicated deterministic structures of the map. We also show how the effect of noise scales on consecutive intervals of multistability.

All analysis, numerical simulations and implementations performed by EJS. Paper

written and revised by EJS with feedback and guidance from PTP.

Published in *Physica D: Nonlinear Phenomena*, Volumes 380-381, 2018, Pages 31-44.

The final publication is available at ScienceDirect via:

<http://dx.doi.org/10.1016/j.physd.2018.06.002>

## 6.2 Paper 2

*Noise-Induced Multistability in the Square Root Map* [85]

Eoghan J. Staunton and Petri T. Piiroinen

This paper expands on the work done in Paper 1. The effects of small-amplitude additive Gaussian white noise on the one-dimensional square root map are investigated, this time focusing on the unexpected effects noise of varying amplitudes has on the system for parameter regions just *outside* intervals of multistability. It is shown that in these regions periodic behaviour that is unstable in the deterministic system can be effectively stabilised by the addition of noise of an appropriate amplitude. Features of noise-induced transitions from stable to stabilised unstable periodic behaviour are highlighted and it is shown how these features can be understood by examining relative levels of expansion and contraction in the deterministic map.

All analysis, numerical simulations and implementations performed by EJS. Paper written and revised by EJS with feedback and guidance from PTP.

Published in *Nonlinear Dynamics*, Volume 95, Issue 1, 2019, Pages 769-782.

The final publication is available at Springer Nature via:

<http://dx.doi.org/10.1007/s11071-018-4595-1>

### 6.3 Paper 3

*Estimating the Dynamics of Systems with Noisy Boundaries* [86]

Eoghan J. Staunton and Petri T. Piironen

In a smooth dynamical system the characteristics of a given reference trajectory can be determined, to lowest order, by examining the linearised system about the reference trajectory. In other words, we can approximate the deviations of trajectories after a given time, with starting points in a neighbourhood of the reference trajectory, by multiplying the initial deviations by the corresponding fundamental matrix solution.

This form of analysis cannot be used directly in nonsmooth systems as the vector field is either not everywhere differentiable or the flow function is not continuous. To account for this, one can derive the *zero-time discontinuity mapping* associated with the discontinuity boundary. The Jacobian of this mapping is known as the *saltation matrix* and its properties can tell us how the crossing of the discontinuity boundary affects the deviations of trajectories from a reference trajectory. In particular, this matrix can be composed with the fundamental matrix solutions of the individual flows on either side of the discontinuity boundary in order to determine the overall fundamental matrix solution of a trajectory that crosses the boundary.

In this paper we derive a saltation matrix for a piecewise-smooth dynamical system in which the position of the discontinuity boundary oscillates according to a mean-reverting stochastic process. The derived saltation matrix contains the entire effect of both the discontinuity and the uncertainty introduced into the system by the noisy boundary, and is composable with the deterministic fundamental matrix solutions of the individual flows to give the overall fundamental matrix solution of a crossing trajectory.

We also present some simple examples of piecewise-smooth systems with stochastically varying boundaries, analysed using the derived *noisy saltation matrix*. In particular

we focus on the analysis of a discontinuous variant of *the Chua circuit*. In this case we apply noise to the system's discontinuity boundaries which are generated by the piecewise-linear nature of the voltage-current response of the Chua diode. We find that our method allows us to analyse the effects of boundary noise on periodic attractors close to bifurcation points. In particular we show that we can use the method to accurately predict the noise amplitudes required to destroy or merge periodic attractors.

All analysis, numerical simulations and implementations performed by EJS. Paper written and revised by EJS with feedback and guidance from PTP.

To appear in *Nonlinear Analysis: Hybrid Systems*, Volume 36, May 2020.

The final publication is available at ScienceDirect via:

<http://dx.doi.org/10.1016/j.nahs.2020.100863>

## 6.4 Paper 4

*Discontinuity Mappings for Stochastic Nonsmooth Systems* [87]

Eoghan J. Staunton and Petri T. Piiroinen

This paper generalises the work done in Paper 3, constructing stochastic zero-time discontinuity mappings in more general settings. For stability and bifurcation analysis involving recurrent behaviour such as periodic orbits, it is important to be able to quantify how trajectories near to a reference trajectory behave by means of a local mapping. In smooth systems these mappings can be computed using the system's variational equations. For piecewise-smooth or hybrid systems the same technique cannot be used without some corrections. This is due to the fact that nearby trajectories can be topologically distinct because they can undergo different sequences of events associated with the system's discontinuity boundaries. To account for this, one can derive zero-time discontinuity mappings associated with boundary interactions. In this paper we derive zero-time discontinuity mappings for

piecewise-smooth vector fields and hybrid dynamical systems in which the position of the discontinuity boundary has a stochastic component. In particular, we derive SZDMs for transversal crossings in hybrid systems and systems with higher-order discontinuities, cases not considered in Paper 3. We also consider non-transversal crossings in a grazing hybrid system. In all cases we consider two types of noise, stochastic oscillations and stochastic surface imperfections, only the former was considered in Paper 3.

All analysis and numerical simulations performed by EJS. Paper written by EJS with feedback and guidance from PTP.

In submission, 2019.

# Bibliography

- [1] O. Makarenkov and J. S. Lamb, “Dynamics and bifurcations of nonsmooth systems: A survey,” *Physica D: Nonlinear Phenomena*, vol. 241, no. 22, pp. 1826–1844, 2012.
- [2] M. di Bernardo, P. Kowalczyk, and A. Nordmark, “Sliding bifurcations: a novel mechanism for the sudden onset of chaos in dry friction oscillators,” *International journal of Bifurcation and chaos*, vol. 13, no. 10, pp. 2935–2948, 2003.
- [3] H. Dankowicz, P. Piiroinen, and A. B. Nordmark, “Low-velocity impacts of quasiperiodic oscillations,” *Chaos, Solitons & Fractals*, vol. 14, no. 2, pp. 241–255, 2002.
- [4] A. Nordmark, H. Dankowicz, and A. Champneys, “Discontinuity-induced bifurcations in systems with impacts and friction: discontinuities in the impact law,” *International journal of non-linear mechanics*, vol. 44, no. 10, pp. 1011–1023, 2009.
- [5] S. Foale and S. R. Bishop, “Bifurcations in impact oscillations,” *Nonlinear dynamics*, vol. 6, no. 3, pp. 285–299, 1994.
- [6] Y. Yoshitake and A. Sueoka, “Forced self-excited vibration with dry friction,” in *Applied nonlinear dynamics and chaos of mechanical systems with discontinuities*, pp. 237–259, World Scientific, 2000.

- 
- [7] M. di Bernardo, F. Garefalo, L. Glielmo, and F. Vasca, “Switchings, bifurcations, and chaos in DC/DC converters,” *IEEE Transactions on Circuits and Systems I: Fundamental Theory and Applications*, vol. 45, no. 2, pp. 133–141, 1998.
- [8] E. Fossas and G. Olivar, “Study of chaos in the buck converter,” *IEEE Transactions on Circuits and Systems I: Fundamental Theory and Applications*, vol. 43, no. 1, pp. 13–25, 1996.
- [9] D. Amrani and D. P. Atherton, “Designing autonomous relay systems with chaotic motion,” in *Decision and Control, 1989., Proceedings of the 28th IEEE Conference on*, pp. 512–517, IEEE, 1989.
- [10] K. Hill, D. S. Abbot, and M. Silber, “Analysis of an arctic sea ice loss model in the limit of a discontinuous albedo,” *SIAM Journal on Applied Dynamical Systems*, vol. 15, no. 2, pp. 1163–1192, 2016.
- [11] P. Kowalczyk and P. Glendinning, “Boundary-equilibrium bifurcations in piecewise-smooth slow-fast systems,” *Chaos: An Interdisciplinary Journal of Nonlinear Science*, vol. 21, no. 2, p. 023126, 2011.
- [12] J. Leifeld, “Non-smooth homoclinic bifurcation in a conceptual climate model,” *European Journal of Applied Mathematics*, vol. 29, no. 5, pp. 891–904, 2018.
- [13] J. G. Donohue and P. T. Piiroinen, “Mathematical modelling of seasonal migration with applications to climate change,” *Ecological modelling*, vol. 299, pp. 79–94, 2015.
- [14] C. P. Fall, E. S. Marland, J. M. Wagner, and J. J. Tyson, eds., *Computational cell biology*, vol. 20 of *Interdisciplinary Applied Mathematics*. Springer-Verlag, New York, 2002.
- [15] E. Santor, L. Suchanek, *et al.*, “Unconventional monetary policies: evolving practices, their effects and potential costs,” *Bank of Canada Review*, vol. 2013, no. Spring, pp. 1–15, 2013.

- [16] J. A. Amador, G. Olivar, and F. Angulo, “Smooth and Filippov models of sustainable development: Bifurcations and numerical computations,” *Differential Equations and Dynamical Systems*, vol. 21, no. 1-2, pp. 173–184, 2013.
- [17] C. W. Gardiner *et al.*, *Handbook of stochastic methods*, vol. 3. Springer Berlin, 1985.
- [18] M. di Bernardo, C. J. Budd, A. R. Champneys, P. Kowalczyk, A. B. Nordmark, G. O. Tost, and P. T. Piiroinen, “Bifurcations in nonsmooth dynamical systems,” *SIAM review*, vol. 50, no. 4, pp. 629–701, 2008.
- [19] R. I. Leine and H. Nijmeijer, *Dynamics and bifurcations of non-smooth mechanical systems*, vol. 18. Springer Science & Business Media, 2013.
- [20] Z. T. Zhusubaliyev and E. Mosekilde, *Bifurcations and chaos in piecewise-smooth dynamical systems*. World Scientific, 2003.
- [21] M. di Bernardo, M. I. Feigin, S. J. Hogan, and M. E. Homer, “Local analysis of c-bifurcations in n-dimensional piecewise-smooth dynamical systems,” *Chaos, Solitons and Fractals: the interdisciplinary journal of Nonlinear Science, and Nonequilibrium and Complex Phenomena*, vol. 11, no. 10, pp. 1881–1908, 1999.
- [22] M. di Bernardo, C. J. Budd, A. R. Champneys, and P. Kowalczyk, *Piecewise-smooth dynamical systems: theory and applications*, vol. 163. Springer Science & Business Media, 2008.
- [23] S. Rajasekar, “Controlling of chaotic motion by chaos and noise signals in a logistic map and a Bonhoeffer–van der Pol oscillator,” *Physical Review E*, vol. 51, no. 1, p. 775, 1995.
- [24] S. J. Linz and M. Lücke, “Effect of additive and multiplicative noise on the first bifurcations of the logistic model,” *Physical Review A*, vol. 33, no. 4, p. 2694, 1986.

- [25] A. Longtin, “Effects of noise on nonlinear dynamics,” in *Nonlinear Dynamics in Physiology and Medicine*, pp. 149–189, Springer, 2003.
- [26] L. Arnold, “Random dynamical systems,” in *Dynamical systems*, pp. 1–43, Springer, 1995.
- [27] W. Horsthemke, *Noise-induced transitions : theory and applications in physics, chemistry, and biology*, vol. 15 of *Springer series in synergetics*. 1984.
- [28] T. Griffin and S. J. Hogan, “Dynamics of discontinuous systems with imperfections and noise,” in *IUTAM Symposium on Chaotic Dynamics and Control of Systems and Processes in Mechanics*, pp. 275–285, Springer, 2005.
- [29] W. Zhang, J. Hu, and J. Lian, “Quadratic optimal control of switched linear stochastic systems,” *Systems & Control Letters*, vol. 59, no. 11, pp. 736–744, 2010.
- [30] D. J. W. Simpson, S. J. Hogan, and R. Kuske, “Stochastic regular grazing bifurcations,” *SIAM Journal on Applied Dynamical Systems*, vol. 12, no. 2, pp. 533–559, 2013.
- [31] D. J. W. Simpson and R. Kuske, “The influence of localized randomness on regular grazing bifurcations with applications to impacting dynamics,” *Journal of Vibration and Control*, p. 1077546316642054, 2016.
- [32] D. J. W. Simpson and R. Kuske, “Stochastic perturbations of periodic orbits with sliding,” *Journal of Nonlinear Science*, vol. 25, no. 4, pp. 967–1014, 2015.
- [33] D. J. W. Simpson and R. Kuske, “Stochastically perturbed sliding motion in piecewise-smooth systems,” *Discrete & Continuous Dynamical Systems - B*, vol. 19, no. 9, pp. 2889–2913, 2014.
- [34] J. Guckenheimer and P. J. Holmes, *Nonlinear oscillations, dynamical systems, and bifurcations of vector fields*, vol. 42. Springer Science & Business Media, 2013.

- [35] Y. A. Kuznetsov, *Elements of applied bifurcation theory*, vol. 112. Springer Science & Business Media, 2013.
- [36] S. Wiggins, *Introduction to applied nonlinear dynamical systems and chaos*, vol. 2. Springer Science & Business Media, 2003.
- [37] S. H. Strogatz, *Nonlinear dynamics and chaos: with applications to physics, biology, chemistry, and engineering*. CRC Press, 2018.
- [38] P. Glendinning, *Stability, instability and chaos: an introduction to the theory of nonlinear differential equations*, vol. 11. Cambridge university press, 1994.
- [39] T. Matsumoto, “A chaotic attractor from Chua’s circuit,” *IEEE Transactions on Circuits and Systems*, vol. 31, no. 12, pp. 1055–1058, 1984.
- [40] H. Lütkepohl, *Handbook of matrices*. John Wiley & Sons, Ltd., Chichester, 1996.
- [41] W. J. F. Govaerts, *Numerical methods for bifurcations of dynamical equilibria*. Society for Industrial and Applied Mathematics (SIAM), Philadelphia, PA, 2000.
- [42] H. Dankowicz and F. Schilder, *Recipes for continuation*, vol. 11 of *Computational Science & Engineering*. Society for Industrial and Applied Mathematics (SIAM), Philadelphia, PA, 2013.
- [43] B. Krauskopf, H. M. Osinga, and J. Galán-Vioque, eds., *Numerical continuation methods for dynamical systems*. Understanding Complex Systems, Springer, Dordrecht, 2007. Path following and boundary value problems, Dedicated to Eusebius J. Doedel for his 60th birthday.
- [44] E. L. Allgower and K. Georg, *Introduction to numerical continuation methods*, vol. 45 of *Classics in Applied Mathematics*. Society for Industrial and Applied Mathematics (SIAM), Philadelphia, PA, 2003. Reprint of the 1990 edition [Springer-Verlag, Berlin; MR1059455 (92a:65165)].

- 
- [45] E. J. Doedel, T. F. Fairgrieve, B. Sandstede, A. R. Champneys, Y. A. Kuznetsov, and X. Wang, “Auto-07p: Continuation and bifurcation software for ordinary differential equations,” tech. rep., 2007.
- [46] A. Dhooge, W. Govaerts, Y. A. Kuznetsov, H. G. E. Meijer, and B. Sautois, “New features of the software MatCont for bifurcation analysis of dynamical systems,” *Math. Comput. Model. Dyn. Syst.*, vol. 14, no. 2, pp. 147–175, 2008.
- [47] M. di Bernardo and S. J. Hogan, “Discontinuity-induced bifurcations of piecewise smooth dynamical systems,” *Philosophical Transactions of the Royal Society A: Mathematical, Physical and Engineering Sciences*, vol. 368, no. 1930, pp. 4915–4935, 2010.
- [48] A. F. Filippov, *Differential equations with discontinuous righthand sides*. Kluwer Academic Publishers, Dordrecht, 1988.
- [49] V. I. Utkin, *Sliding modes in control and optimization*. Communications and Control Engineering Series, Springer-Verlag, Berlin, 1992. Translated and revised from the 1981 Russian original.
- [50] M. R. Jeffrey, “Hidden dynamics in models of discontinuity and switching,” *Physica D: Nonlinear Phenomena*, vol. 273, pp. 34–45, 2014.
- [51] M. R. Jeffrey, “The ghosts of departed quantities in switches and transitions,” *SIAM Review*, vol. 60, no. 1, pp. 116–136, 2018.
- [52] M. A. Aizerman and F. R. Gantmacher, “Determination of stability by linear approximation of a periodic solution of a system of differential equations with discontinuous right-hand sides,” *The Quarterly Journal of Mechanics and Applied Mathematics*, vol. 11, no. 4, pp. 385–398, 1958.
- [53] M. H. Fredriksson and A. B. Nordmark, “Bifurcations caused by grazing incidence in many degrees of freedom impact oscillators,” in *Proceedings of the Royal*

- Society of London A: Mathematical, Physical and Engineering Sciences*, vol. 453, pp. 1261–1276, The Royal Society, 1997.
- [54] A. B. Nordmark, “Non-periodic motion caused by grazing incidence in an impact oscillator,” *Journal of Sound and Vibration*, vol. 145, no. 2, pp. 279–297, 1991.
- [55] M. H. Fredriksson and A. B. Nordmark, “On normal form calculations in impact oscillators,” in *Proceedings of the Royal Society of London A: Mathematical, Physical and Engineering Sciences*, vol. 456, pp. 315–329, The Royal Society, 2000.
- [56] M. di Bernardo, C. J. Budd, and A. R. Champneys, “Normal form maps for grazing bifurcations in n-dimensional piecewise-smooth dynamical systems,” *Physica D: Nonlinear Phenomena*, vol. 160, no. 3-4, pp. 222–254, 2001.
- [57] H. Dankowicz and J. Jerrelind, “Control of near-grazing dynamics in impact oscillators,” *Proceedings of the Royal Society A: Mathematical, Physical and Engineering Sciences*, vol. 461, no. 2063, pp. 3365–3380, 2005.
- [58] W. Chin, E. Ott, H. E. Nusse, and C. Grebogi, “Grazing bifurcations in impact oscillators,” *Physical Review E*, vol. 50, no. 6, p. 4427, 1994.
- [59] A. B. Nordmark, “Universal limit mapping in grazing bifurcations,” *Physical review E*, vol. 55, no. 1, p. 266, 1997.
- [60] B. Øksendal, *Stochastic differential equations: an introduction with applications*. Springer Science & Business Media, 2013.
- [61] N. Wiener, “Differential-space,” *Journal of Mathematics and Physics*, vol. 2, no. 1-4, pp. 131–174, 1923.
- [62] R. M. May, “Simple mathematical models with very complicated dynamics,” *Nature*, vol. 261, pp. 459–467, 1976.

- 
- [63] P.-F. Verhulst, “Recherches mathématiques sur la loi d’accroissement de la population,” *Nouveaux Mémoires de l’Académie Royale des Sciences et Belles-Lettres de Bruxelles*, vol. 18, no. 1, 1845.
- [64] M. Lücke and F. Schank, “Response to parametric modulation near an instability,” *Physical review letters*, vol. 54, no. 14, p. 1465, 1985.
- [65] L. Zhang, P. Shi, C. Wang, and H. Gao, “Robust  $H_\infty$  filtering for switched linear discrete-time systems with polytopic uncertainties,” *International journal of adaptive control and signal processing*, vol. 20, no. 6, pp. 291–304, 2006.
- [66] P. D. Christofides and N. El-Farra, *Control of nonlinear and hybrid process systems: Designs for uncertainty, constraints and time-delays*, vol. 324. Springer Science & Business Media, 2005.
- [67] W. Feng and J.-F. Zhang, “Stability analysis and stabilization control of multi-variable switched stochastic systems,” *Automatica*, vol. 42, no. 1, pp. 169–176, 2006.
- [68] M. F. Dimentberg and D. V. Iourtchenko, “Random vibrations with impacts: a review,” *Nonlinear Dynamics*, vol. 36, no. 2-4, pp. 229–254, 2004.
- [69] M. F. Dimentberg and A. I. Menyailov, “Response of a single-mass vibroimpact system to white-noise random excitation,” *ZAMM-Journal of Applied Mathematics and Mechanics/Zeitschrift für Angewandte Mathematik und Mechanik*, vol. 59, no. 12, pp. 709–716, 1979.
- [70] N. S. Namachchivaya and J. H. Park, “Stochastic dynamics of impact oscillators,” *Journal of applied mechanics*, vol. 72, no. 6, pp. 862–870, 2005.
- [71] D. J. W. Simpson and R. Kuske, “Mixed-mode oscillations in a stochastic, piecewise-linear system,” *Physica D: Nonlinear Phenomena*, vol. 240, no. 14-15, pp. 1189–1198, 2011.

- [72] D. J. W. Simpson and R. Kuske, “The positive occupation time of brownian motion with two-valued drift and asymptotic dynamics of sliding motion with noise,” *Stochastics and Dynamics*, vol. 14, no. 04, p. 1450010, 2014.
- [73] M. P. Bailey, G. Derks, and A. C. Skeldon, “Circle maps with gaps: Understanding the dynamics of the two-process model for sleep–wake regulation,” *European Journal of Applied Mathematics*, vol. 29, no. 5, pp. 845–868, 2018.
- [74] P. T. Piiroinen, H. J. Dankowicz, and A. B. Nordmark, “On a normal-form analysis for a class of passive bipedal walkers,” *International Journal of Bifurcation and Chaos*, vol. 11, no. 09, pp. 2411–2425, 2001.
- [75] H. A. Granada, J. A. Amador, G. Olivar, and S. M. C. L. N. Colombia, “Nonlinear dynamics and non smooth in a model of sustainable development with economic exchange between two societies,” *Blucher Mechanical Engineering Proceedings*, vol. 1, no. 1, pp. 3347–3357, 2012.
- [76] J. Valencia, G. Olivar, C. J. Franco, and I. Dyner, “Qualitative analysis of climate seasonality effects in a model of national electricity market,” in *Analysis, Modelling, Optimization, and Numerical Techniques*, pp. 349–362, Springer, 2015.
- [77] P. Harte, E. Blokhina, O. Feely, D. Fournier-Prunaret, and D. Galayko, “Electrostatic vibration energy harvesters with linear and nonlinear resonators,” *International Journal of Bifurcation and Chaos*, vol. 24, no. 11, p. 1430030, 2014.
- [78] G. Bachar, E. Segev, O. Shtempluck, S. W. Shaw, and E. Buks, “Noise-induced intermittency in a superconducting microwave resonator,” *EPL (Europhysics Letters)*, vol. 89, no. 1, p. 17003, 2010.
- [79] A. Colombo, M. Jeffrey, J. T. Lázaro, and J. M. Olm, *Extended abstracts spring 2016: Nonsmooth dynamics*, vol. 8. Birkhäuser, 2017.

- [80] B. Besselink, N. Van De Wouw, and H. Nijmeijer, “A semi-analytical study of stick-slip oscillations in drilling systems,” *Journal of Computational and Nonlinear Dynamics*, vol. 6, no. 2, p. 021006, 2011.
- [81] M. Tanelli, G. Osorio, M. di Bernardo, S. M. Savaresi, and A. Astolfi, “Existence, stability and robustness analysis of limit cycles in hybrid anti-lock braking systems,” *International Journal of Control*, vol. 82, no. 4, pp. 659–678, 2009.
- [82] M. di Bernardo, K. H. Johansson, and F. Vasca, “Self-oscillations and sliding in relay feedback systems: Symmetry and bifurcations,” *International Journal of Bifurcation and chaos*, vol. 11, no. 04, pp. 1121–1140, 2001.
- [83] S. Coombes, R. Thul, and K. C. Wedgwood, “Nonsmooth dynamics in spiking neuron models,” *Physica D: Nonlinear Phenomena*, vol. 241, no. 22, pp. 2042–2057, 2012.
- [84] E. J. Staunton and P. T. Piiroinen, “Noise and multistability in the square root map,” *Physica D: Nonlinear Phenomena*, vol. 380, pp. 31–44, 2018.
- [85] E. J. Staunton and P. T. Piiroinen, “Noise-induced multistability in the square root map,” *Nonlinear Dynamics*, vol. 95, no. 1, pp. 769–782, 2019.
- [86] E. J. Staunton and P. T. Piiroinen, “Estimating the dynamics of systems with noisy boundaries,” *To appear in Nonlinear Analysis: Hybrid Systems*, vol. 36, May 2020.
- [87] E. J. Staunton and P. T. Piiroinen, “Discontinuity mapping for stochastic nonsmooth systems,” *In submission*, 2019.



# Chapter 7

## Paper 1:

# Noise and Multistability in the Square Root Map

EOGHAN J. STAUNTON, PETRI T. PIIROINEN

School of Mathematics, Statistics and Applied Mathematics,  
National University of Ireland, Galway.

---

**Abstract.** In this paper we describe the complex structure of the basins of attraction of stable periodic orbits of the one-dimensional square root map and how this produces sensitivity to the addition of small amplitude noise. In particular we focus on how noise of varying amplitudes affects the system in parameter regions of attractor coexistence and also how trajectories jump between different periodic behaviours. We show that there is a non-monotonic relationship between the noise amplitude and the proportion of time spent in each periodic behaviour. These relationships will be explained by examining approximations of steady-state

distributions of trajectory deviations due to noise and the complicated deterministic structures of the map. We also show how the effect of noise scales on consecutive intervals of multistability.

---

## 7.1 Introduction

A dynamical system is made up of a set of states  $X$ , known as the state space, and a dynamical rule that specifies the immediate future of all state variables, in terms of past states. Dynamical systems can have discrete or continuous time and in this paper the focus will be on discrete systems or so called *maps*. A deterministic evolution operator,  $f : X \rightarrow X$ , with discrete time  $T \subseteq \mathbb{Z}$  and a continuous state space  $X \subset \mathbb{R}^m$ , is called a map, where the state evolution is defined by  $x_{n+1} = f(x_n)$  for  $x_n \in X$ ,  $n \in T$  [1, 2, 3].

The analysis of dynamical systems, in general, and maps, in particular, can take many different forms depending on the system itself and on the application it represents. In many cases we are mainly interested in the qualitative behaviour of a dynamical system, such as fixed points, periodic orbits and chaos [3, 4]. *Bifurcation* is the name given to a qualitative change in the steady-state behaviour of a dynamical system under parameter variation. In other words, a bifurcation refers to a change in the steady-state behaviour such as a switch from a fixed point to an oscillation between two separate points or any other significant change such as the appearance of high-periodic orbits, quasi-periodicity or chaos.

Traditionally deterministic dynamical systems are used to model real-world phenomena. These models often present a simplified view of real-world systems where, on one hand, the evolution of systems is always smooth and exhibits no interruptions such as impacts, switches, slides or jumps and, on the other hand, the future of any system is completely determined by its present state with no uncertainty (or

noise) [5]. However, independently, both nonsmoothness and noise have been shown to be the drivers of significant changes in qualitative behaviour. In nonsmooth systems we find certain types of qualitative changes in the behaviour of the system, known as *discontinuity induced bifurcations*, that do not occur in the smooth setting [6, 7]. Adding noise to smooth but nonlinear systems has been shown to have the potential to do far more than just blur the outcome of the system in the absence of noise, especially close to bifurcation points [8, 9, 10]. As a result, it is therefore of particular interest to investigate and understand how the inclusion of noise can effect the qualitative dynamics of a nonsmooth system close to discontinuity-induced bifurcations.

In this paper we will focus on the one-dimensional *stochastic square root map* [7, 11, 12] that has its basis in recurrent impacting systems, and that is neither smooth nor deterministic. The square root map is a piecewise smooth map describing the dynamics of, for instance, an *impact oscillator* [13] experiencing low-velocity *grazing* impacts. The map itself exhibits interesting qualitative behaviour as a result of its nonsmoothness and in particular due to the presence of the square root singularity [11, 12, 14, 15, 16, 17, 18, 19]. However, we will consider the map in an uncertain environment by introducing low amplitude additive white noise. In particular we will consider the effects of the introduction of noise on the bifurcation structure of the system for particular parameter values, a structure known as a *period-adding cascade*, which is unique to nonsmooth systems.

The remainder of this paper is structured as follows. In Section 7.2 we will describe the deterministic bifurcation structure of the square root map and the structure of its basins of attraction when periodic attractors coexist. Section 7.3 introduces noise to the square root map and presents numerical observations of the effect of noise on the square root map in regions of multistability. In Section 7.4 we derive approximate steady-state distributions of trajectory deviations due to the addition of Gaussian white noise and in Section 7.5 we combine the results of Sections 7.2 and

7.4 to understand the effect of noise on the qualitative behaviour of the map when two stable periodic orbits coexist observed in Section 7.3. Finally, in Section 7.6 we show how the effect of noise scales in the system and we present our conclusions in Section 7.7.

## 7.2 The Deterministic Square Root Map

### 7.2.1 The Map

We will consider the one-dimensional deterministic square root map

$$x_{n+1} = S(x_n) = \begin{cases} S_L(x_n) = \mu + bx_n, & x_n < 0, \\ S_R(x_n) = \mu - a\sqrt{x_n}, & x_n \geq 0, \end{cases} \quad (7.1)$$

where  $a > 0$ ,  $b > 0$ ,  $S_L(x)$  is the linear part of the map applied on the left ( $L$ ) and  $S_R(x)$  is the square root part applied on the right ( $R$ ). In this paper we will assume that the parameter  $b$  is such that  $0 < b < 1/4$ . For values of  $b$  in this range the deterministic square root map undergoes a period-adding cascade with intervals of multistability as the bifurcation parameter  $\mu$  is decreased [11]. We will discuss the deterministic structures of the square root map in this case in more detail in Section 7.2.3.

### 7.2.2 Symbolic Dynamics

In our analysis we will be mainly interested in the qualitative behaviour of the map (7.1), i.e. whether an iterate is on the left-hand side or the right-hand side of the map rather than the exact numerical value of each iterate. As a result we will describe the dynamics of the square root map through the use of *symbolic sequences*. Any orbit  $\{x_n\}$  may be assigned a symbolic sequence  $\{X_n\}$  comprised of the letters  $L$

and  $R$ , where

$$X_n = \begin{cases} L, & x_n < 0, \\ R, & x_n \geq 0. \end{cases} \quad (7.2)$$

Therefore an  $L$  denotes an iterate on the left, while an  $R$  denotes an iterates on the right. Using symbolic sequences we will describe deterministic  $N$ -periodic orbits by their code  $(R^{n_1}L^{n_2} \dots R^{n_{m-1}}L^{n_m})^\infty$  where  $n_i \in \mathbb{N}$  and  $\sum_i n_i = N$ . On the other hand, an orbit with a corresponding symbolic sequence  $(R^{n_1}L^{n_2} \dots R^{n_{m-1}}L^{n_m})^r$ , where  $r$  is finite, will be described as undergoing  $R^{n_1}L^{n_2} \dots R^{n_{m-1}}L^{n_m}$  behaviour for those  $rN$  iterates.

### 7.2.3 Bifurcations and Deterministic Structures

Nordmark [11, 14] has shown that if  $0 < b < 1/4$  there are values of  $\mu > 0$  for which a stable periodic orbit of period  $m$  with code  $(RL^{m-1})^\infty$  exists for each  $m = 2, 3, \dots$ . Similarly, there are other values of  $\mu > 0$  such that there are two stable periodic orbits coexisting, one with code  $(RL^{m-1})^\infty$  and the other with code  $(RL^m)^\infty$ . These are the only possible attractors except at bifurcation points. We will now derive expressions for the bifurcation points and periodic orbits of the map (7.1) in this case.

For the deterministic system (7.1) orbits of period  $m$  of the form  $(RL^{m-1})^\infty$  exist as attractors over a range in the parameter  $\mu$  given by

$$\mu_m^s < \mu < \mu_m^e. \quad (7.3)$$

Here  $\mu_m^s$  is the threshold value of  $\mu$  for which the period- $m$  orbit loses stability in a *subcritical pitchfork bifurcation* and  $\mu_m^e$  is the value of  $\mu$  for for which the same orbit is created in a *border-collision bifurcation (nonsmooth fold)*. Let  $x_1 < x_2 < \dots < x_{m-1} < 0 < x_m$  denote the points of the period- $m$  orbit. We have that  $x_{m-1} < 0$  and

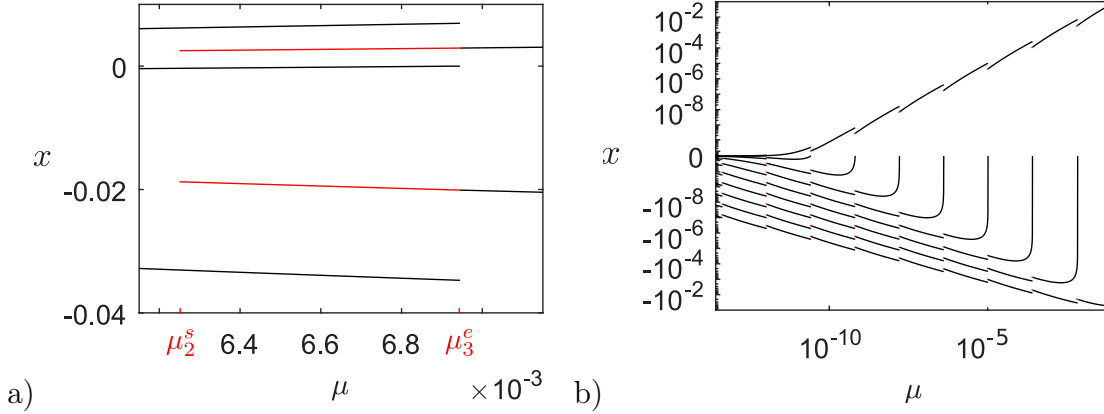


**Figure 7.1:** Bifurcation diagrams for the deterministic square root map,  $S$ , with  $a = 0.5$ ,  $b = 0.2$ . a) The coexistence of attractors  $(RL)^\infty$  and  $(RLL)^\infty$  for  $\mu \in (\mu_2^s, \mu_3^e) \approx (0.00625, 0.00694)$ . The period-2  $(RL)^\infty$  orbit is coloured red on the interval of multistability. b) The period adding cascade of attractors  $(RL^m)^\infty$  for  $m \in \{1, \dots, 10\}$ . On the intervals of  $\mu$  where  $(RL^{m-1})^\infty$  and  $(RL^m)^\infty$  coexist as attractors the iterates of  $(RL^{m-1})^\infty$  are marked in red. A symmetric logarithmic transformation [20] has been applied to the  $x$ -axis and a log transformation has been applied to the  $\mu$ -axis in order to clearly show the structure of the period adding cascade.

so  $x_m = \mu + bx_{m-1} < \mu$  since  $b > 0$  and thus

$$x_1 = \mu - a\sqrt{x_m} > \mu - a\sqrt{\mu}, \quad (7.4)$$

since  $a > 0$ . We also have that

$$x_{m-1} = S_L^{m-2}(x_1) = b^{m-2}x_1 + \sum_{i=0}^{m-3} b^i \mu = b^{m-2}x_1 + \frac{1-b^{m-2}}{1-b}\mu. \quad (7.5)$$

Combining conditions (7.4) and (7.5) we have that a periodic orbit  $(RL^{m-1})^\infty$  exists for

$$b^{m-2}(\mu - a\sqrt{\mu}) + \frac{1-b^{m-2}}{1-b}\mu < 0 \quad (7.6)$$

and thus

$$\mu < \left( \frac{1-b}{1-b^{m-1}} ab^{m-2} \right)^2 =: \mu_m^e. \quad (7.7)$$

Differentiating  $S^m(x_m) = S_L^{m-1}(S_R(x_m))$  with respect to  $x_m$  we find that the

$(RL^{m-1})^\infty$  orbit is an attractor for

$$\left| b^{m-1} \frac{-a}{2\sqrt{x_m}} \right| < 1 \implies \frac{ab^{m-1}}{2\sqrt{x_m}} < 1 \implies x_m > \left[ \frac{ab^m}{2b} \right]^2. \quad (7.8)$$

Therefore, for stability, we must have

$$\mu > \frac{1-b}{1-b^m} \left( \frac{a}{b} \right)^2 \left( \frac{3}{4} \right) b^{2m} =: \mu_m^s. \quad (7.9)$$

In order to have coexistence of  $(RL^{m-2})^\infty$  and  $(RL^{m-1})^\infty$  orbits for all  $m > 3$  we must have

$$\mu_{m-1}^s < \mu_m^e \quad (7.10)$$

and from (7.7) and (7.9) we get that

$$\frac{1-b}{1-b^{m-1}} \left( \frac{a}{b} \right)^2 \left( \frac{3}{4} \right) b^{2(m-1)} < \left( \frac{1-b}{1-b^{m-1}} ab^{m-2} \right)^2, \quad (7.11)$$

which gives that

$$b < \frac{1}{4}. \quad (7.12)$$

In order to have an interval of values of  $\mu$  for which  $(RL^{m-1})^\infty$  is the only attractor we must have that

$$\mu_{m-1}^s > \mu_{m+1}^e. \quad (7.13)$$

Again referring to (7.7) and (7.9) we find that this gives that

$$\frac{3}{4} > b^2 \left( \frac{1-b-b^{m-1}+b^m}{1-2b^m+b^{2m}} \right), \quad (7.14)$$

which is certainly true for all  $b \in (0, 0.25)$ . We now have that

$$\mu_m^e > \mu_{m-1}^s > \mu_{m+1}^e > \mu_m^s \quad (7.15)$$

holds for  $b < \frac{1}{4}$ . Next, if  $\mu \in (\mu_{m-1}^s, \mu_m^e)$  then stable periodic orbits  $(RL^{m-2})^\infty$

and  $(RL^{m-1})^\infty$  coexist; if  $\mu \in (\mu_{m+1}^e, \mu_{m-1}^s)$  then a stable periodic orbit  $(RL^{m-1})^\infty$  exists and is the only attractor as discussed above [11, 14]. If  $\mu \in (\mu_m^s, \mu_{m+1}^e)$  the pattern of coexistence starts again but with  $(RL^{m-1})^\infty$  and  $(RL^m)^\infty$ . We can see this period-adding behaviour and repeating pattern of coexistence clearly in the bifurcation diagram shown in Figure 7.1b) for orbits of period 2 to 11. In Figure 7.1a) we see an example of the coexistence of stable periodic orbits with codes  $(RL)^\infty$  and  $(RLL)^\infty$  on the interval  $(\mu_2^s, \mu_3^e)$ . Following this we will refer to the intervals  $(\mu_m^s, \mu_{m+1}^e)$  on which stable periodic orbits  $(RL^{m-1})^\infty$  and  $(RL^m)^\infty$  coexist as *coexistence intervals* or *intervals of multistability*.

If  $R_m$  and  $L_m^1, L_m^2, \dots, L_m^{m-1}$  are respectively the right iterate and left iterates of the deterministic period- $m$  orbit  $(RL^{m-1})^\infty$  of  $S$  (see (7.1)) then using the fact that

$$S_L^{m-1}(S_R(R_m)) = R_m, \quad (7.16)$$

where  $S_L$  is the linear part (left-hand side) of the square root map and  $S_R$  is the square root part (right-hand side), we find that

$$R_m = \left( \frac{1}{2} \left( -ab^{m-1} + \sqrt{(ab^{m-1})^2 + 4 \sum_{i=0}^{m-1} b^i \mu} \right) \right)^2. \quad (7.17)$$

Hence we have that

$$L_m^1 = \mu - a\sqrt{R_m} \quad \text{and} \quad L_m^i = \mu + bL_m^{i-1} \quad (7.18)$$

for  $i \in \{2, 3, \dots, m-1\}$ .

The square root map is a continuous unimodal map and so Sharkovsky's Theorem [21] holds. As a result, in a region where stable orbits of period- $m$  and period- $(m+1)$  coexist, periodic orbits of period  $n$  exist for every  $n$  such that  $n$  is preceded by either  $m$  or  $m+1$  in the Sharkovsky ordering. This can be used to show that there is an unstable Cantor set of solutions that separate connected components of the basins of

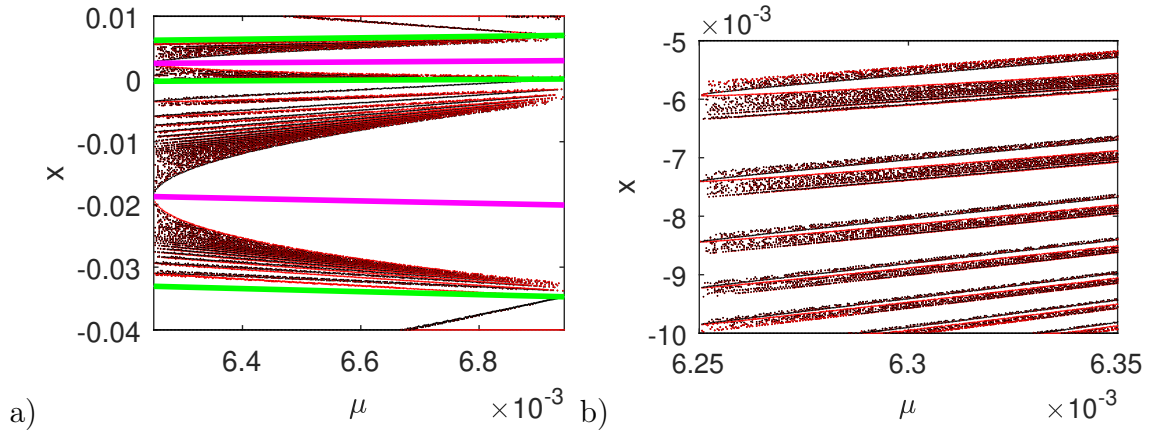


**Figure 7.2:** a) Boundaries of the basins of attraction of the coexisting period-2 and period-3 attractors in the  $(\mu, x)$  plane for  $\mu$  values between  $\mu_2^s$  and  $\mu_3^e$ . Each dot, calculated numerically, represents a basin boundary for a given value of  $\mu$ . This plot reveals the basins of attraction of the two attractors on  $(\mu_2^s, \mu_3^e)$ , showing for each value of  $\mu$  the initial values of  $x$  attracted to the period-two orbit  $(RL)^\infty$  (magenta) or the period-three orbit  $(RL^2)^\infty$  (green). b) A blow-up of a small region in the first showing the persistence of structure indicating that the basins are riddled.  $a = 0.5$ ,  $b = 0.2$ .

attraction of the two stable orbits, i.e. the basins have complicated structure often called *riddled* [22, 23]. An example of this is shown in Figure 7.2 for period-2 and period-3 coexistence.

It will be useful for us to consider the *immediate basin of attraction* of each of the coexisting periodic orbits  $(RL^{m-1})^\infty$  and  $(RL^m)^\infty$  on an interval of multistability  $(\mu_m^s, \mu_{m+1}^e)$ . The immediate basin of a period- $N$  attractor on an interval of multistability is given by the union of largest  $N$  intervals containing the  $N$  iterates of the orbit, such that all initial conditions within those intervals are attracted to the periodic orbit. On the interval of multistability  $(\mu_m^s, \mu_{m+1}^e)$  the closest boundaries of the two immediate basins of attraction are given by unstable periodic orbits. The closest boundary of the basin of attraction of the period- $m$  orbit is given by an unstable period- $2m$  orbit with code  $(RL^{m-1}RL^{m-1})^\infty$ , which is created in a subcritical pitchfork bifurcation as  $\mu$  increases through  $\mu_m^s$ . On the other hand, the closest boundary of the period- $(m+1)$  orbit's basin is given by an unstable period- $(m+1)$  orbit with code  $(RRL^{m-1})^\infty$ , which is created in a border-collision bifurcation as

$\mu$  decreases through  $\mu_{m+1}^e$ . These unstable orbits that form the boundaries of the immediate basins of attraction can be seen in Figure 7.3a) for the case of period-2 and period-3 coexistence.

Here we will primarily be interested in the minimum distance,  $D$ , in terms of absolute difference, from each iterate of a stable periodic orbit to the boundary of its immediate basin of attraction. For example, on  $(\mu_m^s, \mu_{m+1}^e)$

$$D(R_m) = \min\{|R_m - Rp_{2m}^1|, |R_m - Rp_{2m}^2|\}, \quad (7.19)$$

where  $Rp_{2m}^1$  and  $Rp_{2m}^2$  are the two right iterates of the unstable period- $2m$  orbit with code  $(RL^{m-1}RL^{m-1})^\infty$  which is created in a subcritical pitchfork bifurcation as  $\mu$  increases through  $\mu_m^s$ . On the other hand,

$$D(R_{m+1}) = |R_{m+1} - Rg_{m+1}^2|, \quad (7.20)$$

where  $Rg_{m+1}^2$  is the greatest right iterate of the unstable period- $(m+1)$  orbit with code  $(RRL^{m-1})^\infty$ , which is created in a border-collision bifurcation as  $\mu$  decreases through  $\mu_{m+1}^e$ .

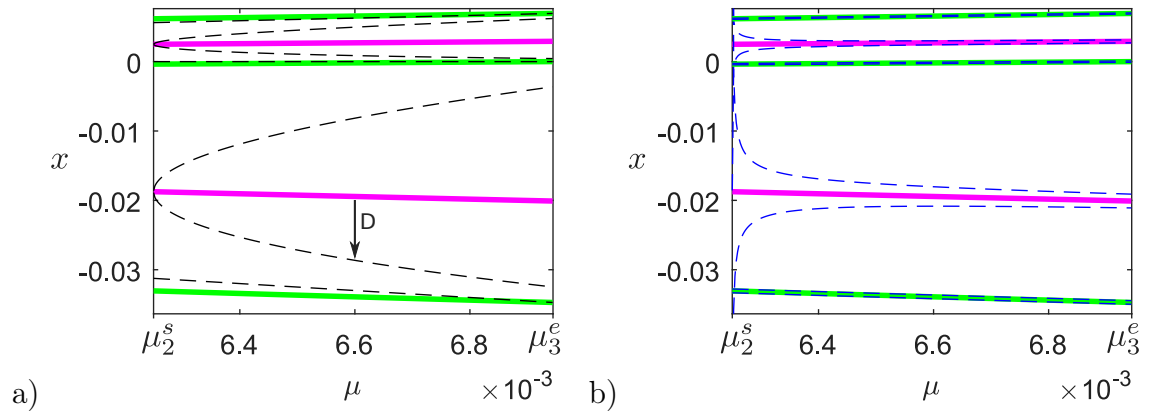


**Figure 7.3:** Analytic bifurcation diagrams of the interval of multistability ( $\mu_2^s, \mu_3^e$ ) showing the stable  $RL$  and  $RLL$  orbits, marked in magenta and green respectively for  $a = 0.5, b = 0.2$ , along with a) Dashed black lines marking the unstable  $RLRL$  and  $RRL$  orbits which give the closest boundaries of their respective basins of attraction. The distance  $D = D(L_2^1)$  is also indicated for  $\mu = 6.6 \times 10^{-3}$ . b) Blue dashed lines indicating one steady-state deviation standard deviation, given by (7.39) from each iterate for a constant small noise amplitude  $\Delta$ .

## 7.3 Noise

### 7.3.1 The Square Root Map With Noise

We wish to examine the effect of uncertainty and noise on the deterministic structures of the square root map (7.1). In particular we are interested in the effect of noise on the period-adding cascade and the intervals of multistability discussed in Section 7.2.3. The complex structure of the basins of attraction in regions of multistability revealed in Section 7.2.3 and Figure 7.2 imply that there can be very different sensitivity to noise as a function of initial conditions. Thus, the addition of noise to the system has the potential to create non-trivial effects on the long-term qualitative behaviour of the map.

Simpson and Kuske [24] show in a careful analysis that noise in impacting systems manifests in the two-dimensional square root map in several different ways including parametric noise, depending on the source of uncertainty. Hogan, Simpson and Kuske [25] show that the square root map in two dimensions with additive Gaussian white

noise arises when the source of uncertainty in the full system is practically independent of the state of the system. In both cases the authors present numerically calculated invariant densities of periodic attractors, while expressions for the approximate Gaussian invariant are obtained via linearisation in [25].

In this paper we consider small amplitude, additive, Gaussian white noise and in Section 7.4 derive approximate steady-state deviation distributions associated with periodic attractors. The square root map with additive Gaussian white noise is given by

$$x_{n+1} = S_a(x_n) = \begin{cases} \mu + bx_n + \xi_n, & x_n < 0, \\ \mu - a\sqrt{x_n} + \xi_n, & x_n \geq 0, \end{cases}$$

$$\xi_n \stackrel{\text{iid}}{\sim} N(0, \Delta^2), \quad (7.21)$$

where  $\xi_n$  are identically distributed independent normal random variables with mean 0 and standard deviation  $\Delta$ .

### 7.3.2 Numerical Observations

The effect of noise on the dynamics of a system with multiple coexisting attractors has long been of interest [26, 27, 28]. In this article we focus on phase-space sensitivity for period- $m$  and period- $(m+1)$  coexistence and the relationship between noise amplitude and the proportion of time spent in either dynamic behaviour. Interestingly, we find that the relationship between the proportion of orbits with varying initial conditions going to each of the coexisting attractors, or at least to  $RL^{m-1}$  and  $RL^m$  behaviour, is non-monotonic. In particular, Figure 7.4 shows the relationship between the noise amplitude  $\Delta$ , and the proportion of time spent in  $RL$  and  $RLL$  behaviour, and in transition ( $RR$ ) between the two behaviours. We numerically calculate this proportion over 5,000 iterates, discounting 195,000 transient iterates. Each bar chart shows the proportion of iterates spent by 1,000 orbits, with linearly spaced initial conditions, in each of the three types of behaviour for given values of  $\mu$ . On the

interval of multistability  $(\mu_2^s, \mu_3^e)$  we see that the relationship depends strongly on the value of  $\mu$ . Here follows a short description of what we see in regions a)-f) of Figure 7.4.

**Figure 7.4a):** For  $\mu$  in a small neighbourhood of  $\mu_2^s$  with  $\mu > \mu_2^s$  (region a)) even the smallest noise amplitude considered was enough to destroy the *RL* attractor. Initially, the proportion of time spent by orbits in *RLL* behaviour increases as the noise amplitude,  $\Delta$ , increases until we only see *RLL* behaviour. After some threshold value of  $\Delta$  as noise amplitude increases further the proportion of time spent by orbits in *RLL* dynamics begins to decrease.

**Figure 7.4b):** For  $\mu$  in region b) we see that the proportion of time spent by orbits in *RLL* behaviour initially increases as  $\Delta$  increases past some threshold value. Increasing  $\Delta$  further results in reaching a maximum proportion for *RLL* close to 1, effectively destroying the *RL* attractor. As the noise amplitude increases beyond this point the proportion of time spent by orbits in *RLL* dynamics begins to decrease and the proportion of time spent by orbits in *RL* dynamics begins to increase once more.

**Figure 7.4c):** For  $\mu$  in region c), closer to the centre of the coexistence interval  $(\mu_2^s, \mu_3^e)$ , the proportion of time spent by orbits in *RLL* behaviour initially increases as the noise amplitude increases past some threshold value. This increase in the proportion of time spent in *RLL* behaviour continues until it reaches some maximum, but in this case, unlike in region b), the *RL* orbit is never destroyed. As the noise amplitude increases further we once again see that the proportion of time spent by orbits in *RL* dynamics begins to increase.

**Figure 7.4d):** Increasing  $\mu$  further, we find that increasing noise amplitude has no significant impact on the observed proportions until it increases above some threshold value. Beyond this value a further increase in noise amplitude leads to a decrease in the proportion of *RLL* behaviour until it appears to reach some minimum. In this case the *RLL* behaviour is never entirely eliminated.

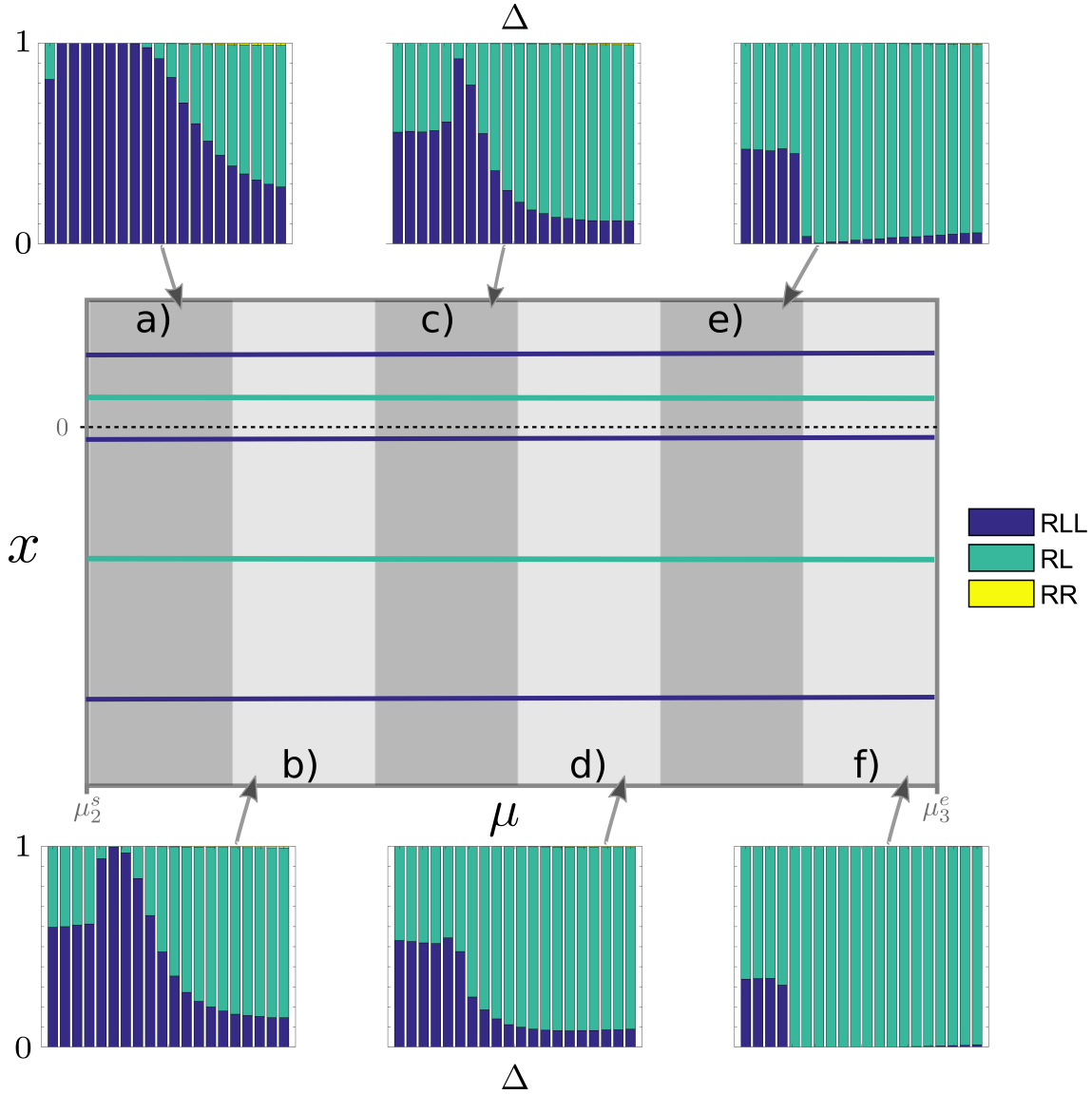


**Figure 7.4:** Each of the bar charts in this schematic shows the changing proportion of time spent in *RL* and *RLL* behaviour for increasing amplitude of additive noise,  $\Delta$  ranging from 0 (deterministic system) to  $2 \times 10^{-4}$ . We plot the different relationships observed for values of  $\mu$  on the interval of multistability  $(\mu_2^s, \mu_3^e)$  and consider dynamics over 5,000 iterates for 1,000 different orbits with linearly spaced initial conditions on the interval  $[-0.04, 0.01]$  neglecting 195,000 transients. (Regions not to scale.)

**Figure 7.4e):** For  $\mu$  in region e) the proportion of time spent by orbits in *RLL* behaviour reduces dramatically as the noise amplitude increases above some threshold value, until the attractor is effectively destroyed, i.e. the proportion of time spent in *RLL* behaviour drops to 0. However, as the noise amplitude is increased further still we see a return of *RLL* behaviour for higher amplitude noise.

**Figure 7.4f):** For  $\mu$  in a small neighbourhood of  $\mu_3^e$  with  $\mu < \mu_3^e$  the proportion of time spent by orbits in *RLL* behaviour reduces as the noise amplitude increases, until the attractor is effectively destroyed once noise amplitude is increased over a certain threshold value. As the noise amplitude is increased further still we see a very weak return of *RLL* behaviour, but only for relatively high amplitude noise.

We have determined numerically that the relationships between the noise amplitude  $\Delta$  and the proportion of *RL* and *RLL* behaviour for  $\mu$  about  $(\mu_2^s, \mu_3^e)$  hold for both additive and parametric, Gaussian and uniform noise. We have observed that these relationships can be determined by looking at either the proportion of iterates spent in each behaviour over a certain period as we have done in Figure 7.4 or by looking at the proportion of orbits in each of the behaviours after a given number of iterates. However the analysis in this paper focuses solely on the case of additive Gaussian white noise and numerical results for parametric noise and other distributions are not shown.

## 7.4 The Evolution of Deviations

In order to more formally understand how the addition of noise affects the qualitative behaviour of the square root map we will now construct an approximation for the distribution of trajectory deviations resulting from the addition of noise to the system. In particular we are interested in how these deviations can be used to explain the relationships between noise amplitude and the proportions of time spent in each coexisting periodic behaviour observed in Section 7.3.2 and Figure 7.4, which will be

further discussed in Section 7.5. There are two potential approaches to approximating such distributions. The first, which we present in Section 7.4.1 involves calculating the actual distribution of trajectory deviations iteratively and approximating any non-Gaussian distributions by a Gaussian. The second approach involves the linearisation of the right-hand side  $S_R(x)$  of the square root map (7.1) and the derivation using this approach is included in 7.A for completeness. Interestingly, both approaches lead to the same estimate despite the fact that there is no explicit linearisation involved in the first approach.

### 7.4.1 Analysis

We consider two trajectories  $\{x_k\}$  and  $\{z_k\}$  with identical initial conditions  $x_0 = z_0 = R_{m+1}$ , i.e. two trajectories with initial conditions equal to the right iterate of the deterministic  $(RL^m)^\infty$  orbit of the system. We then iterate forward using the square root map with additive noise (7.21) in the case of  $x_0$ , letting  $x_{k+1} = S_a(x_k)$ , and the deterministic square root map (7.1) in the case of  $z_0$ , letting  $z_{k+1} = S(z_k)$ . The deviation due to noise in the trajectory  $\{x_k\}$  is then given by the difference  $\{\epsilon_k\} = \{x_k - z_k\}$ . From (7.1) and (7.21) we have that, provided the deviations are not so large as to push  $\{x_k\}$  out of  $RL^m$  behaviour, the error terms  $\epsilon_k$  are given by

$$\epsilon_k = x_k - z_k = \begin{cases} a(\sqrt{R_{m+1}} - \sqrt{R_{m+1} + \epsilon_{k-1}}) + \xi_{k-1}, & k \bmod (m+1) = 1, \\ b\epsilon_{k-1} + \xi_{k-1}, & \text{otherwise,} \end{cases} \quad (7.22)$$

with  $\epsilon_0 = 0$ . Let us now consider the evolution of the trajectory of  $\epsilon_k$  for  $m = 1, 2, \dots$

First we will approximate the distribution of  $W = \sqrt{R_{m+1} + \epsilon_{k-1}}$ , where  $k \bmod (m+1) = 1$ . We have that the *cumulative density function* (CDF)  $G_W(w)$  of  $W$  is given

by

$$\begin{aligned} G_W(w) &= P(W < w) = P\left(\sqrt{R_{m+1} + \epsilon_{k-1}} < w\right) = P\left(\sqrt{R_{m+1} + \epsilon_{n(m+1)}} < w\right) \\ &= P\left(0 \leq R_{m+1} + \epsilon_{n(m+1)} < w^2\right) = \int_0^{w^2} g_Y(y) dy, \end{aligned} \quad (7.23)$$

for  $m = 1, 2, \dots$ , where  $P(E)$  is the probability of the event  $E$ ,  $g_Y(y)$  is the *probability density function* (PDF) of  $Y = R_{m+1} + \epsilon_{n(m+1)}$ , and  $P(R_{m+1} + \epsilon_{n(m+1)} < 0) = 0$  since we have assumed that the deviations are not so large as to push  $\{x_k\}$  out of  $RL^m$  behaviour. Suppose now that  $\epsilon_{n(m+1)}$  is normally distributed with mean 0 and variance  $\sigma_Y^2$ , then  $Y \sim N(R_{m+1}, \sigma_Y^2)$ <sup>1</sup>. This gives that

$$g_W(w) = \frac{d}{dw} \left( \int_0^{w^2} g_Y(y) dy \right) = 2wg_Y(w^2) = \frac{\sqrt{2}w}{\sqrt{\pi}\sigma_Y} \exp\left(-\frac{(w^2 - R_{m+1})^2}{2\sigma_Y^2}\right), \quad (7.24)$$

which is defined for  $w \geq 0$ . The mode of this distribution is given by

$$\frac{d}{dw} (g_W(w)) = \frac{d}{dw} \left( \frac{\sqrt{2}w}{\sqrt{\pi}\sigma_Y} \exp\left(-\frac{(w^2 - R_{m+1})^2}{2\sigma_Y^2}\right) \right) = 0, \quad (7.25)$$

which gives that

$$\frac{\sqrt{2}}{\sqrt{\pi}\sigma_Y} \exp\left(-\frac{(w^2 - R_{m+1})^2}{2\sigma_Y^2}\right) \left(1 - 4w^2 \left(\frac{w^2 - R_{m+1}}{2\sigma_Y^2}\right)\right) = 0 \quad (7.26)$$

and so

$$w = \pm \sqrt{\frac{R_{m+1} \pm \sqrt{R_{m+1}^2 + 2\sigma_Y^2}}{2}}. \quad (7.27)$$

From (7.27) we see that (7.26) has only one positive real solution

$$w^* \approx \sqrt{R_{m+1}} = E(W) \quad (7.28)$$

---

<sup>1</sup>Note that this is guaranteed when  $n = 1$  as  $\epsilon_0 = 0$  and so  $\epsilon_{m+1}$  is the sum of independent random variables  $\sum_{i=0}^m b^{m-i} \xi_i$ .

corresponding to the mode of the distribution  $g_W(w)$ , and the distribution of  $W$  is approximately normal. We approximate  $W$  with a normal random variable  $\widetilde{W}$  with mean  $\sqrt{R_{m+1}} = E(W)$  and variance  $\sigma_{\widetilde{W}}^2$  given by solving  $g_{\widetilde{W}}(\sqrt{R_{m+1}}) = g_W(\sqrt{R_{m+1}})$ , where

$$g_{\widetilde{W}}(\tilde{w}) = \frac{1}{\sqrt{2\pi}\sigma_{\widetilde{W}}} \exp\left(-\frac{(\tilde{w} - \sqrt{R_{m+1}})^2}{2\sigma_{\widetilde{W}}^2}\right) \quad (7.29)$$

and  $g_W(w)$  is given by (7.24), which gives that

$$\sigma_{\widetilde{W}}^2 = \frac{\sigma_Y^2}{4R_{m+1}}. \quad (7.30)$$

Now, given the fact that  $\xi_i \sim N(0, \Delta^2)$  for all  $i$ , we have that

$$\epsilon_{m+1} = \sum_{i=0}^m b^{m-i} \xi_i \sim N\left(0, \sum_{i=0}^m b^{2i} \Delta^2\right) \quad (7.31)$$

and

$$\epsilon_{n(m+1)+1} = a\sqrt{R_{m+1}} - aW + \xi_{n(m+1)}, \quad (7.32)$$

and thus  $\epsilon_k$  is given by a linear combination of approximately normal random variables with mean 0 for all  $k$ . This means that  $\epsilon_k$  is itself normal with mean 0 for all  $k$ . The variances of these distributions are given by

$$\sigma_{\epsilon_k}^2 = \begin{cases} \frac{a^2\sigma_{\epsilon_{k-1}}^2}{4R_{m+1}} + \Delta^2, & k \bmod (m+1) = 1, \\ b^2\sigma_{\epsilon_{k-1}}^2 + \Delta^2, & \text{otherwise.} \end{cases} \quad (7.33)$$

Working mod( $m+1$ ) we can write (7.33) as a system of  $m+1$  difference equations

$\sigma_{\epsilon_{(n+1)(m+1)+k}}^2 = f^k(\sigma_{\epsilon_{n(m+1)+k}}^2)$  with initial conditions given by  $\sigma_{\epsilon_k}^2$  for  $1 \leq k \leq m+1$ .

Letting

$$\frac{a^2\sigma^2}{4R_{m+1}} + \Delta^2 = j(\sigma^2) \quad (7.34)$$

and

$$b^2\sigma^2 + \Delta^2 = h(\sigma^2) \quad (7.35)$$

we can write

$$f^k(\sigma^2) = h^{k-1} \circ j \circ h^{(m+1)-k}(\sigma^2), \quad (7.36)$$

where

$$h^r(\sigma^2) = \overbrace{h \circ h \circ \dots \circ h}^{r \text{ times}}(\sigma^2), \quad r = 1, 2, \dots \quad (7.37)$$

Referring to (7.34)-(7.36) we can now write  $f^k$  explicitly as

$$f^k(\sigma^2) = \left( \frac{ab^m}{2\sqrt{R_{m+1}}} \right)^2 \sigma^2 + \left( \frac{a\Delta}{2\sqrt{R_{m+1}}} \right)^2 \sum_{i=0}^{m-k} b^{2(k+i-1)} + \Delta^2 \sum_{i=0}^{k-1} b^{2i}, \quad (7.38)$$

which has a fixed point  $\hat{\sigma}_{k,(m+1)}^2$  for each of the  $m+1$  difference equations such that

$$\begin{aligned} \hat{\sigma}_{k,(m+1)}^2 &= \Delta^2 \left( \frac{a^2 \sum_{i=k}^m b^{2(i-1)} + 4R_{m+1} \sum_{i=0}^{k-1} b^{2i}}{4R_{m+1} - (ab^m)^2} \right) \\ &= \left( \Delta \sqrt{\frac{4R_{m+1}}{4R_{m+1} - (ab^m)^2} \left( \frac{1 - b^{2k}}{1 - b^2} + \frac{(ab^{k-1})^2}{4R_{m+1}} \left( \frac{1 - b^{2(m+1-k)}}{1 - b^2} \right) \right)} \right)^2. \end{aligned} \quad (7.39)$$

We require  $\hat{\sigma}_{k,(m+1)}^2 > 0$  and so (7.17) and (7.39) imply that

$$4R_{m+1} = \left( -ab^m + \sqrt{(ab^m)^2 + 4 \sum_{i=0}^m b^i \mu} \right)^2 > (ab^m)^2, \quad (7.40)$$

which gives that

$$\mu > \frac{1-b}{1-b^{m+1}} \left( \frac{a}{b} \right)^2 \left( \frac{3}{4} \right) b^{2(m+1)} = \mu_{m+1}^s. \quad (7.41)$$

This implies that the fixed points given in (7.39) exist for values of  $\mu$  in the interval of

stability for the deterministic  $RL^m$  orbit,  $(\mu_{m+1}^s, \mu_{m+1}^e)$ . In addition, (7.39) also gives  $\hat{\sigma}_{k,(m+1)}^2 \rightarrow \infty$  as  $\mu \rightarrow \mu_{m+1}^{s+}$  since the numerator  $\rightarrow a^2 \Delta^2 \left( \sum_{i=k-1}^{m+k-1} b^{2i} \right)$  as  $\mu \rightarrow \mu_{m+1}^{s+}$ , while  $\hat{\sigma}_k^2(m+1) \rightarrow c$  as  $\mu \rightarrow \mu_{m+1}^{e-}$ , where  $c > 0$ . The difference equations (7.38) converge for

$$\left( \frac{ab^m}{2\sqrt{R_{m+1}}} \right)^2 < 1, \quad (7.42)$$

which along with (7.17) gives that

$$\mu \in \left( -\frac{4}{a^2} \sum_{i=0}^m b^{i-2m}, \frac{12}{a^2} \sum_{i=0}^m b^{i-2m} \right) =: A_\mu. \quad (7.43)$$

Now, since  $0 < b < 1/4$  and  $0 < a < 1$ , we have that

$$(\mu_{m+1}^s, \mu_{m+1}^e) \subset \left[ 0, 12 \sum_{i=m}^{2m} 4^i \right] \subset A_\mu \quad (7.44)$$

and so (7.38) converges for all relevant values of the bifurcation parameter  $\mu$ .

The steady-state standard deviations of the deviation distributions  $\hat{\sigma}_{k,(m+1)}$  given in (7.39) are of particular interest. As each of these deviations is associated with an iterate of the deterministic period- $(m+1)$  orbit  $\{L_{m+1}^1, L_{m+1}^2, \dots, L_{m+1}^m, R_{m+1}\}$ , going forward we will emphasise this relationship by writing

$$\hat{\sigma}_{k,(m+1)} = \begin{cases} \hat{\sigma}(L_{m+1}^k), & k \in \{1, 2, \dots, m\}, \\ \hat{\sigma}(R_{m+1}), & k = m+1. \end{cases} \quad (7.45)$$

Referring to equation (7.39) we can now write

$$\begin{aligned} \hat{\sigma}(R_{m+1}) &= \Delta \sqrt{\frac{4R_{m+1}}{4R_{m+1} - (ab^m)^2} \left( \frac{1 - b^{2(m+1)}}{1 - b^2} \right)}, \\ \hat{\sigma}(L_{m+1}^k) &= \Delta \sqrt{\frac{4R_{m+1}}{4R_{m+1} - (ab^m)^2} \left( \frac{1 - b^{2k}}{1 - b^2} + \frac{(ab^{k-1})^2}{4R_{m+1}} \left( \frac{1 - b^{2(m+1-k)}}{1 - b^2} \right) \right)}, \\ \text{for } k &= 1, 2, \dots, m \end{aligned} \quad (7.46)$$

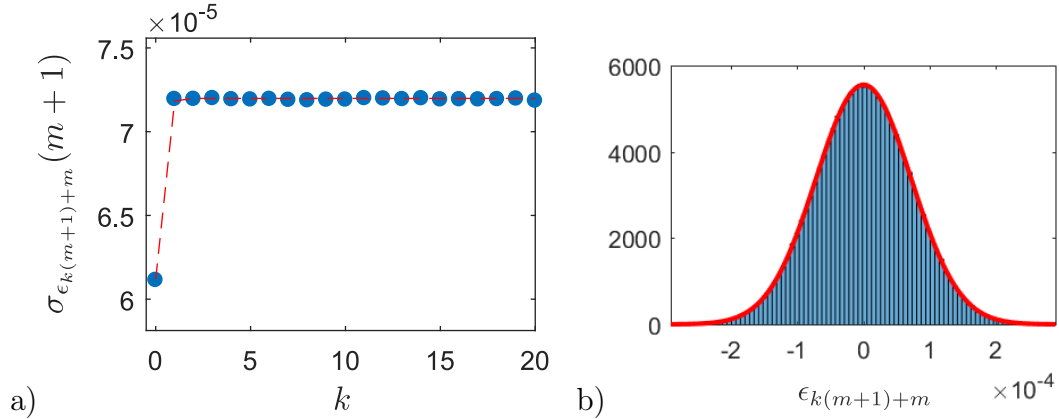


**Figure 7.5:** a) The evolution of the standard deviations of the normal fits of the distributions of the deviations  $\epsilon_m$  and  $\epsilon_{k(m+1)+m}$  such that  $\epsilon_{(k-1)(m+1)+m} < -L_{m+1}^m$  for  $1 \leq k \leq 20$ , fitted using MATLAB<sup>®</sup>'s `fitdist` function, (blue circles) compared to our semi-analytic prediction given by (7.38) (red dashed line). b) The histogram and normal fits of the distributions (red curve) of the deviations  $\epsilon_{20(m+1)+m}$  such that  $\epsilon_{(k-1)(m+1)+m} < -L_{m+1}^m$  for  $1 \leq k \leq 20$ . In both cases we have taken  $m = 2$ ,  $\mu = 6.65 \times 10^{-3}$  and  $\Delta = 6 \times 10^{-5}$ . This gives that  $L_{m+1}^m \approx -1.5564 \times 10^{-4}$  and  $\hat{\sigma}(L_{m+1}^m) \approx 0.7199 \times 10^{-4}$

and note that these are identical to the values for  $\tilde{\sigma}$  given in (7.75), where the linearisation approach is used.

## 7.4.2 Comparison to Numerical Observations

Taking  $m = 2$  as an example and examining the case of deviations on the last left iterate,  $L_3^2$  of the deterministic period-3 orbit for  $\mu \in (\mu_2^s, \mu_3^e)$ , we can see that the analysis in Section 7.4.1 agrees well with our numerical results. Taking one million orbits with initial condition  $x_0 = R_3$  we examine the distribution of the deviations  $\epsilon_{n(3)-1}$  for  $n = 1, 2, \dots, 20$  such that  $\epsilon_{k(3)-1} < -L_3^2$  for  $k < n$ . In Figure 7.5a) we show that the fitted normal distributions (fit using the MATLAB<sup>®</sup> `fitdist` function) of these deviations appear to have an approximately zero mean with standard deviation converging quickly to some limit  $\bar{\sigma}$  as  $n \rightarrow \infty$ . We see that the standard deviations of these fitted distributions closely mirror the approximate standard deviations predicted by our analysis (7.38), in particular the standard deviations do indeed appear to converge to the value of  $\hat{\sigma}(L_3^2)$  given by (7.39). In Figure 7.5b) we compare

an example of these fitted normal distributions to the histogram of the observed numerical deviations and find that the fitted distributions are indeed good fits for the actual distributions. We can therefore use the approximate deviation distributions derived in Section 7.4.1 to better understand the noise induced transitions observed in the square root map.

## 7.5 Deviation Distributions and Noise Thresholds

In this section we examine the threshold noise amplitudes required to induce changes in the qualitative behaviour of the square root maps (7.1) and (7.21). We explain the observed thresholds by examining the relationships between the approximate deviation distributions derived in Section 7.4 and features of the deterministic structures of the square root map described in Section 7.2.

We will explain the relationships between the proportion of time spent in period- $m$  or period- $(m + 1)$  behaviour and noise amplitude shown in Figure 7.4 by investigating the relationships between the distributions of the approximate steady-state deviation distributions we have derived in Section 7.4.1 and the deterministic structures of the square root map investigated in Section 7.2.3. In particular, for each period- $N$  attractor  $\{p_1, p_2, \dots, p_N\}$ , we define  $\varrho$  to be the ratio between the minimum distance from  $p_i$  to the boundary of the immediate basin of attraction, and the standard deviations of the steady-state distributions associated with each iterate (Section 7.2.3),

$$\varrho(p_k) := \frac{D(p_k)}{\hat{\sigma}(p_k)}. \quad (7.47)$$

In order to have the potential to transition from one behaviour to another within an interval of multistability a given orbit must first leave the immediate basin of attraction of its current orbit. Discounting transients, the expected values of the iterates of an orbit within a immediate basin of attraction will be given by the attractor of that basin. As a result, for small amplitude noise, we can consider the

deviations  $\epsilon_{nm+k}^m$  and  $\epsilon_{n(m+1)+k}^{m+1}$  of orbits with initial conditions given by  $R_m$  and  $R_{m+1}$  respectively (see (7.17) and (7.22)). We know from our previous analysis in Section 7.4.1 that the steady-state distributions of these deviations can be well-approximated by normal distributions with mean 0 and standard deviations  $\hat{\sigma}$ . As a result, the ratios  $\varrho$  give us a measure of how likely an orbit is to remain within its current basin of attraction and hence remain in its current periodic behaviour. They also give us the minimum distance, in standard deviations, from the attractor to the basin of attraction of the other coexisting attractor.

For example, in Figure 7.3a) we show the structure of the relevant boundaries of the basins of attraction and in Figure 7.3b) the steady-state deviation distributions for each iterate of each of the stable periodic orbits on the interval  $(\mu_2^s, \mu_3^e)$  of multistability. We see that  $\hat{\sigma} \rightarrow \infty$  and  $D \rightarrow 0$  as  $\mu \rightarrow \mu_2^{s+}$ , but, on the other hand,  $\hat{\sigma} \rightarrow c > 0$  and  $D \rightarrow 0$  as  $\mu \rightarrow \mu_3^{e-}$ . This means that as we approach the ends of the interval of multistability even the smallest amplitude noise will perturb orbits enough to move them out of the main basin of attraction of the period-2  $RL$  orbit (as  $\mu \rightarrow \mu_2^s$ ) and the period-3  $RLL$  orbit (as  $\mu \rightarrow \mu_3^e$ ). Such orbits will then be absorbed by the other behaviour and with high probability remain in that behaviour provided the noise level is not too high. If the noise level is too high, the  $\varrho$  values of the other attractor will be low enough to result in the orbit also being kicked out of that attractor's immediate basin of attraction with high probability.

For a given value of the bifurcation parameter  $\mu$  on the interval of multistability, the overall effect of the addition of noise on the proportion of time spent in each of the two periodic behaviours can be understood by balancing the  $\varrho$  values of the coexisting attractors. We identify three main possible effects of the addition of noise to the system that contribute to the nonmonotonic relationships between noise amplitude and behaviour shown in 7.4. We then explain the observed thresholds of the noise amplitude  $\Delta$  that relate to these features by referring to the balancing of  $\varrho$  values. The three effects considered are highlighted in the example shown in Figure 7.6.

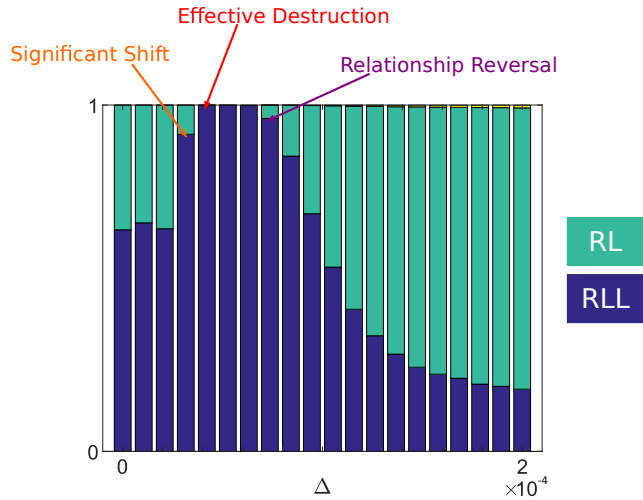


**Figure 7.6:** The threshold values of the noise amplitude  $\Delta$  for which the three effects described in Section 7.5 occur in the square root map with  $a = 0.5$ ,  $b = 0.2$  and  $\mu = 0.0634$ . The bar chart shows the changing proportion of time spent in  $RL$  and  $RLL$  behaviour for increasing amplitude of additive noise,  $\Delta$  ranging from 0 (deterministic system) to  $2 \times 10^{-4}$ .

The first effect we will consider is a *significant shift* in the proportion of time spent in each behaviour after transients are discarded due to the addition of noise. We will compare the proportions in the noisy system with the proportion of time spent in each behaviour in the deterministic system after transients are discarded, i.e. the proportion of phase space taken up by the basin of attraction of each attractor. In the case of the numerical results which follow, we will consider a 15 per cent decrease in the proportion of time spent in the behaviour we are shifting away from as *significant*. In Figure 7.6 the significant shift highlighted is from  $RL$  to  $RLL$  behaviour.

The second effect we will consider is the *effective destruction* of one of the attractors by the addition of noise. We will consider an attractor to be effectively destroyed when the proportion of time spent in that behaviour, after transients are discarded, falls below a given threshold. In the numerical work we present in Section 7.5.2 we have taken this threshold to be 0.0001. In Figure 7.6 the effective destruction highlighted is of the destruction of  $RL$  behaviour.

The final effect we will consider is the *reversal of the relationship* between increasing noise amplitude and the the change in proportion of time spent in each behaviour. If adding noise initially results in the proportion of time spent in period- $m$   $RL^{m-1}$  behaviour *decreasing* as noise amplitude increases, we look for the point when increasing noise amplitude further will result in the proportion of time spent in period- $m$   $RL^{m-1}$  behaviour *increasing* and vice-versa. In the numerical results in Section 7.5.3 we have considered the relationship between noise amplitude and proportion to have reversed when we observe consecutive increases in the proportion which initially decreased, for consecutive increases of  $\Delta$ . In Figure 7.6 we highlight the return of  $RL$  behaviour following its initial decrease and destruction.

In Figure 7.7 we plot the threshold values of the noise amplitude  $\Delta^*$  required to trigger each one of these effects, where it is observed for a given value of  $\mu$  on the interval of multistability  $(\mu_2^s, \mu_3^3)$ , while in Figure 7.8 we plot the related values of  $\varrho$ .

### 7.5.1 Significant Shifts in Behaviour

Let us first focus on the threshold value  $\Delta^*$  of  $\Delta$ , required to induce a significant shift in the proportion of time spent in  $RL$  and  $RLL$  behaviour. In Figure 7.7a) we see that on the interval of multistability the threshold value of the noise amplitude required to induce a significant shift in proportions increases until it spikes at some maximum as  $\mu$  increases from an initial threshold value  $\Delta^*$  of 0 at  $\mu = \mu_2^s \approx 6.25 \times 10^{-3}$ . The threshold value  $\Delta^*$  then decreases to 0 at  $\mu = \mu_3^e \approx 6.94 \times 10^{-3}$ , which is the end of the interval.

This relationship between  $\mu$  and  $\Delta^*$  can be understood by examining the relationship between  $\mu$  and the related values of the ratio  $\varrho$  (see (7.47)). As we have seen in Section 7.4.1  $\hat{\sigma} \rightarrow \infty$  and  $D \rightarrow 0$  as  $\mu \rightarrow \mu_2^{s+}$  while on the other hand,  $\hat{\sigma} \rightarrow c > 0$  and  $D \rightarrow 0$  as  $\mu \rightarrow \mu_3^{e-}$ . This means that at the end points of the interval of stability any noise amplitude greater than zero will eventually perturb orbits enough to move them out of the main basin of attraction of the period-2  $RL$  orbit (as  $\mu \rightarrow \mu_2^s$ ) and

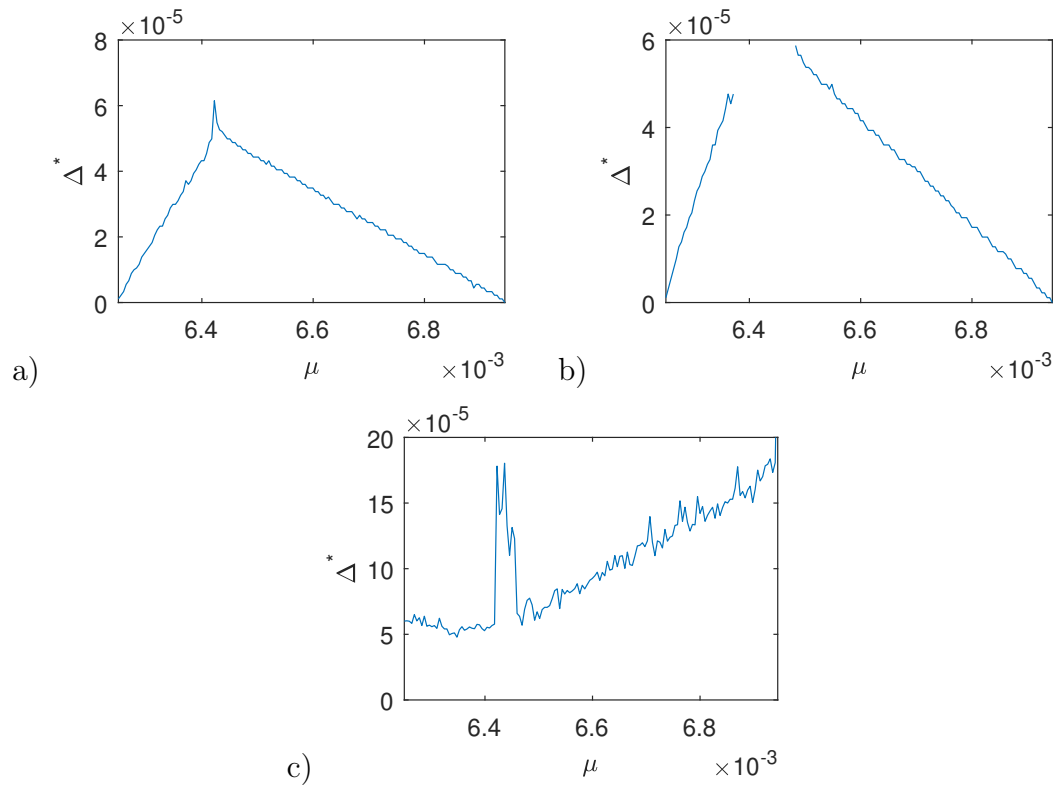


**Figure 7.7:** Numerically calculated threshold noise amplitudes  $\Delta^*$  to a) cause a significant change in the proportion of time spent in the *RL* and *RLL* behaviours, b) to destroy periodic behaviour, and c) to induce a reversal in the proportion changes, for  $\mu \in (\mu_2^s, \mu_3^e) \approx (0.00625, 0.00694)$ .

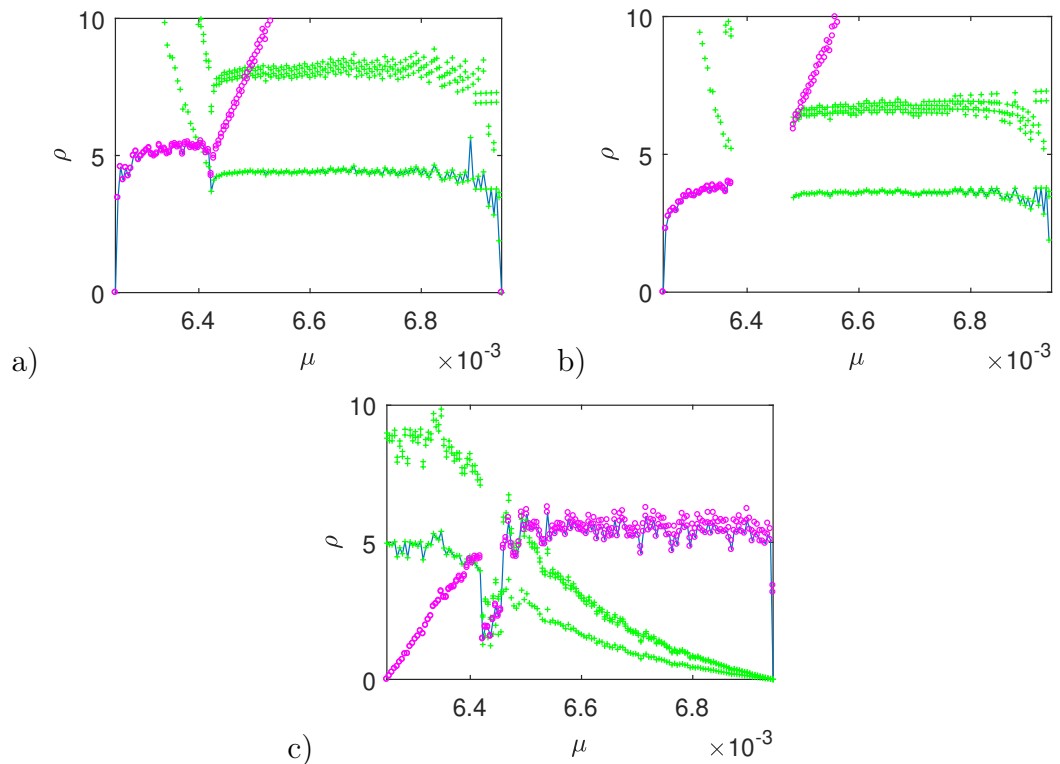


**Figure 7.8:** The  $\rho$  values associated with the threshold  $\Delta$  values shown in Figure 7.7 to a) cause a significant change in the proportion of time spent in the two periodic behaviours, b) destroy periodic behaviour, and c) induce a reversal in the proportion changes (final panel), for  $\mu \in (\mu_2^s, \mu_3^e) \approx (0.00625, 0.00694)$ . Each of the  $\rho$  values of the period-2 orbits are marked with a magenta  $\circ$  while each of the  $\rho$  values of the period-3 orbits are marked with a green  $+$ . In all three cases the blue line traces the minimum  $\rho$  ratio of the attractor whose proportion is diminishing in order to create the feature of the relationship in question.

the period-3 *RLL* orbit (as  $\mu \rightarrow \mu_3^e$ ). At the threshold noise amplitudes  $\Delta^*$  these orbits will be absorbed by the other attractor, where their  $\varrho$  values will be so large that they will have probability  $\approx 0$  of leaving the immediate basin of attraction of the periodic orbit.

Away from the endpoints of the interval, in Figure 7.8a), we see that the threshold noise amplitude  $\Delta^*$  is associated with an approximately constant  $\varrho$  values for the attractor whose proportion is reducing, provided the the  $\varrho$  values are high enough for the other attractor. At these  $\varrho$  values there is sufficient probability for orbits to escape the immediate basin of attraction of the attractor whose proportion is diminishing to result in a significant number of orbits being shifted into the basin of attraction of the other attractor. On the other hand, there is a very small probability of orbits in the other behaviour escaping the immediate basin of attraction of the other attractor once absorbed. The threshold minimum  $\varrho$  values for each attractor are different, which can be explained by noting that for  $\mu \in (\mu_2^s, \mu_3^e)$  we have that  $\varrho(L_2^1) \approx \varrho(R_2)$  while  $\varrho(L_3^1) \approx \varrho(R_3) > \varrho(L_3^2)$ . This means that the probability of leaving the immediate basin of attraction of the period-2 *RL* orbit is approximately equal on each iterate, while on the other hand, the probability of leaving the immediate basin of attraction of the period-3 *RLL* orbit is higher on the last left iterate of each orbit than it is on the other two. The spike in the threshold noise amplitude required to induce a significant shift in proportions where  $\Delta^*$  reaches its maximum at  $\mu_{max}$  is associated with a switch from an initial shift from *RL*  $\rightarrow$  *RLL* behaviour to an initial shift from *RLL*  $\rightarrow$  *RL* behaviour. Around this value of  $\mu$ , the noise amplitude required to reduce the  $\varrho$  values of both attractors to the point where there is sufficient probability for orbits to escape their respective immediate basins of attraction are approximately equal. This means that orbits jump back and forth between the two attractors at approximately the same rate and so we we require an even higher noise amplitude to induce a significant change in proportions.

In Figures 7.9-7.11 we can see how the proportion of iterates spent by orbits with

initial conditions in the immediate basins of attraction of the two coexisting periodic orbits and outside these regions are related to the noise amplitude  $\Delta$ . Close to the endpoints of the interval ( $\mu = 0.0063$  in Figure 7.9 and  $\mu = 0.0068$  in Figure 7.11) we can see that the relationships are similar for all three regions.

In Figure 7.9, close to the left endpoint of the interval,  $\mu_2^s$ , we see that increasing noise amplitude initially results in a fall in period-2 behaviour (where it exists in the deterministic case), until it is effectively destroyed for the same value of noise amplitude in all three cases. We also see *RL* behaviour return in all three cases once  $\Delta$  increases beyond some threshold. In Figure 7.11, close to the right endpoint of the interval,  $\mu_3^e$ , we see that increasing noise amplitude initially results in a fall in *RLL* behaviour until it is effectively destroyed for the same value of noise amplitude in all three cases. On the other hand, in Figure 7.10, close to the value of  $\mu$  for which we have a spike in the value of  $\Delta^*$  required to cause a significant shift in behaviour, we see that increasing  $\Delta$  initially results in a shift towards *RLL* behaviour in the case of the period-2 immediate basin of attraction and a shift towards *RL* behaviour in the case of the period-3 immediate basin. These offsetting effects mean that a higher noise amplitude is required to induce a significant change in proportions when considering the phase space as a whole.

### 7.5.2 The Effective Destruction of Attractors

We now examine the threshold value  $\Delta^*$  of  $\Delta$ , required to effectively destroy one of the attractors where possible, as shown in Figure 7.7b). On the interval of multistability the threshold value of the noise amplitude increases as  $\mu$  increases from an initial threshold value of 0 at  $\mu = \mu_2^s$  until the period-2 attractor can no longer be destroyed. As we increase  $\mu$  further, there is an interval of  $\mu$  values within the interval of multistability for which neither attractor can be effectively destroyed by the addition of noise. Beyond this interval the period-3 *RLL* attractor can be destroyed by the addition of noise above a threshold  $\Delta^*$ . This threshold value

decreases to 0 at  $\mu = \mu_3^e$  at the end of the interval. Examining the related  $\varrho$  values we can get a better understanding of this relationship between the threshold value of the noise amplitude required to destroy an attractor and the bifurcation parameter  $\mu$ . Again we see that at the endpoints of the interval of multistability any noise is sufficient to push all orbits out of the immediate basins of attraction of the period-2 *RL* orbit at  $\mu_2^s$  and out of the immediate basins of attraction of the period-3 *RLL* orbit at  $\mu_3^s$ . Once these orbits are absorbed by the other attractor it has almost zero probability of leaving its immediate basin of attraction as the  $\varrho$  values are very high for the period-3 *RLL* orbit at  $\mu_2^s$  and the the period-2 *RL* orbit at  $\mu_3^s$ .

Away from the endpoints of the interval, in Figure 7.8b), we again see that the threshold noise amplitude  $\Delta^*$  is associated with approximately constant  $\varrho$  values for the attractor which is being effectively destroyed, provided the  $\varrho$  values are high enough for the other attractor. For these  $\varrho$  values there is sufficient probability for all orbits to escape the immediate basin of attraction of the attractor which is being effectively destroyed at a reasonable rate. However at the same  $\varrho$  values there is a very small probability of orbits in the other behaviour escaping the immediate basin of attraction of the other attractor once absorbed. In the centre of the interval, the noise amplitude required to reduce the  $\varrho$  values to a level where a significant number of orbits can escape the immediate basin of one of the orbits will also reduce the  $\varrho$  values of the other attractor to a level where a significant number of orbits will be thrown back. This means that instead of effectively destroying one of the attractors the dynamics will instead switch back and forth between the two behaviours. As a result, for this interval of  $\mu$  values, we can never entirely eliminate the coexistence of the two behaviours. Both behaviours will persist on this interval for any noise amplitude which does not entirely wash out all deterministic dynamics.

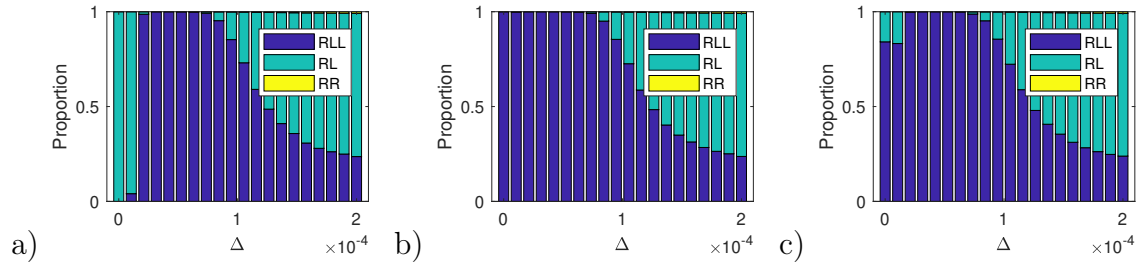


**Figure 7.9:** Bar charts showing how the proportion of iterates in a) the immediate basin of attraction of the period-2 orbit, b) the immediate basin of attraction of the period-3 orbit, and c) outside of the two immediate basins, vary with noise amplitude for  $\mu = 0.0063$ . For each region we consider dynamics over 5,000 iterates, neglecting 195,000 transients, for 1,000 different orbits with linearly spaced initial conditions.

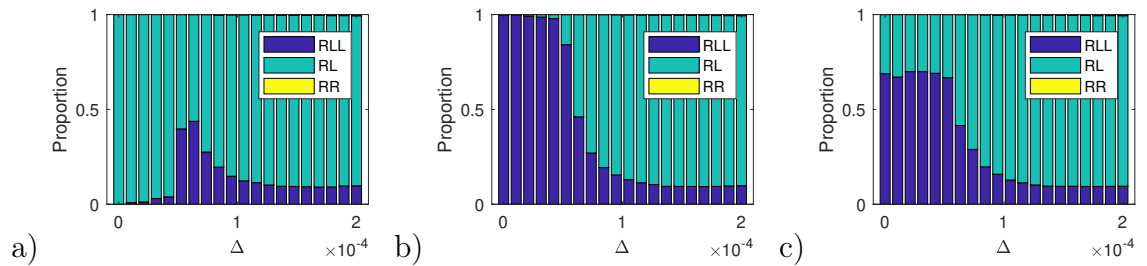


**Figure 7.10:** Bar charts showing how the proportion of iterates in a) the immediate basin of attraction of the period-2 orbit, b) the immediate basin of attraction of the period-3 orbit, and c) outside of the two immediate basins, vary with noise amplitude for  $\mu = 0.00642$ . For each region we consider dynamics over 5,000 iterates, neglecting 195,000 transients, for 1,000 different orbits with linearly spaced initial conditions.

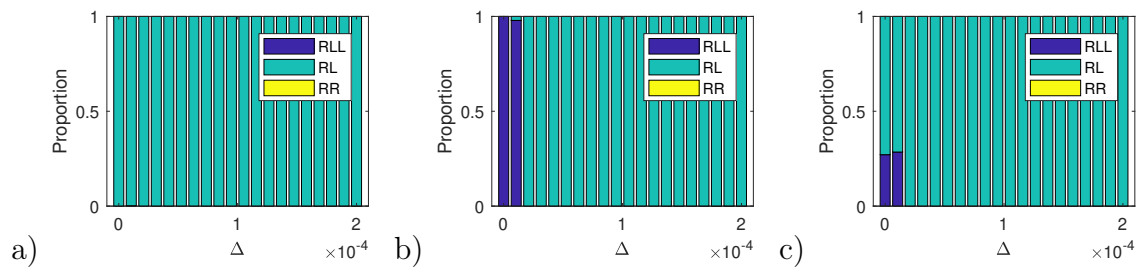


**Figure 7.11:** Bar charts showing how the proportion of iterates in a) the immediate basin of attraction of the period-2 orbit, b) the immediate basin of attraction of the period-3 orbit, and c) outside of the two immediate basins, vary with noise amplitude for  $\mu = 0.0068$ . For each region we consider dynamics over 5,000 iterates, neglecting 195,000 transients, for 1,000 different orbits with linearly spaced initial conditions.

### 7.5.3 The Reversal of Relationships

Finally, we focus on the threshold value  $\Delta^*$  of  $\Delta$ , required for the reversal of the relationship between increasing noise amplitude and the the change in proportion of time spent in each behaviour shown in Figure 7.7c). We note that these threshold values are higher than the maximum threshold values of noise amplitude required to either induce a significant change in proportions of time spent in each behaviour or to effectively destroy one of the attractors. We see that the threshold noise amplitude required to induce a comeback in the attractor whose proportion was initially diminished by the addition of noise appears to fluctuate around a constant level when bringing back period-2 *RL* behaviour on the left end of the interval, and to increase with increasing  $\mu$  when bringing back period-3 *RLL* behaviour on the right end of the interval. In between we see an interval of  $\mu$  values where we require higher noise amplitudes to cause such an effect.

In Figure 7.8c), we see that on either end of the interval of multistability these  $\Delta^*$  values are associated with minimum  $\varrho$  values fluctuating around constant values. At these values of  $\varrho$ , orbits can now escape the immediate basins of attraction of the attractor, to which there was an initial shift in proportions at a significant rate. The difference in the constant they fluctuate around can again be explained at least in part by the fact that  $\varrho(L_2^1) \approx \varrho(R_2)$ , while  $\varrho(L_3^1) \approx \varrho(R_3) > \varrho(L_3^2)$ . This means that the probability of leaving the immediate basin of attraction of the period-2 *RL* orbit is approximately equal on each iterate, while the probability of leaving the immediate basin of attraction of the period-3 *RLL* orbit is higher on the last left iterate of each orbit than it is on the other two. The jump to relatively large-amplitude noise required to induce the effect in the interval away from the endpoints of the interval in multistability can again be explained by the conflict between orbits switching back and forth between behaviours at similar rates due to having  $\varrho$  values which allow orbits to escape at those rates at the lower noise amplitudes.

### 7.5.4 Generalising to Higher Periods

The relationships between the noise amplitude  $\Delta$  and the proportion of time spent in period- $m$  and period- $(m + 1)$  behaviour on the interval of multistability  $(\mu_m^s, \mu_m^e)$  described in sections 7.5.1-7.5.3 can be generalised to higher  $m$  on the interval  $(\mu_m^s, \mu_{m+1}^e)$ . In all cases investigated we have seen that the threshold value of noise amplitude  $\Delta^*$  required to induce a significant shift in the proportion of time spent in each behaviour increases, until it spikes at some maximum as  $\mu$  increases, from an initial threshold value of 0 at  $\mu = \mu_m^s$ .  $\Delta^*$  then decreases to a threshold value of 0 at  $\mu = \mu_{m+1}^e$ , at the end of the interval, just as we saw in the case of period-2 and period-3 coexistence. Similarly, when we look at both the effective destruction of an attractor and the reversal of the relationship between noise amplitude and proportions, the relationships resemble the relationships for period-2 and period-3 coexistence.

Again these relationships can be explained by examining the associated  $\rho$  values. We see that close to the endpoints of the interval of multistability any noise above zero is sufficient to effectively destroy one of the attractors. Elsewhere on the interval, apart from on a small interval of  $\mu$  values, the threshold value  $\Delta^*$  for each feature is associated with a minimum  $\rho$  ratio that fluctuates around some approximately constant value for the attractor whose proportion is diminishing. This is true provided the  $\rho$  values of the other attractor are sufficiently high so that there is no conflict between orbits being thrown back and forth between the two immediate basins of attraction at similar rates.

## 7.6 Scaling

Let us now consider the scaling of  $\rho(p_k)$  on intervals of multistability of increasing period and how this relates to the scaling of the effect of noise on the dynamics of the system. First note that it has been shown by Nordmark [11] amongst others that

the width and location of periodic windows in the one-dimensional square root map decrease geometrically with asymptotic ratio  $b^2$ . Explicitly we can show that

$$\frac{\mu_{m+2}^e}{\mu_{m+1}^e} = b^2 \left( \frac{1 - b^m}{1 - b^{m+1}} \right)^2, \quad \frac{\mu_{m+2}^s}{\mu_{m+1}^s} = b^2 \frac{1 - b^{m+1}}{1 - b^{m+2}}, \quad (7.48)$$

and thus  $\mu_{m+2}^e/\mu_{m+1}^e \approx b^2$  and  $\mu_{m+2}^s/\mu_{m+1}^s \approx b^2$  with

$$\lim_{m \rightarrow \infty} \frac{\mu_{m+2}^e}{\mu_{m+1}^e} = \lim_{m \rightarrow \infty} \frac{\mu_{m+2}^s}{\mu_{m+1}^s} = b^2. \quad (7.49)$$

Using (7.47) and examining the ratio  $\varrho(q_{k+1})/\varrho(p_k)$ , where

$$\{p_1, p_2, \dots, p_m, p_{m+1}\} = \{L_{m+1}^1, L_{m+1}^2, \dots, L_{m+1}^m, R_{m+1}\}$$

are the iterates of the period- $(m+1)$  attractor and  $\{q_i\}$  are the equivalent iterates of the period- $(m+2)$  attractor, evaluated at  $\mu$  and  $\mu' = b^2\mu$ , respectively, we find that

$$\frac{\varrho(q_{k+1})}{\varrho(p_k)} = \frac{D(q_{k+1})}{D(p_k)} \frac{\hat{\sigma}(p_k)}{\hat{\sigma}(q_{k+1})}. \quad (7.50)$$

This scaling has a deterministic part, the distances  $D$ , from the iterate of each attractor to the closest boundary of the iterate's immediate basin of attraction, and a stochastic part, the standard deviation of the deviation distribution associated with each iterate.

First, let us consider the scaling of the deterministic structures of the map on intervals of multistability of increasing period. Recall that

$$D(p_k) = \min\{|p_k - P_{2(m+1)}^{1 \rightarrow k}|, |p_k - P_{2(m+1)}^{2 \rightarrow k}|\} \quad \text{or} \quad D(p_k) = |p_k - G_m^k|, \quad (7.51)$$

where  $P_{2(m+1)}^{1 \rightarrow k}$  and  $P_{2(m+1)}^{2 \rightarrow k}$  are the iterates of the unstable  $(RL^m RL^m)^\infty$  orbit created in a pitchfork bifurcation as  $\mu$  increases through  $\mu_{m+1}^s$ , and  $G_{m+1}^k$  is the iterate of the unstable  $(RRL^{m-1})^\infty$  orbit created in a border-collision bifurcation as  $\mu$  decreases

through  $\mu_{m+1}^e$ . Thus (7.51) gives the distance from  $p_k$  to the closest boundary of the immediate basin of attraction surrounding  $p_k$  on  $(\mu_m^s, \mu_{m+1}^e)$ . In general we find that

$$\frac{q_{m+2}}{p_{m+1}} = \frac{R_{m+2}}{R_{m+1}} = b^2 \left( \frac{-ab^m + \sqrt{(ab^m)^2 + 4 \sum_{i=0}^{m+1} b^i \mu}}{-ab^m + \sqrt{(ab^m)^2 + 4 \sum_{i=0}^m b^i \mu}} \right)^2 \rightarrow b^2 \quad \text{as } m \rightarrow \infty \quad (7.52)$$

and so  $R_{m+1}$  scales as  $b^2$ . Now, since  $L_n^{j+1} = S^{j+1}(R_n) = S_L^j(S_R(R_n))$ , if  $R_{m+1}$  scales as  $b^2$  then the scaling of  $L_{m+1}^k$  is given by

$$\frac{q_{k+1}}{p_k} = \frac{L_{m+2}^{k+1}}{L_{m+1}^k} = b^2 \left( 1 + \frac{b^k \mu}{L_{m+1}^k} \right) = b^2 \left( 1 + \frac{\mathcal{O}(b^{2m+k})}{\mathcal{O}(b^{m+k})} \right) = b^2 (1 + \mathcal{O}(b^m)) \rightarrow b^2 \quad (7.53)$$

as  $m \rightarrow \infty$ . This means that  $q_{k+1}/p_k \approx b^2$  for all  $m$  and  $k$  with

$$\lim_{m \rightarrow \infty} \frac{q_{k+1}}{p_k} = b^2, \quad (7.54)$$

and so the iterates of the attractor scale as  $b^2$  for increasing period.

In the case where the boundaries of the immediate basins are given by the iterates of the unstable  $(RL^n RL^n)^\infty$  orbit created in a pitchfork bifurcation as  $\mu$  increases through  $\mu_{n+1}^s$  we have that

$$\frac{Rp_{2(m+2)}^{1,2}}{Rp_{2(m+1)}^{1,2}} = b^2 \left( \frac{ab^m \pm \sqrt{-3(ab^m)^2 + 4 \sum_{i=0}^{m+1} b^i \mu}}{ab^m \pm \sqrt{-3(ab^m)^2 + 4 \sum_{i=0}^m b^i \mu}} \right)^2 \rightarrow b^2 \quad \text{as } m \rightarrow \infty \quad (7.55)$$

and

$$\frac{Lp_{2(m+2)}^{1,2 \rightarrow k+1}}{Lp_{2(m+1)}^{1,2 \rightarrow k}} = b^2 \left( 1 + \frac{b^k \mu}{Lp_{2(m+1)}^{1,2 \rightarrow k}} \right) = b^2 (1 + \mathcal{O}(b^m)) \rightarrow b^2 \quad \text{as } m \rightarrow \infty, \quad (7.56)$$

which gives that  $P_{2(m+2)}^{1,2 \rightarrow k+1} / P_{2(m+1)}^{1,2 \rightarrow k} \approx b^2$  for all  $m$  and  $k$  with

$$\lim_{m \rightarrow \infty} \frac{P_{2(m+2)}^{1,2 \rightarrow k+1}}{P_{2(m+1)}^{1,2 \rightarrow k}} = b^2. \quad (7.57)$$

Equation (7.57) together with (7.54) gives that in this case the distance to the boundary of the immediate basin of attraction  $D$  scales as  $b^2$ .

Let us now look at the case where the boundaries of the immediate basins are given by the iterates of the unstable  $(RRL^{n-1})^\infty$  orbit created in a border-collision bifurcation as  $\mu$  decreases through  $\mu_{n+1}^e$ . The first right iterate  $Rg_{m+1}^1$  of the  $(RRL^{m-1})^\infty$  orbit created in a border-collision bifurcation at  $\mu_{m+1}^e$  is contained in the interval

$$\begin{aligned} A_{RRL^{m-1}R} &= \left( \left( \frac{\mu}{a} \right)^2 \left( 1 - \frac{\mu}{a^2} \left( \sum_{i=0}^{m-1} b^{-i} \right)^2 \right)^2, \left( \frac{\mu}{a} \right)^2 \left( 1 - \frac{\mu}{a^2} \left( \sum_{i=0}^{m-2} b^{-i} \right)^2 \right)^2 \right) \\ &:= (\mathcal{L}^m, \mathcal{U}^m), \end{aligned} \quad (7.58)$$

where  $A_{X_1 X_2 \dots X_m}$  is the set of values  $x_1 \in \mathbb{R}$  such that the sequence  $x_1, x_2, \dots, x_m$  generated under iteration by  $S$  has the symbolic representation  $X_1, X_2, \dots, X_m$ . Note that this interval is positive valued for  $\mu < \mu_{m+1}^e$  and  $\mathcal{L}^m = 0$  at the boundary collision bifurcation at  $\mu_{m+1}^e$ . We find that

$$\frac{\mathcal{L}^{m+1}}{\mathcal{L}^m} = b^4 \left( \frac{1 - \frac{\mu}{a^2} \left( \sum_{i=0}^{m-2} b^{-i} + b \right)^2}{1 - \frac{\mu}{a^2} \left( \sum_{i=0}^{m-2} b^{-i} \right)^2} \right)^2 \rightarrow b^4 \quad \text{as } m \rightarrow \infty. \quad (7.59)$$

Similarly we find that

$$\frac{\mathcal{U}^{m+1}}{\mathcal{U}^m} \rightarrow b^4 \quad \text{as } m \rightarrow \infty, \quad (7.60)$$

and so the lower and upper bounds of the interval containing  $Rg_{m+1}^1$  scale as  $b^4$  which implies that  $Rg_{m+1}^1$  scales as  $b^4$ . Now since  $Rg_{m+1}^1 = S(Rg_{m+1}^1) = S_R(Rg_{m+1}^1)$ ,

if  $Rg_{m+1}^1$  scales as  $b^4$ , the scaling of  $Rg_{m+1}^2$  is given by

$$\frac{Rg_{m+2}^2}{Rg_{m+1}^2} = \frac{\mu' - a\sqrt{Rg_{m+2}^1}}{\mu - a\sqrt{Rg_{m+1}^1}} = \frac{b^2\mu - a\sqrt{b^4Rg_{m+1}^1}}{\mu - a\sqrt{Rg_{m+1}^1}} = b^2. \quad (7.61)$$

The scaling of  $Lg_{m+1}^k$  is given by

$$\frac{Lg_{m+2}^k}{Lg_{m+1}^k} = b^2 \left( 1 + \frac{b^k\mu}{Lg_{m+1}^k} \right) = b^2 (1 + \mathcal{O}(b^m)) \rightarrow b^2 \quad \text{as } m \rightarrow \infty. \quad (7.62)$$

Finally, we have that  $G_{m+2}^{k+1}/G_{m+1}^k \approx b^2$  for all  $m$  and  $k$  with

$$\lim_{m \rightarrow \infty} \frac{G_{m+2}^{k+1}}{G_{m+1}^k} = b^2. \quad (7.63)$$

We now have that

$$\lim_{m \rightarrow \infty} \frac{D(q_{k+1})}{D(p_k)} = b^2 \quad (7.64)$$

and so all the relevant deterministic structures of the map scale as  $b^2$ .

Let us next consider the stochastic part of the  $\varrho$  ratio given in (7.50). Taking  $\Delta$  and  $\Delta'$  as the noise amplitudes in the cases of  $\hat{\sigma}(p_k)$  and  $\hat{\sigma}(q_{k+1})$ , respectively, we find that

$$\frac{\hat{\sigma}(p_k)}{\hat{\sigma}(q_{k+1})} = \frac{\Delta}{\Delta'} \sqrt{\left( \frac{-2ab^m \sqrt{(ab^m)^2 + 4 \sum_{i=0}^{m+1} b^i \mu} + (ab^m)^2 + 4 \sum_{i=0}^{m+1} b^i \mu}{-2ab^m \sqrt{(ab^m)^2 + 4 \sum_{i=0}^m b^i \mu} + (ab^m)^2 + 4 \sum_{i=0}^m b^i \mu} \right)^2 \times} \quad (7.65)$$

$$\sqrt{\left( \frac{a^2 \sum_{i=k}^m b^{2(i-1)} + \left( 2(ab^m)^2 - 2ab^m \sqrt{(ab^m)^2 + 4 \sum_{i=0}^m b^i \mu} + 4 \sum_{i=0}^m b^i \mu \right) \sum_{i=0}^{k-1} b^{2i}}{a^2 \sum_{i=k}^m b^{2(i-1)} + \left( 2(ab^m)^2 - 2ab^m \sqrt{(ab^m)^2 + 4 \sum_{i=0}^{m+1} b^i \mu} + 4 \sum_{i=0}^{m+1} b^i \mu \right) \sum_{i=0}^k b^{2i}} \right)^2}$$

and so  $\hat{\sigma}(p_k)/\hat{\sigma}(q_{k+1}) \approx \Delta/\Delta'$  with

$$\lim_{m \rightarrow \infty} \frac{\hat{\sigma}(p_k)}{\hat{\sigma}(q_{k+1})} = \frac{\Delta}{\Delta'}. \quad (7.66)$$

This means that the scaling of the stochastic part depends only on the noise amplitude. Combining (7.50) with (7.64) and (7.66) we find that  $\varrho(q_{k+1})/\varrho(p_k) \approx b^2\Delta/\Delta'$  with

$$\lim_{m \rightarrow \infty} \frac{\varrho(q_{k+1})}{\varrho(p_k)} = b^2 \frac{\Delta}{\Delta'} \quad (7.67)$$

and so choosing the noise amplitude to be  $\Delta' = b^2\Delta$  on the interval of multistability  $(\mu_{m+1}^s, \mu_{m+2}^e)$  will result in a similar effect of noise on the dynamics of the map as choosing the noise amplitude to be  $\Delta$  on the interval  $(\mu_m^s, \mu_{m+1}^e)$ .

## 7.7 Discussion

In this paper we have investigated the effects of small amplitude additive Gaussian white noise on the dynamical behaviour of the square root map (7.1) in regions of multistability. The focus on this map comes from Simpson *et al.* [25] who added white noise to the forcing term in a one-dimensional impact oscillator. They showed that the corresponding normal form of the grazing bifurcation is a two-dimensional square root map with additive Gaussian white noise. Following this, we have shown that the introduction of small amplitude additive Gaussian white noise to the square root map (7.21) has the potential to induce significant changes in the qualitative behaviour of the system.

In particular, we have investigated the effect of noise on the period-adding cascade of the map, which exists for  $0 < b < 1/4$  in the deterministic system. The period-adding cascade is such that there are values of the bifurcation parameter  $\mu > 0$  for which a stable periodic orbit of period  $m$  exists for each  $m = 2, 3, \dots$ , and also such that there are two coexisting stable periodic orbits, one period- $(m+1)$  orbit and one period- $m$

orbit. Our focus is on intervals  $(\mu_m^s, \mu_{m+1}^e)$  of multistability, where both the period- $m$  and the period- $(m + 1)$  orbits are stable. In Section 7.2 we derived expressions for the relevant bifurcation points and periodic orbits. We also showed that the basins of attraction on intervals of multistability have a complex intermingled structure. The boundaries of the immediate basins of the coexisting periodic orbits are given by unstable periodic orbits, born in a border-collision bifurcation at  $\mu_{m+1}^e$  in the case of the period- $(m + 1)$  attractor and destroyed in a subcritical pitchfork bifurcation in the case of the period- $m$  attractor.

In Section 7.3.2 we have identified relationships between the noise amplitude and the proportion of time spent in the two different periodic behaviours of intervals of multistability  $(\mu_m^s, \mu_{m+1}^e)$ , where both the period- $m$  and the period- $(m + 1)$  orbits are stable in the deterministic system. These relationships have been shown numerically in Section 7.3.2 (see Figure 7.4) to depend on the value of the bifurcation parameter  $\mu$  and to be non-monotonic.

In order to better understand the relationships shown in Figure 7.4 we first derived approximate Gaussian steady-state deviation distributions associated with each of the coexisting periodic attractors in Section 7.4.1. These approximate distributions were shown in Section 7.4.2 to be a good fit provided the noise amplitude is not too high. We then explained the non-monotonic relationships between noise amplitude and periodic behaviour seen in Figure 7.4 by examining how our estimates of the steady-state distributions of deviations due to noise interact with the deterministic structures of the map.

For  $p_k$ , an iterate of a deterministic periodic attractor, we let  $\varrho(p_k)$  (see (7.47)) be the ratio of the minimum distance from  $p_k$  to the boundary of its immediate basin of attraction, to the standard deviation of the steady state deviation distribution associated with  $p_k$ . In Section 7.5 we have shown that the threshold noise amplitudes associated with three distinguishing features of the non-monotonic relationships between noise amplitude and the proportion of time spent in different periodic

behaviours, are associated with threshold values of the ratio  $\varrho$ . The distinguishing features we considered were; a significant shift in the proportions of iterates spent in each periodic behaviour (Section 7.5.1), the effective destruction of an attractor (Section 7.5.2), i.e. the noise amplitude required to have less than 0.01 per cent of iterates spent in the destroyed behaviour, and the reversal of the direction of the shift in proportions (Section 7.5.3), i.e. if increasing noise amplitude initially resulted in an increase (decrease) in the proportion of iterates spent in period- $m$  behaviour this is the noise amplitude required for this proportion to decrease (increase) once more. Where they occur, these three features are observed in the same order as listed above when noise amplitude increases from 0. The relationship between noise amplitude and proportions is highly dependent on the value of  $\mu$ .

For all three features of the nonmonotonic relationships identified, we showed that the threshold noise amplitudes were associated with an approximately constant minimal  $\varrho$  value for the attractor whose proportion was diminishing, apart from on a small interval of  $\mu$  values on the interior of the interval of multistability and at the endpoints. This can be understood by recognising that  $\varrho$  effectively gives us a measure of the likelihood that a trajectory can escape the immediate basin of attraction of its current behaviour due to the effects of the addition of noise. The lower the minimum  $\varrho$  ratio of an attractor the higher the rate of trajectories escaping its immediate basin of attraction and having the potential to be absorbed by the other attractor. As all three features we have identified are associated with trajectories being pushed from one periodic behaviour to another at a particular rate it is unsurprising that this link exists when the  $\varrho$  ratios of the other attractor are high enough so that the rate at which trajectories are being pushed out of its behaviour is negligible. This link breaks down as we approach the endpoints of the interval of multistability and the size of the basin of attraction of one of the iterates tends to zero. When the size of an attractor's basin is effectively zero any amplitude of noise is sufficient to destroy the periodic behaviour associated with the attractor. It also breaks down when  $\varrho$  ratios of the other attractor are low enough so that the rate at

which trajectories are being pushed out of its behaviour is no longer negligible. In this case an even higher amplitude is required for one effect to dominate the other and produce a significant overall change in proportions.

Finally, in Section 7.6 we investigated how the effect of the addition of noise scales on intervals of multistability of increasing minimal periodic orbit by investigating the scaling of  $\rho$ . Our results revealed that choosing the noise amplitude to be  $\Delta' = b^2\Delta$  on the interval of multistability  $(\mu_{m+1}^s, \mu_{m+2}^e)$  will result in a similar effect of noise on the dynamics of the map as choosing the noise amplitude to be  $\Delta$  on the interval  $(\mu_m^s, \mu_{m+1}^e)$  for large  $m$ .

It remains to be shown how these results can be extended to the case of the two-dimensional square root map derived as an approximation for the full nonsmooth ordinary differential equation (ODE) system describing an impact oscillator near grazing [14, 29] and indeed to the full ODE system itself. In [30] we have also considered the one-dimensional map studied here for values of  $\mu$  outside intervals of multistability and how noise influences periodic behaviour in that case.

## Funding

Eoghan J. Staunton is supported by an Irish Research Council Postgraduate Scholarship, Award Number GOIPG/2015/3500.

## Acknowledgements

We are grateful for the hospitality of CRM, Barcelona, where this work was started and to Professor Paul Glendinning for his helpful input in the early stages of this research. We are also grateful for the helpful comments and suggestions of the reviewer, in particular in relation to the linearisation approach to the approximation of the distribution of trajectory deviations.

## Declaration of Interests

None: The authors declare that they have no competing interests.

# Bibliography

- [1] J. Guckenheimer and P. J. Holmes, *Nonlinear oscillations, dynamical systems, and bifurcations of vector fields*, vol. 42. Springer Science & Business Media, 2013.
- [2] S. Wiggins, *Introduction to applied nonlinear dynamical systems and chaos*, vol. 2. Springer Science & Business Media, 2003.
- [3] Y. A. Kuznetsov, *Elements of applied bifurcation theory*, vol. 112. Springer Science & Business Media, 2013.
- [4] J. Guckenheimer, “On the bifurcation of maps of the interval,” *Inventiones mathematicae*, vol. 39, no. 2, pp. 165–178, 1977.
- [5] O. Makarenkov and J. S. Lamb, “Dynamics and bifurcations of nonsmooth systems: A survey,” *Physica D: Nonlinear Phenomena*, vol. 241, no. 22, pp. 1826–1844, 2012.
- [6] M. Di Bernardo, C. J. Budd, A. R. Champneys, P. Kowalczyk, A. B. Nordmark, G. O. Tost, and P. T. Piiroinen, “Bifurcations in nonsmooth dynamical systems,” *SIAM review*, vol. 50, no. 4, pp. 629–701, 2008.
- [7] M. Bernardo, C. Budd, A. R. Champneys, and P. Kowalczyk, *Piecewise-smooth dynamical systems: theory and applications*, vol. 163. Springer Science & Business Media, 2008.

- [8] S. Rajasekar, “Controlling of chaotic motion by chaos and noise signals in a logistic map and a bonhoeffer–van der pol oscillator,” *Physical Review E*, vol. 51, no. 1, p. 775, 1995.
- [9] S. Linz and M. Lücke, “Effect of additive and multiplicative noise on the first bifurcations of the logistic model,” *Physical Review A*, vol. 33, no. 4, p. 2694, 1986.
- [10] A. Longtin, “Effects of noise on nonlinear dynamics,” in *Nonlinear Dynamics in Physiology and Medicine*, pp. 149–189, Springer, 2003.
- [11] A. B. Nordmark, “Universal limit mapping in grazing bifurcations,” *Physical review E*, vol. 55, no. 1, p. 266, 1997.
- [12] H. E. Nusse, E. Ott, and J. A. Yorke, “Border-collision bifurcations: An explanation for observed bifurcation phenomena,” *Physical Review E*, vol. 49, no. 2, p. 1073, 1994.
- [13] S. Bishop, “Impact oscillators,” *Philosophical Transactions of the Royal Society of London A: Mathematical, Physical and Engineering Sciences*, vol. 347, no. 1683, pp. 347–351, 1994.
- [14] A. B. Nordmark, “Non-periodic motion caused by grazing incidence in an impact oscillator,” *Journal of Sound and Vibration*, vol. 145, no. 2, pp. 279–297, 1991.
- [15] V. Avrutin, P. S. Dutta, M. Schanz, and S. Banerjee, “Influence of a square-root singularity on the behaviour of piecewise smooth maps,” *Nonlinearity*, vol. 23, no. 2, p. 445, 2010.
- [16] P. T. Piiroinen, L. N. Virgin, and A. R. Champneys, “Chaos and period-adding; experimental and numerical verification of the grazing bifurcation,” *Journal of Nonlinear Science*, vol. 14, no. 4, pp. 383–404, 2004.
- [17] W. Chin, E. Ott, H. E. Nusse, and C. Grebogi, “Grazing bifurcations in impact oscillators,” *Physical Review E*, vol. 50, no. 6, p. 4427, 1994.

- [18] W. Chin, E. Ott, H. E. Nusse, and C. Grebogi, “Universal behavior of impact oscillators near grazing incidence,” *Physics Letters A*, vol. 201, no. 2-3, pp. 197–204, 1995.
- [19] F. Casas, W. Chin, C. Grebogi, and E. Ott, “Universal grazing bifurcations in impact oscillators,” *Physical review E*, vol. 53, no. 1, p. 134, 1996.
- [20] J. B. W. Webber, “A bi-symmetric log transformation for wide-range data,” *Measurement Science and Technology*, vol. 24, no. 2, p. 027001, 2012.
- [21] O. Sharkovsky, “Coexistence of the cycles of a continuous mapping of the line into itself,” *Ukrainskij matematicheskij zhurnal*, vol. 16, no. 01, pp. 61–71, 1964.
- [22] J. C. Alexander, J. A. Yorke, Z. You, and I. Kan, “Riddled basins,” *International Journal of Bifurcation and Chaos*, vol. 2, no. 04, pp. 795–813, 1992.
- [23] J. C. Sommerer and E. Ott, “Intermingled basins of attraction: uncomputability in a simple physical system,” *Physics Letters A*, vol. 214, no. 5-6, pp. 243–251, 1996.
- [24] D. J. W. Simpson and R. Kuske, “The influence of localized randomness on regular grazing bifurcations with applications to impacting dynamics,” *Journal of Vibration and Control*, p. 1077546316642054, 2016.
- [25] D. J. W. Simpson, S. J. Hogan, and R. Kuske, “Stochastic regular grazing bifurcations,” *SIAM Journal on Applied Dynamical Systems*, vol. 12, no. 2, pp. 533–559, 2013.
- [26] S. L. de Souza, I. L. Caldas, R. L. Viana, A. M. Batista, and T. Kapitaniak, “Noise-induced basin hopping in a gearbox model,” *Chaos, Solitons & Fractals*, vol. 26, no. 5, pp. 1523–1531, 2005.
- [27] S. L. de Souza, A. M. Batista, I. L. Caldas, R. L. Viana, and T. Kapitaniak, “Noise-induced basin hopping in a vibro-impact system,” *Chaos, Solitons & Fractals*, vol. 32, no. 2, pp. 758–767, 2007.

- [28] S. Kraut, U. Feudel, and C. Grebogi, “Preference of attractors in noisy multistable systems,” *Physical Review E*, vol. 59, no. 5, p. 5253, 1999.
- [29] M. H. Fredriksson and A. B. Nordmark, “Bifurcations caused by grazing incidence in many degrees of freedom impact oscillators,” in *Proceedings of the Royal Society of London A: Mathematical, Physical and Engineering Sciences*, vol. 453, pp. 1261–1276, The Royal Society, 1997.
- [30] E. J. Staunton and P. T. Piiroinen, “Noise-induced multistability in the square root map,” *Nonlinear Dynamics*, vol. 95, no. 1, pp. 769–782, 2019.

## 7.A Appendix: A Linearisation Approach

An alternative approximation to the one given in Section 7.4.1 for the steady-state deviation distributions associated with each iterate of the deterministic period- $(m+1)$  orbit can be found by linearising the square root part of the map  $S_R(x)$  about  $R_{m+1}$ . Local to the periodic orbit this allows us to replace (7.21) with the piecewise-linear map with additive noise

$$x_{n+1} = S'_a(x_n) = \begin{cases} \mu + bx_n + \xi_n, & x_n < 0, \\ \mu - \frac{a}{2}\sqrt{R_{m+1}} - \frac{a}{2\sqrt{R_{m+1}}}x_n + \xi_n, & x_n \geq 0, \end{cases}$$

$$\xi_n \stackrel{\text{iid}}{\sim} N(0, \Delta^2). \quad (7.68)$$

The return map local to  $R_{m+1}$  is now given by the linear map

$$r(x) = A - Bx + \xi'$$

$$\xi' \sim N\left(0, \Delta^2 \frac{1 - b^{2(m+1)}}{1 - b^2}\right), \quad (7.69)$$

where

$$A = \sum_{i=0}^{m-1} b^i \mu + b^m \left(\mu - \frac{a}{2}R_{m+1}\right), \quad B = \frac{ab^m}{2\sqrt{R_{m+1}}}, \quad \xi' = \sum_{i=1}^{m+1} b^{m+1-i} \xi_i, \quad (7.70)$$

and

$$\xi_i \stackrel{\text{iid}}{\sim} N(0, \Delta^2). \quad (7.71)$$

Similarly, the return maps local to  $L_{m+1}^k$  for  $k = 1, 2, \dots, m$  are given by the linear maps

$$r(x) = A - Bx + \xi'$$

$$\xi' \sim N\left(0, \Delta^2 \left(\frac{1 - b^{2k}}{1 - b^2} + \left(\frac{ab^{k-1}}{2\sqrt{R_{m+1}}}\right)^2 \frac{1 - b^{2(m+1-k)}}{1 - b^2}\right)\right), \quad (7.72)$$

where

$$\begin{aligned}
 A &= \sum_{i=0}^{k-2} b^i \mu + b^{k-1} \left( \mu - \frac{a}{2} R_{m+1} \right) - \frac{ab^{k-1}}{2\sqrt{R_{m+1}}} \sum_{i=k-1}^{m-1} b^i \mu, \\
 B &= \frac{ab^m}{2\sqrt{R_{m+1}}}, \quad \xi' = \sum_{i=1}^k b^{k-i} \xi_{i+m+1-k} - \frac{ab^{k-1}}{2\sqrt{R_{m+1}}} \sum_{i=1}^{m+1-k} b^{m+1-k-i} \xi_i,
 \end{aligned} \tag{7.73}$$

and

$$\xi_i \stackrel{\text{iid}}{\sim} N(0, \Delta^2). \tag{7.74}$$

In the absence of noise the iterates of the period- $(m+1)$  orbit are stable fixed points of their corresponding linear return maps. As a result, their associated invariant distributions are Gaussian with mean 0 and standard deviations given by

$$\begin{aligned}
 \tilde{\sigma}(R_{m+1}) &= \Delta \sqrt{\frac{4R_{m+1}}{4R_{m+1} - (ab^m)^2} \left( \frac{1 - b^{2(m+1)}}{1 - b^2} \right)}, \\
 \tilde{\sigma}(L_{m+1}^k) &= \Delta \sqrt{\frac{4R_{m+1}}{4R_{m+1} - (ab^m)^2} \left( \frac{1 - b^{2k}}{1 - b^2} + \frac{(ab^{k-1})^2}{4R_{m+1}} \left( \frac{1 - b^{2(m+1-k)}}{1 - b^2} \right) \right)}, \\
 \text{for } k &= 1, 2, \dots, m.
 \end{aligned} \tag{7.75}$$

We note that these steady-state deviation distributions of the linearised map are equal to the approximations  $\hat{\sigma}$  (see (7.46)) derived by an alternative method in Section 7.4.1.

# Chapter 8

## Paper 2:

# Noise-Induced Multistability in the Square Root Map

EOGHAN J. STAUNTON, PETRI T. PIIROINEN

School of Mathematics, Statistics and Applied Mathematics,  
National University of Ireland, Galway.

---

**Abstract.** The effects of small-amplitude additive Gaussian white noise on the one-dimensional square root map are investigated. In particular the focus is on the unexpected effects noise of varying amplitudes has on the system for parameter regions just outside intervals of multistability. It is shown that in these regions periodic behaviour that is unstable in the deterministic system can be effectively stabilised by the addition of noise of an appropriate amplitude. Features of noise-induced transitions from stable to stabilised unstable periodic behaviour are highlighted and it is shown how these features can be understood by examining relative

levels of expansion and contraction in the deterministic map.

---

## 8.1 Introduction

An impact oscillator is a forced mechanical system that undergoes impacts at rigid stops. Many real-world mechanical systems including systems arising in engineering, for instance moored ships impacting a dock or rattling gears are modelled using impact oscillators [1]. It is important to understand such systems in order to avoid problems, such as wear and noise. In particular, since real-world systems, including mechanical systems, are subject to uncertainties, we must also investigate how stochastic noise can affect such systems. In the case of impact oscillators, noise could for instance arise due to background vibrations or measurement errors.

In this paper we will investigate the effects of the additive noise on the qualitative behaviour of a piecewise-smooth map known as the *square root map* [2, 3, 4, 5, 6]. The map can be derived as an approximation for solutions of a piecewise-smooth ordinary differential equation describing the dynamics of an *impact oscillator* near *grazing* (low-velocity) impacts [2, 7] and it exhibits non-standard qualitative behaviour as a result of a discontinuity in its first derivative.

In smooth nonlinear systems the addition of noise has been shown to have the greatest effect on the outcome of the system in the neighbourhood of *bifurcation points* [8, 9, 10]. Bifurcation points are values of the system parameters that separate regions of parameter space where we observe topologically equivalent dynamics [11, 12, 13, 14]. In nonsmooth dynamical systems, such as the square root map, we find certain types of bifurcations that do not occur in the smooth setting, known as *discontinuity induced bifurcations* [15, 16]. We will focus on the effect of the introduction of noise near bifurcation points in the *period-adding cascade* of the square root map, a bifurcation structure which is unique to nonsmooth systems.

The remainder of this paper is organised as follows. In Section 8.2 we will describe the deterministic bifurcation structure of the square root map. Section 8.3 introduces noise to the square root map and presents our numerical observations of the effect of noise on the square root map in the neighbourhood of regions of multistability. In Section 8.4.1- 8.4.2 we examine relative levels of contraction and expansion in the deterministic square root map in order to explain the distinguishing features of the noise induced transitions between periodic behaviours observed in Section 8.3. We then examine how the steady state trajectory deviation distributions derived in [17] can interact with the deterministic features of the map to produce such transitions given appropriate noise amplitude in Section 8.4.3-8.4.4. A concluding discussion is presented in Section 8.5.

## 8.2 The Deterministic Square Root Map

### 8.2.1 The Map

We will first consider the one-dimensional square root map

$$x_{n+1} = S(x_n) = \begin{cases} S_L(x_n) = \mu + bx_n, & x_n < 0, \\ S_R(x_n) = \mu - a\sqrt{x_n}, & x_n \geq 0, \end{cases} \quad (8.1)$$

where  $a > 0$ ,  $0 < b < 1$ ,  $S_L(x)$  is the linear part of the map applied on the left-hand side, and  $S_R(x)$  is the square root part applied on the right. In this paper we will assume that the parameter  $b$  is such that  $0 < b < \frac{1}{4}$ . For values of  $b$  in this range the deterministic square root map undergoes a period-adding cascade with intervals of multistability as the bifurcation parameter  $\mu$  is decreased [3]. We will discuss the deterministic structures of the square root map in this case more detail in Section 8.2.3.

### 8.2.2 Symbolic Dynamics

Here we will be interested in the qualitative behaviour of the map (8.1), i.e. whether an iterate is on the left-hand side of the map or on the right-hand side of the map, than the exact numerical value of each iterate. As a result we will describe the dynamics of the square root map through the use of *symbolic sequences*. Any orbit  $\{x_n\}$  may be assigned a symbolic sequence  $\{X_n\}$  comprised of the letters  $L$  and  $R$ , where

$$X_n = \begin{cases} L, & x_n < 0, \\ R, & x_n \geq 0. \end{cases} \quad (8.2)$$

Therefore, an  $L$  denotes an iterate on the left, while an  $R$  denotes an iterate on the right. Using symbolic sequences we will describe deterministic  $N$ -periodic orbits by their code  $(R^{n_1}L^{n_2} \dots R^{n_{m-1}}L^{n_m})^\infty$ , where  $n_i \in \mathbb{N}$  and  $\sum n_i = N$ . On the other hand, an orbit with a corresponding symbolic sequence  $(R^{n_1}L^{n_2} \dots R^{n_{m-1}}L^{n_m})^r$ , where  $r$  is finite, will be described as undergoing  $R^{n_1}L^{n_2} \dots R^{n_{m-1}}L^{n_m}$  behaviour or dynamics for those  $rN$  iterates.

### 8.2.3 Bifurcations and Deterministic Structures

For  $\mu < 0$  the map (8.1) has a globally stable fixed point. In the case where  $\mu > 0$  Nordmark and other authors [2, 3, 5, 16] have shown that:

1. If  $0 < b < \frac{1}{4}$  there is a period-adding cascade of stable periodic orbits. That is, there are values of  $\mu > 0$  for which a stable periodic orbit of period  $m$  with code  $(RL^{m-1})^\infty$  exists for each  $m = 2, 3, \dots$  with  $m \rightarrow \infty$  as  $\mu \rightarrow 0$ . Moreover adjacent periodic windows overlap, i.e. there are values of  $\mu > 0$  such that there are two stable periodic orbits, one with period  $m$  and code  $(RL^{m-1})^\infty$  and the other with period  $m+1$  and code  $(RL^m)^\infty$ . These are the only possible attractors except at bifurcation points.
2. If  $\frac{1}{4} < b < \frac{2}{3}$  there is a period-adding cascade of stable periodic orbits such

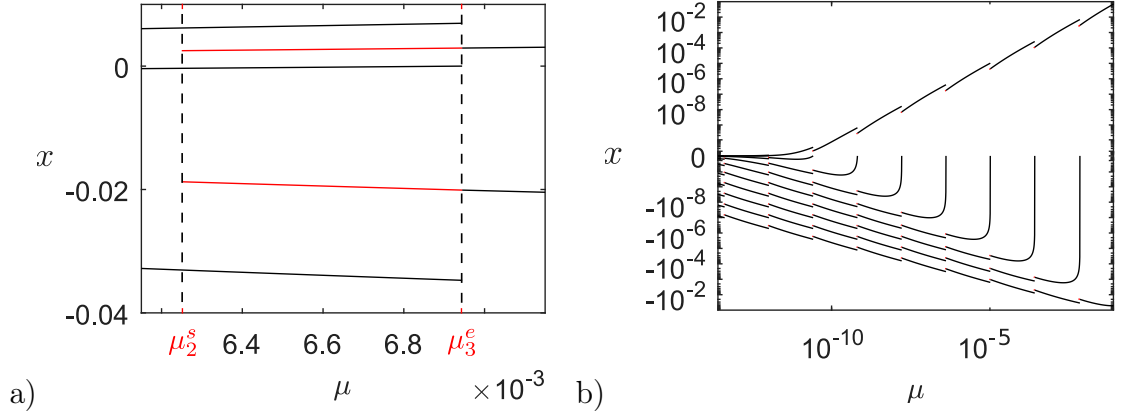


**Figure 8.1:** Bifurcation diagrams for the deterministic square root map,  $S$ , with  $a = 0.5$ ,  $b = 0.2$ . The threshold  $\mu$  values for stability and existence are given by (8.4) and (8.5) while the iterates of the periodic orbits are given by (8.8) and (8.9). a) The coexistence of attractors  $(RL)^\infty$  and  $(RLL)^\infty$  for  $\mu$  about the interval  $(\mu_2^s, \mu_3^e)$ . The period-2  $(RL)^\infty$  orbit is coloured red on the interval of multistability. b) The period adding cascade of attractors  $(RL^m)^\infty$  for  $m \in \{1, \dots, 10\}$ . On the intervals of  $\mu$  where  $(RL^{m-1})^\infty$  and  $(RL^m)^\infty$  coexist as attractors the iterates of  $(RL^{m-1})^\infty$  are marked in red. A symmetric logarithmic transformation [18] has been applied to the  $x$ -axis in order to clearly show the structure of the period adding cascade.

that stable periodic orbits of period  $m$  with code  $(RL^{m-1})^\infty$  exist for each  $m = 2, 3, \dots$ . However, between period- $m$  and period- $m + 1$  windows we now see chaotic attractors.

3. If  $\frac{2}{3} < b < 1$  as  $\mu$  decreases towards zero there are a finite number of period-addings followed by a chaotic attractor on an interval of  $\mu$  values that extends to  $\mu = 0$ .

We will focus on the first case where there is a period-adding cascade of stable periodic attractors with overlaps between adjacent periodic windows where we observe multistability. A bifurcation diagram for this case is shown in Figure 8.1. In the deterministic system (8.1) orbits of period  $m$  of the form  $(RL^{m-1})^\infty$  exist as attractors over the range in the parameter  $\mu$  given by

$$\mu_m^s < \mu < \mu_m^e, \quad (8.3)$$

where

$$\mu_m^s = \frac{1-b}{1-b^m} \left(\frac{a}{b}\right)^2 \left(\frac{3}{4}\right) b^{2m} \quad (8.4)$$

is the threshold value for the stability of the period- $m$  orbit and

$$\mu_m^e = \left[ \frac{1-b}{1-b^{m-1}} a b^{m-2} \right]^2 \quad (8.5)$$

is the threshold value for its existence. We also have that

$$\mu_m^e > \mu_{m-1}^s > \mu_{m+1}^e > \mu_m^s \quad (8.6)$$

holds for  $b < \frac{1}{4}$ . This implies that if  $\mu \in (\mu_{m-1}^s, \mu_m^e)$  then the stable periodic orbits  $(RL^{m-2})^\infty$  and  $(RL^{m-1})^\infty$  coexist. On the other hand, if  $\mu \in (\mu_{m+1}^e, \mu_{m-1}^s)$  then a stable periodic orbit  $(RL^{m-1})^\infty$  exists and is the only attractor. If  $\mu \in (\mu_m^s, \mu_{m+1}^e)$  the pattern of coexistence starts again. We can see this period-adding behaviour and repeating pattern of coexistence clearly in the bifurcation diagram shown in Figure 8.1b) for orbits of period 2 to 11. In Figure 8.1a) we see an example of the coexistence of stable periodic orbits with codes  $(RL)^\infty$  and  $(RLL)^\infty$  on the interval  $(\mu_2^s, \mu_3^e)$ . We will refer to the intervals,  $(\mu_m^s, \mu_{m+1}^e)$  on which stable periodic orbits  $(RL^{m-1})^\infty$  and  $(RL^m)^\infty$  coexist as *coexistence intervals* or *intervals of multistability*.

If  $R_m$  and  $L_m^1, L_m^2, \dots, L_m^{m-1}$  are, respectively, the right iterate and left iterates of the deterministic period  $m$  orbit  $(RL^{m-1})^\infty$  of  $S$  (see (8.1)) then using the fact that

$$S_L^{m-1}(S_R(R_m)) = R_m, \quad (8.7)$$

where  $S_L$  is the linear part (left-hand side) of the square root map and  $S_R$  is the the square root part (right-hand side), we find that

$$R_m = \left( \frac{1}{2} \left( -ab^{m-1} + \sqrt{(ab^{m-1})^2 + 4 \sum_{i=0}^{m-1} b^i \mu} \right) \right)^2. \quad (8.8)$$

Hence we have that

$$L_m^1 = \mu - a\sqrt{R_m} \quad \text{and} \quad L_m^i = \mu + bL_m^{i-1} \quad (8.9)$$

for  $i \in \{2, 3, \dots, m-1\}$ .

## 8.3 The Addition of Noise

### 8.3.1 The Square Root Map With Noise

We wish to examine the effect of uncertainty and noise on the square root map (8.1). In particular we are interested in the effect of noise on the period-adding cascade close to intervals of multistability, as discussed in Section 8.2.3.

Simpson and Kuske [19] show in a careful analysis that noise in impacting systems manifests itself in the corresponding two-dimensional square root map in several different ways, including coloured parametric noise. This is especially the case where there is coloured noise in the impacting dynamics of the full system. Hogan, Simpson and Kuske [20] show that the square root map in two dimensions with additive Gaussian white noise arises when the source of uncertainty in the full system is practically independent of the state of the system.

In this paper we consider small amplitude, additive, Gaussian white noise. However, our investigations indicate similar results for both additive and parametric noise of various distributions although we will not consider these noise formulations here. The square root map with additive Gaussian white noise that we consider is

$$\begin{aligned} x_{n+1} &= S_a(x_n) = \begin{cases} \mu + bx_n + \xi_n, & x_n < 0, \\ \mu - a\sqrt{x_n} + \xi_n, & x_n \geq 0, \end{cases} \\ \xi_n &\stackrel{\text{iid}}{\sim} N(0, \Delta^2), \end{aligned} \quad (8.10)$$

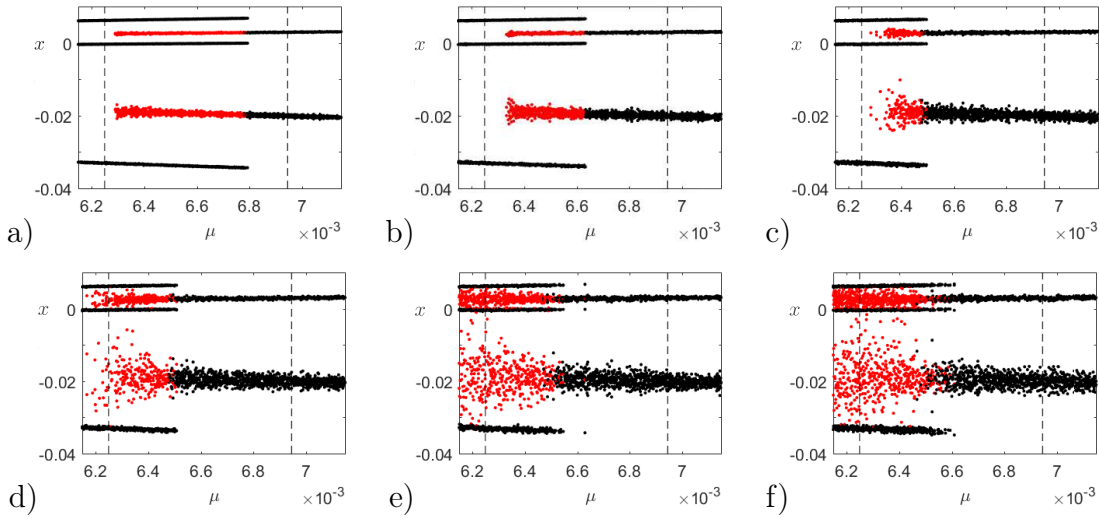


**Figure 8.2:** Bifurcation diagrams for the square root map with additive Gaussian white noise (8.10), with increasing levels of noise amplitude,  $\Delta =$  a)  $2 \times 10^{-5}$ , b)  $4 \times 10^{-5}$ , c)  $6 \times 10^{-5}$ , d)  $8 \times 10^{-5}$ , e)  $1 \times 10^{-4}$ , f)  $1.2 \times 10^{-4}$ , for  $\mu$  in a neighbourhood of the coexistence interval  $(\mu_2^s, \mu_3^e)$ . The deterministic values of  $\mu_2^s$  and  $\mu_3^e$  are indicated by dashed lines. Where the two periodic behaviours coexist the iterates of the behaviour with lower period are marked in red. For the corresponding deterministic bifurcation diagram refer to Figure 8.1a).

where  $\xi_n$  are identically distributed independent normal random variables with mean 0 and standard deviation  $\Delta$ .

### 8.3.2 Numerical Observations

The effect of noise on the dynamics of a system with multiple coexisting attractors has long been of interest [21, 22, 23]. In this article we focus on phase-space sensitivity for values of the bifurcation parameter  $\mu$  close to intervals where period- $m$  and period- $(m+1)$  attractors coexist (8.6), but actually outside the interval itself. Investigating the effect of noise close to regions of multistability and the potential for such noise to attenuate the effect of bifurcation points has been done for the Duffing oscillator in [24]. Our numerical results indicate that a similar phenomenon occurs here in the square root map.

First, examining the neighbourhood of the coexistence interval  $(\mu_2^s, \mu_3^e)$  as a whole,

in Figure 8.2 we plot numerically computed bifurcation diagrams for the square root map with additive Gaussian white noise (8.10) of varying amplitude. The corresponding analytic bifurcation diagram for the deterministic square root map (8.1) is shown in Figure 8.1a). For low noise amplitude we see both a reduction in the effective value of  $\mu_3^e$ , the threshold for the existence of the period-3 orbit and an increase in the effective value of  $\mu_2^s$ , the threshold for the stability of the period-2 orbit. This results in an effective shortening of the interval of multistability at both end points compared to the deterministic system (see Figure 8.1a)). However, beyond some threshold further increases in noise amplitude appear to lead to an effective increase in the length of the coexistence interval. We see a weak return of *RLL* behaviour for higher values of  $\mu$  but the effective value remains below the deterministic value of  $\mu_3^s$ . On the other hand, *RL* behaviour appears to return for all values of  $\mu > \mu_2^s$  and potentially extends into the region  $\mu < \mu_2^s$ . In this paper we are particularly interested in investigating the apparent presence of period-2 behaviour in a region where it is unstable in the corresponding deterministic system.

The bifurcation diagrams shown in Figure 8.2 leads us to believe that for fixed  $\mu$  close to  $\mu_2^s$  with increasing noise amplitude we first see a decrease in the probability of being in *RL* behaviour to some minimum followed by an increase in this probability as  $\mu$  increases further. Looking at both the proportion of points in *RL* behaviour at a certain point in time and the proportion of time spent in *RL* behaviour over a long time period we have confirmed these relationships between noise amplitude and behaviour for additive noise. In particular, Figure 8.3 shows the relationship between the noise amplitude  $\Delta$  and the proportion of time spent in *RL* behaviour, *RLL* behaviour and in transition between the two behaviours over 5,000 iterates, discounting 195,000 transients, for additive white noise where  $\mu < \mu_2^s$ . The bar chart shows the proportion of iterates spent by 1,000 orbits with linearly spaced initial conditions in each of the three types of behaviour. We see that, as expected, the deterministic system ( $\Delta = 0$ ) exhibits only *RLL* behaviour once transients are discounted. This is also the case for the lowest noise amplitudes investigated.

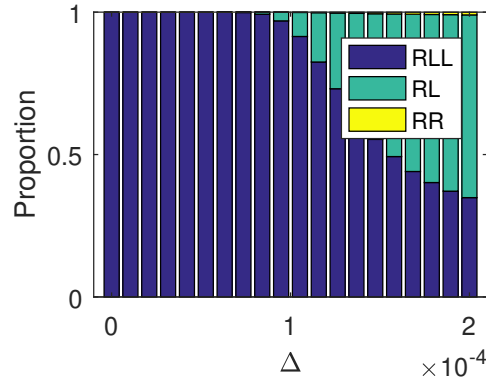


**Figure 8.3:** Bar chart showing the changing proportion of time spent in  $RL$  &  $RLL$  behaviour and transition ( $RR$ ) for increasing amplitude of additive noise,  $\Delta$ , where  $a = 0.5$  and  $b = 0.2$  and  $\mu = 0.00623 < \mu_2^s = 0.00625$ . We plot the different relationships observed, considering dynamics over 5,000 iterates for 1,000 different orbits with linearly spaced initial conditions on the interval  $[-0.04, 0.01]$  neglecting 195,000 transients.

However, once the amplitude has been increased beyond some threshold  $\Delta^*$ , we see that the addition of noise appears to induce some level of multistability, where both  $RL$  and  $RLL$  behaviours are present. This phenomenon could be considered to be a *phenomenological bifurcation* or *p-bifurcation* [25]. A p-bifurcation refers to a qualitative change in the topology of the stationary distribution of a dynamical system. Here we see that noise above the threshold amplitude causes the stationary monostable distribution of the square root map to become multistable.

### 8.3.3 The Evolution of Deviations

In order to more formally understand how the addition of noise affects the qualitative behaviour of the square root map we will use an approximation for the distribution of trajectory deviations resulting from the addition of noise to the system derived in [17]. In particular we are interested in how these deviations can be related to the persistence of unstable periodic behaviour. Using an approach involving linearisation the authors of [20] have derived approximate invariant Gaussian densities associated with periodic attractors of the square root map in two dimensions.

We consider two trajectories,  $\{x_k\}$  and  $\{z_k\}$ , with identical initial conditions  $x_0 = z_0 = R_{m+1}$ , i.e. two trajectories with initial conditions equal to the right iterate of the deterministic  $(RL^m)^\infty$  orbit of the system. We then iterate forward using the square root map with additive noise (8.10) in the case of  $x_0$ , letting  $x_{k+1} = S_a(x_k)$ , and the deterministic square root map (8.1) in the case of  $z_0$ , letting  $z_{k+1} = S(z_k)$ . The deviation due to noise in the trajectory  $\{x_k\}$  is then given by the difference  $\{\epsilon_k\} = \{x_k - z_k\}$ . From (8.1) and (8.10) we have that, provided the deviations are not so large as to push  $\{z_k\}$  out of  $RL^m$  behaviour, the error terms  $\epsilon_k$  are given by

$$\epsilon_k = x_k - z_k = \begin{cases} a\psi_{k-1} + \xi_{k-1}, & k \bmod (m+1) = 1, \\ b\epsilon_{k-1} + \xi_{k-1}, & \text{otherwise,} \end{cases} \quad (8.11)$$

with  $\epsilon_0 = 0$  and  $\psi_{k-1} = \sqrt{R_{m+1}} - \sqrt{R_{m+1} + \epsilon_{k-1}}$ . Referring to [17] we have that  $\epsilon_k$  is distributed approximately normal for all  $k$  with distribution  $N(0, \sigma_{\epsilon_k}^2)$ . Here the variances are given by

$$\sigma_{\epsilon_k}^2 = \begin{cases} \frac{a^2 \sigma_{\epsilon_{k-1}}^2}{4R_{m+1}} + \Delta^2, & k \bmod (m+1) = 1, \\ b^2 \sigma_{\epsilon_{k-1}}^2 + \Delta^2, & \text{otherwise.} \end{cases} \quad (8.12)$$

Working mod  $(m+1)$  we can write (8.12) as a system of  $m+1$  difference equations

$$\sigma_{\epsilon_{(n+1)(m+1)+k}}^2 = f_k(\sigma_{\epsilon_{n(m+1)+k}}^2) \quad (8.13)$$

with initial conditions given by  $\sigma_{\epsilon_k}^2$  for  $1 \leq k \leq m+1$ . The map  $f_k$  has a fixed point  $\hat{\sigma}_{k,(m+1)}^2$  for each of the  $m+1$  difference equations such that

$$\hat{\sigma}_{k,(m+1)}^2 = \Delta^2 \left( \frac{a^2 \sum_{i=k}^m b^{2(i-1)} + 4R_{m+1} \sum_{i=0}^{k-1} b^{2i}}{4R_{m+1} - (ab^m)^2} \right). \quad (8.14)$$

We require  $\hat{\sigma}_{k,(m+1)}^2 > 0$  and so (8.8) and (8.14) imply that

$$4R_{m+1} = \left( -ab^m + \sqrt{(ab^m)^2 + 4 \sum_{i=0}^m b^i \mu} \right)^2 > (ab^m)^2, \quad (8.15)$$

which gives that

$$\mu > \frac{3}{4} \left( \frac{1-b}{1-b^{m+1}} \right) (ab^m)^2 = \mu_{m+1}^s \quad (8.16)$$

and so the fixed points given in (8.14) exist for values of  $\mu$  in the interval of stability for the deterministic  $(RL^m)^\infty$  orbit,  $(\mu_{m+1}^s, \mu_{m+1}^e)$ , with  $\hat{\sigma}_{k,(m+1)}^2 \rightarrow \infty$  as  $\mu \rightarrow \mu_{m+1}^+$  since the numerator  $\rightarrow a^2 \Delta^2 \left( \sum_{i=k-1}^{m+k-1} b^{2i} \right)$  as  $\mu \rightarrow \mu_{m+1}^+$ . On the other hand,  $\hat{\sigma}_{k,(m+1)}^2 \rightarrow c$  where  $c > 0$  as  $\mu \rightarrow \mu_{m+1}^-$ .

The difference equations (8.13) converge for

$$\mu \in \left( -4a^{-2} \sum_{i=0}^m b^{i-2m}, 12a^{-2} \sum_{i=0}^m b^{i-2m} \right) := A_\mu. \quad (8.17)$$

Now, since  $0 < b < \frac{1}{4}$  and  $0 < a < 1$  we have that

$$(\mu_{m+1}^s, \mu_{m+1}^e) \subset \left[ 0, 12 \sum_{i=m}^{2m} 4^i \right] \subset A_\mu \quad (8.18)$$

and so (8.13) converges for all relevant values of the bifurcation parameter  $\mu$  and all  $k$ .

Taking  $m = 2$  as an example and examining the case of deviations on the last left iterate  $L_3^2$  of the deterministic period-3 orbit for  $\mu < \mu_2^s$ , we can see that the analysis in Section 8.3.3 agrees well with our numerical results. Taking one million orbits with initial condition  $x_0 = R_3$  we examine the distribution of the deviations  $\epsilon_{n(3)-1}$  for  $n = 1, 2, \dots, 100$ , such that  $\epsilon_{k(3)-1} < -L_3^2$  for  $k < n$ . In Figure 8.4a) we show that the fitted normal distributions, (fit using the MATLAB<sup>®</sup> `fitdist` function) of these deviations appear to have an approximately zero mean with standard deviation

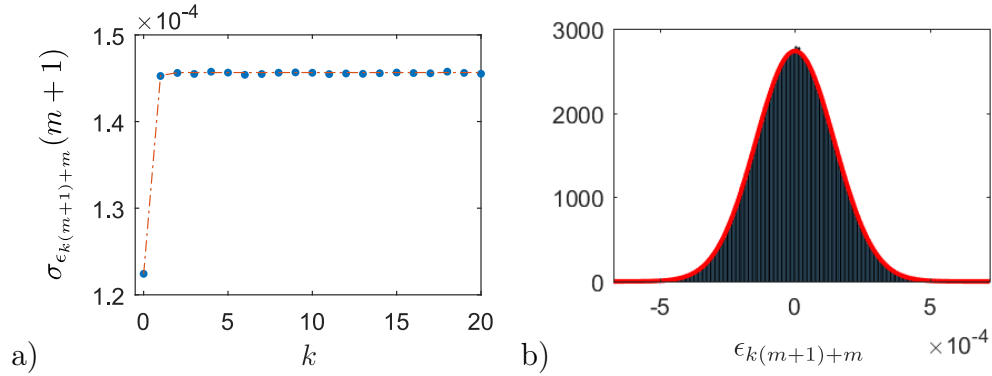


**Figure 8.4:** a) The evolution of the standard deviations of the normal fits of the distributions of the deviations  $\epsilon_m$  and  $\epsilon_{k(m+1)+m}$  such that  $\epsilon_{(k-1)(m+1)+m} < -L_{m+1}^m$  for  $1 \leq k \leq 20$ , fitted using MATLAB<sup>®</sup>'s `fitdist` function, (blue circles) compared to our semi-analytic prediction given by (8.13) (red dashed line). b) The histogram and normal fits of the distributions (red curve) of the deviations  $\epsilon_{7(m+1)+m}$  such that  $\epsilon_{(k-1)(m+1)+m} < -L_{m+1}^m$  for  $1 \leq k \leq 7$ .

converging quickly to some limit,  $\bar{\sigma}$  as  $n \rightarrow \infty$ . We see that the standard deviations of these fitted distributions closely mirror the approximate standard deviations predicted by our analysis (8.13), in particular the standard deviations do indeed appear to converge to the value of  $\hat{\sigma}_{2,3}$  given by (8.14). In Figure 8.4b) we compare an example of these fitted normal distributions to the histogram of the observed numerical deviations and find that the fitted distributions are indeed good fits for the actual distributions. We can therefore use the approximate deviation distributions derived in Section 8.3.3 to better understand the noise induced transitions observed in the square root map.

## 8.4 The Persistence of Unstable Behaviour Due to Noise

Let us now return to examine in more detail the potential for repeated intervals of persistent  $RL^{m-1}$  dynamics in a noisy system of sufficiently high noise amplitude with  $\mu < \mu_m^s$ , as observed in Figure 8.2 in the  $m = 2$  case. A related phenomenon for a system with  $\mu > \mu_m^s$  is that the proportion of time spent by the system in

$RL^{m-1}$  behaviour falls to almost zero as noise amplitude increases to some threshold value, effectively destroying the attractor. However, for noise amplitudes above this threshold  $RL^{m-1}$  behaviour returns [17].

In order to explain the persistence of unstable periodic behaviour in the stochastic square root map (8.10), in Section 8.4.1 we will first look for qualitative similarities in observed noise-induced transitions from stable to unstable periodic behaviour. These transitions are essential in inducing multistability in regions in which only one stable periodic attractor exists in the deterministic system (8.1). Without them the system would simply remain in a noisy version of the stable periodic orbit. We will then explain why the observed similarities between noise-induced transitions exist by referring to features of the deterministic square root map (8.1) in Section 8.4.2. By referring to Section 8.3.3 in Section 8.4.3 we will show additive Gaussian white noise can induce transitions of the form observed and in Section 8.4.4 we will present examples of such transitions observed in numerical simulations.

### 8.4.1 The Transition

In the numerical simulations we have found that noise-induced transitions between  $RLL$  and  $RL$  behaviour display certain similarities. In particular, we have observed that the transitions tend to take the following symbolic form

$$RLLRLL \dots RLL\underline{RLLRRLRRL} \dots RLRL. \quad (8.19)$$

The significant feature of the symbolic representation of the transition (8.19) is the repeated  $R$  corresponding to repeated iteration by  $S_R$  on the right-hand side of the square root map (8.1).

In general we see that the features of this transition are repeated as we look at transitions from  $RL^m$  behaviour to  $RL^{m-1}$  behaviour for increasing  $m$ . In particular

we observe transitions of the form

$$RL^m RL^m \dots \underline{RL^m RL^{m-1} RL^{k-2} RL^{m-1} RL^{m-1} \dots} \dots RL^{m-1} RL^{m-1} \quad (8.20)$$

for  $\mu$  in a neighbourhood of  $\mu_m^s$  such that  $\mu < \mu_m^s$  and  $k \in \{2, 3, \dots, m\}$ . The most significant feature of transitions of the form given in (8.20) is the sequence  $RL^{k-2}R$  for  $k \in \{2, 3, \dots, m\}$ , again corresponding to iterations on the right-hand side of the map being repeated more quickly than is usual for a settled system with  $\mu < \mu_m^s$ .

### 8.4.2 Contraction and Expansion

In order to understand the effect of noise on the square root map, and the importance of the form of the transition characterised by (8.20), we will look at the sets associated with the occurrence of this symbolic sequence in the deterministic dynamical system (8.1). Let  $A_{X_1 X_2 \dots X_m}$  denote the set of values  $x_1 \in \mathbb{R}$  such that the sequence  $x_1, x_2, \dots, x_m$ , generated under iteration by (8.1) has the symbolic representation  $X_1, X_2, \dots, X_m$ . For example, the set  $A_{LL}$  is the set of values to the left of zero, i.e. less than zero, that remain on the left after a single iteration. We can construct  $A_{LL}$  as

$$\begin{aligned} A_{LL} &:= \{x \in (-\infty, 0) : S(x) < 0\} \\ &= \{x \in (-\infty, 0) : \mu + bx < 0\} = \left(-\infty, -\frac{\mu}{b}\right) \end{aligned} \quad (8.21)$$

and similarly we find

$$\begin{aligned} A_{LR} &:= \left(-\frac{\mu}{b}, 0\right), \\ A_{RR} &:= \left(0, \left(\frac{\mu}{a}\right)^2\right), \\ A_{RL} &:= \left(\left(\frac{\mu}{a}\right)^2, \infty\right). \end{aligned} \quad (8.22)$$

Noting that

$$A_{X_0 X_1 \dots X_m} = \{x \leq 0 : S(x) \in A_{X_1 \dots X_m}\} \quad (8.23)$$

for  $X_0 = L$  or  $R$  respectively, we can find the set  $A_{\{X_i\}}$  associated with any symbolic sequence  $\{X_i\}$  of finite length iteratively.

The sets  $A_{X_1 X_2 \dots X_m}$  become small very quickly as the length of the sequence  $X_1, X_2, \dots, X_m$  increases. In fact the sets associated with the longest symbolic sequences lie outside  $[\mu - a\sqrt{\mu}, \mu]$ , the settled range of the map. The small sizes of these intervals, or their location outside the map's settled range, lead us to believe that the noise-induced transition mechanism observed in simulations is not likely based entirely on being pushed into one of the sets associated with a longer sequence, which were derived based on the deterministic mapping. As a result we wish to investigate the properties of the sets associated with shorter sequences.

We have noted previously that the most significant feature of the transition given in (8.20) is the sequence  $RL^{k-2}R$  corresponding to iterations on the right being repeated more quickly than is usual for a settled system. As a result we would like to see what the images of  $A_{RL^{k-2}R}$  look like under iteration by  $S$ . The nature of these images may give us a better understanding of why close-together iterations on the right-hand side of the map lead to a transition to  $RL^{m-1}$  behaviour. First we recall from (8.22) that

$$A_{RR} = \left(0, \left(\frac{\mu}{a}\right)^2\right) \quad (8.24)$$

and note that

$$A_{RL^{k-2}R} = \left(\left(\frac{\mu}{a} \sum_{i=0}^{k-3} b^{-i}\right)^2, \left(\frac{\mu}{a} \sum_{i=0}^{k-2} b^{-i}\right)^2\right) \quad (8.25)$$

for  $k \in \{3, 4, \dots, m\}$ . These sets are located just to the right of zero and their relative sizes are shown in Figure 8.5a. As a result, a small positive deviation due to low amplitude noise could push settled  $RL^m$  dynamics (a slightly blurred version of the stable deterministic  $(RL^m)^\infty$  orbit) into one of these sets. This is because  $L_{m+1}^m$ ,

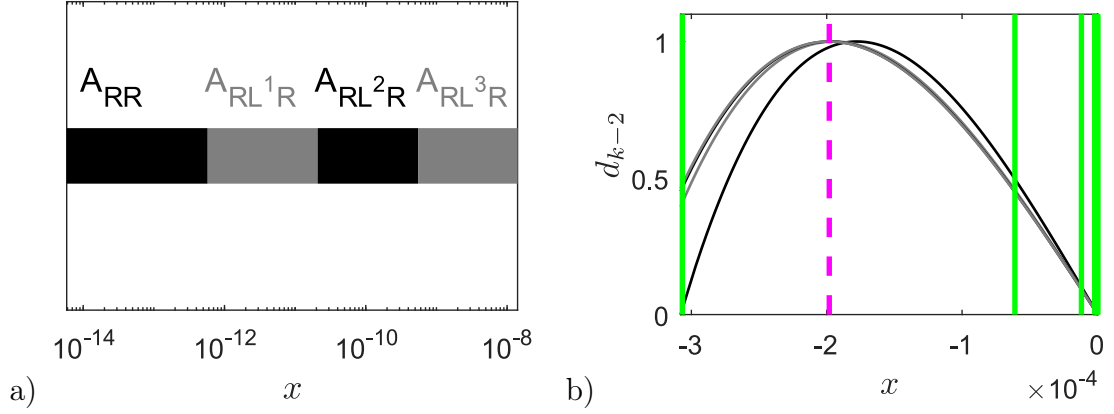


**Figure 8.5:** a) Graphical representation on a log scale of the sets  $A_{RL^{k-2}R}$  for  $k \in \{2, 3, \dots, 5\}$  for  $\mu = 0.99\mu_5^s$ . b) The distributions,  $(x_{k-2}(s), d_{k-2}(s))$ , of the images of the sets  $A_{RL^{k-2}R}$  under  $g_{k-2}$  for  $k \in \{2, \dots, 5\}$  where  $\mu = 0.99\mu_5^s$ .  $L_5^1$ , the first left iterate of the unstable  $(RL^4)^\infty$  orbit, is indicated by the dashed magenta line. The 6 iterates of the stable  $(RL^5)^\infty$  orbit are indicated by solid green lines.

the  $m^{\text{th}}$  left iterate of that stable orbit, is very close to zero.

Let us now look at the images of these sets under iteration by  $S$ . We have that the  $(k-1)^{\text{th}}$  and  $k^{\text{th}}$  images of  $A_{RL^{k-2}R}$  under iteration by the square root map (8.1) are given by

$$\begin{aligned} S^{k-1}(A_{RL^{k-2}R}) &= (0, \mu) \quad \text{and} \\ S^k(A_{RL^{k-2}R}) &= (\mu - a\sqrt{\mu}, \mu). \end{aligned} \quad (8.26)$$

Any trajectory  $\{x_0, x_1, x_2, \dots\}$  iterated under the deterministic square root map (8.1) with initial condition  $x_0 < 0$  will be increasing for the first  $j$  iterations, where  $j \in \mathbb{N}$  is the minimum such that  $x_j > 0$ . This is as a result of the fact that  $\mu > 0$  and  $0 < b < \frac{1}{4}$ . Furthermore since  $x_{j-1} < 0$  we will have that  $x_j \in (0, \mu)$ . Any trajectory with initial condition  $x_0 \in ((\mu/a)^2, \infty) = A_{RL}$  will be such that  $x_1 < 0$ , while (8.26) gives that the image of  $(0, (\mu/a)^2) = A_{RR}$  is  $(0, \mu)$  and so any trajectory with initial condition  $x_0 < 0$  will also eventually enter the set  $(0, \mu)$ . Finally the image of the set  $(0, \mu)$  under a single iteration of the square root map  $S((0, \mu)) = (\mu - a\sqrt{\mu}, \mu)$ . This means that for any trajectory iterated under the square root map  $\exists N \in \mathbb{N}$  such

that  $\forall n > N$  we have  $x_n \in [\mu - a\sqrt{\mu}, \mu]$  and so this gives us no more information as to why repeated iterations on the right tend to result in a transition to  $RL^{m-1}$  behaviour.

Instead we will examine the relative levels of expansion and contraction experienced by elements of  $A_{RL^{k-2}R}$  under iteration by  $S$ . We show that for  $\mu$  in a neighbourhood of  $\mu_m^s$ , the first iterate on the left of the unstable deterministic orbit  $(RL^{m-1})^\infty$  is ‘close’ to  $x_t^{k-2}$  where  $x_t^{k-2}$  is the mode of the distribution of the  $k^{\text{th}}$  image of the set  $A_{RL^{k-2}R}$  for  $k \in \{2, 3, \dots, m\}$ .

For  $x \in A_{RL^{k-2}R}$  we have that  $x > 0$  and

$$\begin{aligned} S^k(x) &= S_R(S_L^{k-2}(S_R(x))) \\ &= \mu - a\sqrt{\mu \sum_{i=0}^{k-2} b^i - ab^{k-2}\sqrt{x}} := g_{k-2}(x). \end{aligned} \quad (8.27)$$

This gives that that

$$g'_{k-2}(x) = \frac{a^2 b^{k-2}}{4} \frac{1}{\sqrt{x} \sqrt{\mu \sum_{i=0}^{k-2} b^i - ab^{k-2}\sqrt{x}}}, \quad (8.28)$$

where the dash ' indicates differentiation with respect to  $x$ . We observe that  $g'_{k-2}(x) \rightarrow \infty$  as  $x \rightarrow 0^+$  and as  $x \rightarrow \left( \left( \frac{\mu}{a} \sum_{i=0}^{k-2} b^{-i} \right)^2 \right)^{-}$ . This means that the level of expansion experienced by elements of the interval  $A_{RL^{k-2}R}$  over the course of two close together iterations on the right tends to infinity as we approach the endpoints. On the other hand, the elements of  $A_{RL^{k-2}R}$  that experience the least expansion over the course of two close together iterations on the right are the points about  $x_c^{k-2}$ , where  $x_c^{k-2}$  is such that the second derivative of  $g_{k-2}$  with respect to  $x$ ,  $g''_{k-2}(x_c^{k-2}) = 0$ . As a result, the image of linearly spaced points in  $A_{RL^{k-2}R}$  will be concentrated about

$g_{k-2}(x_c^{k-2}) = x_t^{k-2}$  with distribution  $(x_{k-2}(s), d_{k-2}(s))$ , where

$$x_{k-2}(s) = g_{k-2}(s) = \mu - a \sqrt{\mu \sum_{i=0}^{k-2} b^i - ab^{k-2} \sqrt{s}} \quad (8.29)$$

and

$$d_{k-2}(s) = \frac{1}{g'_{k-2}(s)} = \frac{4\sqrt{s}}{a^2 b^{k-2}} \sqrt{\mu \sum_{i=0}^{k-2} b^i - ab^{k-2} \sqrt{s}}, \quad (8.30)$$

for  $s \in A_{RL^{k-2}R}$ . Calculating the second derivative of  $g_{k-2}$  we find that

$$g''_{k-2}(x) = \frac{a^2 b^{k-2}}{16} \frac{3ab^{k-2} \sqrt{x} - 2\mu \sum_{i=0}^{k-2} b^i}{\left(x \left(\mu \sum_{i=0}^{k-2} b^i - ab^{k-2} \sqrt{x}\right)\right)^{\frac{3}{2}}}. \quad (8.31)$$

Now,  $x_c^{k-2}$  is given by finding the roots of (8.31) and thus

$$g''_{k-2}(x_c^{k-2}) = 0 \implies x_c^{k-2} = \frac{4}{9} \left(\frac{\mu}{a}\right)^2 \left(\sum_{i=0}^{k-2} b^{-i}\right)^2, \quad (8.32)$$

which gives that

$$S(x_c^{k-2}) = \mu - a \sqrt{x_c^{k-2}} = \left(1 - \frac{2}{3} \sum_{i=0}^{k-2} b^{-i}\right) \mu \quad (8.33)$$

and

$$x_t^{k-2} = S^k(x_c^{k-2}) = g(x_c^{k-2}) = \mu - a \sqrt{\frac{\mu}{3} \sum_{i=0}^{k-2} b^i}. \quad (8.34)$$

The point  $x_t^{k-2}$ , around which the image of  $A_{RL^{k-2}R}$  for  $k \in \{2, \dots, m\}$  is concentrated after undergoing two close together iterations on the right, is close to  $L_m^1$ , the first left iterate of the  $(RL^{m-1})^\infty$  orbit of the deterministic system.

When  $\mu$  is in the neighbourhood of  $\mu_m^s$  points in  $A_{RL^{k-2}R}$ , where  $2 \leq k \leq m$ , undergo

two iterations on the right-hand side of the map by  $S_R$  in the first  $k \leq m$  iterates. This corresponds to iterations on the right-hand side of the map being repeated more quickly than is usual for a settled system where it takes at least  $m + 1$  iterates to repeat iterations on the right. The distribution of the image of  $A_{RL^{k-2}R}$  after  $k$  iterates, the first and last of which are by  $S_R$ , along with the high number of iterates required by orbits to enter  $RL^m$  behaviour for  $x_0 \in A_{RL^{k-2}R}$ , gives us a significant insight into why the sequence  $RL^{k-2}R$  is such an important feature of the noise induced transition from  $RL^m$  to  $RL^{m-1}$  behaviour in the noisy version of the square root map.

To illustrate this, in Figure 8.5b) we plot the distributions  $(x_{k-2}(s), d_{k-2}(s))$  given in (8.30), of the images of the sets  $A_{RL^{k-2}R}$  after undergoing two close together iterations on the right for  $m = 5$  and  $k \in \{2, \dots, 5\}$  where  $\mu < \mu_5^s$ . We observe that the modes of all four distributions are very close to the first left iterate of the unstable  $(RL^4)^\infty$  orbit, especially when compared to their distance to any of the iterates of the stable  $RL^5$  orbit. As a result of this, any orbit that enters one of the sets  $A_{RL^{k-2}}$  for  $k \in \{2, 3, \dots, 5\}$ , when  $\mu < \mu_5^s$ , will take a long time to exit  $RL^4$  behaviour and converge to  $(RL^5)^\infty$ , the only stable attractor in the system in that case. In general any noisy  $RL^m$  orbit pushed into one of the sets  $A_{RL^{k-2}R}$  for  $k \in \{2, 3, \dots, m\}$  has the potential to transition into  $RL^{m-1}$  behaviour for a sustained period of time.

In order to illustrate this behaviour let us take the  $m = 2$  case and examine the transition from  $RLL$  to  $RL$  behaviour as an example. We will consider values of  $\mu < \mu_2^s$  in a small neighbourhood of  $\mu_2^s$  where this orbit is unstable. In this case we have only one choice of  $k$  corresponding to close together iterations by  $S_R$ ,  $k = m = 2$ , and so we are concerned only with the images of the set  $A_{RR}$ . After two iterations on the right the distribution of linearly spaced orbits in  $A_{RR}$ , given by (8.30) and shown in Figure 8.6a), is concentrated around  $x_t$  (8.34), close to  $L_2^1$ , the left iterate of the  $(RL)^\infty$  orbit of the deterministic system. Orbits with initial conditions close to  $L_2^1$  will take a significant number of iterates to leave  $RL$  behaviour and converge to the

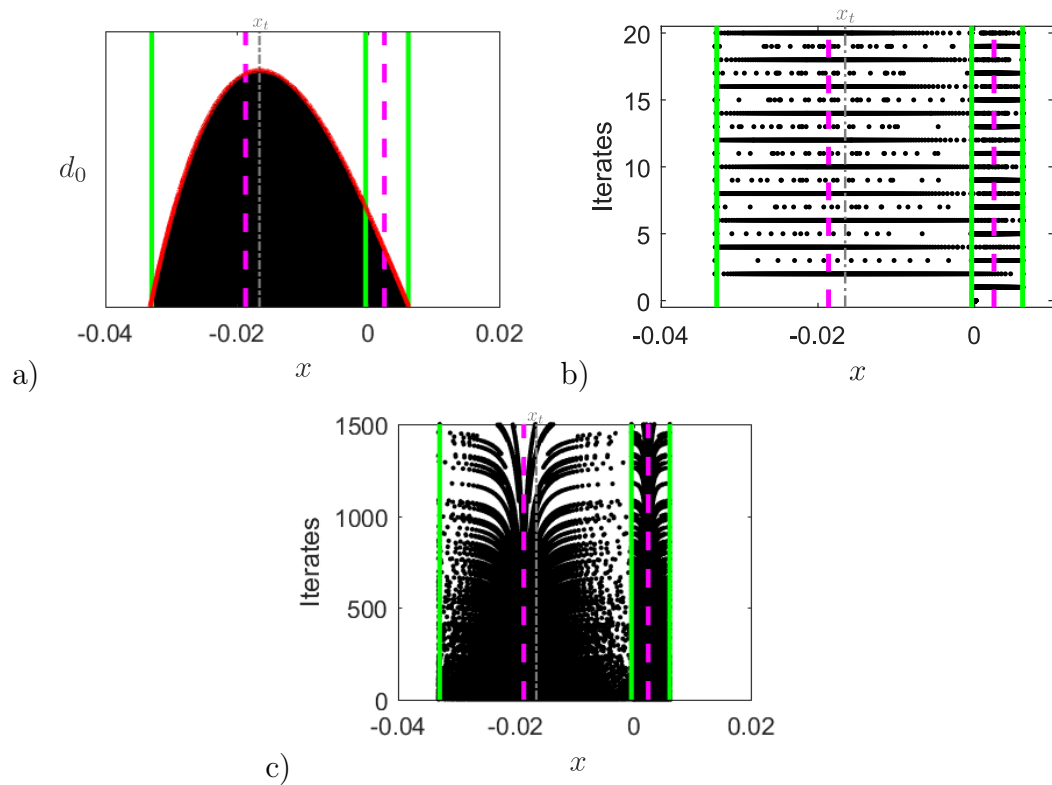


**Figure 8.6:** a) Histogram showing the distribution of the image of 100,000 linearly spaced points in  $A_{RR}$  after two iterations,  $S^2(A_{RR})$  along with  $d_0(s)$  in red. b) and c) Iterates of 300 linearly spaced points in  $A_{RR}$  under the square root map  $S$ , 20 times and until divergence from  $RL$  behaviour respectively. In all three cases we have taken  $\mu < \mu_2^s$ . The iterates of the stable  $(RLL)^\infty$  orbit of the system are marked in green, the iterates of the unstable  $(RL)^\infty$  orbit of the system are marked in dashed magenta and  $x_t$  is marked in dash-dotted grey.

$(RLL)^\infty$  attractor for such values of  $\mu$ . This is clearly illustrated by Figures 8.6b) and 8.6c). We examine 300 orbits with linearly spaced initial conditions in  $A_{RR}$ . We observe that, as a result of this distribution, a significant proportion of the orbits with initial conditions in  $A_{RR}$  do not exit  $RL$  behaviour until after a substantial number of iterations. Indeed, after 1500 iterates a proportion of the orbits are still in  $RL$  behaviour.

In general, the number of iterates required by orbits with different initial conditions to enter  $RLL$  behaviour for the first time for  $\mu$  in a neighbourhood of  $\mu_2^s$  has a very complicated structure. We have plotted this for the entire settled range of the map  $[\mu - a\sqrt{\mu}, \mu]$ , and in more detail, for the subset  $A_{RR}$  in Figure 8.7. This complicated structure is analogous to the *riddled* structure of the basins of attraction of the coexisting periodic attractors on intervals of multistability as discussed in [17].

We can now fully understand why a double  $R$ , corresponding to repeated iterations on the right, is such an important feature of the noise-induced transition from  $RLL$  to  $RL$  behaviour in the noisy version of the square root map (8.10). Our analysis suggests that trajectories entering  $A_{RR}$  could take a significant number of iterates to return to  $RLL$  behaviour due to the deterministic structures of the map. We also can see that, as  $L_3^2$ , the second left iterate of the deterministic  $(RLL)^\infty$  orbit is close to zero for  $\mu$  in a neighbourhood of  $\mu_2^s$  ( $|L_3^2| \lll 1$ ), small deviations due to noise would be enough to push an orbit from  $RLL$  behaviour near the deterministic orbit into the set  $A_{RR} = (0, (\mu/a)^2)$ . The combination of these features means that noise has the potential to push trajectories from  $RLL$  behaviour into  $A_{RR}$  and as a result concentrate these trajectories around the unstable  $(RL)^\infty$  orbit of the deterministic system where they have the potential to remain for a significant number of iterates.

### 8.4.3 Deviation Distributions Under Repeated Iteration on the Right

We can now combine our knowledge of the steady-state deviations of the period- $(m+1)$  orbit derived in Section 8.3.3, the expansion and contraction undergone during repeated iterations on the right-hand side of the square root map described in Section 8.4.2 and the complicated structure of the relationship between initial conditions and the number of iterates required to transition to the stable period- $(m+1)$  orbit in the deterministic map shown in Figure 8.7 to better understand the persistence of unstable periodic behaviour. Again, taking the  $m=2$  case as an example, we know from Section 8.4.2 that deviations  $\epsilon_{n(3)-1}$  such that  $-L_3^2 < \epsilon_{n(3)-1} < -L_3^2 + (\mu/a)^2$  will induce consecutive iterations on the right, symbolically  $RR$ .

We consider the steady-state distribution of  $L_3^2 + \epsilon_{n(3)-1}$ , i.e. the normal distribution with mean  $L_3^2$  and standard deviation  $\hat{\sigma}_{2,3}$ . We then truncate this distribution to the interval  $(0, (\mu/a)^2) = A_{RR}$  to find the distribution  $Tf$  which is shown in Figure 8.7b). Mapping this distribution under consecutive iterations on the right gives us the distribution  $S_R^2(Tf)$ , shown in Figure 8.7c). We see the mode of this distribution is close to the unstable left iterate of the  $RL$  orbit, and in a region where orbits will take a significant number of iterates to return to  $RLL$  behaviour. In fact, taking  $\mu = 0.99\mu_2^s$  and  $\Delta = 1.2 \times 10^{-4}$  we find that the expected number of iterates to return to period-3 behaviour for an orbit whose deviation has pushed the last left iterate on the right-hand side is given by

$$E(\text{Iterates to return} \mid \epsilon_{(n+1)(3)-1} \in (-L_3^2, -L_3^2 + (\mu/a)^2)) \approx 175, \quad (8.35)$$

with standard deviation

$$\sigma(\text{Iterates to return} \mid \epsilon_{(n+1)(3)-1} \in (-L_3^2, -L_3^2 + (\mu/a)^2)) \approx 255, \quad (8.36)$$

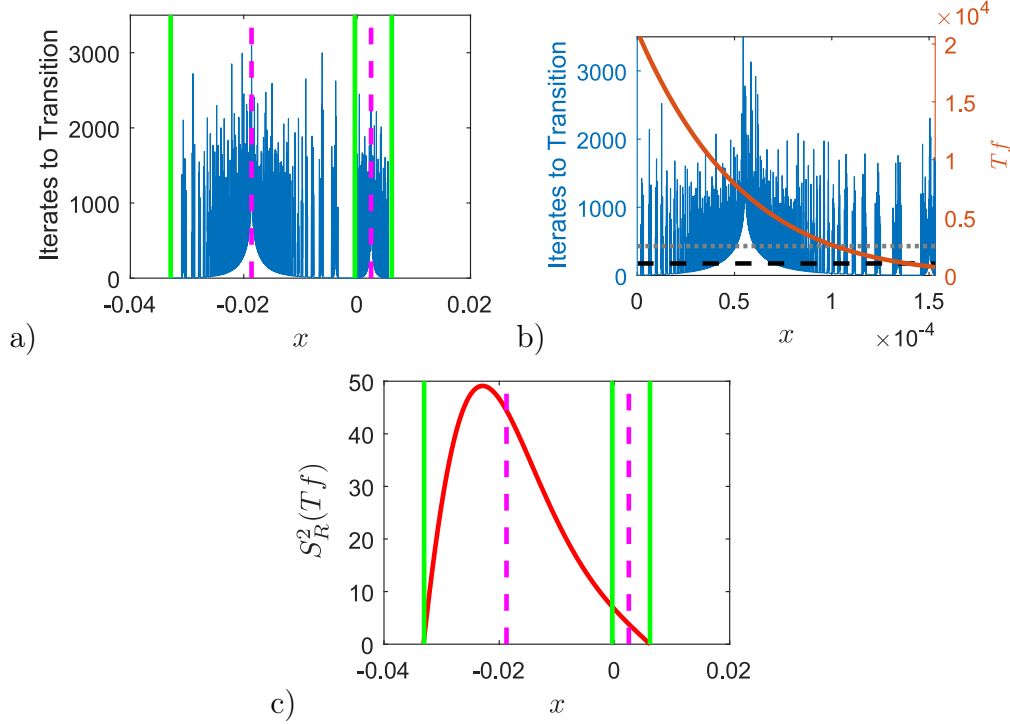


**Figure 8.7:** a) The number of iterates required for orbits with a range of initial conditions to transition to  $RLL$  behaviour in the deterministic system where  $\mu < \mu_2^s$  shown in blue. b) The steady-state distribution of the last left iterate of the  $RLL$  orbit truncated to  $A_{RR}$ ,  $Tf$  in red, along with  $E(\text{Iterates to return to period-3 behaviour}) \approx 175$  marked in dashed black and  $E(\text{Iterates to return to period-3 behaviour})$  plus one standard deviation  $\approx 430$  in dotted grey. c) The distribution of iterates with deviations  $\epsilon_{n(3)-1}$  such that  $-L_3^2 < \epsilon_{n(3)-1} < -L_3^2 + (\mu/a)^2$  after undergoing repeated iterations on the right-hand side of the square root map in red. For the distributions in both b) and c) we have taken  $\Delta = 1.2 \times 10^{-4}$ . In all cases the iterates of the stable  $RLL$  orbit are indicated by solid green lines and the iterates of the unstable  $RL$  orbit are indicated by dashed magenta lines.

where we iterate forward using the deterministic square root map (8.1). These values indicate that noise has the potential to induce transitions to  $RL$  behaviour for a significant number of iterates even when this behaviour is unstable in the corresponding deterministic system.

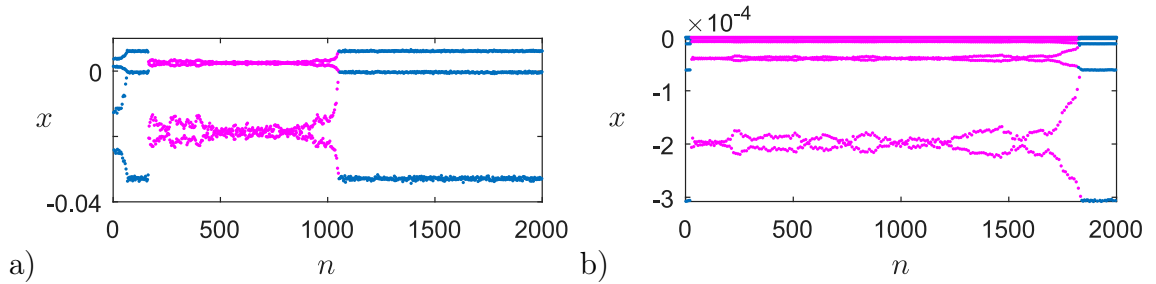


**Figure 8.8:** a) An example of a noise-induced transition from settled  $RLL$  to persistent  $RL$  behaviour in the square root map with additive noise and  $\mu < \mu_2^s$  and the associated noisy signal. Here  $\Delta = 1.2 \times 10^{-4}$  and  $\mu = 0.0062$ . b) An example of a noise-induced transition from settled  $RL^5$  to persistent  $RL^4$  behaviour in the square root map with additive noise and  $\mu < \mu_5^s$ . Here  $k = 4$ .

#### 8.4.4 Examples

In Figure 8.8a) we show an example of a transition from  $RLL$  to  $RL$  behaviour of the form given in (8.19) along with the associated noisy signal. We focus on the characteristics of the noisy signal  $\xi_0, \xi_1, \dots, \xi_7$  associated with the eight iterates  $x_0, x_1, \dots, x_7$  represented by the underlined portion of the symbolic sequence (8.19) and note that none of the individual noise terms have an exceptionally large magnitude. Instead in Figure 8.9 we see that the transition is triggered by the accumulated deviation term  $\epsilon_5 > -L_3^2$ , which pushes the trajectory into the set  $A_{RR}$  resulting in repeated iterations on the right.

In Figure 8.9b) we also see that the orbit in the noisy system remains in  $RL$  behaviour for a far longer period of time than the equivalent orbit with the same initial condition  $x_7$  in the deterministic system. This means that noise can play a role in maintaining  $RL$  behaviour in systems with  $\mu < \mu_2^s$ , in essence further “stabilising” an orbit which is unstable in the associated deterministic system. We have not yet been able to find any precise characteristics of a noisy signal that is likely to result in this further “stabilisation” however it is something we intend to look at in the future.

In Figure 8.8b) we show an example of a transition of the form given in (8.20), for  $m = 5$  and  $k = 4$ . From results of experimental simulation of noisy square root

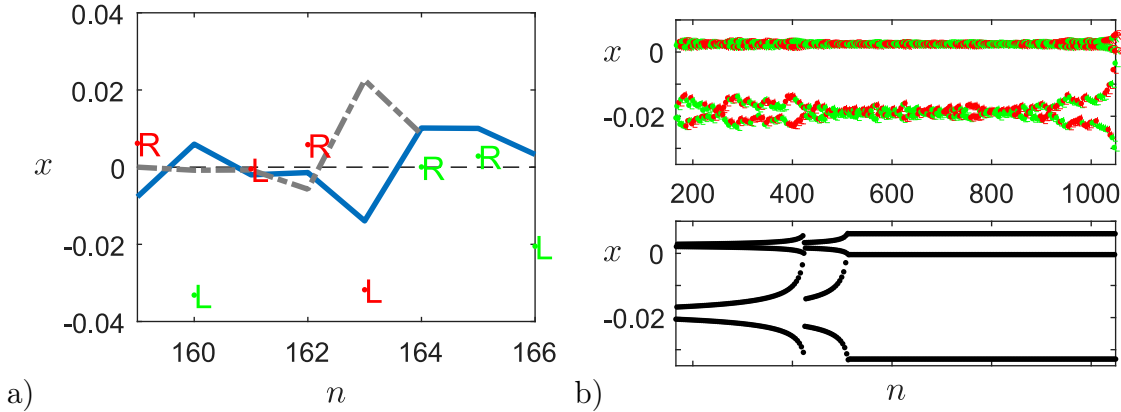


**Figure 8.9:** a) The iterates  $x_0, \dots, x_7$  associated with the eight underlined terms in the symbolic sequence (8.19) in the case of the transition shown in Figure 8.8a). We also show their associated noise terms  $\xi_0, \dots, \xi_7$  in blue and the associated deviation terms of the first 6 iterates  $\epsilon_0, \dots, \epsilon_5$  in dash-dotted grey (not to scale). b) A close-up look at the persistent noise induced  $RL$  behaviour shown in in Figure 8.8a) and the associated deterministic square root map dynamics with initial condition given by  $x_7$ , where the iterates  $x_0, \dots, x_7$  are the iterates associated with the eight underlined terms in the symbolic sequence (8.19).

maps with  $\mu$  in a neighbourhood of  $\mu_m^s$  such that  $\mu < \mu_m^s$  for different values of  $m$  it appears that transitions with certain  $k$  values occur more frequently and other  $k$  values are associated with the “best” transitions. For example, in the  $m = 5$  case many of the “best” transitions were associated with symbolic sequences of the form given in (8.20) with  $k = 4$ . We hypothesise that this is related to both the size and the ordering of the sets  $A_{RL^{k-2}R}$  to the right of zero. For example  $A_{RR}$  becomes vanishingly small as  $m$  increases and so orbits are less likely to enter this set. On the other hand, when  $k = m$  the set  $A_{RL^{m-2}R}$  is the largest of these intervals, but is also located the furthest to the right and so requires a large deviation for orbits to enter. If an orbit does enter this set it is likely to be near to the left endpoint and so its image after two close together iterations on the right-hand side of the square root map is not likely to be too close to  $L_m^1$ , resulting in a “weak” transition. As a result, we believe that “strong” transitions will generally be associated with  $k$  values that are greater than 2 and less than  $m$ . The sets  $A_{RL^{m-2}R}$  for  $k \in \{3, \dots, m-1\}$  are larger than  $A_{RR}$  but closer to the left than  $A_{RL^{m-2}R}$  and so noisy orbits are more

likely to have iterates landing near the centre of these sets, whose images after two close together iterations on the right will be near to  $L_m^1$  and thus result in a strong transition.

## 8.5 Discussion

This paper is concerned with the effects of the introduction of small amplitude additive Gaussian white noise on the dynamics of the square root map (8.1). This noise formulation (8.10) was shown in [20] to be consistent with state-independent noise in piecewise-smooth ordinary differential equations describing an impact oscillator with low-velocity impacts. Our investigations show that introducing noise of this type to the one-dimensional square root map has the potential to induce significant changes in the qualitative behaviour of the system.

In particular, we have investigated the effect of noise on the period-adding cascade of the map, which exists for  $0 < b < \frac{1}{4}$  in the deterministic system. This period-adding cascade is such that there are values of the bifurcation parameter  $\mu > 0$  for which a stable periodic orbit of period  $m$  exists for each  $m = 2, 3, \dots$ , and also such that there are two stable periodic orbits, one period- $(m + 1)$  orbit and one period- $m$  orbit.

In Section 8.3.2 (see Figures 8.2-8.3) we have shown numerical evidence for the persistence of unstable periodic behaviour in the neighbourhood of intervals of multistability due to the addition of noise to the system. In other words, noise of sufficient amplitude effectively induces multistability in these regions in a p-bifurcation. In such regions we identified features of noise-induced transitions from stable to unstable periodic behaviour, including the transition's symbolic representation which is given by (8.20). In Section 8.4.1-8.4.2 we have highlighted that the defining feature of these transitions is the presence of two iterations on the right-hand side of the map, separated by a small number of iterations on the left, i.e. less than the number of iterates on the left of the unstable periodic orbit.

Our investigations revealed that trajectories that are iterated in the order given by (8.20) become concentrated around the unstable periodic orbit due to relative levels of expansion and contraction during iteration. Such trajectories are likely to take a significant number of iterates to return to the stable periodic behaviour (see Figure 8.6).

Finally, we show in Section 8.4.3-8.4.4 that noise-induced transitions from stable to unstable periodic behaviour can be understood by examining how estimates of the steady-state distributions of deviations due to noise derived in [17] interact with the deterministic structures of the map. We also present examples of such transitions, from period-3 to period-2 behaviour and from period-6 to period-5 behaviour, in numerical simulations in Figures 8.8-8.9.

In addition to the investigation required to more formally understand what features of a noisy signal are required to drive “strong” transitions and to further “stabilise” unstable behaviour once a noise-induced transition occurs, several problems remain for future work. In particular, it remains to be shown how these results can be extended to the case of the two-dimensional square root map derived as an approximation for the full system describing an impact oscillator near grazing and indeed to the full ODE system itself.

## Funding

Eoghan Staunton is supported by an Irish Research Council Government of Ireland Postgraduate Scholarship, Award Number GOIPG/2015/3500.

## Conflicts of Interest

The authors declare that they have no conflict of interest.

## Acknowledgements

We are grateful for the hospitality of CRM, Barcelona, where this work was started and to Paul Glendinning for his helpful input in the early stages.

# Bibliography

- [1] S. Bishop, “Impact oscillators,” *Philosophical Transactions of the Royal Society of London A: Mathematical, Physical and Engineering Sciences*, vol. 347, no. 1683, pp. 347–351, 1994.
- [2] A. B. Nordmark, “Non-periodic motion caused by grazing incidence in an impact oscillator,” *Journal of Sound and Vibration*, vol. 145, no. 2, pp. 279–297, 1991.
- [3] A. B. Nordmark, “Universal limit mapping in grazing bifurcations,” *Physical review E*, vol. 55, no. 1, p. 266, 1997.
- [4] V. Avrutin, P. S. Dutta, M. Schanz, and S. Banerjee, “Influence of a square-root singularity on the behaviour of piecewise smooth maps,” *Nonlinearity*, vol. 23, no. 2, p. 445, 2010.
- [5] H. E. Nusse, E. Ott, and J. A. Yorke, “Border-collision bifurcations: An explanation for observed bifurcation phenomena,” *Physical Review E*, vol. 49, no. 2, p. 1073, 1994.
- [6] W. Chin, E. Ott, H. E. Nusse, and C. Grebogi, “Grazing bifurcations in impact oscillators,” *Physical Review E*, vol. 50, no. 6, p. 4427, 1994.
- [7] P. T. Piiroinen, L. N. Virgin, and A. R. Champneys, “Chaos and period-adding; experimental and numerical verification of the grazing bifurcation,” *Journal of Nonlinear Science*, vol. 14, no. 4, pp. 383–404, 2004.

- [8] S. Rajasekar, “Controlling of chaotic motion by chaos and noise signals in a logistic map and a bonhoeffer–van der pol oscillator,” *Physical Review E*, vol. 51, no. 1, p. 775, 1995.
- [9] S. Linz and M. Lücke, “Effect of additive and multiplicative noise on the first bifurcations of the logistic model,” *Physical Review A*, vol. 33, no. 4, p. 2694, 1986.
- [10] A. Longtin, “Effects of noise on nonlinear dynamics,” in *Nonlinear Dynamics in Physiology and Medicine*, pp. 149–189, Springer, 2003.
- [11] J. Guckenheimer, “On the bifurcation of maps of the interval,” *Inventiones mathematicae*, vol. 39, no. 2, pp. 165–178, 1977.
- [12] J. Guckenheimer and P. J. Holmes, *Nonlinear oscillations, dynamical systems, and bifurcations of vector fields*, vol. 42. Springer Science & Business Media, 2013.
- [13] Y. A. Kuznetsov, *Elements of applied bifurcation theory*, vol. 112. Springer Science & Business Media, 2013.
- [14] S. Wiggins, *Introduction to applied nonlinear dynamical systems and chaos*, vol. 2. Springer Science & Business Media, 2003.
- [15] M. Di Bernardo, C. J. Budd, A. R. Champneys, P. Kowalczyk, A. B. Nordmark, G. O. Tost, and P. T. Piiroinen, “Bifurcations in nonsmooth dynamical systems,” *SIAM review*, vol. 50, no. 4, pp. 629–701, 2008.
- [16] M. Bernardo, C. Budd, A. R. Champneys, and P. Kowalczyk, *Piecewise-smooth dynamical systems: theory and applications*, vol. 163. Springer Science & Business Media, 2008.
- [17] E. J. Staunton and P. T. Piiroinen, “Noise and multistability in the square root map,” *Physica D: Nonlinear Phenomena*, vol. 380-381, pp. 31 – 44, 2018.

- [18] J. B. W. Webber, “A bi-symmetric log transformation for wide-range data,” *Measurement Science and Technology*, vol. 24, no. 2, p. 027001, 2012.
- [19] D. J. W. Simpson and R. Kuske, “The influence of localized randomness on regular grazing bifurcations with applications to impacting dynamics,” *Journal of Vibration and Control*, p. 1077546316642054, 2016.
- [20] D. J. W. Simpson, S. J. Hogan, and R. Kuske, “Stochastic regular grazing bifurcations,” *SIAM Journal on Applied Dynamical Systems*, vol. 12, no. 2, pp. 533–559, 2013.
- [21] S. L. de Souza, I. L. Caldas, R. L. Viana, A. M. Batista, and T. Kapitaniak, “Noise-induced basin hopping in a gearbox model,” *Chaos, Solitons & Fractals*, vol. 26, no. 5, pp. 1523–1531, 2005.
- [22] S. L. de Souza, A. M. Batista, I. L. Caldas, R. L. Viana, and T. Kapitaniak, “Noise-induced basin hopping in a vibro-impact system,” *Chaos, Solitons & Fractals*, vol. 32, no. 2, pp. 758–767, 2007.
- [23] S. Kraut, U. Feudel, and C. Grebogi, “Preference of attractors in noisy multistable systems,” *Physical Review E*, vol. 59, no. 5, p. 5253, 1999.
- [24] E. S. Medeiros, I. L. Caldas, M. S. Baptista, and U. Feudel, “Trapping phenomenon attenuates the consequences of tipping points for limit cycles,” *Scientific reports*, vol. 7, p. 42351, 2017.
- [25] L. Arnold and P. Boxler, “Stochastic bifurcation: instructive examples in dimension one,” in *Diffusion Processes and Related Problems in Analysis, Volume II*, pp. 241–255, Springer, 1992.

# Chapter 9

## Paper 3:

# Estimating the Dynamics of Systems with Noisy Boundaries

EOGHAN J. STAUNTON, PETRI T. PIIROINEN

School of Mathematics, Statistics and Applied Mathematics,  
National University of Ireland, Galway.

---

**Abstract.** In a smooth dynamical system the characteristics of a given reference trajectory can be determined, to lowest order, by examining the linearised system about the reference trajectory. In other words, we can approximate the deviations of trajectories after a given time, with starting points in a neighbourhood of the reference trajectory, by multiplying the initial deviations by the corresponding fundamental matrix solution.

This form of analysis cannot be used directly in nonsmooth systems as the vector field is either not everywhere differentiable or the flow function is not continuous. To account for this, one can derive the *zero-time*

*discontinuity mapping* (ZDM) associated with the discontinuity boundary. The Jacobian of this mapping is known as the *saltation matrix* and its properties can tell us how the crossing of the discontinuity boundary affects the deviations of trajectories from a reference trajectory. In particular, this matrix can be composed with the fundamental matrix solutions of the individual flows on either side of the discontinuity boundary in order to determine the overall fundamental matrix solution of a trajectory that crosses the boundary.

In this paper we derive a saltation matrix for a piecewise-smooth dynamical system in which the position of the discontinuity boundary oscillates according to a mean-reverting stochastic process. The derived saltation matrix contains the entire effect of both the discontinuity and the uncertainty introduced into the system by the noisy boundary, and is composable with the deterministic fundamental matrix solutions of the individual flows to give the overall fundamental matrix solution of a crossing trajectory.

We also present some simple examples of piecewise-smooth systems with stochastically varying boundaries, analysed using the derived *noisy saltation matrix*. In particular we focus on the analysis of a discontinuous variant of *the Chua circuit*. In this case we apply noise to the system's discontinuity boundaries which are generated by the piecewise-linear nature of the voltage-current response of the Chua diode. We find that our method allows us to analyse the effects of boundary noise on periodic attractors close to bifurcation points. In particular we show that we can use the method to accurately predict the noise amplitudes required to destroy or merge periodic attractors.

---

## 9.1 Introduction

Piecewise-smooth dynamical systems are characterised by sudden changes in system properties. Many real-world systems can be well modelled as piecewise-smooth or hybrid systems, where the smooth evolution of the system is interrupted by discrete events. Some examples of naturally arising piecewise-smooth systems are electronic systems with switches [1, 2], mechanical systems involving friction or impacts [3, 4], and control problems involving nonsmoothness such as relay control [5]. Other systems that can be well modelled as piecewise-smooth include economic or sociological systems involving decision thresholds [6, 7], climate systems such as models with sharp ice-cap boundaries, box models of thermohaline circulation, or ocean convection models with nonsmooth convective mixing functions [8, 9, 10], and ecological systems such as migrational models with time-dependent switches [11]. Piecewise-smooth dynamical systems can exhibit behaviour not seen in smooth systems including discontinuity-induced bifurcations, such as grazing bifurcations,  $C$ -bifurcations and others [12, 13, 14, 15, 16].

In real-world systems a level of noise and uncertainty is ubiquitous. Noise can enter dynamical systems through measurement noise or through a high number of unknown degrees of freedom. Brownian motion, for example, occurs as a result of a collisions with a huge number of water molecules whose own complicated motion is explained by the molecular-kinetic theory of heat, while Johnson-Nyquist noise refers to fluctuations due to thermal agitation present in systems due to their temperature being higher than absolute zero [17]. As a result, it is necessary to study piecewise-smooth systems such as those described above in the presence of noise. The study of the impact of noise on piecewise-smooth systems is a relatively new but growing field, and noise has been shown to have a significant effect on a variety of piecewise-smooth systems. In-depth studies have been carried out by Simpson, Kuske and Hogan into the effects of noise on grazing bifurcations in impacting systems [18, 19] and by Simpson and Kuske on periodic orbits with sliding [20]. Li, Jiang and Hong showed

that additive noise on the dynamics of a piecewise-smooth rotor/stator rubbing system has the potential to induce explosive and dangerous bifurcations or to have positive effects on the rotor system by pushing the dynamics from destructive dry friction backward whirl motion to no-rub motion [21]. Kim and Wang successfully predicted the distribution of the onset of a non-smooth saddle-node bifurcation from the Fokker-Planck equation corresponding to a newly developed scaled normal form and verified their results numerically and experimentally using a double-well Duffing analog circuit [22].

Much of the existing work in this area focuses on applying noise to the smooth evolution of piecewise-smooth systems between switching events. In this paper we will study the effects of applying noise to the discontinuity boundaries of discontinuous piecewise-smooth systems where switching events occur. In particular, we will look to apply linearisation techniques to such systems. These systems are appropriate for modelling real-world phenomena where the primary sources of noise are the discrete events which interrupt smooth evolution. For example, one could consider switched control systems or electronic systems with noisy switches, mechanical systems with stochastically vibrating impact surfaces or sociological/economical systems with uncertain decision thresholds.

Since the first variational equations along trajectories in piecewise-smooth systems that interact with discontinuity boundaries are locally ill-posed, the linearisation of deterministic piecewise-smooth systems themselves require special techniques when compared to smooth systems [13, 16, 23]. In Section 9.2.1 we give a brief overview of the methods that are most relevant to the current paper. In particular we follow the theory of Aizerman and Gantmacher [24], which allows us to calculate the saltation or jump matrix that accounts for the discontinuous jump in the time evolution of the fundamental solution matrix. Previously linearisation techniques and saltation matrices have been used effectively in the analysis and simulation of piecewise-smooth systems where noise is applied to the system's dynamics, rather than its

discontinuity boundaries. For example, linearisation techniques and deterministic saltation matrices are used by Bizzari, Brambilla *et al.* [25, 26, 27] to analyse and accurately simulate the effects of noise on piecewise-smooth models of fractional phase-locked loops, analog mixed signal circuits and microelectromechanical system oscillators. Our aim is to generalise existing linearisation techniques to allow one to linearise piecewise-smooth systems in which trajectories cross noisy discontinuity boundaries transversally.

This paper is organised as follows. In Section 9.2 we describe linearisation techniques for transversal crossings in piecewise-smooth systems and extend the methods to systems with stochastically varying discontinuity boundaries. Section 9.3 introduces a stochastic process that is suitable to describe the stochastic component of the position of a discontinuity boundary. Section 9.4 provides some examples including a discontinuous formulation of the Chua circuit in Section 9.4.3. The paper concludes in Section 9.5 with a discussion on possible generalisations to other types of piecewise-smooth systems including hybrid systems and continuous piecewise-smooth systems with higher-order discontinuities.

## 9.2 Basic Analysis

### 9.2.1 Discontinuity Mappings and Saltation Matrices

In a smooth dynamical system the characteristics of a given reference trajectory can be determined, to lowest order, by examining the linearised system about the reference trajectory. Here we will describe dynamical systems as initial-value problems (IVPs) given by

$$\dot{\mathbf{x}} = \mathbf{f}(\mathbf{x}), \quad \mathbf{x}(0) = \mathbf{x}_0, \quad (9.1)$$

where  $\mathbf{x} \in \mathbb{R}^n$  is the state,  $\dot{\mathbf{x}} \in \mathbb{R}^n$  the time derivative of the state and  $\mathbf{f}$ , which is  $\mathcal{C}^k$ , the corresponding vector field. We also define the flow function  $\phi(\mathbf{x}, t)$ , which is  $\mathcal{C}^k$  in its arguments, as the collection of trajectories given by  $\mathbf{f}$ , such that the unique

solution to (9.1) can be written

$$\mathbf{x}(t) = \phi(\mathbf{x}_0, t). \quad (9.2)$$

The deviation of a trajectory with an initial condition  $\mathbf{x}_0 \approx \mathbf{x}_0^{\text{ref}}$  in a small neighbourhood of the reference trajectory based at  $\mathbf{x}_0^{\text{ref}}$  is given by

$$\phi(\mathbf{x}_0, t) - \phi(\mathbf{x}_0^{\text{ref}}, t) = \phi_{\mathbf{x}}(\mathbf{x}_0^{\text{ref}}, t)(\mathbf{x}_0 - \mathbf{x}_0^{\text{ref}}) + \mathcal{O}(\|\mathbf{x}_0 - \mathbf{x}_0^{\text{ref}}\|), \quad (9.3)$$

where the Jacobian  $\phi_{\mathbf{x}}(\mathbf{x}_0^{\text{ref}}, t)$  can be found as the solution to the IVP

$$\dot{\Phi}(\mathbf{x}, t) = \mathbf{f}_{\mathbf{x}}(\phi(\mathbf{x}_0^{\text{ref}}, t))\Phi(\mathbf{x}, t), \quad \Phi(\mathbf{x}, 0) = \mathbf{I}, \quad (9.4)$$

with  $\Phi(\mathbf{x}, t) = \phi_{\mathbf{x}}(\mathbf{x}, t)$

This form of analysis cannot be used in nonsmooth systems as  $\mathbf{f}$  may not be everywhere differentiable, or  $\phi(\mathbf{x}_0^{\text{ref}}, t)$  may not be continuous. To account for this we derive the zero-time discontinuity mapping (ZDM) associated with the discontinuity boundary [28, 29]. When crossing a discontinuity boundary, one must compose this extra mapping with the flow maps on either side of the boundary. In the case of transversal crossings the Jacobian of this mapping is known as the *saltation matrix* and its properties can tell us how the crossing of the discontinuity boundary affects the deviations of trajectories in the neighbourhood of a given reference trajectory.

Let the discontinuity boundary be defined by

$$\mathcal{D} = \{\mathbf{x} : h(\mathbf{x}) = 0\}, \quad (9.5)$$

where  $h: \mathbb{R}^n \rightarrow \mathbb{R}$  is at least  $\mathcal{C}^1$ . An incoming trajectory that intersects with the discontinuity boundary at some state  $\mathbf{x}_{\text{in}}$  is mapped by a jump map  $\mathbf{j}$  to an outgoing state  $\mathbf{x}_{\text{out}}$ , somewhere in the state space as shown in Figure 9.1. Here, we assume the reference trajectory, with initial point  $\mathbf{x}_0^{\text{ref}}$ , intersects the discontinuity boundary

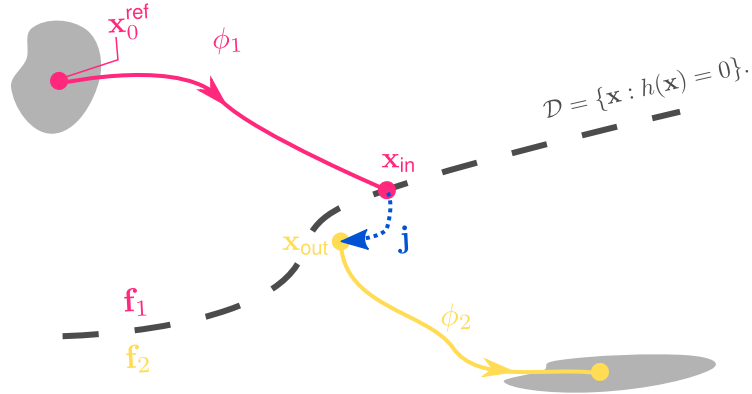


**Figure 9.1:** Schematic of a reference trajectory starting at  $\mathbf{x}_0^{\text{ref}}$  crossing a discontinuity boundary transversally in a hybrid dynamical system.

at time  $t_{\text{ref}}$ , i.e.

$$h(\phi_1(\mathbf{x}_0^{\text{ref}}, t_{\text{ref}})) = 0, \quad (9.6)$$

where  $\phi_1$  is the flow function prior to reaching  $\mathcal{D}$  with corresponding vector field  $\mathbf{f}_1$ . After the discontinuity the flow function is given by  $\phi_2$  with corresponding vector field  $\mathbf{f}_2$ , and so after a time  $T > t_{\text{ref}}$  the trajectory reaches the point

$$\mathbf{x}_T^{\text{ref}} = \phi_2(\mathbf{j}(\phi_1(\mathbf{x}_0^{\text{ref}}, t_{\text{ref}})), T - t_{\text{ref}}). \quad (9.7)$$

We further assume that the vector fields  $\mathbf{f}_1$  and  $\mathbf{f}_2$  and their corresponding flows are smoothly extendible in a neighbourhood of  $\mathbf{x}_{\text{in}}$  and  $\mathbf{x}_{\text{out}}$ , respectively. Since we are interested in a representation of the flow of the overall system for trajectories with initial conditions  $\mathbf{x}_0 \approx \mathbf{x}_0^{\text{ref}}$  and total time  $T$  we study the mapping

$$\phi(\mathbf{x}_0, T) = \phi_2(\mathbf{j}(\phi_1(\mathbf{x}_0, t)), T - t), \quad (9.8)$$

where  $t = t(\mathbf{x}_0)$  is the time of flight to reach the discontinuity boundary. Note that

$$t(\mathbf{x}_0) = t_{\text{ref}} + t(\phi_1(\mathbf{x}_0, t_{\text{ref}})), \quad (9.9)$$

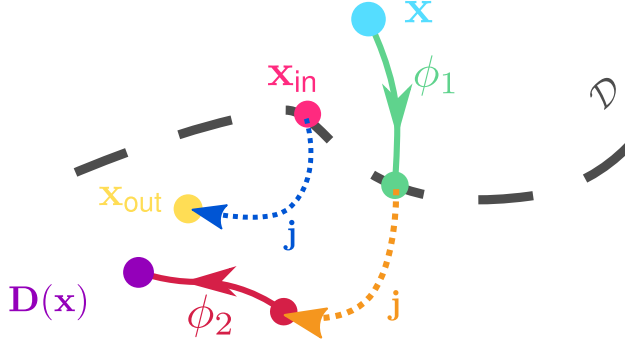


**Figure 9.2:** Deriving the zero-time discontinuity mapping  $\mathbf{D}(\mathbf{x})$  for transversal boundary crossings.  $\mathbf{D}$  takes a point  $\mathbf{x}$  in the neighbourhood of  $\mathbf{x}_{\text{in}}$ , to the boundary by evolving for a time  $t(\mathbf{x})$  under the flow associated with  $\mathbf{f}_1$  (green), applies the jump mapping  $\mathbf{j}$  (orange) and corrects for zero time by evolving for  $-t(\mathbf{x})$  under the flow associated with  $\mathbf{f}_2$  (red).

where  $t(\phi_1(\mathbf{x}_0, t_{\text{ref}}))$  is possibly negative. Using this we can write

$$\phi(\mathbf{x}_0, T) = \phi_2(\mathbf{D}(\phi_1(\mathbf{x}_0, t_{\text{ref}})), T - t_{\text{ref}}), \quad (9.10)$$

where the ZDM

$$\mathbf{D}(\mathbf{x}) = \phi_2(\mathbf{j}(\phi_1(\mathbf{x}, t(\mathbf{x}))), -t(\mathbf{x})), \quad (9.11)$$

which is shown in Figure 9.2, takes a point in a neighbourhood of  $\mathbf{x}_{\text{in}}$  and maps it to a point in a neighbourhood of  $\mathbf{x}_{\text{out}}$  by moving backwards and forwards by the same amount of time along the trajectories given by  $\phi_1$  and  $\phi_2$  and applying the jump map  $\mathbf{j}$ .

The Jacobian of  $\mathbf{D}$ , evaluated at  $\mathbf{x}_{\text{in}}$ , is given by

$$\mathbf{D}_{\mathbf{x}}(\mathbf{x}_{\text{in}}) = \mathbf{j}_{\mathbf{x}}(\mathbf{x}_{\text{in}}) + \frac{(\mathbf{f}_{\text{out}} - \mathbf{j}_{\mathbf{x}}(\mathbf{x}_{\text{in}})\mathbf{f}_{\text{in}})h_{\mathbf{x}}(\mathbf{x}_{\text{in}})}{h_{\mathbf{x}}(\mathbf{x}_{\text{in}})\mathbf{f}_{\text{in}}}, \quad (9.12)$$

where  $\mathbf{f}_{\text{in}} = \mathbf{f}_1(\mathbf{x}_{\text{in}})$  and  $\mathbf{f}_{\text{out}} = \mathbf{f}_2(\mathbf{x}_{\text{out}})$ . Using this we can construct the overall Jacobian of a flow that crosses the discontinuity boundary at  $\mathbf{x}_{\text{in}}$  as

$$\phi_{\mathbf{x}}(\mathbf{x}_0^{\text{ref}}, T) = \phi_{2,\mathbf{x}}(\mathbf{x}_{\text{out}}, T - t_{\text{ref}})\mathbf{D}_{\mathbf{x}}(\mathbf{x}_{\text{in}})\phi_{1,\mathbf{x}}(\mathbf{x}_0^{\text{ref}}, t_{\text{ref}}). \quad (9.13)$$

In the case where  $h$  and  $\mathbf{j}$  are explicitly time-dependent (9.12) becomes

$$\mathbf{D}_{\mathbf{x}}(\mathbf{x}_{\text{in}}) = \mathbf{j}_{\mathbf{x}}(\mathbf{x}_{\text{in}}, t_{\text{ref}}) + \frac{(\mathbf{f}_{\text{out}} - (\mathbf{j}_{\mathbf{x}}(\mathbf{x}_{\text{in}}, t_{\text{ref}})\mathbf{f}_{\text{in}} + \mathbf{j}_t(\mathbf{x}_{\text{in}}, t_{\text{ref}}))h_{\mathbf{x}}(\mathbf{x}_{\text{in}}, t_{\text{ref}})}{h_t(\mathbf{x}_{\text{in}}, t_{\text{ref}}) + h_{\mathbf{x}}(\mathbf{x}_{\text{in}}, t_{\text{ref}})\mathbf{f}_{\text{in}}}. \quad (9.14)$$

In this article we will restrict our attention to the case where the jump mapping on the boundary is the identity mapping, i.e. the case where  $\mathbf{j}(\mathbf{x}) = \mathbf{x}$ . Given this restriction (9.14) becomes

$$\mathbf{D}_{\mathbf{x}}(\mathbf{x}_{\text{in}}) = \mathbf{I} + \frac{(\mathbf{f}_{\text{out}} - \mathbf{f}_{\text{in}})h_{\mathbf{x}}(\mathbf{x}_{\text{in}}, t_{\text{ref}})}{h_t(\mathbf{x}_{\text{in}}, t_{\text{ref}}) + h_{\mathbf{x}}(\mathbf{x}_{\text{in}}, t_{\text{ref}})\mathbf{f}_{\text{in}}}, \quad (9.15)$$

where  $\mathbf{I}$  is the identity matrix.

We note that, in the case of a continuous piecewise smooth system,  $\mathbf{f}_{\text{out}} = \mathbf{f}_{\text{in}}$  and so (9.15) reduces to  $\mathbf{D}_{\mathbf{x}}(\mathbf{x}_{\text{in}}) = \mathbf{I}$ . In other words, the presence of the discontinuity boundary has no first order/linear effects and the overall Jacobian is given simply by

$$\phi_{\mathbf{x}}(\mathbf{x}_0^{\text{ref}}, T) = \phi_{2,\mathbf{x}}(\mathbf{x}_{\text{out}}, T - t_{\text{ref}})\phi_{1,\mathbf{x}}(\mathbf{x}_0^{\text{ref}}, t_{\text{ref}}). \quad (9.16)$$

## 9.2.2 Noisy Boundaries

We are interested in deriving the saltation matrix for piecewise-smooth systems where the position of the discontinuity boundaries  $\mathcal{D}$  vary randomly in time. The vector fields on either side of the discontinuity boundary remain entirely deterministic, and we once again require that they are locally smoothly extendible beyond the boundary.

As in the deterministic case (cf. (9.5)), we define the discontinuity boundary  $\mathcal{D}$  as the zeros of a function  $h$ . In particular, for a noisy boundary the function  $h$  must have a stochastic component. For a stochastically oscillating boundary we let  $h$  take the form

$$h(\mathbf{x}, t) = \hat{h}(\mathbf{x}) - \hat{p}(t) - P(t). \quad (9.17)$$

The functions  $\hat{h}$  and  $\hat{p}$  are deterministic and  $P$  is a stochastic process with small

amplitude. We further require that  $P$  is a mean reverting stochastic process that is at least once differentiable, has mean 0 and does not depend on  $\mathbf{x}$ . The stochastic process  $P$  represents random fluctuations in the position of the boundary and its first derivative defines the stochastic component of the boundary's velocity. Requiring the process to be mean-reverting with mean 0 ensures that the boundary will not have any long-term drift in its position. The analysis that follows in this paper is suitable for any stochastic process  $P$  that meets these requirements. In Section 9.3 we present an example of one such process which is then used in the numerical examples considered in Section 9.4.

Now, since the position of the boundary fluctuates randomly according to the stochastic process  $P(t)$  with small amplitude, the time of flight  $t_{\text{ref}}$  from the starting point  $\mathbf{x}_0^{\text{ref}}$  of a reference trajectory to the boundary is a random variable (cf. (9.6)). Furthermore, since the vector fields on either side of the discontinuity boundary and the jump map are deterministic the distribution of the saltation matrix can be entirely determined by knowledge of the distribution of  $t_{\text{ref}}$  and the stochastic process  $P(t)$ .

Let  $\hat{t}_{\text{ref}}$  be the time of flight from  $\mathbf{x}_0^{\text{ref}}$  to the boundary in the absence of noise, i.e.

$$\hat{h}(\phi_1(\mathbf{x}_0^{\text{ref}}, \hat{t}_{\text{ref}})) - \hat{p}(\hat{t}_{\text{ref}}) = 0. \quad (9.18)$$

Given that  $P(t)$  represents small amplitude mean-reverting noise with mean 0, we have that the true time of flight to the boundary  $t_{\text{ref}} \approx \hat{t}_{\text{ref}}$ . Since  $P(t)$  is assumed to be at least once differentiable, for  $t \approx \hat{t}_{\text{ref}}$ , we can expand about  $\hat{t}_{\text{ref}}$  to find that

$$\begin{aligned} h(\phi_1(\mathbf{x}_0^{\text{ref}}, t), t) &= \hat{h}(\phi_1(\mathbf{x}_0^{\text{ref}}, t)) - \hat{p}(t) - P(t) \\ &\approx \left[ \hat{h}(\phi_1(\mathbf{x}_0^{\text{ref}}, \hat{t}_{\text{ref}})) - \hat{p}(\hat{t}_{\text{ref}}) \right] - P(\hat{t}_{\text{ref}}) \\ &\quad + \left[ \hat{h}_{\mathbf{x}}(\phi_1(\mathbf{x}_0^{\text{ref}}, \hat{t}_{\text{ref}})) \mathbf{f}_1(\phi_1(\mathbf{x}_0^{\text{ref}}, \hat{t}_{\text{ref}})) - \left( \frac{d\hat{p}}{dt} + \frac{dP}{dt} \right) (\hat{t}_{\text{ref}}) \right] (t - \hat{t}_{\text{ref}}) \\ &= \Delta t_{\text{ref}} \left[ \hat{h}_{\mathbf{x}}(\hat{\mathbf{x}}_{\text{in}}) \hat{\mathbf{f}}_{\text{in}} - (\hat{v} + V) (\hat{t}_{\text{ref}}) \right] - P(\hat{t}_{\text{ref}}), \end{aligned} \quad (9.19)$$

where

$$\hat{\mathbf{x}}_{\text{in}} = \phi_1(\mathbf{x}_0^{\text{ref}}, \hat{t}_{\text{ref}}), \quad \Delta t_{\text{ref}} = t_{\text{ref}} - \hat{t}_{\text{ref}}, \quad \hat{\mathbf{f}}_{\text{in}} = \mathbf{f}_1(\hat{\mathbf{x}}_{\text{in}}), \quad \hat{v}(t) = \frac{d\hat{p}}{dt}, \quad V(t) = \frac{dP}{dt}. \quad (9.20)$$

Equation (9.19) implies that  $\Delta t_{\text{ref}}$  is given to first order by

$$\Delta t_{\text{ref}} \approx \frac{P(\hat{t}_{\text{ref}})}{\hat{h}_{\mathbf{x}}(\hat{\mathbf{x}}_{\text{in}})\hat{\mathbf{f}}_{\text{in}} - \hat{v}(\hat{t}_{\text{ref}}) - V(\hat{t}_{\text{ref}}|P(\hat{t}_{\text{ref}}))}, \quad (9.21)$$

where  $V(t|P(t))$  is the random component of the velocity of the boundary conditional on its position at time  $t$ . The random variable  $t_{\text{ref}}$  is now given by

$$t_{\text{ref}} = \hat{t}_{\text{ref}} + \Delta t_{\text{ref}}, \quad (9.22)$$

where  $\hat{t}_{\text{ref}}$  is a constant. Note that this approximation for the distribution of  $\Delta t_{\text{ref}}$  will break down if

$$\hat{h}_{\mathbf{x}}(\hat{\mathbf{x}}_{\text{in}})\hat{\mathbf{f}}_{\text{in}} - \hat{v}(\hat{t}_{\text{ref}}) \approx V(\hat{t}_{\text{ref}}|P(\hat{t}_{\text{ref}})). \quad (9.23)$$

This means that the approximation breaks down if the normal velocity to the boundary in the absence of random fluctuations is similar in magnitude to the velocity of the random fluctuations causing near-zero velocity crossings. In other words, if the trajectory grazes the discontinuity boundary.

### 9.2.3 Derivation of the Noisy Saltation Matrix

In this section we derive the ZDM for a system with a stochastically varying boundary. In order to deal with the fact that the boundary varies stochastically in time we will extend the state space and vector field to

$$\tilde{\mathbf{x}} = (\mathbf{x}, \Delta t_{\text{ref}}, t)^T \quad \text{and} \quad \tilde{\mathbf{f}} = (\mathbf{f}, 0, 1)^T, \quad (9.24)$$

respectively. We can now think of the realisation of the deterministic trajectory in the stochastic system as

$$\tilde{\phi}(\hat{\mathbf{x}}_0^{\text{ref}}, T) = \tilde{\phi}((\mathbf{x}_0^{\text{ref}}, 0, 0)^T, T) = (\phi(\mathbf{x}_0^{\text{ref}}, T), 0, T)^T, \quad (9.25)$$

where  $\hat{\mathbf{x}}_0^{\text{ref}} = (\mathbf{x}_0^{\text{ref}}, 0, 0)^T$ . Our approach will be to linearise about this realisation of the deterministic trajectory in the stochastic system. We denote the values associated with the deterministic ZDM as

$$\hat{\mathbf{x}}_{\text{in}} = \tilde{\phi}_1(\hat{\mathbf{x}}_0^{\text{ref}}, \hat{t}_{\text{ref}}), \quad \hat{\mathbf{f}}_{\text{in}} = \tilde{\mathbf{f}}_1(\hat{\mathbf{x}}_{\text{in}}), \quad \hat{\mathbf{x}}_{\text{out}} = \hat{\mathbf{x}}_{\text{in}}, \quad \hat{\mathbf{f}}_{\text{out}} = \tilde{\mathbf{f}}_2(\hat{\mathbf{x}}_{\text{out}}). \quad (9.26)$$

For simplicity, we will now drop the tildes and refer to  $\mathbf{x}$  and  $\mathbf{f}$  when considering the extended state space, where there is no ambiguity. Following this, we are thus studying the stochastic ZDM (SZDM)

$$\phi(\mathbf{x}_0, T) = \phi_2(\phi_1(\mathbf{x}_0, t), T - t), \quad (9.27)$$

where the random variable  $t = t(\mathbf{x}_0)$  is the time of flight from  $\mathbf{x}_0$  to the boundary. We have that

$$t(\mathbf{x}_0) = t_{\text{ref}} + t(\phi_1(\mathbf{x}_0, t_{\text{ref}})) = \hat{t}_{\text{ref}} + \Delta t_{\text{ref}} + t(\phi_1(\mathbf{x}_0, t_{\text{ref}})), \quad (9.28)$$

and so we can write (9.27) as

$$\begin{aligned} \phi(\mathbf{x}_0, T) = \phi_2(\phi_2(\phi_2(\phi_1(\phi_1(\phi_1(\mathbf{x}_0, \hat{t}_{\text{ref}}), \Delta t_{\text{ref}}), t(\phi_1(\mathbf{x}_0, t_{\text{ref}}))), \\ -t(\phi_1(\mathbf{x}_0, t_{\text{ref}}))), -\Delta t_{\text{ref}}), T - \hat{t}_{\text{ref}}). \end{aligned} \quad (9.29)$$

This gives that

$$\phi(\mathbf{x}_0, T) = \phi_2(\tilde{\mathbf{D}}^*(\phi_1(\mathbf{x}_0, \hat{t}_{\text{ref}})), T - \hat{t}_{\text{ref}}), \quad (9.30)$$

where

$$\tilde{\mathbf{D}}^*(\mathbf{x}) = \phi_2(\phi_2(\phi_1(\phi_1(\mathbf{x}, \Delta t_{\text{ref}}), t(\phi_1(\mathbf{x}, \Delta t_{\text{ref}}))), -\Delta t_{\text{ref}}), -t(\phi_1(\mathbf{x}, \Delta t_{\text{ref}}))). \quad (9.31)$$

Setting

$$t^*(\mathbf{x}) = t(\phi_1(\mathbf{x}, \Delta t_{\text{ref}})) + \Delta t_{\text{ref}}, \quad (9.32)$$

we rewrite (9.31) as

$$\tilde{\mathbf{D}}^*(\mathbf{x}) = \phi_2(\phi_1(\mathbf{x}, t^*(\mathbf{x})), -t^*(\mathbf{x})). \quad (9.33)$$

Differentiating  $\tilde{\mathbf{D}}^*$  with respect to  $\mathbf{x}$  we find

$$\begin{aligned} \tilde{\mathbf{D}}_{\mathbf{x}}^*(\mathbf{x}) &= \phi_{2,\mathbf{x}}(\phi_1(\mathbf{x}, t^*(\mathbf{x})), -t^*(\mathbf{x}))\mathbf{I}\phi_{1,\mathbf{x}}(\mathbf{x}, t^*(\mathbf{x})) \\ &\quad + [\phi_{2,\mathbf{x}}(\phi_1(\mathbf{x}, t^*(\mathbf{x})), -t^*(\mathbf{x}))\mathbf{I}\phi_{1,t}(\mathbf{x}, t^*(\mathbf{x})) - \phi_{2,t}(\phi_1(\mathbf{x}, t^*(\mathbf{x})), -t^*(\mathbf{x}))]t_{\mathbf{x}}^*(\mathbf{x}). \end{aligned} \quad (9.34)$$

At  $\mathbf{x} = \hat{\mathbf{x}}_{\text{in}}$ ,  $t^*(\mathbf{x}) = t^*(\hat{\mathbf{x}}_{\text{in}}) = 0$  we find

$$\tilde{\mathbf{D}}_{\mathbf{x}}^*(\hat{\mathbf{x}}_{\text{in}}) = \mathbf{I} + (\hat{\mathbf{f}}_{\text{in}} - \hat{\mathbf{f}}_{\text{out}})t_{\mathbf{x}}^*(\hat{\mathbf{x}}_{\text{in}}). \quad (9.35)$$

It now remains to find an expression for  $t_{\mathbf{x}}^*(\hat{\mathbf{x}}_{\text{in}})$ . By definition,  $t = t^*(\mathbf{x})$  is a solution to the equation

$$h(\phi_1(\mathbf{x}, t)) = 0. \quad (9.36)$$

Now, differentiating  $h$  with respect to  $t$  and evaluating at  $(\mathbf{x}, t) = (\hat{\mathbf{x}}_{\text{in}}, t^*(\hat{\mathbf{x}}_{\text{in}})) = (\hat{\mathbf{x}}_{\text{in}}, 0)$ , we obtain

$$h_{\mathbf{x}}(\phi_1(\hat{\mathbf{x}}_{\text{in}}, 0))\phi_{1,t}(\hat{\mathbf{x}}_{\text{in}}, 0) = h_{\mathbf{x}}(\hat{\mathbf{x}}_{\text{in}})\hat{\mathbf{f}}_{\text{in}}. \quad (9.37)$$

By the implicit function theorem it follows that  $t^*(\mathbf{x})$  is a  $\mathcal{C}^1$  function in a neighbourhood of  $\hat{\mathbf{x}}_{\text{in}}$  such that

$$t_{\mathbf{x}}^*(\hat{\mathbf{x}}_{\text{in}}) = -\frac{h_{\mathbf{x}}(\hat{\mathbf{x}}_{\text{in}})}{h_{\mathbf{x}}(\hat{\mathbf{x}}_{\text{in}})\hat{\mathbf{f}}_{\text{in}}}. \quad (9.38)$$

Projecting back onto the state space  $(\mathbf{x}, \Delta t_{\text{ref}})$  (9.38) becomes

$$\begin{aligned} t_{\mathbf{x}}^*(\hat{\mathbf{x}}_{\text{in}}) &= -\frac{h_{\mathbf{x}}(\hat{\mathbf{x}}_{\text{in}})}{h_{\mathbf{x}}(\hat{\mathbf{x}}_{\text{in}})\hat{\mathbf{f}}_{\text{in}} - \hat{v}(\hat{t}_{\text{ref}}) - V(\hat{t}_{\text{ref}}|P(\hat{t}_{\text{ref}}) = 0)} \\ &= \left( -\frac{\hat{h}_{\mathbf{x}}(\hat{\mathbf{x}}_{\text{in}})}{\hat{h}_{\mathbf{x}}(\hat{\mathbf{x}}_{\text{in}})\hat{\mathbf{f}}_{\text{in}} - \hat{v}(\hat{t}_{\text{ref}}) - V(\hat{t}_{\text{ref}}|P(\hat{t}_{\text{ref}}) = 0)}, 1 \right) \end{aligned} \quad (9.39)$$

since the second component of  $t_{\mathbf{x}}^*(\hat{\mathbf{x}}_{\text{in}})$  is

$$\left. \frac{\partial t^*(\mathbf{x})}{\partial \Delta t_{\text{ref}}} \right|_{\mathbf{x}=\hat{\mathbf{x}}_{\text{in}}} = 1, \quad (9.40)$$

by definition. Projecting from the state space given in (9.24) to the state space  $(\mathbf{x}, \Delta t_{\text{ref}})$  we can now write

$$\tilde{\mathbf{D}}_{\mathbf{x}}^*(\hat{\mathbf{x}}_{\text{in}}) = \mathbf{I} + \frac{(\hat{\mathbf{f}}_{\text{out}} - \hat{\mathbf{f}}_{\text{in}})h_{\mathbf{x}}(\hat{\mathbf{x}}_{\text{in}})}{h_{\mathbf{x}}(\hat{\mathbf{x}}_{\text{in}})\hat{\mathbf{f}}_{\text{in}} - \hat{v}(\hat{t}_{\text{ref}}) - V(\hat{t}_{\text{ref}}|P(\hat{t}_{\text{ref}}) = 0)} = \begin{pmatrix} \mathbf{D}_{\mathbf{x}}^*(\hat{\mathbf{x}}_{\text{in}}) & \hat{\mathbf{f}}_{\text{in}} - \hat{\mathbf{f}}_{\text{out}} \\ 0 & 1 \end{pmatrix}, \quad (9.41)$$

where

$$\mathbf{D}_{\mathbf{x}}^*(\hat{\mathbf{x}}_{\text{in}}) = \mathbf{I} + \frac{(\hat{\mathbf{f}}_{\text{out}} - \hat{\mathbf{f}}_{\text{in}})\hat{h}_{\mathbf{x}}(\hat{\mathbf{x}}_{\text{in}})}{\hat{h}_{\mathbf{x}}(\hat{\mathbf{x}}_{\text{in}})\hat{\mathbf{f}}_{\text{in}} - \hat{v}(\hat{t}_{\text{ref}}) - V(\hat{t}_{\text{ref}}|P(\hat{t}_{\text{ref}}) = 0)}, \quad (9.42)$$

and find that

$$\tilde{\phi}_{\mathbf{x}}(\hat{\mathbf{x}}_0^{\text{ref}}, T) = \tilde{\phi}_{2,\mathbf{x}}(\hat{\mathbf{x}}_{\text{out}}, T - \hat{t}_{\text{ref}})\tilde{\mathbf{D}}_{\mathbf{x}}^*(\hat{\mathbf{x}}_{\text{in}})\tilde{\phi}_{1,\mathbf{x}}(\hat{\mathbf{x}}_{\text{in}}, \hat{t}_{\text{ref}}). \quad (9.43)$$

Here the Jacobians  $\tilde{\phi}_{1,\mathbf{x}}(\mathbf{x}, t)$  and  $\tilde{\phi}_{2,\mathbf{x}}(\mathbf{x}, t)$  of the flows  $\tilde{\phi}_1$  and  $\tilde{\phi}_2$  are given by

$$\tilde{\phi}_{i,\mathbf{x}} = \begin{pmatrix} \phi_{i,\mathbf{x}} & \mathbf{0} \\ 0 & 1 \end{pmatrix}, \quad i = 1, 2, \quad (9.44)$$

where  $\phi_{i,\mathbf{x}}$  can be found as the solutions of the initial-value problems

$$\dot{\Phi}(\mathbf{x}, t) = \mathbf{f}_{\mathbf{x}}(\phi_i(\mathbf{x}, t))\Phi(\mathbf{x}, t), \quad \Phi(\mathbf{x}, 0) = \mathbf{I}, \quad i = 1, 2. \quad (9.45)$$

The Jacobians  $\phi_{i,\mathbf{x}}$  are entirely smooth and deterministic and the effects of both nonsmoothness and noise are contained within  $\tilde{\mathbf{D}}_{\mathbf{x}}^*(\hat{\mathbf{x}}_{\text{in}})$ . The distribution of deviations of a trajectory with an initial condition  $\mathbf{x}_0 \approx \mathbf{x}_0^{\text{ref}}$ , in a small neighbourhood of the reference trajectory based at  $\mathbf{x}_0^{\text{ref}}$  in the original state space, is now given to first order by

$$\tilde{\phi}(\tilde{\mathbf{x}}_0, T) - \tilde{\phi}(\hat{\mathbf{x}}_0^{\text{ref}}, T) \approx \tilde{\phi}_{\mathbf{x}}(\hat{\mathbf{x}}_0^{\text{ref}}, T)(\tilde{\mathbf{x}}_0 - \hat{\mathbf{x}}_0^{\text{ref}}), \quad (9.46)$$

where  $\tilde{\mathbf{x}}_0 = (\mathbf{x}_0, \Delta t_{\text{ref}})^T$  and  $\Delta t_{\text{ref}}$  is the distribution given by (9.21), before projecting back. As a result, in the original state space we find that

$$\phi(\mathbf{x}_0, T) - \phi(\hat{\mathbf{x}}_0^{\text{ref}}, T) \approx \phi_{\mathbf{x}}(\hat{\mathbf{x}}_0^{\text{ref}}, T)(\mathbf{x}_0 - \hat{\mathbf{x}}_0^{\text{ref}}) + \phi_{2,\mathbf{x}}(\hat{\mathbf{x}}_{\text{out}}, T - \hat{t}_{\text{ref}})(\hat{\mathbf{f}}_{\text{in}} - \hat{\mathbf{f}}_{\text{out}})\Delta t_{\text{ref}}, \quad (9.47)$$

where

$$\phi_{\mathbf{x}}(\hat{\mathbf{x}}_0^{\text{ref}}, T) = \phi_{2,\mathbf{x}}(\hat{\mathbf{x}}_{\text{out}}, T - \hat{t}_{\text{ref}})\mathbf{D}_{\mathbf{x}}^*(\hat{\mathbf{x}}_{\text{in}})\phi_{1,\mathbf{x}}(\hat{\mathbf{x}}_0^{\text{ref}}, \hat{t}_{\text{ref}}). \quad (9.48)$$

Note that in the case of a continuous piecewise-smooth system, as in the deterministic case, this approach indicates that there are no linear effects of a stochastically varying boundary. In continuous systems  $\hat{\mathbf{f}}_{\text{out}} = \hat{\mathbf{f}}_{\text{in}}$  and so (9.47) reduces to

$$\phi(\mathbf{x}_0, T) - \phi(\hat{\mathbf{x}}_0^{\text{ref}}, T) \approx \phi_{\mathbf{x}}(\hat{\mathbf{x}}_0^{\text{ref}}, T)(\mathbf{x}_0 - \hat{\mathbf{x}}_0^{\text{ref}}) = \phi_{2,\mathbf{x}}(\hat{\mathbf{x}}_{\text{out}}, T - \hat{t}_{\text{ref}})\phi_{1,\mathbf{x}}(\hat{\mathbf{x}}_0^{\text{ref}}, \hat{t}_{\text{ref}})(\mathbf{x}_0 - \hat{\mathbf{x}}_0^{\text{ref}}). \quad (9.49)$$

To consider the effects of noisy boundaries in continuous systems we must thus extend our approach to higher orders. However, such analysis lies outside the scope of this article, but is investigated by the authors in [30].

## 9.2.4 Poincaré Map

Although the methods described in the previous sections are very useful in determining the characteristics of a given reference trajectory to lowest order, it will sometimes be useful to use the approach of a Poincaré map. In particular this method is extremely useful when analysing periodic solutions as it allows us to treat periodic

solutions as fixed points of discrete maps. We first introduce a Poincaré section  $\mathcal{P}$ , a codimension-one surface given by

$$\mathcal{P} = \{\mathbf{x} : g_{\mathcal{P}}(\mathbf{x}) = 0\}, \quad (9.50)$$

where  $g_{\mathcal{P}}: \mathbb{R}^n \rightarrow \mathbb{R}$  is at least  $\mathcal{C}^1$  and a periodic solution intersects  $\mathcal{P}$  transversally at some point  $\mathbf{x}_{\mathcal{P}} \in \mathcal{P}$ . We then define the Poincaré map  $\mathbf{M}_{\mathcal{P}}$  for points in the neighbourhood of  $\mathbf{x}_{\mathcal{P}}$  such that  $\mathbf{M}_{\mathcal{P}}$  maps a point on  $\mathcal{P}$  to the subsequent intersection of the corresponding trajectory with  $\mathcal{P}$ , provided it exists. Since it is generally impossible to find a closed form for  $\mathbf{M}_{\mathcal{P}}$  we again rely on linearisation, approximating the evolution of deviations by

$$\mathbf{M}_{\mathcal{P}}(\mathbf{x}) - \mathbf{M}_{\mathcal{P}}(\mathbf{x}_{\mathcal{P}}) \approx \mathbf{M}_{\mathcal{P},\mathbf{x}}(\mathbf{x}_{\mathcal{P}})(\mathbf{x} - \mathbf{x}_{\mathcal{P}}). \quad (9.51)$$

To compute  $\mathbf{M}_{\mathcal{P},\mathbf{x}}(\mathbf{x}_{\mathcal{P}})$  we define  $t_{\mathcal{P}}(\mathbf{x})$  as the time of flight from a point  $\mathbf{x}$  on  $\mathcal{P}$  to its trajectory's next intersection with  $\mathcal{P}$ , which gives that

$$\mathbf{M}_{\mathcal{P}}(\mathbf{x}) = \phi(\mathbf{x}, t_{\mathcal{P}}(\mathbf{x})). \quad (9.52)$$

Let  $t_{\mathcal{P}}(\mathbf{x}_{\mathcal{P}}) = T$  be the period of the periodic solution. Provided

$$g_{\mathcal{P},\mathbf{x}}(\mathbf{x}_{\mathcal{P}})\phi_t(\mathbf{x}_{\mathcal{P}}, T) \neq 0 \quad (9.53)$$

the implicit function theorem gives that  $t_{\mathcal{P}}$  is differentiable function in a neighbourhood of  $\mathbf{x}_{\mathcal{P}}$  with derivative

$$t_{\mathcal{P},\mathbf{x}}(\mathbf{x}_{\mathcal{P}}) = -\frac{g_{\mathcal{P},\mathbf{x}}(\mathbf{x}_{\mathcal{P}})\phi_{\mathbf{x}}(\mathbf{x}_{\mathcal{P}}, T)}{g_{\mathcal{P},\mathbf{x}}(\mathbf{x}_{\mathcal{P}})\phi_t(\mathbf{x}_{\mathcal{P}}, T)}. \quad (9.54)$$

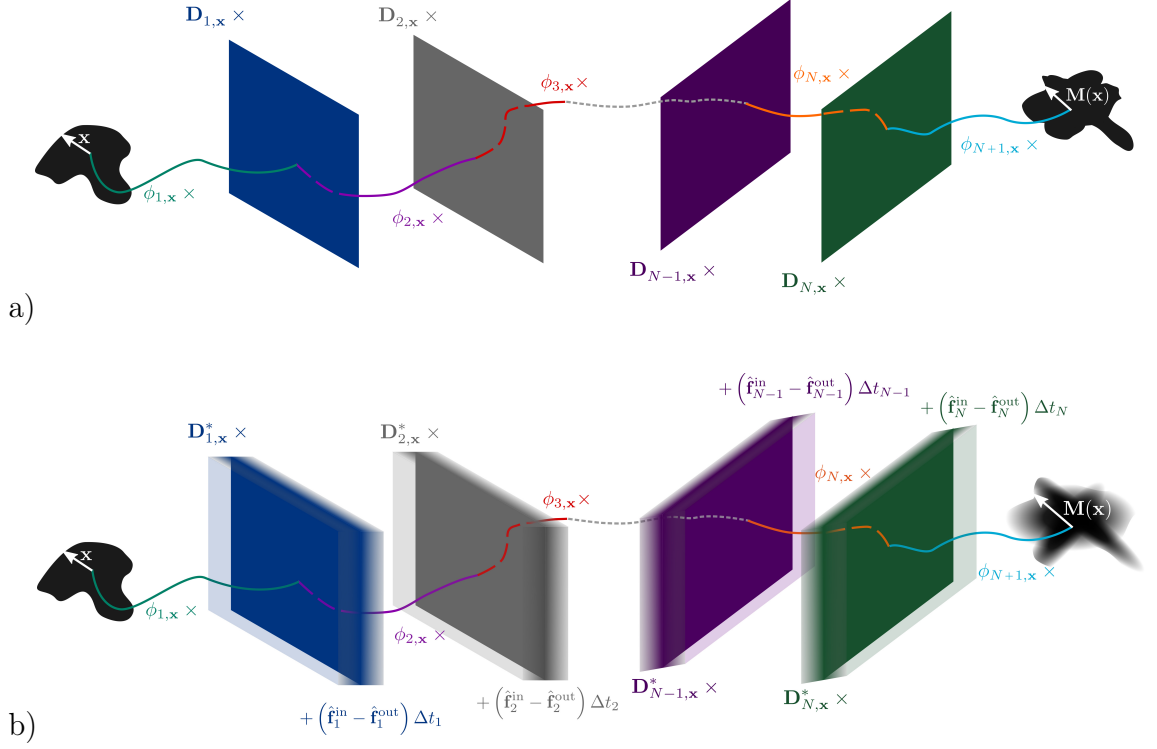


**Figure 9.3:** Schematic showing the iterative construction of  $M(\mathbf{x})$  in the absence of noise (a) and in the presence of noise (b). Here  $\mathbf{A} \times$  indicates multiplication on the left by the matrix  $\mathbf{A}$ .

Differentiating (9.52), using the chain rule and evaluating at  $\mathbf{x}_{\mathcal{P}}$  gives

$$\begin{aligned} \mathbf{M}_{\mathcal{P},\mathbf{x}}(\mathbf{x}_{\mathcal{P}}) &= \phi_{\mathbf{x}}(\mathbf{x}_{\mathcal{P}}, T) + \phi_t(\mathbf{x}_{\mathcal{P}}, T) t_{\mathcal{P},\mathbf{x}}(\mathbf{x}_{\mathcal{P}}) \\ &= \left( \mathbf{I} - \frac{\phi_t(\mathbf{x}_{\mathcal{P}}, T) g_{\mathcal{P},\mathbf{x}}(\mathbf{x}_{\mathcal{P}})}{g_{\mathcal{P},\mathbf{x}}(\mathbf{x}_{\mathcal{P}}) \phi_t(\mathbf{x}_{\mathcal{P}}, T)} \right) \phi_{\mathbf{x}}(\mathbf{x}_{\mathcal{P}}, T), \end{aligned} \quad (9.55)$$

where

$$\mathbf{P}_{\mathcal{P}} = \mathbf{I} - \frac{\phi_t(\mathbf{x}_{\mathcal{P}}, T) g_{\mathcal{P},\mathbf{x}}(\mathbf{x}_{\mathcal{P}})}{g_{\mathcal{P},\mathbf{x}}(\mathbf{x}_{\mathcal{P}}) \phi_t(\mathbf{x}_{\mathcal{P}}, T)} \quad (9.56)$$

is a projection matrix.

### 9.2.5 Summary

Assume we want to define a map  $\mathbf{M}$  that describes the distribution about a periodic trajectory that crosses  $N$  noisy boundaries with switches so that

$$\mathbf{x}_{k+1} = \mathbf{M}(\mathbf{x}_k), \quad k = 0, 1, \dots \quad (9.57)$$

This can be done if we let the map  $\mathbf{M}$  be defined as

$$\mathbf{M}(\mathbf{x}) = \phi_{N+1,\mathbf{x}} \mathbf{K}_N(\mathbf{x}), \quad (9.58)$$

where

$$\begin{aligned} \mathbf{K}_n(\mathbf{x}) &= \mathbf{D}_{n,\mathbf{x}}^* \phi_{n,\mathbf{x}} \mathbf{K}_{n-1}(\mathbf{x}) + \left( \hat{\mathbf{f}}_n^{\text{in}} - \hat{\mathbf{f}}_n^{\text{out}} \right) \Delta t_n, \quad n \geq 1, \\ \mathbf{K}_0(\mathbf{x}) &= \mathbf{x}. \end{aligned} \quad (9.59)$$

In (9.59)  $\mathbf{D}_{n,\mathbf{x}}^*$  is the random saltation matrix associated with the  $n^{\text{th}}$  switch, given by (9.42),  $\phi_{n,\mathbf{x}}$  is the Jacobian associated with the  $n^{\text{th}}$  smooth portion of the reference trajectory and  $\hat{\mathbf{f}}_n^{\text{in}}$  and  $\hat{\mathbf{f}}_n^{\text{out}}$  are respectively the values of the incoming and outgoing vector fields of the reference trajectory at the  $n^{\text{th}}$  crossing. Note that, when  $\Delta t_i = 0$ , for all  $i$ , the map  $\mathbf{M}$  simplifies to the standard mapping for deterministic trajectories with  $N$  boundary crossings as described in [13, 16]. A schematic showing the iterative process of constructing the map  $\mathbf{M}$  is given in Figure 9.3.

The map  $\mathbf{M}$  gives a first-order approximation of the evolution of the distribution about a trajectory that crosses  $N$  noisy discontinuity boundaries and so will only give useful results in the case where  $\hat{\mathbf{f}}_n^{\text{in}} \neq \hat{\mathbf{f}}_n^{\text{out}}$ , otherwise  $\hat{\mathbf{f}}_n^{\text{in}} - \hat{\mathbf{f}}_n^{\text{out}} = 0$  and  $\mathbf{D}_{n,\mathbf{x}}^*$  reduces to the identity matrix. For the mapping  $\mathbf{M}$  to have a valid construction we must have that the stochastic processes  $P_n(t)$  describing the stochastic components of the discontinuity boundaries

1. are at least once differentiable,
2. are of small amplitude,
3. are mean reverting,
4. have mean 0.

Furthermore, we require all crossings to be transversal and our approximation assumes that the addition of noise does not change the number of times a boundary is crossed by a trajectory.

## 9.3 Introducing Noise

### 9.3.1 A Zero-Mean Mean-Reverting Process

In this section we will derive an example of a stochastic process  $P(t)$  that meets our differentiability and mean reversion requirements to be used in the numerical examples considered in Section 9.4. In particular, we will consider the mean-reverting Gaussian process  $P(t)$ , with long term mean 0, given by

$$V(t) = \frac{dP}{dt} = -cP + \Sigma\xi(t), \quad P(0) = P_0, \quad (9.60)$$

where  $\xi(t)$  is the Ornstein-Uhlenbeck Itô Process [31] given by

$$d\xi(t) = -\theta\xi(t)dt + \sigma dW_t, \quad \xi(0) = \xi_0. \quad (9.61)$$

This gives that

$$\xi(t) = e^{-\theta t}\xi_0 + \sigma \int_0^t e^{\theta(s-t)} dW_s, \quad (9.62)$$

$$\xi(t) \sim N\left(e^{-\theta t}\xi_0, \frac{\sigma^2(1 - e^{-2\theta t})}{2\theta}\right) = N(\mu_\xi(t), \sigma_\xi^2(t)), \quad (9.63)$$

while

$$P(t) = \begin{cases} \mu_P(t) + \frac{\sigma\Sigma}{c-\theta} \int_0^t e^{\theta(s-t)} - e^{c(s-t)} dW_s & \text{if } c \neq \theta, \\ \mu_P(t) + \sigma\Sigma \int_0^t e^{\theta(s-t)}(t-s) dW_s & \text{if } c = \theta, \end{cases} \quad (9.64)$$

$$P(t) \sim N(\mu_P(t), \sigma_P^2(t)), \quad (9.65)$$

where

$$\mu_P(t) = \begin{cases} e^{-ct} P_0 + (e^{-\theta t} - e^{-ct}) \frac{\Sigma \xi_0}{c-\theta} & \text{if } c \neq \theta, \\ e^{-ct} (P_0 + \Sigma t \xi_0) & \text{if } c = \theta, \end{cases} \quad (9.66)$$

and

$$\sigma_P^2(t) = \begin{cases} \left(\frac{\sigma\Sigma}{c-\theta}\right)^2 \left[ \frac{1-e^{-2\theta t}}{2\theta} + \frac{1-e^{-2ct}}{2c} - \frac{2(1-e^{-(\theta+c)t})}{\theta+c} \right] & \text{if } c \neq \theta, \\ (\sigma\Sigma)^2 \left[ \frac{1}{4\theta^3} - e^{-2\theta t} \left( \frac{t^2}{2\theta} + \frac{t}{2\theta^2} + \frac{1}{4\theta^3} \right) \right] & \text{if } c = \theta. \end{cases} \quad (9.67)$$

Finally

$$V(t) = \begin{cases} \mu_V(t) + \frac{\sigma\Sigma}{\theta-c} \int_0^t \theta e^{\theta(s-t)} - c e^{c(s-t)} dW_s & \text{if } c \neq \theta, \\ \mu_V(t) + \sigma\Sigma \int_0^t \theta e^{\theta(s-t)} (s-t + \frac{1}{\theta}) dW_s & \text{if } c = \theta, \end{cases} \quad (9.68)$$

$$V(t) \sim N(\mu_V(t), \sigma_V^2(t)), \quad (9.69)$$

where

$$\mu_V(t) = \Sigma \mu_\xi(t) - c \mu_P(t), \quad (9.70)$$

and

$$\sigma_V^2(t) = \begin{cases} \left(\frac{\sigma\Sigma}{\theta-c}\right)^2 \left[ \theta^2 \left( \frac{1-e^{-2\theta t}}{2\theta} \right) + c^2 \left( \frac{1-e^{-2ct}}{2c} \right) - 2\theta c \left( \frac{1-e^{-(\theta+c)t}}{\theta+c} \right) \right] & \text{if } c \neq \theta, \\ (\sigma\Sigma)^2 \left( \frac{1}{4\theta} - e^{-2\theta t} \left( \frac{t^2\theta}{2} - \frac{t}{2} + \frac{1}{4\theta} \right) \right) & \text{if } c = \theta. \end{cases} \quad (9.71)$$

The joint distribution of  $P(t)$  and  $V(t)$  is a bivariate Gaussian distribution with

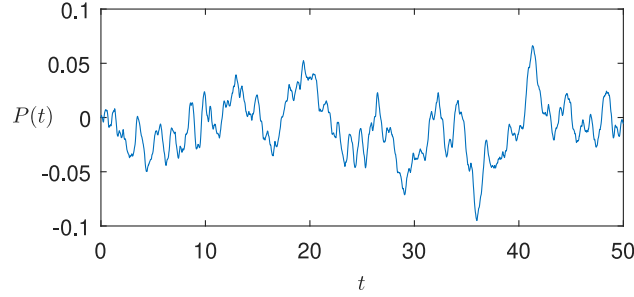


**Figure 9.4:** Sample time series for  $P(t)$ , the corresponding velocity process is shown in Figure 9.5.

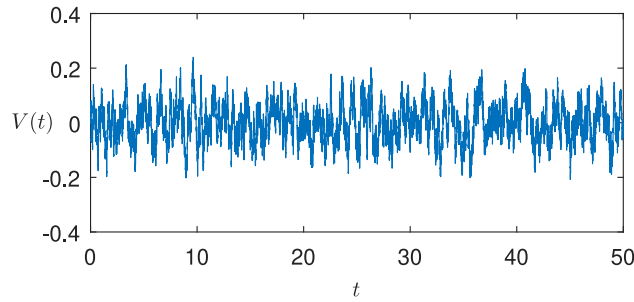


**Figure 9.5:** Sample time series for  $V(t)$ , the corresponding position process is shown in Figure 9.4.

mean  $\mu_{PV}(t) = (\mu_P(t), \mu_v(t))^T$  and covariance matrix  $\Sigma_{PV}$  given by

$$\Sigma_{PV} = \begin{pmatrix} \sigma_P^2(t) & Cov(P(t)V(t)) \\ Cov(P(t)V(t)) & \sigma_V^2(t) \end{pmatrix} = \begin{pmatrix} \sigma_P^2(t) & \sigma_{PV}(t) \\ \sigma_{PV}(t) & \sigma_V^2(t) \end{pmatrix}, \quad (9.72)$$

where

$$\sigma_{PV}(t) = \begin{cases} -c\sigma_P^2(t) + \frac{(\sigma\Sigma)^2 (c - \theta - (c + \theta)e^{-2\theta t} + 2\theta e^{-(c+\theta)t})}{2\theta(c^2 - \theta^2)} & \text{if } c \neq \theta, \\ -\theta\sigma_P^2(t) + \frac{(\sigma\Sigma)^2}{2\theta} \left( \frac{1 - e^{-2\theta t}}{2\theta} - te^{-2\theta t} \right) & \text{if } c = \theta. \end{cases} \quad (9.73)$$

The stochastic position process  $P(t)$  derived in this section has several useful properties. First, since the process is mean reverting with long-term mean 0, applying the process  $P$  to a discontinuity boundary in a piecewise-smooth system will not cause the position of the boundary to drift over time. We also note that the position process

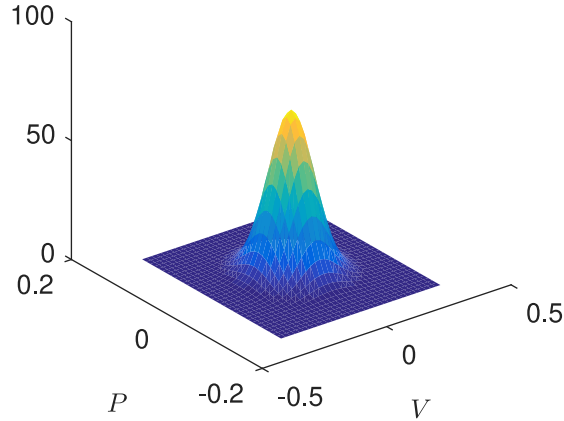


**Figure 9.6:** Sample joint Distribution of  $P(t)$  and  $V(t)$ .

has a well defined corresponding velocity process  $V(t)$ , allowing us to construct both the random saltation matrix  $\mathbf{D}^*(\hat{\mathbf{x}}_{\text{in}})$  and the first-order estimate of the random variable  $\Delta t_{\text{ref}}$  associated with a given boundary crossing. Finally, provided the time  $t$  between consecutive boundary crossings is large compared to the frequency of the stochastic oscillations, i.e. assuming  $e^{-ct} \approx e^{-\theta t} \approx 0$ , the position and velocity of the boundary at a crossing can be well estimated as independent of the position and velocity at the previous crossing. This is very useful when using this approach to analyse the effect of noise on periodic orbits, see Section 9.4 for examples. Sample time series for  $P(t)$  and  $V(t)$  are shown in Figures 9.4 and 9.5, respectively.

### 9.3.2 The Distribution of $\Delta t_{\text{ref}}$

From (9.21) in Section 9.2.2, we see that the approximate distribution  $f_{\Delta}$  of  $\Delta t_{\text{ref}}$  is given by the ratio of the two components of a bivariate Gaussian distribution with non-zero correlation such as the one shown in Figure 9.6. Following the results of Cedilnik *et al.* [32] we find that, when  $P_0 = \xi_0 = 0$ , the distribution of  $\Delta t_{\text{ref}}$  is given by

$$f_{\Delta}(\delta) = \frac{\sigma_V \sigma_P \sqrt{1 - \rho^2} \left[ e^{-\alpha/2} + \sqrt{2\pi} \beta \xi(\beta) e^{(\beta^2 - \alpha)/2} \right]}{\pi(\sigma_V^2 \delta^2 + 2\sigma_{PV} \delta + \sigma_P^2)}, \quad (9.74)$$

evaluated at  $\hat{t}_{\text{ref}}$ , where

$$\rho = \frac{\sigma_{PV}}{\sigma_P \sigma_V}, \quad (9.75)$$

$$\alpha = \left( \frac{\mu_{V'}}{\sigma_V} \right)^2 \left( \frac{1}{1 - \rho^2} \right), \quad (9.76)$$

$$\beta = \frac{\rho \frac{\mu_{V'} \delta}{\sigma_V} + \frac{\mu_{V'} \sigma_P}{\sigma_V^2}}{\sqrt{1 - \rho^2} \sqrt{\delta^2 - 2\rho \frac{\sigma_P}{\sigma_V} \delta + \left( \frac{\sigma_P}{\sigma_V} \right)^2}}, \quad (9.77)$$

$$\xi(\beta) = \frac{1}{2} \operatorname{erf} \left( \frac{\beta}{\sqrt{2}} \right) \quad (9.78)$$

and

$$\mu_{V'} = \hat{h}(\mathbf{x}_{\text{in}}) \hat{\mathbf{f}}_{\text{in}} - \hat{v}(\hat{t}_{\text{ref}}). \quad (9.79)$$

## 9.4 Examples

In this section we present some illustrative examples, comparing our linearisation approach to the results of numerical simulation of the sample systems. In all cases our numerical simulations use the analytic solution to the simple piecewise-smooth ODEs considered, an Euler-Maruyama scheme with fixed timestep [33] for the integration of the stochastic process  $P(t)$  local to the boundary and linear interpolation to find the boundary-crossing time lying between two consecutive timesteps.

First, in Section 9.4.1 show how the linearisation given in (9.47) performs in a two-dimensional piecewise-smooth system where the vector fields on either side of the discontinuity boundary are nonlinear. Next, in Section 9.4.2 we look at a simple two-dimensional piecewise-linear system, showing how our method can accurately predict basin of attraction escapes close to bifurcation. Finally, in Section 9.4.3 we consider the Chua circuit, a real-world example in three dimensions. In this example we focus on the effect of noise on periodic attractors in the Chua circuit. In particular, we use the methods described in Section 9.2.5 to estimate the noise

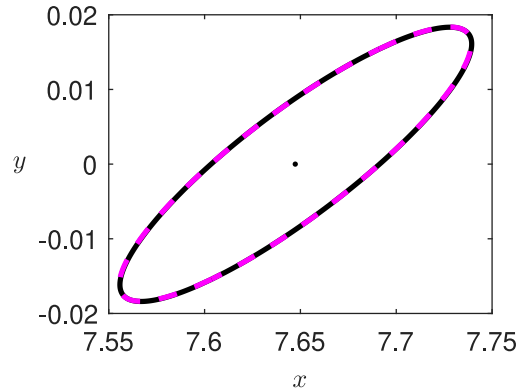


**Figure 9.7:** The image of the perimeter of the circle of radius 0.01 about  $\hat{\mathbf{x}}_0^{\text{ref}}$  (solid black) after time  $T$ , compared to the linear approximation given by (9.88) (dashed magenta). The image  $\hat{\mathbf{x}}_T^{\text{ref}}$  of  $\hat{\mathbf{x}}_0^{\text{ref}}$  is indicated by the black dot.

amplitude required for trajectories to be pushed out of periodic behaviour that is stable in the corresponding deterministic system and to merge coexisting periodic attractors.

### 9.4.1 A Two Region Piecewise Smooth System

As an initial example we will consider the piecewise-smooth system in the plane given by

$$\dot{\mathbf{x}} = \begin{cases} \mathbf{f}_1(\mathbf{x}) = (1, \cos(x))^T, & \mathbf{x} \in S^-, \\ \mathbf{f}_2(\mathbf{x}) = (y^2, -1)^T, & \mathbf{x} \in S^+, \end{cases} \quad (9.80)$$

where  $\mathbf{x} = (x, y)^T$  is the state space variable and  $\mathbf{f}_1$  and  $\mathbf{f}_2$  are the vector fields in  $S^-$  and  $S^+$ , respectively. The two regions

$$S^- = \{\mathbf{x}: x < 0\}, \quad S^+ = \{\mathbf{x}: x \geq 0\} \quad (9.81)$$

are separated by the discontinuity boundary

$$\hat{\mathcal{D}} = \{\mathbf{x}: \hat{h}(\mathbf{x}) = 0\}, \quad (9.82)$$

where  $\hat{h}(\mathbf{x}) = x$ . Let us now take the trajectory with starting point  $\hat{\mathbf{x}}_0^{\text{ref}} = (-1, 2)^T$  as our reference trajectory. This trajectory crosses the discontinuity boundary  $\hat{\mathcal{D}}$  after time  $\hat{t}_{\text{ref}} = 1$  at  $\hat{\mathbf{x}}_{\text{in}} = (0, 2 + \sin(1))^T = (0, \hat{y}_{\text{in}})^T$ . The incoming vector field is given by  $\hat{\mathbf{f}}_{\text{in}} = \mathbf{f}_1(\hat{\mathbf{x}}_{\text{in}}) = (1, 1)^T$  and the outgoing vector field is given by  $\hat{\mathbf{f}}_{\text{out}} = \mathbf{f}_2(\hat{\mathbf{x}}_{\text{in}}) = ((\hat{y}_{\text{in}})^2, -1)^T$ . We will consider this trajectory after time  $T = \hat{t}_{\text{ref}} + \hat{y}_{\text{in}} = 1 + \hat{y}_{\text{in}}$  and note that

$$\hat{\mathbf{x}}_T^{\text{ref}} = \phi(\hat{\mathbf{x}}_0^{\text{ref}}, T) = \phi_2(\phi_1(\hat{\mathbf{x}}_0^{\text{ref}}, 1), \hat{y}_{\text{in}}) = \left( \frac{\hat{y}_{\text{in}}^3}{3}, 0 \right)^T, \quad (9.83)$$

where  $\hat{\mathbf{f}}_{\text{end}} = \mathbf{f}_2(\hat{\mathbf{x}}_T^{\text{ref}}) = (0, -1)^T$ . Our choice of  $T > \hat{t}_{\text{ref}}$  here is arbitrary, and we have chosen  $T = \hat{t}_{\text{ref}} + \hat{y}_{\text{in}}$  for clean calculations. Using (9.15), we can now construct the deterministic saltation matrix associated with this crossing as

$$\mathbf{D}_{\mathbf{x}}(\hat{\mathbf{x}}_{\text{in}}) = \mathbf{I} + \frac{(\mathbf{f}_{\text{out}} - \mathbf{f}_{\text{in}})\hat{h}_{\mathbf{x}}}{\hat{h}_{\mathbf{x}}\mathbf{f}_{\text{in}}} = \begin{pmatrix} \hat{y}_{\text{in}}^2 & 0 \\ -2 & 1 \end{pmatrix}, \quad (9.84)$$

where  $\hat{h}_{\mathbf{x}} = (1 \ 0)$ . From (9.4) we find that

$$\phi_{1,\mathbf{x}}(\hat{\mathbf{x}}_0^{\text{ref}}, 1) = \begin{pmatrix} 1 & 0 \\ 1 - \cos(1) & 1 \end{pmatrix} \quad (9.85)$$

and

$$\phi_{2,\mathbf{x}}(\hat{\mathbf{x}}_{\text{in}}, \hat{y}_{\text{in}}) = \begin{pmatrix} 1 & \hat{y}_{\text{in}}^2 \\ 0 & 1 \end{pmatrix}, \quad (9.86)$$

giving

$$\phi_{\mathbf{x}}(\hat{\mathbf{x}}_0^{\text{ref}}, T) = \phi_{2,\mathbf{x}}(\hat{\mathbf{x}}_{\text{in}}, \hat{y}_{\text{in}})\mathbf{D}_{\mathbf{x}}(\hat{\mathbf{x}}_{\text{in}})\phi_{1,\mathbf{x}}(\hat{\mathbf{x}}_0^{\text{ref}}, 1) = \begin{pmatrix} -\cos(1)\hat{y}_{\text{in}}^2 & \hat{y}_{\text{in}}^2 \\ -(\cos(1) + 1) & 1 \end{pmatrix}. \quad (9.87)$$

In a deterministic system, we can now estimate the position a trajectory with starting point  $\hat{\mathbf{x}}_0 = \hat{\mathbf{x}}_0^{\text{ref}} + \epsilon$ ,  $|\epsilon| \lll 1$ , in a small neighbourhood of  $\hat{\mathbf{x}}_0^{\text{ref}}$ , after time  $T$  by

$$\phi(\hat{\mathbf{x}}_0, T) \approx \hat{\mathbf{x}}_T^{\text{ref}} + \phi_{\mathbf{x}}(\hat{\mathbf{x}}_0^{\text{ref}}, T)\epsilon. \quad (9.88)$$

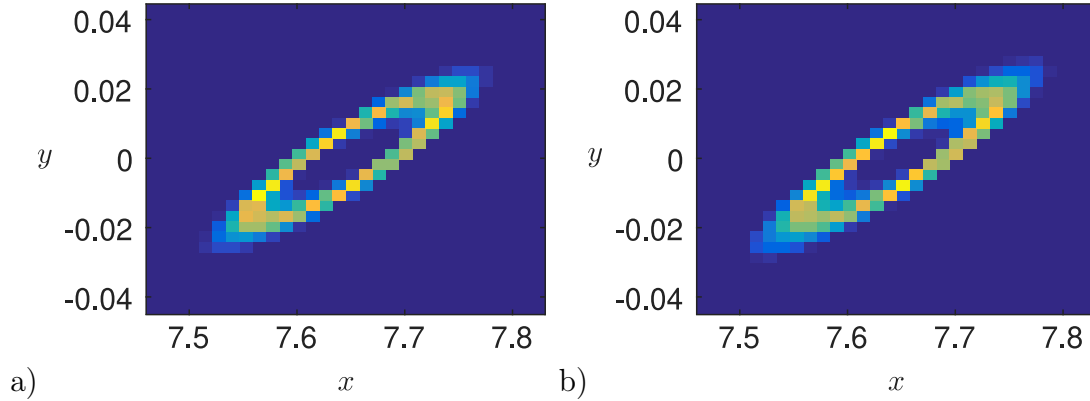


**Figure 9.8:** The distribution of the image of 1,000 linearly spaced points on the perimeter of the circle of radius 0.01 about  $\hat{\mathbf{x}}_0^{\text{ref}}$  after time  $T$ , given by a) numerical simulation of the full nonlinear stochastic system using an Euler-Maruyama Scheme with fixed timestep  $dt = 5 \times 10^{-7}$ , and b) the approximation (9.90). Here  $\theta = 20$ ,  $c = 45$ ,  $\sigma = 0.5$  and  $\Sigma = 1.4$ . This gives that the long term standard deviation of  $P$  and  $V$  are  $\sigma_P^* \approx 2.046 \times 10^{-3}$  and  $\sigma_V^* \approx 6.139 \times 10^{-2}$ , respectively while the normal velocity to the discontinuity boundary in the deterministic case is  $\hat{h}_{\mathbf{x}} \hat{\mathbf{f}}_{\text{in}} = 1$ .

An example of this can be seen in Figure 9.7.

Suppose now that the boundary  $\hat{\mathcal{D}}$  given in (9.82) is replaced by the stochastically varying boundary  $\mathcal{D}$  given by

$$\mathcal{D} = \{\mathbf{x} : h(\mathbf{x}, t) = 0\}, \quad (9.89)$$

where  $h(\mathbf{x}, t) = x - P(t)$  and  $P(t)$  is the stochastic process given in Section 9.3.1. Referring to Section 9.2.3, we find that in this new noisy system

$$\phi(\hat{\mathbf{x}}_0, T) \approx \hat{\mathbf{x}}_T^{\text{ref}} + \phi_{\mathbf{x}}^*(\hat{\mathbf{x}}_0^{\text{ref}}, T)\epsilon + (\hat{\mathbf{f}}_{\text{in}} - \hat{\mathbf{f}}_{\text{out}})\Delta t_{\text{ref}}, \quad (9.90)$$

where  $\Delta t_{\text{ref}}$  is the random component of the time of flight to  $\mathcal{D}$  for the reference

trajectory, and

$$\begin{aligned}\phi_{\mathbf{x}}^*(\hat{\mathbf{x}}_0^{\text{ref}}, T) &= \phi_{2,\mathbf{x}}(\hat{\mathbf{x}}_{\text{in}}, \hat{y}_{\text{in}}) \mathbf{D}_{\mathbf{x}}^*(\hat{\mathbf{x}}_{\text{in}}) \phi_{1,\mathbf{x}}(\hat{\mathbf{x}}_0^{\text{ref}}, 1) \\ &= \frac{\phi_{2,\mathbf{x}}(\hat{\mathbf{x}}_{\text{in}}, \hat{y}_{\text{in}})}{1 - V^*} \begin{pmatrix} \hat{y}_{\text{in}}^2 - V^* & 0 \\ -2 & 1 - V^* \end{pmatrix} \phi_{1,\mathbf{x}}(\hat{\mathbf{x}}_0^{\text{ref}}, 1),\end{aligned}\quad (9.91)$$

where  $V^* = V(\hat{t}_{\text{ref}}|P(\hat{t}_{\text{ref}}))$  is the random velocity of the boundary at  $\hat{t}_{\text{ref}}$ . In Figure 9.8 we compare this estimate to simulation of the entire system. In both cases we consider a sample of 1000 trajectories for each initial condition. We clearly see that the approximation gives a good estimate of the distribution produced by the full simulation of the system. In particular, we have calculated the generalised 2-dimensional Kolmogorov-Smirnov test (K-S test) statistic, derived by Fasano and Franceschini [34], on the two samples to be  $D_{KS} \approx 0.016793$  using the MATLAB<sup>®</sup> routine `kstest2d.m` [35]. As with all forms of linearisation, the estimate becomes less accurate as the perturbations away from the reference trajectory increase. In other words, our method breaks down if either the initial neighbourhood of the reference trajectory or the amplitude of the noise becomes too large.

## 9.4.2 A Limit Cycle in a Piecewise-Linear System

In this section we will consider the effects of boundary noise on a periodic attractor. Consider the piecewise-linear system in the plane given by

$$\dot{\mathbf{x}} = \begin{cases} \mathbf{f}_1(\mathbf{x}) = \mathbf{A}_L \mathbf{x} + \mathbf{u}_L, & \mathbf{x} \in S^-, \\ \mathbf{f}_2(\mathbf{x}) = \mathbf{A}_R \mathbf{x} + \mathbf{u}_R, & \mathbf{x} \in S^+, \end{cases}\quad (9.92)$$

where  $\mathbf{x} = (x, y)^T$  is the state space variable and  $\mathbf{f}_1$  and  $\mathbf{f}_2$  are the vector fields in  $S^-$  and  $S^+$ , respectively. The two regions

$$S^- = \{\mathbf{x}: x < 0\}, \quad S^+ = \{\mathbf{x}: x \geq 0\}\quad (9.93)$$

are separated by the discontinuity boundary

$$\hat{\mathcal{D}} = \{\mathbf{x}: \hat{h}(\mathbf{x}) = 0\}, \quad (9.94)$$

where  $\hat{h}(\mathbf{x}) = x$ . We let

$$\mathbf{A}_L = \begin{pmatrix} 2\gamma & -1 \\ \gamma^2 + 1 & 0 \end{pmatrix}, \quad \mathbf{u}_L = \begin{pmatrix} 0 \\ \gamma^2 + 1 \end{pmatrix} \quad (9.95)$$

and

$$\mathbf{A}_R = \begin{pmatrix} T & -1 \\ D & 0 \end{pmatrix}, \quad \mathbf{u}_R = \begin{pmatrix} 0 \\ a \end{pmatrix}. \quad (9.96)$$

It has been shown by Freire *et al.* [36] that when  $a > 0$  and  $T < 0$ , a stable limit cycle bifurcates as  $\gamma$  increases through 0 in a *focus-center-limit cycle bifurcation*. This limit cycle exists provided  $\gamma$  is sufficiently small.

In particular, when  $D < 0$  this system has a repellor spiral equilibrium in the left-half plane at  $\mathbf{x}_L^{eq} = (-1, -2\gamma)^T$  and a saddle in the right half plane at  $\mathbf{x}_R^{eq} = (-a/D, -Ta/D)^T$ . In this case the stable limit cycle surrounds the repellor spiral in the left-half plane and is bounded by the stable and unstable manifolds of the saddle in the right-half plane. In fact the stable manifold of the saddle at  $\mathbf{x}_R^{eq}$  gives the boundary of the basin of attraction of the stable limit cycle, as shown for  $T = D = -1$ ,  $a = 1$  and  $\gamma = 7 \times 10^{-2}$  in Figure 9.9. For some  $\gamma_c > 0$  this stable limit cycle is destroyed in a homoclinic bifurcation.

Now, let  $\phi_L$  and  $\phi_R$  be the solutions to (9.92) in  $S^-$  and  $S^+$ , respectively. Using the methods described in Section 9.2.1, we can calculate the *monodromy matrix*,  $\mathbf{M}$ , associated with the periodic solution  $\bar{\mathbf{x}}(t)$  with period  $\tau$ , when it exists. Taking an initial condition  $\mathbf{x}_0^{\text{ref}} \in S^-$ , we find

$$\mathbf{M} = \phi_{L,\mathbf{x}}(\hat{\mathbf{x}}_2, \tau - \hat{t}_2 - \hat{t}_1) \mathbf{D}_{2,\mathbf{x}}(\hat{\mathbf{x}}_2) \phi_{R,\mathbf{x}}(\hat{\mathbf{x}}_1, \hat{t}_2) \mathbf{D}_{1,\mathbf{x}}(\hat{\mathbf{x}}_1) \phi_{L,\mathbf{x}}(\mathbf{x}_0^{\text{ref}}, \hat{t}_1), \quad (9.97)$$

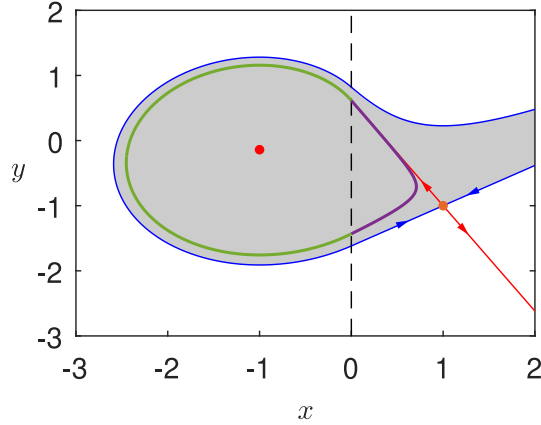


**Figure 9.9:** Stable limit cycle shown in green (on  $S^-$ ) and purple (on  $S^+$ ) for the system given by (9.92)-(9.96) with  $T = D = -1$ ,  $a = 1$  and  $\gamma = 7 \times 10^{-2}$ . The stable and unstable manifolds of the saddle are shown in blue and red respectively and the basin of attraction of the limit cycle is shaded grey.

where  $\phi_L(\mathbf{x}_0^{\text{ref}}, \hat{t}_1) = \hat{\mathbf{x}}_1 = (0, y_1)^T$ ,  $\phi_R(\hat{\mathbf{x}}_1, \hat{t}_2) = \hat{\mathbf{x}}_2 = (0, y_2)^T$  and  $\hat{h}(\hat{\mathbf{x}}_1) = \hat{h}(\hat{\mathbf{x}}_2) = 0$ .

The saltation matrices are given by

$$\mathbf{D}_{1,\mathbf{x}} = \begin{pmatrix} 1 & 0 \\ \frac{\gamma^2+1-a}{y_1} & 1 \end{pmatrix} \text{ and } \mathbf{D}_{2,\mathbf{x}} = \begin{pmatrix} 1 & 0 \\ \frac{a-(\gamma^2+1)}{y_2} & 1 \end{pmatrix}, \quad (9.98)$$

and the fundamental solution matrices are given by

$$\phi_{L,\mathbf{x}}(t) = e^{\gamma t} \begin{pmatrix} \cos(t) + \gamma \sin(t) & -\sin(t) \\ (1 + \gamma^2) \sin(t) & \cos(t) - \gamma \sin(t) \end{pmatrix} \quad (9.99)$$

and

$$\phi_{R,\mathbf{x}}(t) = \frac{1}{\sqrt{\Delta}} \begin{pmatrix} \lambda_1 e^{\lambda_1 t} - \lambda_2 e^{\lambda_2 t} & e^{\lambda_2 t} - e^{\lambda_1 t} \\ D(e^{\lambda_1 t} - e^{\lambda_2 t}) & \lambda_1 e^{\lambda_2 t} - \lambda_2 e^{\lambda_1 t} \end{pmatrix}, \quad (9.100)$$

where  $\Delta = T^2 - 4D$  and  $\lambda_{1,2} = \frac{1}{2}(T \pm \sqrt{\Delta})$ .

The eigenvalues of the monodromy matrix  $\mathbf{M}$  are known as the *characteristic multipliers* or *Floquet multipliers*  $\rho_i$  of the periodic orbit. The multiplier associated with perturbations along the periodic solution is always unity, which we will label  $\rho_1$ . The value of the remaining multipliers, or multiplier in this case since the system under

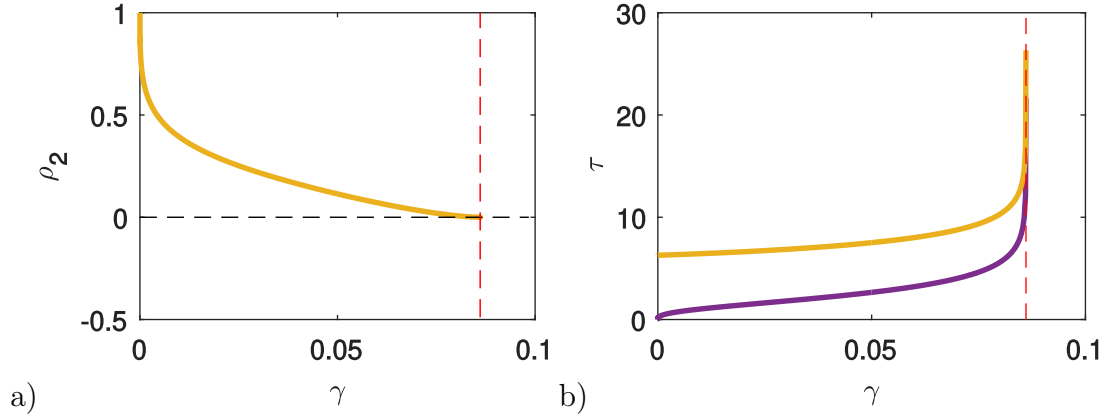


**Figure 9.10:** a) The characteristic multiplier  $\rho_2$  and b) the period of the limit cycle  $\tau$  in the system given by (9.92)-(9.96) with  $T = D = -1$  and  $a = 1$  shown in yellow. The dashed red line indicates the value of  $\gamma_c$ , the value of  $\gamma$  for which the stable limit cycle is destroyed in a homoclinic connection. The purple line in b) indicates  $t_R$  the time spent by the orbit in  $S^+$  each period.

consideration is 2-dimensional, determines the local stability of the periodic orbit. In particular, if the remaining multipliers have magnitude less than unity the periodic orbit under consideration is stable.

Alternatively, choosing a Poincaré section  $\mathcal{P}$  defined by  $g_{\mathcal{P}}(\mathbf{x}) = 0$  and containing  $\mathbf{x}_0^{\text{ref}}$ , one can examine the eigenvalues of the matrix

$$\mathbf{M}_{\mathcal{P},\mathbf{x}}(\mathbf{x}_0^{\text{ref}}) = \left( I - \frac{\mathbf{f}_0^{\text{ref}} g_{\mathcal{P},\mathbf{x}}(\mathbf{x}_{\mathcal{P}})}{g_{\mathcal{P},\mathbf{x}}(\mathbf{x}_{\mathcal{P}}) \mathbf{f}_0^{\text{ref}}} \right) \mathbf{M}, \quad (9.101)$$

where  $\mathbf{f}_0^{\text{ref}} = \mathbf{F}(\mathbf{x}_0^{\text{ref}})$ . The matrix  $\mathbf{M}_{\mathcal{P},\mathbf{x}}(\mathbf{x}_0^{\text{ref}})$  has a zero eigenvalue  $\nu_1$  corresponding to  $\rho_1$ , and the periodic solution is stable if the other eigenvalue  $\nu_2$  has magnitude less than 1. For example, choosing  $\mathbf{x}_0^{\text{ref}} = (x_0^{\text{ref}}, y_0^{\text{ref}})^T \in S^-$  such that  $\mathbf{f}_0^{\text{ref}} = \mathbf{f}_1(\mathbf{x}_0^{\text{ref}}) = \mathbf{A}_L \mathbf{x}_0^{\text{ref}} + \mathbf{u}_L = (0 \ f)^T$ , for  $f \in \mathbb{R}$ , i.e. such that  $2\gamma x_0^{\text{ref}} = y_0^{\text{ref}}$  and

$$g_{\mathcal{P}}(\mathbf{x}) = g_{\mathcal{P}}((x, y)) = y - y_0^{\text{ref}}, \quad (9.102)$$

we find that

$$\mathbf{P}_{\mathcal{P}} := \left( I - \frac{\mathbf{f}_0^{\text{ref}} g_{\mathcal{P},\mathbf{x}}(\mathbf{x}_{\mathcal{P}})}{g_{\mathcal{P},\mathbf{x}}(\mathbf{x}_{\mathcal{P}}) \mathbf{f}_0^{\text{ref}}} \right) = \begin{pmatrix} 1 & 0 \\ 0 & 0 \end{pmatrix}. \quad (9.103)$$

For simplicity, without loss of generality, when considering the stable limit cycle of system (9.92) we will always use the initial condition  $\mathbf{x}_0^{\text{ref}} = (x_0^{\text{ref}}, y_0^{\text{ref}})^T \in S^-$ , such that  $2\gamma x_0^{\text{ref}} = y_0^{\text{ref}}$  and the associated Poincaré section given by (9.102).

In Figure 9.10a) we plot the value of the characteristic multiplier  $\rho_2$  for  $0 < \gamma < \gamma_c$ . We see that  $\rho_2$  decreases from 1 as  $\gamma$  increases, indicating that the periodic orbit is stable for all values of  $\gamma$  in this range. Figure 9.10b) shows how the period of the periodic orbit evolves as we increase  $\gamma$ . When  $\gamma = 0$  the equilibrium in the left-half plane  $\mathbf{x}_L^{\text{eq}}$ , is a center. As  $\gamma$  increases through zero the stable periodic orbit is born in a focus-center-limit cycle bifurcation from the most external periodic orbit of the center. The center in question is tangent to the discontinuity surface at the origin which has period  $\tau = 2\pi$ . As  $\gamma$  increases towards  $\gamma_c$  the portion of the periodic orbit in the right half-plane  $S^+$  approaches the stable and unstable manifolds of the saddle  $\mathbf{x}_R^{\text{eq}}$  and the period  $\tau$  approaches infinity.

We are interested in studying the system (9.92)-(9.96) when there is uncertainty associated with the position of the discontinuity surface. In other words, we consider the system (9.92)-(9.96) when the boundary  $\hat{\mathcal{D}}$  given in (9.94) is replaced by the stochastically varying boundary  $\mathcal{D}$  given by

$$\mathcal{D} = \{\mathbf{x}: h(\mathbf{x}, t) = 0\}, \quad (9.104)$$

where  $h(\mathbf{x}, t) = x - P(t)$  and  $P(t)$  is the stochastic process given in Section 9.3.1.

In particular, let us consider the effect of noise on the family of stable periodic orbits born in the focus-center-focus bifurcation described above. Using the methods described in Section 9.2.2, we can calculate the *random monodromy matrix*,  $\widetilde{\mathbf{M}}^*$ , associated with the deterministic periodic solution  $\bar{\mathbf{x}}(t)$  with period  $\tau$  when it exists. First, we extend our state space to include the random variables  $\Delta t_1$  and  $\Delta t_2$  associated with the differences in the time of crossing of the boundary associated with the two crossings each period. Now, we once again take an initial condition

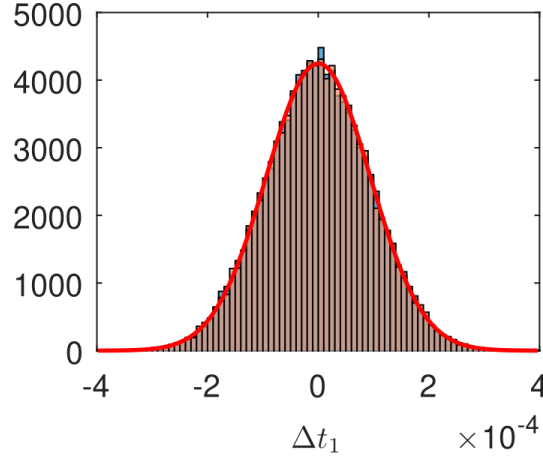


**Figure 9.11:** This figure shows the distribution of  $\Delta t_1$ . The blue histogram is calculated by numerical simulations of the full system, the red histogram is calculated from a random sample of the distribution given in (9.107) and the curve is the analytic form of the distribution given in (9.74). Here  $T = D = -1$ ,  $a = 1$ ,  $\gamma = 0.05$ ,  $c = \theta = 20$ ,  $\sigma = 0.2$ ,  $\Sigma = 0.1$  and the sample size  $N = 50,000$ .

$\mathbf{x}_0^{\text{ref}} \in S^-$  and find

$$\widetilde{\mathbf{M}}^* = \tilde{\phi}_{L,\mathbf{x}}(\hat{\mathbf{x}}_2, \tau - \hat{t}_2 - \hat{t}_1) \widetilde{\mathbf{D}}_{2,\mathbf{x}}^*(\hat{\mathbf{x}}_2) \tilde{\phi}_{R,\mathbf{x}}(\hat{\mathbf{x}}_1, \hat{t}_2) \widetilde{\mathbf{D}}_{1,\mathbf{x}}^*(\hat{\mathbf{x}}_1) \tilde{\phi}_{L,\mathbf{x}}(\hat{\mathbf{x}}_0^{\text{ref}}, \hat{t}_1). \quad (9.105)$$

Using this, we find that orbits starting at  $\mathbf{x}_0$  in the neighbourhood of  $\hat{\mathbf{x}}_0^{\text{ref}}$  will have deviations given by

$$\begin{aligned} & \phi_{L,\mathbf{x}}(\tau - \hat{t}_2 - \hat{t}_1) \mathbf{D}_{2,\mathbf{x}}^*(\hat{\mathbf{x}}_2) \phi_{R,\mathbf{x}}(\hat{t}_2) \mathbf{D}_{1,\mathbf{x}}^*(\hat{\mathbf{x}}_1) \phi_{L,\mathbf{x}}(\hat{t}_1) (\mathbf{x}_0 - \hat{\mathbf{x}}_0^{\text{ref}}) \\ & + \phi_{L,\mathbf{x}}(\tau - \hat{t}_2 - \hat{t}_1) \mathbf{D}_{2,\mathbf{x}}^*(\hat{\mathbf{x}}_2) \phi_{R,\mathbf{x}}(\hat{t}_2) (0, \gamma^2 + 1 - a)^T \Delta t_1 \\ & + \phi_{L,\mathbf{x}}(\tau - \hat{t}_2 - \hat{t}_1) (0, a - (\gamma^2 + 1))^T \Delta t_2 \end{aligned} \quad (9.106)$$

after one orbit. We can also consider the associated Poincaré mapping on the surface  $\mathcal{P}$  given by (9.102), premultiplying (9.106) by the matrix  $\mathbf{P}_{\mathcal{P}}$  to project the deviations onto  $\mathcal{P}$ . This allows for easier geometric interpretation of the distribution of deviations about the deterministic periodic orbit.

Referring to (9.21), we can approximate the random variables  $\Delta t_1$  and  $\Delta t_2$  to first

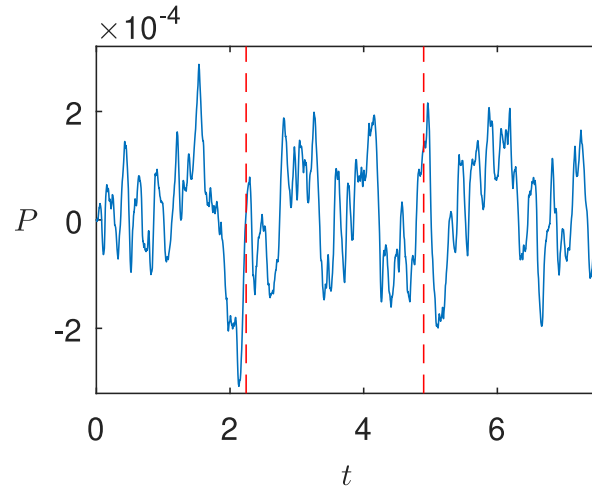


**Figure 9.12:** This figure shows the sample path of the position process  $P$  over one period of the stable limit cycle of the deterministic piecewise linear system. Here  $T = D = -1$ ,  $a = 1$ ,  $\gamma = 0.05$ ,  $c = \theta = 20$ ,  $\sigma = 0.2$ ,  $\Sigma = 0.1$ . The red dashed lines indicate the deterministic crossing times  $\hat{t}_1$  and  $\hat{t}_2$ .

order by

$$\Delta t_i = -\frac{P(\hat{t}_i)}{\hat{y}_i + V(\hat{t}_i|P(\hat{t}_i))} \quad \text{for } i = 1, 2. \quad (9.107)$$

When the noise amplitude is not too large these give very good approximations to the actual distributions. For example, it can be seen in Figure 9.11 that this is a good approximation to the actual distribution of  $\Delta t_1$  in the case where  $T = D = -1$ ,  $a = 1$ ,  $\gamma = 0.05$ ,  $c = \theta = 20$ ,  $\sigma = 0.2$ , and  $\Sigma = 0.1$ . In Figure 9.12 we plot a sample path of  $P$ , the  $x$ -coordinate of the boundary given these parameter values. We note that for the value of  $c = \theta$  chosen,  $e^{-ct_m} \approx 0$ , where  $t_m$  is the minimum time between boundary crossings in the deterministic system. This means that during linearisation we can treat boundary positions at consecutive crossings as independent. We can see this visually by observing the large number of full oscillations of  $P$  between subsequent crossing times in Figure 9.12.

In Figure 9.13 we plot the distribution of trajectories with initial condition  $\mathbf{x}_0^{\text{ref}}$ , after one deterministic period  $\tau$ . In Figure 9.13a) we show the results of numerical simulation of 100,000 individual trajectories and in Figure 9.13b) we show the linear approximation given in (9.106). We again use an Euler-Maruyama scheme with a

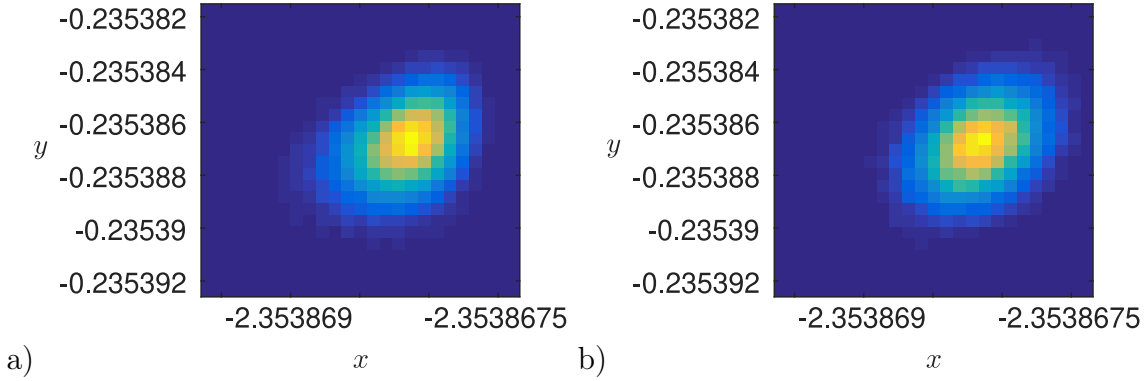


**Figure 9.13:** The distribution of the end points of 100,000 trajectories with starting point  $\mathbf{x}_0^{\text{ref}}$ , after one deterministic period  $\tau$ , given by a) numerical simulation using an Euler-Maruyama scheme with fixed timestep  $dt = 10^{-6}$  and b) approximated using (9.106). Here  $T = D = -1$ ,  $a = 1$ ,  $\gamma = 0.05$ ,  $c = \theta = 20$ ,  $\sigma = 0.2$  and  $\Sigma = 0.1$ . This gives that the long term standard deviation of  $P$  and  $V$  are  $\sigma_P^* \approx 1.118 \times 10^{-4}$  and  $\sigma_V^* \approx 2.236 \times 10^{-3}$ , respectively.

fixed timestep for numerical simulation of the stochastic process  $P(t)$  local to the boundary and the analytic solution to the linear ODEs. We see good agreement between the numerical simulations and the approximations. We find that the 2-dimensional Kolmogorov-Smirnov test statistic calculated on the two samples is  $D_{KS} \approx 0.032279$ .

In Figure 9.14 we plot the distribution of the associated Poincaré mapping on the surface  $\mathcal{P}$  given by (9.102) in order to more easily compare our approximation with the numerical simulations. It is clear to see that there is good agreement between the two distributions which are centred around the deterministic value  $x_0^{\text{ref}}$ . In Figure 9.15 we plot the distribution after 100 periods and once again observe good agreement between the two distributions. We see that both the linearised distribution and the distribution in the full system appear to converge to invariant distributions. We note that in both Figure 9.14 and Figure 9.15 the linear approximation fails to capture some of the skewness displayed by the true distribution.

In Figure 9.16 we plot the proportion of trajectories with initial conditions  $\mathbf{x}_0 = \mathbf{x}_{SM} + (\epsilon, 0)^T$  on the Poincaré section given by (9.102), which escape the basin of

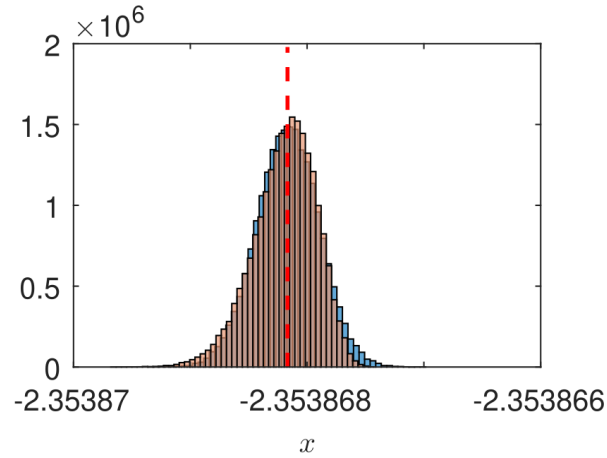


**Figure 9.14:** The distribution of the  $x$ -coordinates of 100,000 trajectories with starting point  $\mathbf{x}_0^{\text{ref}}$ , on their first return to the Poincaré section  $\mathcal{P}$ , given by numerical simulation using an Euler-Maruyama scheme with fixed timestep  $dt = 10^{-6}$  in red and approximated using (9.106) in blue. Here  $T = D = -1$ ,  $a = 1$ ,  $\gamma = 0.05$ ,  $c = \theta = 20$ ,  $\sigma = 0.2$  and  $\Sigma = 0.1$ . The value of  $x_0^{\text{ref}}$  is highlighted by the red dashed line. This gives that the long term standard deviation of  $P$  and  $V$  are  $\sigma_P^* \approx 1.118 \times 10^{-4}$  and  $\sigma_V^* \approx 2.236 \times 10^{-3}$ , respectively.

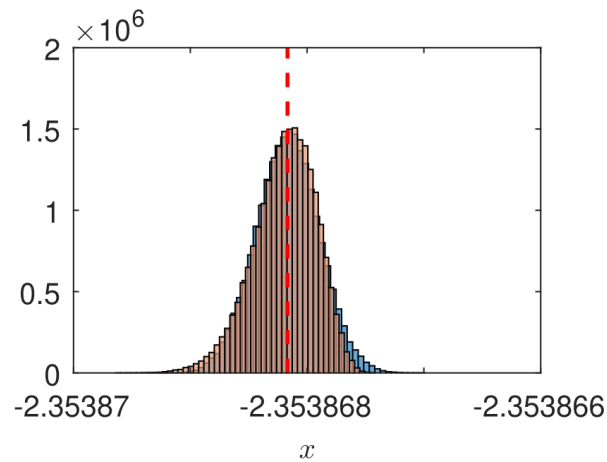


**Figure 9.15:** The distribution of the  $x$ -coordinates of 100,000 trajectories with starting point  $\mathbf{x}_0^{\text{ref}}$ , on their 100<sup>th</sup> return to the Poincaré section  $\mathcal{P}$ , given by numerical simulation using an Euler-Maruyama scheme with fixed timestep  $dt = 2 \times 10^{-6}$  in red and approximated using (9.106) in blue. Here  $T = D = -1$ ,  $a = 1$ ,  $\gamma = 0.05$ ,  $c = \theta = 20$ ,  $\sigma = 0.2$  and  $\Sigma = 0.1$ . The value of  $x_0^{\text{ref}}$  is highlighted by the red dashed line. This gives that the long term standard deviation of  $P$  and  $V$  are  $\sigma_P^* \approx 1.118 \times 10^{-4}$  and  $\sigma_V^* \approx 2.236 \times 10^{-3}$ , respectively.

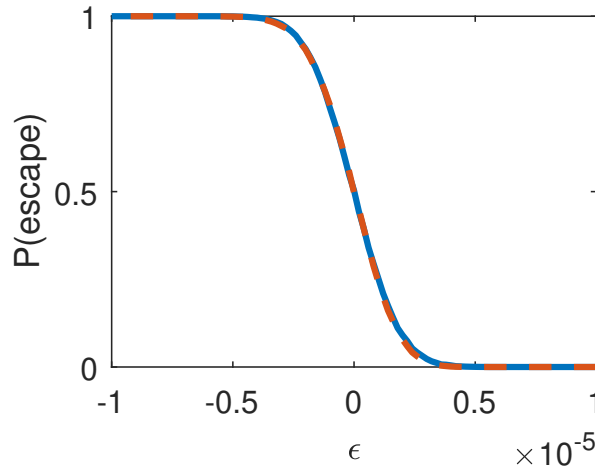


**Figure 9.16:** The proportion of trajectories with initial conditions  $\mathbf{x}_0 = \mathbf{x}_{SM} + (\epsilon, 0)^T$  about the deterministic stable manifold of  $\mathbf{x}_R^{eq}$  escaping the basin of attraction of the stable limit cycle, given by numerical simulation using an Euler-Maruyama scheme with fixed timestep  $dt = 2 \times 10^{-6}$  in dashed red, and approximated using (9.106) and linearising about the deterministic limit cycle in blue. Here  $T = D = -1$ ,  $a = 1$ ,  $\gamma \approx 0.086038$ ,  $c = \theta = 20$ ,  $\sigma = 0.4$  and  $\Sigma = 0.2$ . This gives that the long term standard deviation of  $P$  and  $V$  are  $\sigma_P^* \approx 2.236 \times 10^{-4}$  and  $\sigma_V^* \approx 4.472 \times 10^{-3}$ , respectively.

attraction of the stable limit cycle during their first return to the Poincaré section. Here  $\mathbf{x}_{SM}$  is the intersection of the deterministic stable manifold of the saddle located in  $S^+$  and the Poincaré section at  $(x_{SM}, y_0^{\text{ref}})^T$ . This stable manifold represents the boundary of the basin of attraction of the limit cycle in the deterministic system and so it is interesting to understand how the introduction of noise affects trajectories in its vicinity. In particular we consider the case when  $\gamma$  is close to  $\gamma_c$  the value of  $\gamma$  for which the deterministic periodic orbit is destroyed in a homoclinic bifurcation. The proportions are calculated by numerical simulation of 50,000 individual trajectories and approximated using (9.106).

As we would expect, trajectories located significantly outside the deterministic basin of attraction ( $\epsilon < 0$ ) never enter it, while those located significantly inside ( $\epsilon > 0$ ) never escape. On the other hand, trajectories with initial conditions close to the boundary of the deterministic basin have the potential to display the opposite behaviour to that which is observed in the deterministic system. We again see

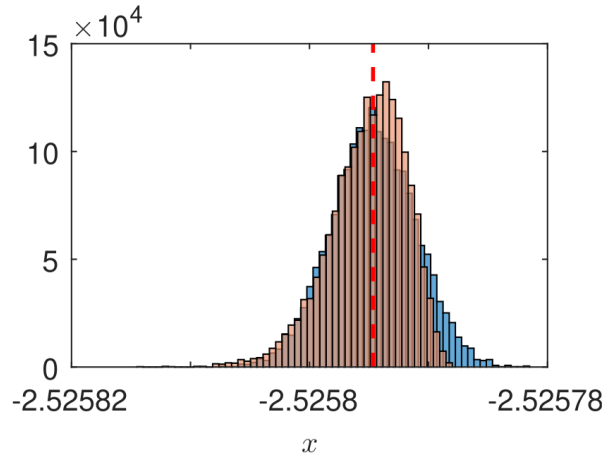


**Figure 9.17:** The distribution of the  $x$ -coordinates of the trajectories with starting point  $\mathbf{x}_0$  such that  $\mathbf{x}_{SM} - \mathbf{x}_0 = 10^{-6}$ , on their first return to the Poincaré section  $\mathcal{P}$ , provided they have remained inside the deterministic basin of attraction. We plot the distribution given by numerical simulation using an Euler-Maruyama scheme with fixed timestep  $2 \times dt = 10^{-6}$  in red and the distribution approximated using (9.106) in blue. Here  $T = D = -1$ ,  $a = 1$ ,  $\gamma \approx 0.086038$ ,  $c = \theta = 20$ ,  $\sigma = 0.4$  and  $\Sigma = 0.2$ . The value of  $x_0^{\text{ref}}$  is highlighted by the red dashed line.

good agreement between numerical simulations and our linear approximations about the deterministic periodic orbit, meaning that our approximation can give us good predictions of behaviour in this region. The approximation of the distribution of those trajectories which are inside the deterministic basin of attraction upon their first return to  $\mathcal{P}$  is also well approximated by our linearisation.

For example, choosing an initial condition just outside the deterministic basin, in Figure 9.17 we show the distribution of the trajectories that have not escaped, as given by both numerical simulation and linearisation. In this case numerical simulations predicted that 74.79 per cent of trajectories would escape the basin while linearisation predicted 74.42 per cent. Furthermore, since the characteristic multiplier of the deterministic periodic orbit tends to 0 as  $\gamma$  approaches  $\gamma_c$  the strong levels of contraction experienced by deviations away from the periodic orbit result in a tight distribution centred about the deterministic periodic orbit after one period. This implies that any escapes will take place before the first return to the Poincaré surface.

### 9.4.3 The Chua Circuit

To show how we can use the methods derived to predict the effects of boundary noise on attractors in a real-world system close to bifurcation points, we will now consider an example from electronics. Electronic systems are a rich source of both piecewise-smooth [14, 16] and noisy dynamical behaviour [17, 37]. In particular, electronic systems are of interest as they can contain noisy switches and comparators or switching thresholds subject to uncertain time delays. It is important to understand how noise of this type can affect the behaviour of electronic systems.

Here, as a simple example, we will consider the classical example of the Chua circuit. The Chua circuit a nonlinear circuit that was created with the aim of being the simplest autonomous circuit capable of generating chaos [38, 39]. It was the first physical system for which the presence of chaos was shown experimentally, numerically and mathematically [40]. The circuit, shown in Figure 9.18, contains four linear elements and one nonlinear resistor known as a *Chua diode*. It can be easily and cheaply constructed using standard electronic components [41]. The Chua circuit can be described by the system of ordinary differential equations

$$\begin{aligned}\frac{dV_1}{dt} &= \frac{1}{C_1}(G(V_2 - V_1) - f(V_1)), \\ \frac{dV_2}{dt} &= \frac{1}{C_2}(G(V_1 - V_2) + I_3), \\ \frac{dI_3}{dt} &= -\frac{1}{L}(V_2 + R_0 I_3),\end{aligned}\tag{9.108}$$

where  $V_1$ ,  $V_2$  and  $I_3$  are the voltages and current shown in the circuit diagram in Figure 9.18 and

$$G = \frac{1}{R}.\tag{9.109}$$

The function

$$f(V_1) = G_b V_1 + \frac{1}{2}(G_a - G_b)(|V_1 + E| - |V_1 - E|),\tag{9.110}$$

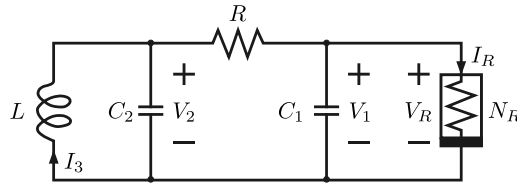


**Figure 9.18:** Circuit diagram of the Chua circuit. The circuit consists of four linear elements (a linear inductor  $L$  with internal resistance  $R_0$ , a linear resistor  $R$  and two capacitors  $C_1$  and  $C_2$ ) and a nonlinear resistor  $N_R$ , called the Chua diode.

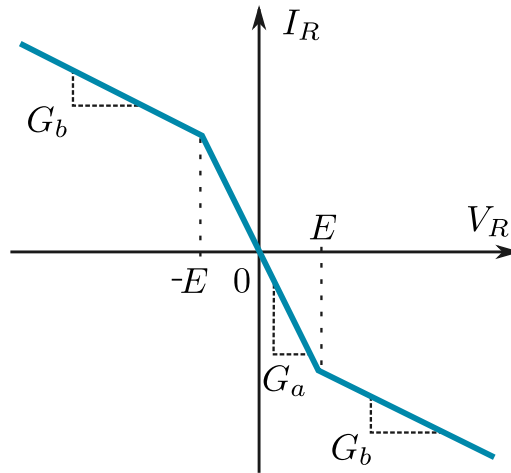


**Figure 9.19:** Typical  $V$ - $I$  characteristic of the Chua diode.

gives the piecewise linear voltage-current characteristic of the Chua diode  $N_R$  with inner slope  $G_a$  and outer slope  $G_b$ , as shown in Figure 9.19.

Here we are only interested in the qualitative behaviour of the circuit. We rescale (9.108) in order to eliminate one of the parameters and obtain the dimensionless system

$$\begin{aligned}\frac{dx}{dt'} &= \alpha(y - x - g(x)), \\ \frac{dy}{dt'} &= x - y + z, \\ \frac{dz}{dt'} &= -(\beta y + \gamma z),\end{aligned}\tag{9.111}$$

where

$$g(x) = m_1 x + \frac{1}{2}(m_0 - m_1)(|x + 1| - |x - 1|).\tag{9.112}$$

The dimensionless variables and parameters are defined as

$$x := V_1/E, \quad y := V_2/E, \quad z := I_3(R/E), \quad (9.113)$$

$$\alpha := C_2/C_1, \quad \beta := \frac{R^2 C_2}{L}, \quad \gamma := \frac{RR_0 C_2}{L}, \quad m_0 := RG_a, \quad m_1 := RG_b, \quad (9.114)$$

and the dimensionless time is

$$t' := \frac{t}{RC_2}. \quad (9.115)$$

We let  $\mathcal{D}^-$  and  $\mathcal{D}^+$  denote the two discontinuity boundaries given by  $x = -1$  and  $x = 1$ , respectively. We will denote the regions given by  $x < -1$ ,  $|x| \leq 1$  and  $x > 1$ , as  $S^-$ ,  $S^0$  and  $S^+$ , respectively. The system (9.111) has up to three equilibria, namely

$$\begin{aligned} \mathbf{x}_{\text{eq}}^0 &= (0, 0, 0)^T, \\ \mathbf{x}_{\text{eq}}^- &= \frac{m_0 - m_1}{\gamma m_1 + \beta m_1 + \beta} (\gamma + \beta, \gamma, -\beta)^T, \\ \mathbf{x}_{\text{eq}}^+ &= -\mathbf{x}_{\text{eq}}^-. \end{aligned} \quad (9.116)$$

Here  $\mathbf{x}_{\text{eq}}^0$  always exists, while  $\mathbf{x}_{\text{eq}}^-$  and  $\mathbf{x}_{\text{eq}}^+$  only exist provided  $\mathbf{x}_{\text{eq}}^- \in S^-$  and  $\mathbf{x}_{\text{eq}}^+ \in S^+$ .

Despite its simplicity the Chua circuit displays a huge variety of complex behaviours. The circuit is one of the most well-studied nonsmooth dynamical systems, and Chua himself estimated that, just ten years after the circuit had been introduced, more than two hundred papers analysing its dynamics had been published [42]. In these studies a wide range of both periodic and nonperiodic attractors have been found. For example, in [43] and [44] Chua reports on both the period-doubling and intermittency routes to chaos and presents two galleries of strange attractors. For a large gallery of attractors in various shapes and forms that have been found in the Chua circuit see [45].

In this section we will consider how noise on the system's two discontinuity boundaries  $\mathcal{D}^-$  and  $\mathcal{D}^+$  affects the Chua circuit, comparing our first-order approximations to numerical simulations obtained using an Euler-Maruyama scheme with a fixed

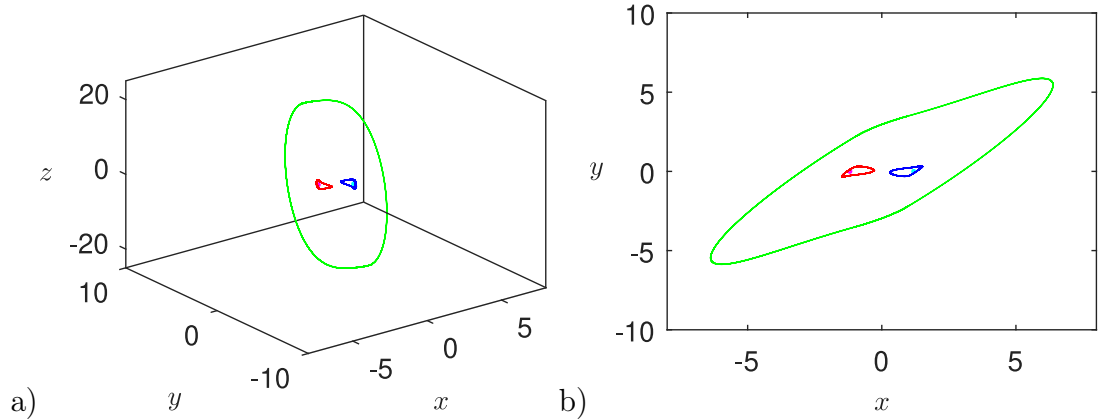


**Figure 9.20:** Five coexisting attractors in the Chua circuit with  $\alpha = 8.4$ ,  $\beta = 12$ ,  $\gamma = -0.005$ ,  $m_0 = -1.2$  and  $m_1 = 0.05$ . a) in 3-dimensional phase space, b) projected onto the  $x - y$  plane.

timestep and the analytic solutions of the system ODEs. In particular, we will investigate the effect on some interesting dynamical behaviours reported by Stankevich *et al.* [46], where the authors describe the phenomenon of *hidden attractors* in the Chua circuit. An attractor is called a hidden attractor if its basin of attraction does not intersect with the neighbourhood of an equilibrium point, otherwise it is called a *self-excited attractor* [47].

#### 9.4.3.1 Escaping Periodic Attractors

First we will consider the case where  $\alpha = 8.4$ ,  $\beta = 12$ ,  $\gamma = -0.005$ ,  $m_0 = -1.2$  and  $m_1 \in (0.02, 0.14765)$ . For these parameter values the system (9.111) has five coexisting attractors as shown in Figure 9.20. These attractors include the equilibrium points  $\mathbf{x}_{\text{eq}}^-$  and  $\mathbf{x}_{\text{eq}}^+$  given in (9.116). The system also has three periodic attractors. There are two small symmetric period-1 periodic orbits,  $\mathbf{C}^-$  and  $\mathbf{C}^+$  that cross  $\mathcal{D}^-$  and  $\mathcal{D}^+$  twice, respectively. The final attractor is a large period-1 orbit  $\mathbf{C}^\infty$ , which crosses both  $\mathcal{D}^-$  and  $\mathcal{D}^+$  twice. The three periodic attractors,  $\mathbf{C}^-$ ,  $\mathbf{C}^+$  and  $\mathbf{C}^\infty$ , are hidden attractors as if we choose initial conditions in the vicinity of any equilibrium point (stable or unstable), we will reach one of the stable equilibrium points. The smaller symmetric periodic attractors  $\mathbf{C}^-$  and  $\mathbf{C}^+$  are born in a saddle-node bifurcation as

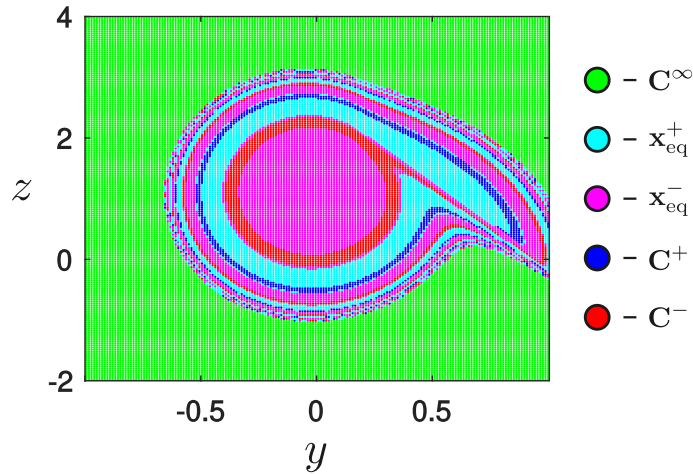


**Figure 9.21:** The basins of attraction of five coexisting attractors in the Chua circuit with  $\alpha = 8.4$ ,  $\beta = 12$ ,  $\gamma = -0.005$ ,  $m_0 = -1.2$  and  $m_1 = 0.05$  on the  $x = -1$  discontinuity boundary.

the parameter  $m_1$  decreases through  $m_1 \approx 0.14765$ .

The basins of attraction have a complicated intermingled structure. We are most interested in the structure of these basins on the discontinuity boundaries  $\mathcal{D}^-$  and  $\mathcal{D}^+$ . In Figure 9.21 we plot the basins of attraction of all five attractors on the discontinuity boundary  $\mathcal{D}^-$  in the neighbourhood of  $\mathbf{C}^-$ 's two intersections with the boundary. The basin of the large periodic attractor  $\mathbf{C}^\infty$  is indicated in green, the basins of the symmetric periodic attractors  $\mathbf{C}^-$  and  $\mathbf{C}^+$  are shown in red and blue, respectively, while the basins of the two stable equilibria  $\mathbf{x}_{\text{eq}}^-$  and  $\mathbf{x}_{\text{eq}}^+$  are indicated by magenta and cyan, respectively. We see that the basins of  $\mathbf{x}_{\text{eq}}^-$ ,  $\mathbf{x}_{\text{eq}}^+$ ,  $\mathbf{C}^-$  and  $\mathbf{C}^+$  consist of bands that are spiralled together, and their boundaries have fractal structures. The basin of the large periodic attractor  $\mathbf{C}^\infty$  surrounds the other basins. The attractors themselves are shown in Figure 9.20 and are coloured by the same code as the basins in Figure 9.21.

As we have discussed in Section 9.2.3, the inclusion of noise on the boundary causes no linear effect on a continuous-piecewise-linear system such as the Chua circuit. Consequently, the first order approximation derived in Section 9.2.3 is insufficient in this case. However the inclusion of noise on either of the boundaries certainly has an

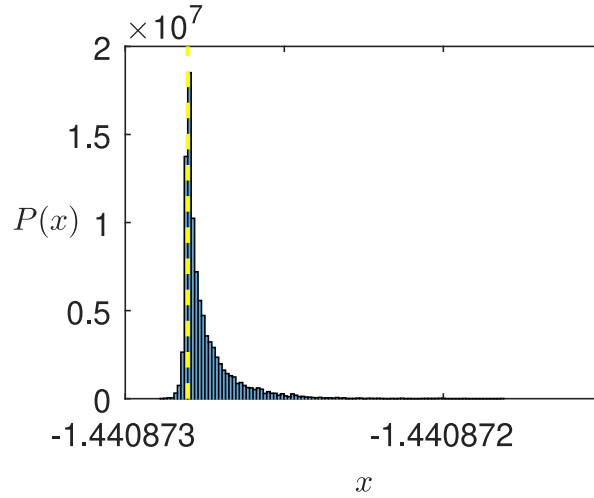


**Figure 9.22:** PDF Histogram of  $x$  co-ordinates of 10,000 trajectories with initial conditions  $\mathbf{x}_0^{\text{ref}} = (x_0^{\text{ref}}, y_0^{\text{ref}}, z_0^{\text{ref}})^T \in \mathbf{C}^-$ , such that  $\mathbf{x}_0^{\text{ref}} \in S^-$  and  $\dot{x} = 0$ , after one period in a system with a noisy boundary given by numerical simulation using an Euler-Maruyama scheme with fixed timestep  $dt = 10^{-6}$ . Here the values of the deterministic parameters are  $\alpha = 8.4$ ,  $\beta = 12$ ,  $\gamma = -0.005$ ,  $m_0 = -1.2$  and  $m_1 = 0.145$  while the values of the parameters for the stochastic process are  $\sigma = \Sigma = 0.4$  and  $c = \theta = 50$ . The dashed line indicates the value of  $x_0^{\text{ref}}$ . This gives that the long term standard deviation of  $P$  and  $V$  are  $\sigma_P^* \approx 2.262 \times 10^{-4}$  and  $\sigma_V^* \approx 1.131 \times 10^{-2}$ , respectively.

effect on the Chua circuit as shown in Figure 9.22. We will return to this issue in Section 9.4.3.2.

Let us first consider a discontinuous model of the Chua circuit. We replace the continuous-piecewise-linear function given in (9.112) with the discontinuous piecewise linear function

$$g(x) = \begin{cases} m_1 x + m_1 - m_0 & \text{if } x < -1, \\ (m_0 - \epsilon)x & \text{if } |x| \leq 1, \\ m_1 x + m_0 - m_1 & \text{if } x > 1, \end{cases} \quad (9.117)$$

where  $\epsilon$  is the level of discontinuity. For small values of  $\epsilon$  the hidden attractors  $\mathbf{C}^-$  and  $\mathbf{C}^+$  persist and can be found by numerical continuation. These attractors are destroyed in saddle-node bifurcations if the magnitude of  $\epsilon$  grows too large. For example, in the case where  $m_1 = 0.145$  they exist when  $-0.06211 < \epsilon < 0.00205$  as shown in Figure 9.23.

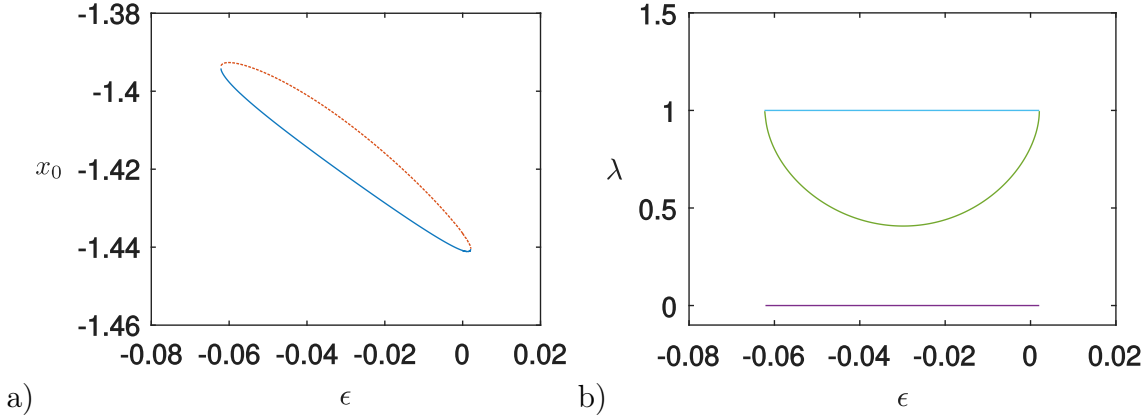


**Figure 9.23:** Bifurcation diagrams showing the saddle bifurcations of  $\mathbf{C}^-$  as the magnitude of  $\epsilon$  grows. In a) we plot the  $x$ -coordinate of the intersection of  $\mathbf{C}^-$  with the Poincaré section given by  $\{\mathbf{x} \in S^- : \dot{x} = 0\}$  as  $\epsilon$  varies (solid) alongside the corresponding  $x$ -coordinate of the coexisting unstable periodic orbit (dashed). In b) we plot the eigenvalues of the Jacobian of  $\mathbf{C}^-$ . Here  $\alpha = 8.4$ ,  $\beta = 12$ ,  $\gamma = -0.005$ ,  $m_0 = -1.2$  and  $m_1 = 0.145$ .

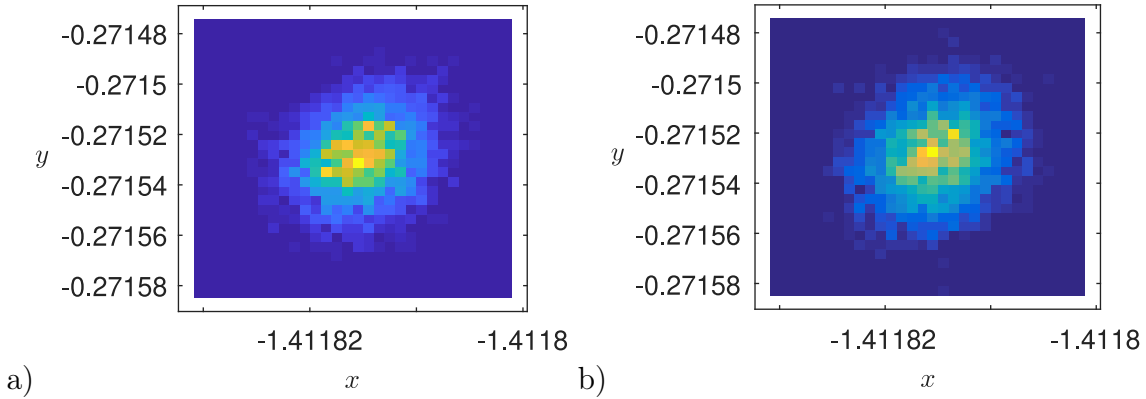


**Figure 9.24:** The distribution of the  $(x, y)$ -co-ordinates of 5,000 trajectories with initial conditions  $\mathbf{x}_0^{\text{ref}} = (x_0^{\text{ref}}, y_0^{\text{ref}}, z_0^{\text{ref}}) \in \mathbf{C}^-$  such that  $\mathbf{x}_0^{\text{ref}} \in S^-$  and  $\dot{x} = 0$ , after 20 periods in a system with a noisy boundary, on the Poincaré section  $\{(x, y, z) : z = z_0^{\text{ref}}\}$ . Given by a) Numerical simulation of the whole system using an Euler-Maruyama scheme with fixed timestep  $dt = 10^{-7}$  and b) first-order approximation. Here the values of the deterministic parameters are  $\alpha = 8.4$ ,  $\beta = 12$ ,  $\gamma = -0.005$ ,  $m_0 = -1.2$ ,  $m_1 = 0.145$  and  $\epsilon = -0.0434079$  while the values of the parameters for the stochastic process are  $\sigma = \Sigma = 0.4$  and  $c = \theta = 50$ . This gives that the long term standard deviation of  $P$  and  $V$  are  $\sigma_P^* \approx 2.262 \times 10^{-4}$  and  $\sigma_V^* \approx 1.131 \times 10^{-2}$ , respectively.

In Figure 9.24 we compare the distribution of the  $(x, y)$ -co-ordinates of 5,000 trajectories starting in the deterministic periodic orbit  $\mathbf{C}^-$  at  $(x_0^{\text{ref}}, y_0^{\text{ref}}, z_0^{\text{ref}})^T$  on their twentieth return to the Poincaré section given by  $z = z_0^{\text{ref}}$  in the discontinuous system ( $\epsilon \approx -0.0434$ ) with our first-order approximation (9.47). We see that there our approximation shows good agreement with the results given by simulation of the full system. Concretely, we find that the Kolmogorov-Smirnov statistic given by the two-dimensional K-S test on the two samples shown in Figure 9.24 is  $D_{KS} \approx 0.037356$ . This approximation will continue to give us accurate results provided the size of the noise does not become too large relative to the size of the discontinuity.

We will now consider the effect of noise on the periodic attractors  $\mathbf{C}^-$  and  $\mathbf{C}^+$ . In particular, we will focus on the potential for noise to effectively destroy an attractor. We consider a trajectory with an initial condition on the deterministic periodic attractor  $\mathbf{C}^-$  (as the system is symmetric it is sufficient to consider just one of the attractors).

We note that in order for noise to push such a trajectory out of periodic behaviour it must first push the trajectory out of the orbit's basin of attraction. This can only happen after a boundary crossing, as this is when errors are introduced into the system. If a trajectory remains within the attractor's basin immediately after a boundary crossing it will remain there until the next crossing as the trajectory's evolution between crossings is entirely deterministic. As a result, in order to understand the probability of a trajectory escaping periodic behaviour, we can simply consider the distribution of trajectories immediately after crossing the noisy boundary projected onto the deterministic boundary. In particular, we analyse how this distribution interacts with the deterministic system's basins of attraction. In order to have escaping trajectories the distribution must cross the closest boundary of  $\mathbf{C}^-$ 's basin. The closest boundary in this case is given by the stable manifold of  $\mathbf{C}_u^-$ , where  $\mathbf{C}_u^-$  is the corresponding unstable periodic orbit.

In order to estimate whether noise will push orbits out of periodic behaviour we will

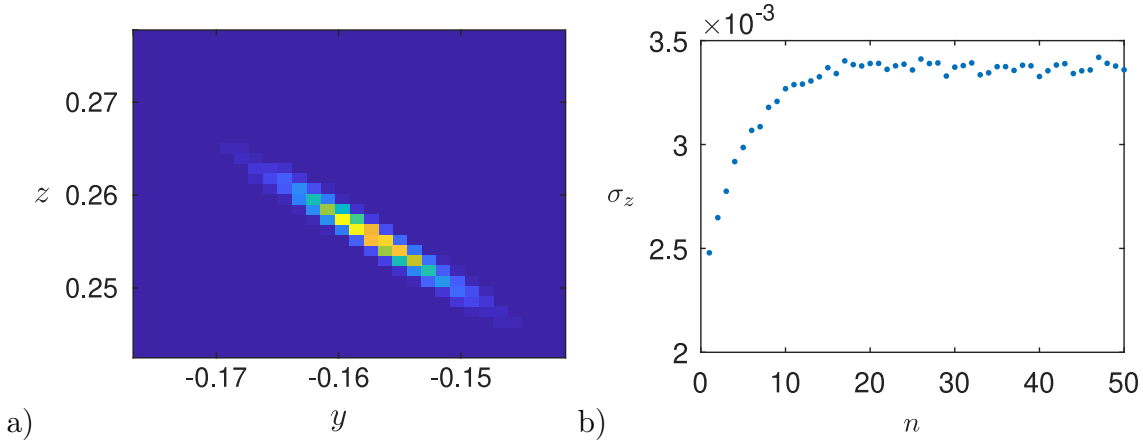


**Figure 9.25:** a) Steady state distribution of orbit errors on the discontinuity boundary  $\mathcal{D}^-$  for trajectories with initial condition on the periodic orbit  $\mathbf{C}^-$ . b) Convergence of the standard deviation in the  $z$ -direction,  $\sigma_z$ , to its steady state value for the distribution shown in a).

consider the linearised distribution of trajectories projected onto the deterministic discontinuity boundary  $\mathcal{D}^-$ , immediately after crossing the noisy boundary. There are two such crossings each period, corresponding to the two deterministic crossings, at  $\hat{\mathbf{x}}_1$  and  $\hat{\mathbf{x}}_2$ . These distributions are given by maps, which can be easily calculated by referring to (9.57)-(9.59) in Section 9.2.5. Since the eigenvalues of the stochastic maps have expected magnitude less than unity (corresponding to the eigenvalues of the periodic orbit's deterministic Poincaré map) and small variance the maps converge to steady-state invariant distributions as shown in Figure 9.25.

These distributions linearly approximate the corresponding distributions in the full system. We will also linearly approximate the closest boundary of the basin of attraction by taking the eigenvector of the deterministic Poincaré map of  $\mathbf{C}_u^-$  corresponding to the eigenvalue with magnitude less than unity. In other words, we take the stable manifolds of the fixed points of the linearised Poincaré maps  $\mathbf{P}_i : \mathcal{D}^- \rightarrow \mathcal{D}^-$  defined in neighbourhoods of  $\hat{\mathbf{x}}_i$  for  $i = 1, 2$ . As a further simplification, instead of the linearised distributions obtained from the map, we will consider the corresponding invariant ellipses. These are the ellipses centred on the mean of the distributions (the  $(y, z)$ -coordinates of  $\hat{\mathbf{x}}_i$ ) with major and minor axes given by the eigenvalues

and eigenvectors of the covariance matrix of the invariant distribution. The major and minor radii of the ellipses are given by  $R\gamma_I\mathbf{w}_I$  and  $R\gamma_{II}\mathbf{w}_{II}$ , respectively where  $\gamma_I$  is the largest eigenvalue with corresponding eigenvector  $\mathbf{w}_I$ . Here  $R$  represents the number of standard deviations of the invariant distribution contained within the ellipse.

Figures 9.26 and 9.27 show how we can use the invariant linearised distributions found, along with knowledge of the deterministic system, to estimate the effect of noise on periodic dynamics close to bifurcation. In particular we consider the case where  $\epsilon = -0.0618516$ . In Figure 9.26 we see that when  $\Sigma = \sigma = 0.5875$  the closest basin boundary is approximately tangent to the 7-standard deviation ellipse about  $\hat{\mathbf{x}}_1$ , while the 7-standard deviation ellipse about  $\hat{\mathbf{x}}_2$  is entirely contained within the basin of attraction of  $\mathbf{C}^-$ . If our linear prediction is accurate this would indicate that a given trajectory has a very low probability of escaping periodic behaviour each time it interacts with the noisy boundary. Indeed we observe that in this case the noise amplitude is not sufficiently high to push any of the 3000 sample trajectories out of periodic behaviour over 200 simulated periods in the full system. Furthermore, the distribution from the full system after 200 periods corresponds very well to the linearised prediction of the invariant distribution.

On the other hand in Figure 9.27 we see that when  $\Sigma = \sigma = 0.7$  the closest basin boundary is approximately tangent to the 5-standard deviation ellipse about  $\hat{\mathbf{x}}_1$  while the 7-standard deviation ellipse about  $\hat{\mathbf{x}}_2$  extends outside the basin of attraction of  $\mathbf{C}^-$ . This indicates that there is potential for trajectories to escape the basin of attraction of  $\mathbf{C}^-$  and hence be pushed out of periodic behaviour during each interaction with the noisy boundary. This is particularly true when crossing the boundary close to  $\hat{\mathbf{x}}_1$ . The simulation of the full system confirms this prediction. A small, but significant, number of the sample of 3000 trajectories simulated are pushed out of the basin of attraction of  $\mathbf{C}^-$  over 200 simulated periods in the full system. The distribution of the trajectories remaining in the basin attraction after 200

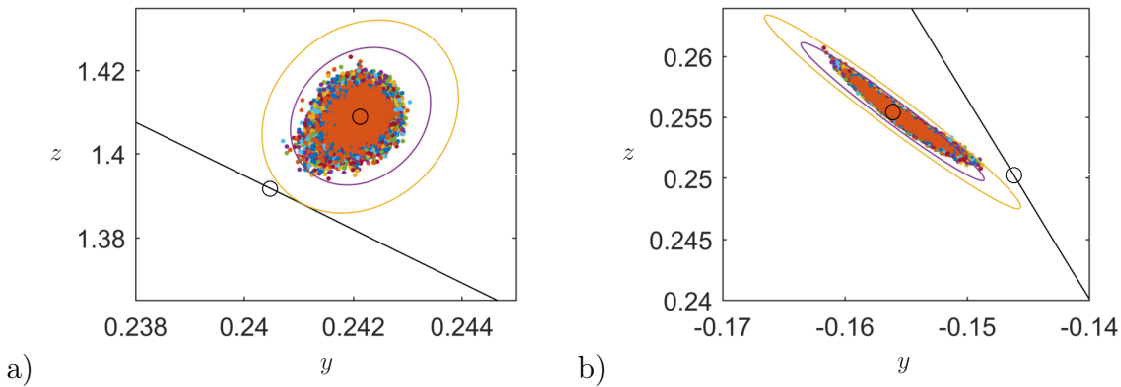


**Figure 9.26:** Invariant ellipses with  $R = 5$  and  $R = 7$  corresponding to the invariant distributions associated with the two intersections a)  $\hat{\mathbf{x}}_1$  and b)  $\hat{\mathbf{x}}_2$  of  $\mathbf{C}^-$  with  $\mathcal{D}^-$ . The linearised basin boundaries are indicated by the black line, the intersections of  $\mathbf{C}^-$  and  $\mathbf{C}_u^-$  with the boundary are indicated by black circles. The distribution of points plotted corresponds to the intersection of 3000 trajectories with initial conditions on the deterministic periodic orbit with  $\mathcal{D}^-$  on their 100th to 200th returns projected onto the deterministic boundary. Here the values of the deterministic parameters are  $\alpha = 8.4$ ,  $\beta = 12$ ,  $\gamma = -0.005$ ,  $m_0 = -1.2$ ,  $m_1 = 0.145$  and  $\epsilon = -0.0618516$  while the values of the parameters for the stochastic process are  $\Sigma = \sigma = 0.5875$  and  $c = \theta = 50$ . This gives that the long term standard deviation of  $P$  and  $V$  are  $\sigma_P^* \approx 4.881 \times 10^{-4}$  and  $\sigma_V^* \approx 2.441 \times 10^{-2}$ , respectively. The fixed timestep for the Euler-Maruyama scheme is  $dt = 2 \times 10^{-6}$ .

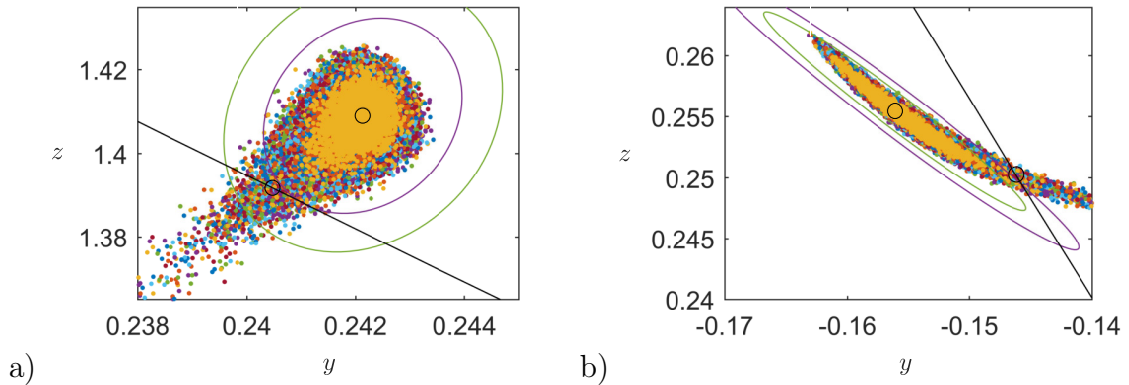


**Figure 9.27:** Invariant ellipses with  $R = 5$  and  $R = 7$  corresponding to the invariant distributions associated with the two intersections a)  $\hat{\mathbf{x}}_1$  and b)  $\hat{\mathbf{x}}_2$  of  $\mathbf{C}^-$  with the deterministic boundary at  $x = -1$ . The linearised basin boundaries are indicated by the black line, the intersections of  $\mathbf{C}^-$  and  $\mathbf{C}_u^-$  with the boundary are indicated by black circles. The distribution of points plotted corresponds to the intersection of 3000 trajectories with initial conditions on the deterministic periodic orbit with  $\mathcal{D}^-$  on their 100th to 200th returns projected onto the deterministic boundary simulated using an Euler-Maruyama scheme with fixed timestep  $dt = 2 \times 10^{-6}$ . Here the values of the deterministic parameters are  $\alpha = 8.4$ ,  $\beta = 12$ ,  $\gamma = -0.005$ ,  $m_0 = -1.2$ ,  $m_1 = 0.145$  and  $\epsilon = -0.0618516$  while the values of the parameters for the stochastic process are  $\Sigma = \sigma = 0.7$  and  $c = \theta = 50$ . This gives that the long term standard deviation of  $P$  and  $V$  are  $\sigma_P^* \approx 6.930 \times 10^{-4}$  and  $\sigma_V^* \approx 3.464 \times 10^{-2}$ , respectively.

periods is also skewed towards the basin boundary when compared to the linearised distribution.

Suppose now that we consider a system where the noise amplitude on  $\mathcal{D}^-$  is  $\Sigma = \sigma = 0.5875$  and the noise amplitude on  $\mathcal{D}^+$  is  $\Sigma = \sigma = 0.7$ . By symmetry we find that in this system the periodic orbit  $\mathbf{C}^-$  (which crosses  $\mathcal{D}^-$ ) would remain robust while the periodic orbit  $\mathbf{C}^+$  (which crosses  $\mathcal{D}^+$ ) would allow trajectories to escape.

In general, we note that it requires a high-noise amplitude to push trajectories out of periodic behaviour, even close to its destruction in a saddle-bifurcation. Examining the periodic orbit further we find that this is a result of the structure of the invariant manifolds associated with it. The eigenvector of the periodic orbit's monodromy matrix associated with the eigenvalue that approaches unity as we approach the saddle bifurcation points almost along the periodic orbit. The eigenvalue associated

with the other eigenvector takes a value close to zero, as shown in Figure 9.23. This means that trajectories undergo very strong contraction towards the periodic orbit except along the direction which is almost along the periodic orbit, even close to the bifurcation.

### 9.4.3.2 The Continuous Case

Let us now return to the continuous case. Since a first-order approximation is insufficient here, with  $\mathbf{D}_x^*(\mathbf{x}_{\text{in}})$  collapsing to the identity matrix and  $\hat{\mathbf{f}}_{\text{in}} = \hat{\mathbf{f}}_{\text{out}}$ , we will instead consider a pseudo-second order approximation replacing equation (9.47) with

$$\begin{aligned} \phi(\mathbf{x}_0, T) - \phi(\hat{\mathbf{x}}_0^{\text{ref}}, T) &\approx \phi_x(\hat{\mathbf{x}}_0^{\text{ref}}, T)(\mathbf{x}_0 - \hat{\mathbf{x}}_0^{\text{ref}}) \\ &+ \phi_{2,x}(\hat{\mathbf{x}}_{\text{out}}, T - \hat{t}_{\text{ref}}) \left( (\hat{\mathbf{f}}_{\text{in}} - \hat{\mathbf{f}}_{\text{out}})\Delta t_{\text{ref}} + (\hat{\mathbf{g}}_{\text{in}} - \hat{\mathbf{g}}_{\text{out}})\Delta t_{\text{ref}}^2 \right), \end{aligned} \quad (9.118)$$

where

$$\hat{\mathbf{g}}_{\text{in}} = \dot{\hat{\mathbf{f}}}_1(\hat{\mathbf{x}}_{\text{in}}), \quad \text{and} \quad \hat{\mathbf{g}}_{\text{out}} = \dot{\hat{\mathbf{f}}}_2(\hat{\mathbf{x}}_{\text{out}}), \quad (9.119)$$

are the incoming and outgoing second derivatives of  $\mathbf{x}$  with respect to time evaluated at the deterministic boundary crossing point  $\hat{\mathbf{x}}_{\text{in}}$ .

This approximation is a natural extension of our method for continuous systems. In the first-order approximation we introduce an error  $(\hat{\mathbf{f}}_{\text{in}} - \hat{\mathbf{f}}_{\text{out}})\Delta t_{\text{ref}}$  each time we cross a stochastically varying boundary. We note that this is simply a first order Taylor expansion of  $\phi_2(\phi_1(\hat{\mathbf{x}}_{\text{in}}, \Delta t_{\text{ref}}), -\Delta t_{\text{ref}})$  about  $\Delta t_{\text{ref}} = 0$ , while our pseudo-second order approximation simply replaces this with the second order Taylor expansion. This approach leads to good approximations in the case of the Chua circuit. For example, Figure 9.28 approximates the distribution of the positions of the trajectories simulated in Figure 9.22 using (9.118). We clearly see good agreement between the simulation of the full system and our approximation.

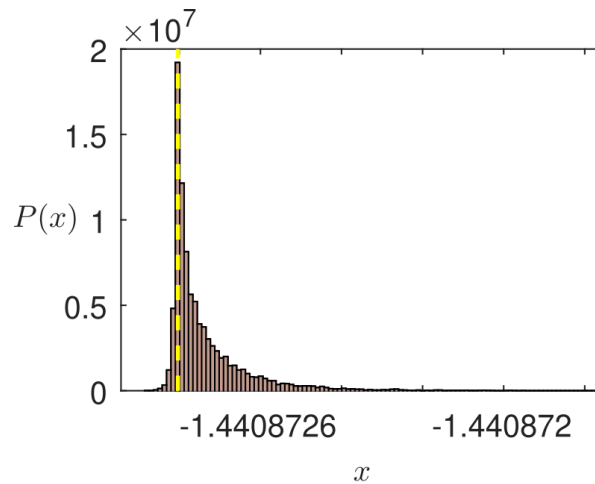


**Figure 9.28:** Approximation of the distribution of the positions of the trajectories simulated in Figure 9.22 using (9.118).

Indeed, our first-order approximation begins to break down as  $\epsilon$  approaches 0, i.e. as our system approaches a continuous system. In this case, using the second-order approximation results in significant improvements. For example, in Figure 9.29a) we compare our first order approximation to simulation of the full system, where  $\epsilon = -6.21 \times 10^{-5}$ , and see that our approximation in this case is pretty poor. In Figure 9.29b) we compare the same data to our second order approximation and observe that there is now very good agreement. The importance of the second-order terms decreases as the level of discontinuity of the system's vector field increases. For example in Figure 9.30 we compare the first and second order approximations when  $\epsilon = -5.589 \times 10^{-4}$ . The authors consider second order approximations and the case of continuous piecewise-smooth systems in more detail along with other generalisations in [30].

#### 9.4.3.3 Merging Periodic Attractors

We will now consider the case where  $\alpha = 8.4$ ,  $\beta = 12$ ,  $\gamma = -0.005$ ,  $m_0 = 0.121$  and  $m_1 \in (-1.13, -1.0929)$ . In this case the system (9.111) has three coexisting attractors,  $\mathbf{x}_{\text{eq}}^0$ , the equilibrium at the origin and two symmetric period-1 limit cycles  $\mathbf{C}^1$  and  $\mathbf{C}^1$  which cross both  $\mathcal{D}^-$  and  $\mathcal{D}^+$  twice. These attractors are shown in

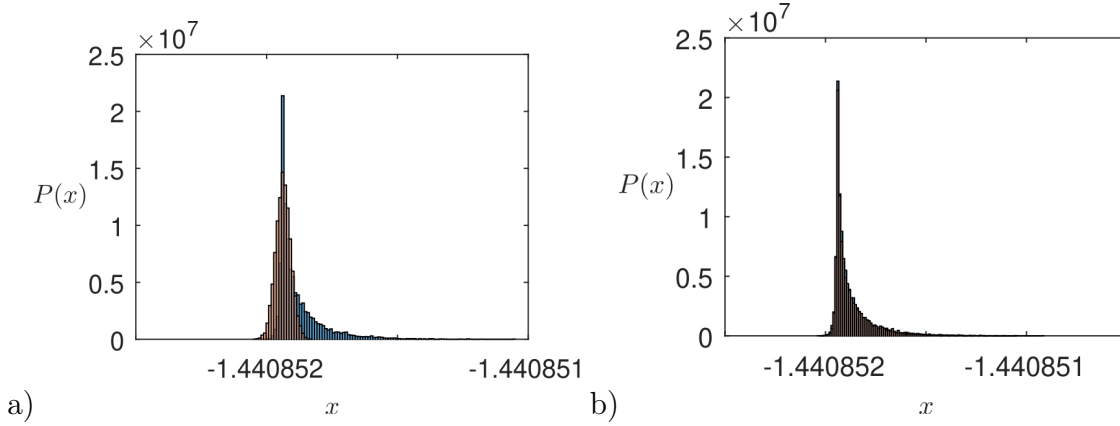


**Figure 9.29:** The distribution of  $x$  co-ordinates of 10,000 trajectories with initial conditions  $\mathbf{x}_0^{\text{ref}} = (x_0^{\text{ref}}, y_0^{\text{ref}}, z_0^{\text{ref}})^T \in \mathbf{C}^-$ , such that  $\mathbf{x}_0^{\text{ref}} \in S^-$  and  $\dot{x} = 0$ , after one period in a system with a noisy boundary in blue compared to a) first-order approximation and b) second order approximation overlayed in red. Here the values of the deterministic parameters are  $\alpha = 8.4$ ,  $\beta = 12$ ,  $\gamma = -0.005$ ,  $m_0 = -1.2$ ,  $m_1 = 0.145$  and  $\epsilon = -6.21 \times 10^{-5}$ , while the values of the parameters for the stochastic process are  $\sigma = \Sigma = 0.4$  and  $c = \theta = 50$ . This gives that the long term standard deviation of  $P$  and  $V$  are  $\sigma_P^* \approx 2.262 \times 10^{-4}$  and  $\sigma_V^* \approx 1.131 \times 10^{-2}$ , respectively. The numerically simulated distribution in blue used an Euler-Maruyama scheme with fixed timestep  $dt = 10^{-6}$ .

Figure 9.31, where  $\mathbf{C}^1$  and  $\mathbf{C}^1$  and marked in red and blue, respectively, while  $\mathbf{x}_{\text{eq}}^0$  is indicated by the black dot. Unlike the first example in Section 9.4.3.1, in this case both periodic attractors are self-excited with the equilibria at  $\mathbf{x}_{\text{eq}}^-$  and  $\mathbf{x}_{\text{eq}}^+$  located on the boundary of their basins [46]. The symmetric periodic attractors are born in a pitchfork bifurcation at  $m_1 \approx -1.0929$ , where a single period-1 attractor is split into two period-1 attractors and an unstable period-1 orbit.

The intersection of the basins of attraction of all three coexisting attractors with the discontinuity boundary  $\mathcal{D}^-$  are shown in Figure 9.32, for these parameter values. The area of phase space for which trajectories diverge is coloured cyan, while the basins of attraction of the two periodic attractors  $\mathbf{C}^1$ ,  $\mathbf{C}^2$  and the equilibrium  $\mathbf{x}_{\text{eq}}^-$  are coloured by the same code as used in Figure 9.31. We once again see that the basins are intertwined and have a complex structure.

As with the case of  $\mathbf{C}^-$  and  $\mathbf{C}^+$  in Section 9.4.3.1 the periodic attractors  $\mathbf{C}^1$  and

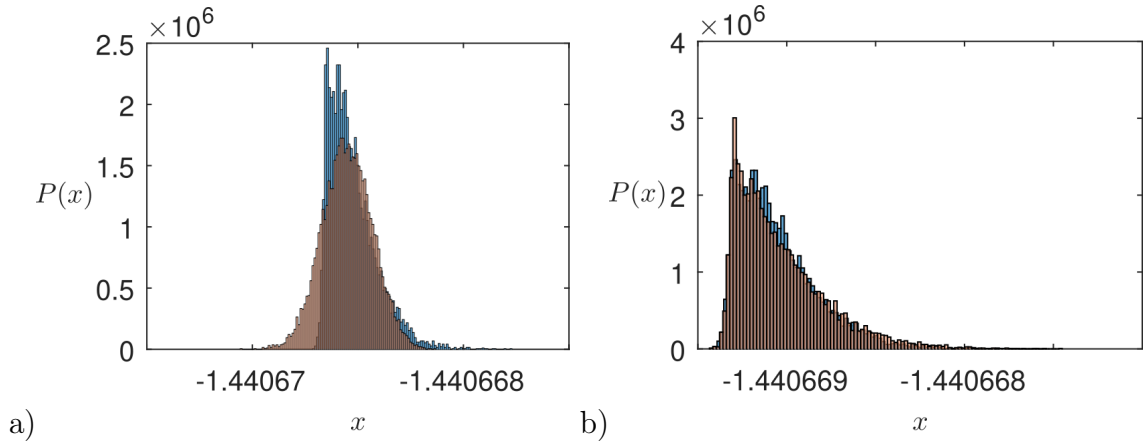


**Figure 9.30:** The distribution of  $x$  co-ordinates of 10,000 trajectories with initial conditions  $\mathbf{x}_0^{\text{ref}} = (x_0^{\text{ref}}, y_0^{\text{ref}}, z_0^{\text{ref}})^T \in \mathbf{C}^-$ , such that  $\mathbf{x}_0^{\text{ref}} \in S^-$  and  $\dot{x} = 0$ , after one period in a system with a noisy boundary in blue compared to a) first-order approximation and b) second order approximation overlaid in red. Here the values of the deterministic parameters are  $\alpha = 8.4$ ,  $\beta = 12$ ,  $\gamma = -0.005$ ,  $m_0 = -1.2$ ,  $m_1 = 0.145$  and  $\epsilon = -5.589 \times 10^{-4}$ , while the values of the parameters for the stochastic process are  $\sigma = \Sigma = 0.4$  and  $c = \theta = 50$ . This gives that the long term standard deviation of  $P$  and  $V$  are  $\sigma_P^* \approx 2.262 \times 10^{-4}$  and  $\sigma_V^* \approx 1.131 \times 10^{-2}$ , respectively. The numerically simulated distribution in blue used an Euler-Maruyama scheme with fixed timestep  $dt = 10^{-6}$ .

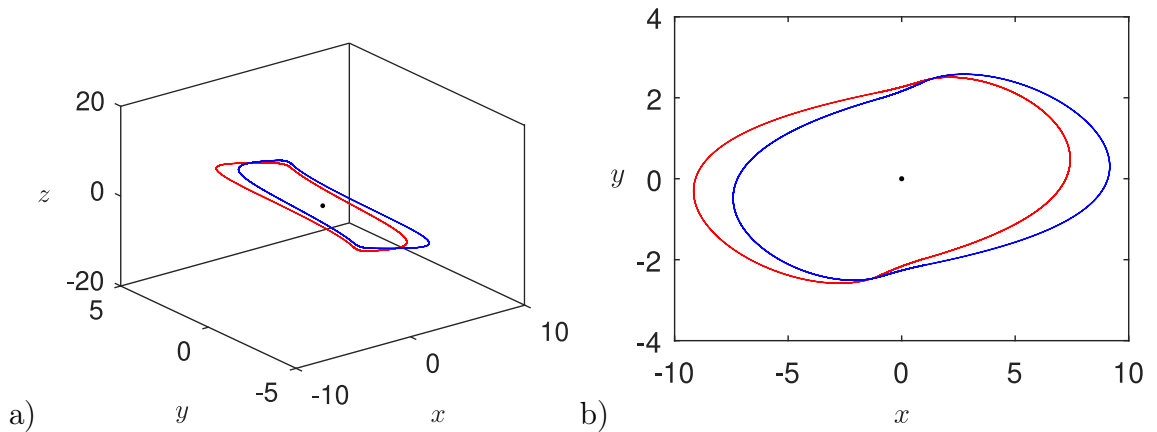


**Figure 9.31:** Three coexisting attractors in the Chua circuit with  $\alpha = 8.4$ ,  $\beta = 12$ ,  $\gamma = -0.005$ ,  $m_0 = 0.121$  and  $m_1 = -1.1$ . a) in 3-dimensional phase space, b) projected onto the  $x - y$  plane.

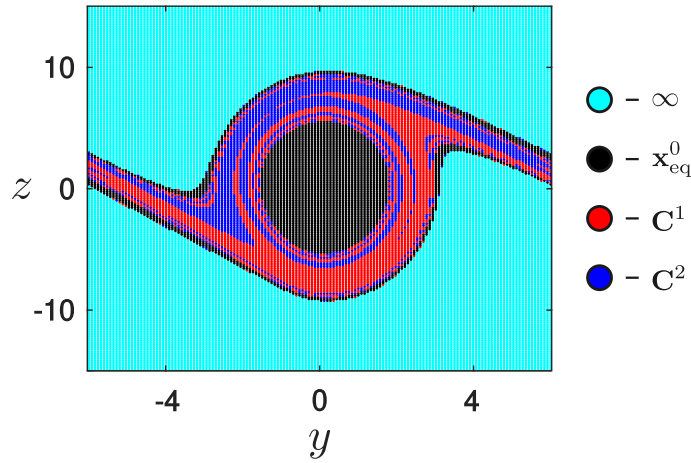


**Figure 9.32:** The basins of attraction of three coexisting attractors in the Chua circuit with  $\alpha = 8.4$ ,  $\beta = 12$ ,  $\gamma = -0.005$ ,  $m_0 = 0.121$  and  $m_1 = -1.1$  on the  $x = -1$  discontinuity boundary.

$\mathbf{C}^2$  persist in the discontinuous Chua system provided the magnitude of  $\epsilon$  is not too large and can be found by numerical continuation. In Figure 9.33 we plot the eigenvalues of the Jacobian  $\mathbf{C}^1$  along with the  $x$ -coordinate of the intersection of  $\mathbf{C}^1$  with the Poincaré section given by  $\mathcal{P} = \{(x, y, z) : x < -1, \dot{x} = 0\}$ . These attractors merge in pitchfork bifurcations if the magnitude of  $\epsilon$  becomes too large. For example, when  $m_1 = -1.1$ ,  $\mathbf{C}^1$  and  $\mathbf{C}^2$  persist as separate attractors for  $\epsilon \in (-0.2098, 1.847)$ , as shown in Figure 9.33.

Again we consider the effects of boundary noise on the system's periodic attractors. First we will use the linearisation method to predict whether noise will cause the two periodic attractors  $\mathbf{C}^1$  and  $\mathbf{C}^2$  to *merge* close to the pitchfork bifurcation at  $\epsilon \approx -0.2098$ . In other words we will try to predict when the distribution of trajectories starting in the deterministic  $\mathbf{C}^1$  orbit will overlap significantly with the corresponding distribution about  $\mathbf{C}^2$ . In this case we assume that the noise processes  $P^-(t)$  and  $P^+(t)$  on  $\mathcal{D}^-$  and  $\mathcal{D}^+$ , respectively, have the same characteristic parameter values  $c = \theta = 50$  and  $\sigma = \Sigma = 0.95$ . As a result the system is entirely symmetric and we can consider the distribution of trajectories starting in  $\mathbf{C}^1$  as a mirror of the distribution of trajectories starting in  $\mathbf{C}^2$ .

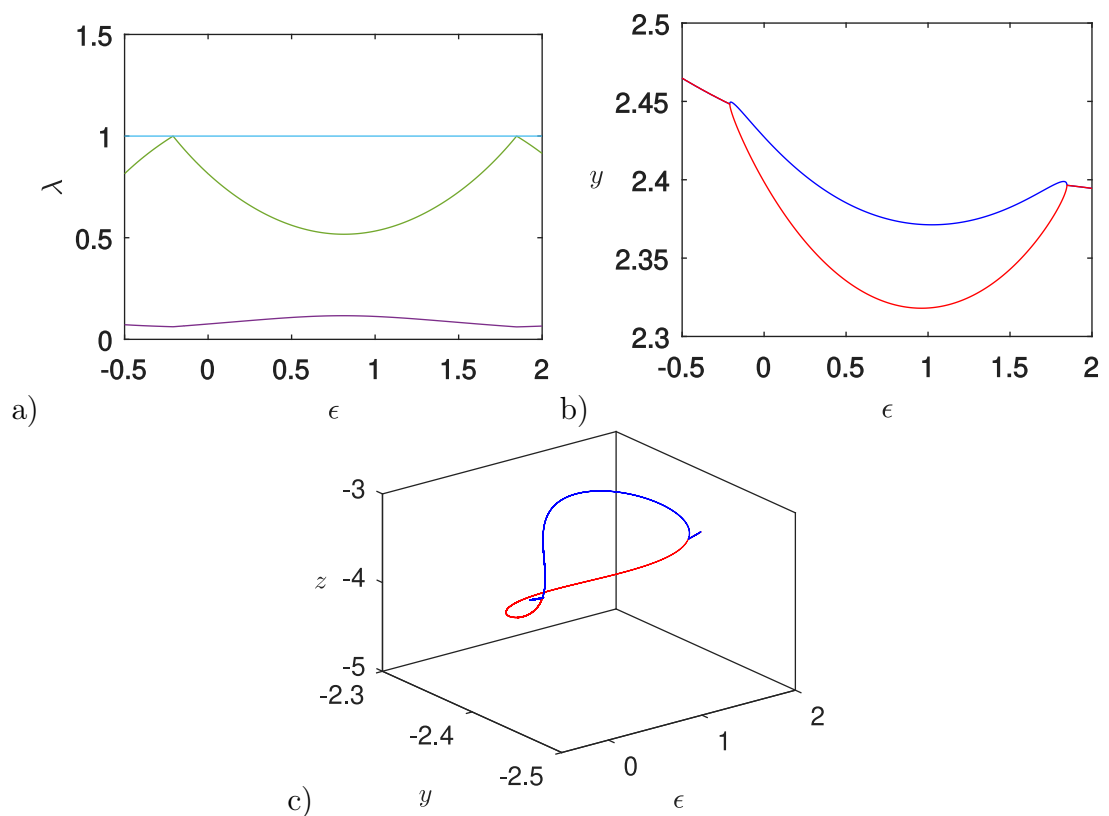


**Figure 9.33:** Bifurcation diagram showing the pitchfork bifurcations of  $\mathbf{C}^1$  and as  $\mathbf{C}^2$  the magnitude of  $\epsilon$  grows. We plot a) the eigenvalues of the Jacobians of  $\mathbf{C}^{1,2}$ , b) the  $y$ -coordinate of one of the intersections of  $\mathbf{C}^1$  and  $\mathbf{C}^2$  with  $\mathcal{D}^+$  and c) the  $(y, z)$ -coordinates of one of the intersections of  $\mathbf{C}^1$  and  $\mathbf{C}^2$  with  $\mathcal{D}^-$  as  $\epsilon$  varies. Here  $\alpha = 8.4$ ,  $\beta = 12$ ,  $\gamma = -0.005$ ,  $m_0 = 0.121$  and  $m_1 = -1.1$ .

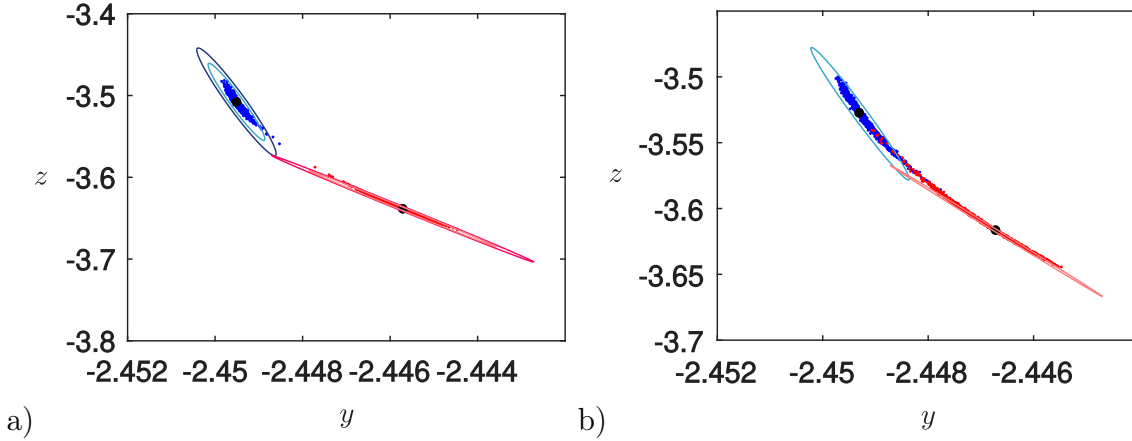


**Figure 9.34:** Invariant ellipses corresponding to the invariant linearised distributions associated with the intersections  $\hat{\mathbf{x}}_4^1$ , and  $\hat{\mathbf{x}}_2^2$ , of  $\mathbf{C}^1$  and  $\mathbf{C}^2$  with  $\mathcal{D}^-$ , respectively. The distribution of points plotted corresponds to the intersection of 1000 trajectories with initial conditions on the deterministic periodic orbit with  $\mathcal{D}^-$  on their 1000th return projected onto the deterministic boundary simulated using an Euler-Maruyama scheme with fixed timestep  $dt = 10^{-6}$ . The stochastic parameters are  $c = \theta = 50$  and  $\sigma = \Sigma = 0.95$ . This gives that the long term standard deviation of  $P$  and  $V$  are  $\sigma_P^* \approx 1.276 \times 10^{-3}$  and  $\sigma_V^* \approx 6.38 \times 10^{-2}$ , respectively. The deterministic parameters are  $\alpha = 8.4$ ,  $\beta = 12$ ,  $\gamma = -0.005$ ,  $m_0 = 0.121$ ,  $m_1 = -1.1$ . In a) we take  $\epsilon \approx -0.20595$  and plot ellipses for  $R = 5$  and  $R = 7$ . In b) we take  $\epsilon \approx -0.20800$  and plot ellipses for  $R = 5$ .

In Figure 9.34a) we consider the case where  $\epsilon \approx -0.20595$ . We find that, as in the previous example, the linearised distributions about the four boundary crossing points of the two periodic orbits on the boundary converge to invariant distributions. We take the standard deviation ellipses associated with these distributions and consider how they interact. We find that for  $\epsilon \approx -0.20595$  the ellipses will first intersect when we consider approximately  $R = 7$  standard deviations. This indicates that there is vanishingly small probability that the distribution of trajectories starting in  $\mathbf{C}^1$  will overlap with the distribution of trajectories starting in  $\mathbf{C}^2$ . Simulation of the full system validates this fact. We find that there is no overlap between the distributions of 1000 orbits starting in each of the periodic orbits after 1000 periods.

In Figure 9.34b) we consider the case where  $\epsilon \approx -0.20800$ . In this case we find that the ellipses have a significant intersection when we consider  $R = 5$  standard

deviations. This indicates that there is significant probability that the distribution of trajectories starting in  $\mathbf{C}^1$  will overlap with the distribution of trajectories starting in  $\mathbf{C}^2$ . Simulation of the full system once again confirms this. We find that there is a significant overlap between the distributions of 1000 orbits starting in each of the periodic orbits after 1000 periods resulting in the effective merging of the two periodic attractors.

## 9.5 Summary and Discussion

We have shown that it is possible to generalise techniques for the linearisation of discontinuous piecewise-smooth systems to systems in which the position of the discontinuity boundary varies according to a differentiable stochastic process  $P(t)$ .

In Section 9.2 we generalised the concept of a saltation matrix to account for the presence of noise on the boundary. We showed that this can be done by extending the original state space variable  $\mathbf{x}$ , with corresponding vector field  $\mathbf{f}$ , to the state space variable  $(\mathbf{x}, t, \Delta t_{\text{ref}})^T$ , with corresponding vector field  $(\mathbf{f}, 1, 0)^T$ , before projecting our results back to the original space. Here  $\Delta t_{\text{ref}}$  is the random variable corresponding to the difference in the time of intersection of the reference trajectory with the discontinuity boundary in the stochastic system compared to the deterministic system.

Section 9.3 introduced  $P(t)$ , a stochastic process suitable to describe the stochastic component of the position of a discontinuity boundary. This stochastic process has many desirable characteristics including differentiability giving it a well defined velocity, a long-term mean of zero meaning the boundary will not tend to drift, and approximately zero covariance over longer timescales.

Section 9.4 gave some examples of how linearisation can be used to investigate the effects of boundary noise on discontinuous piecewise smooth systems. We showed that the derived method is suitable for the analysis of discontinuous nonlinear systems in

Section 9.4.1 and in Section 9.4.2 we used linearisation to predict basin of attraction escapes in a 2-dimensional piecewise-linear system. Finally, Section 9.4.3 investigated the effects of boundary noise on a 3-dimensional discontinuous piecewise-linear model of the Chua circuit. In particular we used linearisation to predict the effects of noise on both hidden and self-excited periodic attractors in regimes where the system is multistable.

This paper also noted some of the weaknesses of the derived method. In particular we have discussed how the method is not applicable to continuous systems with higher-order discontinuities. The generalisation of the derived mapping to continuous systems, where a higher-order approximation is required, and hybrid systems, where the map on the boundary is not the identity (potentially imposing further conditions on the properties of  $P(t)$ ), is the focus of ongoing investigation by the authors [30]. This work also considers non-transversal interactions with stochastic discontinuity boundaries and boundaries with stochastic components that depend on the system's state variables, cases which have not been investigated in the current work.

## Funding

Eoghan J. Staunton is supported by an Irish Research Council Postgraduate Scholarship, Award Number GOIPG/2015/3500.

## Declarations of Interest

None.

# Bibliography

- [1] M. di Bernardo, F. Garefalo, L. Glielmo, and F. Vasca, “Switchings, bifurcations, and chaos in DC/DC converters,” *IEEE Transactions on Circuits and Systems I: Fundamental Theory and Applications*, vol. 45, no. 2, pp. 133–141, 1998.
- [2] E. Fossas and G. Olivar, “Study of chaos in the buck converter,” *IEEE Transactions on Circuits and Systems I: Fundamental Theory and Applications*, vol. 43, no. 1, pp. 13–25, 1996.
- [3] S. Foale and S. R. Bishop, “Bifurcations in impact oscillations,” *Nonlinear dynamics*, vol. 6, no. 3, pp. 285–299, 1994.
- [4] Y. Yoshitake and A. Sueoka, “Forced self-excited vibration with dry friction,” in *Applied nonlinear dynamics and chaos of mechanical systems with discontinuities*, pp. 237–259, World Scientific, 2000.
- [5] D. Amrani and D. P. Atherton, “Designing autonomous relay systems with chaotic motion,” in *Decision and Control, 1989., Proceedings of the 28th IEEE Conference on*, pp. 512–517, IEEE, 1989.
- [6] E. Santor, L. Suchanek, *et al.*, “Unconventional monetary policies: evolving practices, their effects and potential costs,” *Bank of Canada Review*, vol. 2013, no. Spring, pp. 1–15, 2013.
- [7] J. A. Amador, G. Olivar, and F. Angulo, “Smooth and Filippov models of

- sustainable development: Bifurcations and numerical computations,” *Differential Equations and Dynamical Systems*, vol. 21, no. 1-2, pp. 173–184, 2013.
- [8] K. Hill, D. S. Abbot, and M. Silber, “Analysis of an arctic sea ice loss model in the limit of a discontinuous albedo,” *SIAM Journal on Applied Dynamical Systems*, vol. 15, no. 2, pp. 1163–1192, 2016.
- [9] P. Kowalczyk and P. Glendinning, “Boundary-equilibrium bifurcations in piecewise-smooth slow-fast systems,” *Chaos: An Interdisciplinary Journal of Nonlinear Science*, vol. 21, no. 2, p. 023126, 2011.
- [10] J. Leifeld, “Non-smooth homoclinic bifurcation in a conceptual climate model,” *European Journal of Applied Mathematics*, pp. 1–14, 2018.
- [11] J. G. Donohue and P. T. Piiroinen, “Mathematical modelling of seasonal migration with applications to climate change,” *Ecological modelling*, vol. 299, pp. 79–94, 2015.
- [12] M. di Bernardo, C. J. Budd, A. R. Champneys, P. Kowalczyk, A. B. Nordmark, G. O. Tost, and P. T. Piiroinen, “Bifurcations in nonsmooth dynamical systems,” *SIAM review*, vol. 50, no. 4, pp. 629–701, 2008.
- [13] R. I. Leine and H. Nijmeijer, *Dynamics and bifurcations of non-smooth mechanical systems*, vol. 18. Springer Science & Business Media, 2013.
- [14] Z. T. Zhusubaliyev and E. Mosekilde, *Bifurcations and chaos in piecewise-smooth dynamical systems*. World Scientific, 2003.
- [15] M. Di Bernardo, M. I. Feigin, S. Hogan, and M. E. Homer, “Local analysis of c-bifurcations in n-dimensional piecewise-smooth dynamical systems,” *Chaos, Solitons and Fractals: the interdisciplinary journal of Nonlinear Science, and Nonequilibrium and Complex Phenomena*, vol. 11, no. 10, pp. 1881–1908, 1999.

- 
- [16] M. di Bernardo, C. J. Budd, A. R. Champneys, and P. Kowalczyk, *Piecewise-smooth dynamical systems: theory and applications*, vol. 163. Springer Science & Business Media, 2008.
- [17] C. W. Gardiner *et al.*, *Handbook of stochastic methods*, vol. 3. Springer Berlin, 1985.
- [18] D. J. W. Simpson, S. J. Hogan, and R. Kuske, “Stochastic regular grazing bifurcations,” *SIAM Journal on Applied Dynamical Systems*, vol. 12, no. 2, pp. 533–559, 2013.
- [19] D. J. W. Simpson and R. Kuske, “The influence of localized randomness on regular grazing bifurcations with applications to impacting dynamics,” *Journal of Vibration and Control*, p. 1077546316642054, 2016.
- [20] D. J. W. Simpson and R. Kuske, “Stochastic perturbations of periodic orbits with sliding,” *Journal of Nonlinear Science*, vol. 25, no. 4, pp. 967–1014, 2015.
- [21] Z. Li, J. Jiang, and L. Hong, “Noise-induced transition in a piecewise smooth system by generalized cell mapping method with evolving probabilistic vector,” *Nonlinear Dynamics*, vol. 88, no. 2, pp. 1473–1485, 2017.
- [22] J. Kim and K. Wang, “Predicting non-stationary and stochastic activation of saddle-node bifurcation in non-smooth dynamical systems,” *Nonlinear Dynamics*, vol. 93, no. 2, pp. 251–258, 2018.
- [23] T. S. Parker and L. O. Chua, “Efficient solution of the variational equation for piecewise-linear differential equations,” *International journal of circuit theory and applications*, vol. 14, no. 4, pp. 305–314, 1986.
- [24] M. A. Aizerman and F. R. Gantmacher, “Determination of stability by linear approximation of a periodic solution of a system of differential equations with discontinuous right-hand sides,” *The Quarterly Journal of Mechanics and Applied Mathematics*, vol. 11, no. 4, pp. 385–398, 1958.

- [25] F. Bizzarri, A. Brambilla, and S. Callegari, “Efficient and reliable small-signal estimate of quantization noise contribution to phase noise in  $\Delta\Sigma$  Fractional- $N$  PLL,” *IEEE Transactions on Circuits and Systems I: Regular Papers*, vol. 64, no. 6, pp. 1494–1503, 2017.
- [26] D. Agrawal, F. Bizzarri, A. Brambilla, and A. A. Seshia, “Numerical verification of an analytical model for phase noise in mems oscillators,” *IEEE transactions on ultrasonics, ferroelectrics, and frequency control*, vol. 63, no. 8, pp. 1204–1207, 2016.
- [27] M. Biggio, F. Bizzarri, A. Brambilla, and M. Storace, “Accurate and efficient psd computation in mixed-signal circuits: A time-domain approach,” *IEEE Transactions on Circuits and Systems II: Express Briefs*, vol. 61, no. 11, pp. 905–909, 2014.
- [28] J. Adolfsson, H. Dankowicz, and A. Nordmark, “3d passive walkers: Finding periodic gaits in the presence of discontinuities,” *Nonlinear Dynamics*, vol. 24, no. 2, pp. 205–229, 2001.
- [29] H. Dankowicz and P. T. Piiroinen, “Exploiting discontinuities for stabilization of recurrent motions,” *Dynamical Systems*, vol. 17, no. 4, pp. 317–342, 2002.
- [30] E. J. Staunton and P. T. Piiroinen, “Discontinuity mapping for stochastic nonsmooth systems,” *Submitted*, 2019.
- [31] B. Øksendal, *Stochastic differential equations: an introduction with applications*. Springer Science & Business Media, 2013.
- [32] A. Cedilnik, K. Kosmelj, and A. Blejec, “The distribution of the ratio of jointly normal variables,” *Metodoloski zvezki*, vol. 1, no. 1, p. 99, 2004.
- [33] P. E. Kloeden and E. Platen, *Numerical solution of stochastic differential equations*, vol. 23. Springer Science & Business Media, 2013.

- [34] G. Fasano and A. Franceschini, “A multidimensional version of the Kolmogorov–Smirnov test,” *Monthly Notices of the Royal Astronomical Society*, vol. 225, no. 1, pp. 155–170, 1987.
- [35] B. Lau, “multdist GitHub repository.” <https://github.com/brian-lau/multdist>, Commit: 868acf6b7bca1fe65451ced4acad9a59ee77cca5, Accessed 9 September 2019, 2013.
- [36] E. Freire, E. Ponce, and F. Torres, “Canonical discontinuous planar piecewise linear systems,” *SIAM Journal on Applied Dynamical Systems*, vol. 11, no. 1, pp. 181–211, 2012.
- [37] A. Demir and A. Sangiovanni-Vincentelli, *Analysis and simulation of noise in nonlinear electronic circuits and systems*, vol. 425. Springer Science & Business Media, 2012.
- [38] T. Matsumoto, “A chaotic attractor from Chua’s circuit,” *IEEE Transactions on Circuits and Systems*, vol. 31, no. 12, pp. 1055–1058, 1984.
- [39] L. O. Chua, “The genesis of Chua’s circuit,” *International Journal of Electronics Communication*, vol. 46, no. 4, pp. 250–257, 1992.
- [40] L. O. Chua, M. Komuro, and T. Matsumoto, “The double scroll family,” *IEEE transactions on circuits and systems*, vol. 33, no. 11, pp. 1072–1118, 1986.
- [41] M. P. Kennedy, “Robust op amp realization of Chua’s circuit,” *Frequenz*, vol. 46, no. 3-4, pp. 66–80, 1992.
- [42] L. O. Chua, “Chua’s circuit 10 years later,” *International Journal of Circuit Theory and Applications*, vol. 22, no. 4, pp. 279–305, 1994.
- [43] L. O. Chua, “A zoo of strange attractors from the canonical Chua’s circuits,” in *Circuits and Systems, 1992., Proceedings of the 35th Midwest Symposium on*, pp. 916–926, IEEE, 1992.

- [44] L. O. Chua, “Global unfolding of Chua’s circuit,” *IEICE Transactions on Fundamentals of Electronics, Communications and Computer Sciences*, vol. 76, no. 5, pp. 704–734, 1993.
- [45] E. Bilotta and P. Pantano, *A gallery of Chua attractors*, vol. 61. World Scientific, 2008.
- [46] N. V. Stankevich, N. V. Kuznetsov, G. A. Leonov, and L. O. Chua, “Scenario of the birth of hidden attractors in the Chua circuit,” *International Journal of Bifurcation and Chaos*, vol. 27, no. 12, p. 1730038, 2017.
- [47] G. A. Leonov and N. V. Kuznetsov, “Hidden attractors in dynamical systems. from hidden oscillations in Hilbert–Kolmogorov, Aizerman, and Kalman problems to hidden chaotic attractor in Chua circuits,” *International Journal of Bifurcation and Chaos*, vol. 23, no. 01, p. 1330002, 2013.

# Chapter 10

## Paper 4:

# Discontinuity Mappings for Stochastic Nonsmooth Systems

EOGHAN J. STAUNTON, PETRI T. PIROINEN

School of Mathematics, Statistics and Applied Mathematics,  
National University of Ireland, Galway.

---

**Abstract.** For stability and bifurcation analysis involving recurrent behaviour such as periodic orbits, it is important to be able to quantify how nearby trajectories behave by means of a local mapping. In smooth systems these mappings can be computed using the system's variational equations. For piecewise-smooth or hybrid systems the same technique cannot be used without some corrections. This is due to the fact that nearby trajectories can be topologically distinct because they can undergo different sequences of events associated with the system's discontinuity boundaries. To account for this, one can derive *zero-time discontinuity*

*mappings* associated with boundary interactions. In this paper we derive zero-time discontinuity mappings for piecewise-smooth vector fields and hybrid dynamical systems in which the position of the discontinuity boundary has a stochastic component. In particular, we consider systems with stochastically oscillating boundaries and systems with stochastic imperfections on the discontinuity boundary.

---

## 10.1 Introduction

In many cases, modelling of real-world systems in engineering and science naturally gives rise to piecewise-smooth or hybrid dynamical systems. These systems are characterised by having various kinds of discontinuities or switching events. For example, the study of mechanical systems with impacts or friction [1, 2, 3, 4, 5, 6], switching in electrical circuits [7, 8] and relay control systems [9, 10] all naturally lead to such nonsmooth systems. Piecewise-smooth models have also been used to model cellular mitosis [11], climate systems [12], migration [13], ocean convection [14], thermohaline circulation [15] and economic or sociological systems involving decision thresholds [16, 17].

The dynamical systems resulting from these models exhibit all of the behaviour of smooth systems. For example we find invariant sets such as equilibria, periodic orbits and chaotic sets and these sets can undergo smooth bifurcations. However, several unique phenomena also occur in nonsmooth systems including types of bifurcations referred to as *discontinuity-induced bifurcations* (DIBs). Examples include *grazing* bifurcations, *border-collision/boundary-equilibrium* bifurcations, *sliding* bifurcations, *sticking* bifurcations and others [18, 19, 20, 21, 22]. These bifurcations are often caused by the fact that nearby trajectories can undergo different sequences of events by either crossing or not crossing discontinuity boundaries at different times and so

are topologically distinct.

In order to analyse stability and bifurcations in piecewise-smooth and hybrid systems we need to be able to establish the fate of topologically distinct trajectories in the neighbourhood of a reference trajectory. We then quantify this information in a local mapping defined in the neighbourhood such as a fixed-time mapping or Poincaré mapping. In smooth systems these mappings can be constructed using variational equations. For piecewise-smooth or hybrid systems the variational equations are locally ill-posed, and so require special techniques when compared to smooth systems [19, 23].

Discontinuity mappings (DMs) are the key tools that enable us to construct local mappings for trajectories in piecewise-smooth or hybrid dynamical systems, which in turn allow us to study DIBs involving periodic orbits and other invariant sets that are more complex than fixed points [3, 22, 24]. Discontinuity mappings are maps defined locally near the point where a reference trajectory intersects with a discontinuity boundary, encapsulating the effect of switching flows and any other discontinuities associated with the boundary intersection. For piecewise-smooth or hybrid systems, fixed-time mappings associated with trajectories that interact with one or more discontinuity boundaries can be obtained by composing fixed-time mappings for the smooth portions of the flow with the DMs associated with each interaction. The corresponding Poincaré mapping can then be found by appending a final local projection onto the associated Poincaré section. In this paper we will focus on *zero-time discontinuity mappings* (ZDMs), that, as their name suggests, take place in zero time.

In real-world systems a level of noise and uncertainty is ubiquitous. As a result it is necessary to study piecewise-smooth systems, such as those described above, in the presence of noise. The study of how noise affects piecewise-smooth systems is a relatively new field. In-depth studies have been carried out into the effects of noise on grazing bifurcations in impacting systems [25, 26] and on periodic orbits with

sliding [27]. In this paper we will study the effects noisy discontinuity boundaries have on the dynamics of piecewise-smooth systems. We will consider two types of boundary noise, noisy oscillations about the boundary's deterministic position and small noisy imperfections on the deterministic boundary's surface. In particular, we will look to construct *stochastic zero-time discontinuity mappings* (SZDMs) for such systems. These mappings can then be used in a variety of ways. For example they could be used to analyse the effects of boundary noise on bifurcations of invariant sets such as periodic orbits in hybrid and piecewise-smooth systems or to efficiently simulate such systems numerically.

Previously the authors have constructed SZDMs for the particular case of discontinuous piecewise-smooth systems (Filippov systems) with transversal boundary crossings and a stochastically oscillating boundary [28]. That paper showed how SZDMs can be effectively used to estimate and analyse the effects of noise on the dynamics of discontinuous systems. In particular, it showed as an example how SZDMs can be used to predict how noise can affect the periodic attractors of a discontinuous variant of the Chua circuit. This paper will extend the results of that work to a more general class of nonsmooth systems. We will derive SZDMs for transversal crossings in hybrid systems and systems with higher-order discontinuities, cases not considered in [28]. We will also consider non-transversal crossings in a grazing hybrid system. In all cases we will consider two types of noise, stochastic oscillations and stochastic surface imperfections, only the former was considered in [28].

The remainder of this paper is organised as follows. Section 10.2 describes deterministic hybrid and piecewise-smooth systems and the use of ZDMs in that context. In Section 10.3 we present a method of constructing temporal stochastic processes suitable to describe the stochastic component of the position of a discontinuity boundary. We also describe how we can use these processes to construct a spatial stochastic processes on  $\mathbb{R}^n$  suitable to describe the stochastic component of *rugged* boundaries, where the small-scale structure is uncertain. In Section 10.4 we describe linearisation

techniques for stochastic hybrid systems with transversal discontinuity-boundary interactions. In Section 10.5 we consider transversal crossings in continuous piecewise-smooth vector fields with higher-order discontinuities and stochastic boundaries as the errors introduced by noise in this case can not be captured by linearisation. Finally, in Section 10.6 we construct SZDMs for a sample hybrid system undergoing grazing, in particular we consider an impact oscillator with many degrees of freedom. We then present some illustrative examples in Section 10.7 and the paper concludes in Section 10.8 with a discussion on possible further generalisations.

## 10.2 Deterministic Piecewise-smooth and Hybrid Dynamical Systems

In this paper we will describe smooth dynamical systems as initial-value problems (IVPs) given by

$$\dot{\mathbf{x}} = \mathbf{f}(\mathbf{x}), \quad \mathbf{x}(0) = \mathbf{x}_0, \quad (10.1)$$

where  $\mathbf{x} \in \mathbb{R}^n$  is the state,  $\dot{\mathbf{x}} \in \mathbb{R}^n$  is the time derivative of the state and  $\mathbf{f}$ , which is  $\mathcal{C}^k$  ( $k \geq 1$ ), is the corresponding vector field. We also define the flow function  $\phi(\mathbf{x}, t)$ , which is  $\mathcal{C}^k$  in its arguments, as the collection of trajectories given by  $\mathbf{f}$ , such that the unique solution to (10.1) can be written as

$$\mathbf{x}(t) = \phi(\mathbf{x}_0, t). \quad (10.2)$$

We will further define piecewise-smooth dynamical systems as IVPs given by

$$\begin{aligned} \dot{\mathbf{x}} &= \mathbf{f}_i(\mathbf{x}), \quad \mathbf{x} \in \mathcal{S}_i \\ \mathbf{x}(0) &= \mathbf{x}_0, \end{aligned} \quad (10.3)$$

where  $\cup_i \mathcal{S}_i = \mathbb{R}^n$  and each  $\mathcal{S}_i$ , with corresponding  $\mathcal{C}^k$  vector field  $\mathbf{f}_i$ , has a nonempty

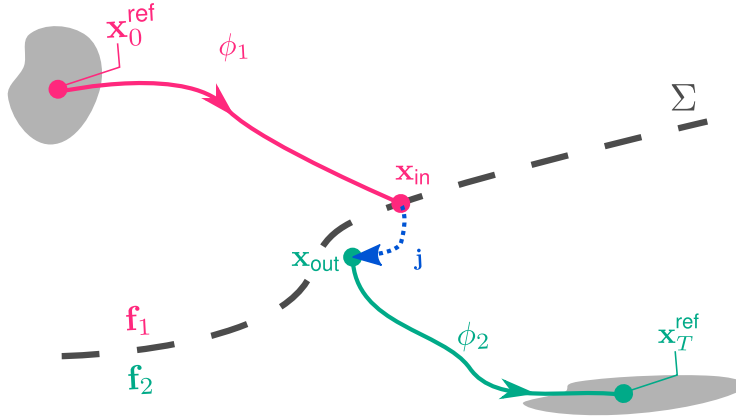


**Figure 10.1:** Schematic of a reference trajectory intersecting a discontinuity boundary transversally in a hybrid system.

interior. The indices  $i$  range over some finite indexing set and the intersection  $\Sigma_{ij} = \mathcal{S}_i \cap \mathcal{S}_j$  is either the empty set or an  $(n - 1)$ -dimensional manifold that is the boundary between  $\mathcal{S}_i$  and  $\mathcal{S}_j$ . A hybrid system is a generalisation of a piecewise-smooth dynamical system where a non-identity mapping  $\mathbf{j}_{ij}$  is applied on the boundary  $\Sigma_{ij}$ . In other words, a hybrid system is a dynamical system defined by the IVP

$$\begin{aligned} \dot{\mathbf{x}} &= \mathbf{f}_i(\mathbf{x}), \quad \mathbf{x} \in \mathcal{S}_i, \\ \mathbf{x}(0) &= \mathbf{x}_0, \end{aligned} \tag{10.4}$$

plus the set of jump maps

$$\mathbf{x} \rightarrow \mathbf{j}_{ij}(\mathbf{x}), \quad \mathbf{x} \in \Sigma_{ij}. \tag{10.5}$$

### 10.2.1 Transversal Crossings

Suppose now that we wish to calculate the local mapping of a trajectory that interacts with at least one of the system discontinuity boundaries  $\Sigma_{ij}$ . This will require us to define a DM associated with each boundary interaction local to the point of intersection of the trajectory with the boundary. In this paper we will restrict our attention to trajectories that cross at codimension-1 points. In other words, we

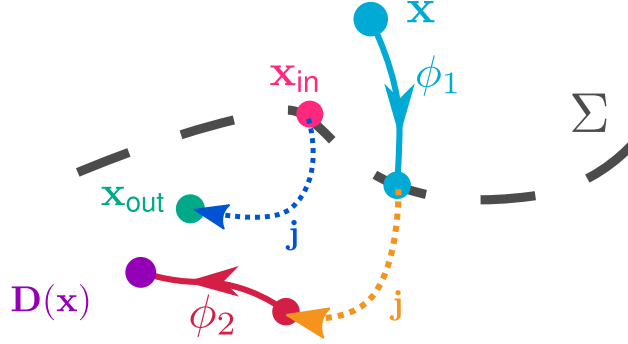


**Figure 10.2:** Deriving the zero-time discontinuity mapping  $\mathbf{D}(\mathbf{x})$  for transversal boundary crossings.  $\mathbf{D}$  takes a point  $\mathbf{x}$  in the neighbourhood of  $\mathbf{x}_{\text{in}}$ , to the boundary by evolving for a time  $t(\mathbf{x})$  under the flow associated with  $\mathbf{f}_1$  (blue), applies the jump mapping  $\mathbf{j}$  (orange) and corrects for zero time by evolving for  $-t(\mathbf{x})$  under the flow associated with  $\mathbf{f}_2$  (red).

will ignore cases where two or more discontinuity boundaries intersect. Given this restriction, when constructing the DM locally, we can consider a piecewise-smooth or hybrid system with two regions separated by a single discontinuity boundary such as the one shown in Figure 10.1. Appropriately relabelling  $\mathbf{f}_i, \mathbf{f}_j, \mathcal{S}_i, \mathcal{S}_j$  and  $\Sigma_{ij}$  locally, we consider the system defined by the IVP

$$\begin{aligned} \dot{\mathbf{x}} &= \begin{cases} \mathbf{f}_1(\mathbf{x}) & \mathbf{x} \in S^-, \\ \mathbf{f}_2(\mathbf{x}) & \mathbf{x} \in S^+, \end{cases} & \mathbf{x}(0) = \mathbf{x}_0, \\ \mathbf{x} &\rightarrow \mathbf{j}(\mathbf{x}), & \mathbf{x} \in \Sigma. \end{aligned} \quad (10.6)$$

We let the discontinuity boundary

$$\Sigma = \{\mathbf{x} : h(\mathbf{x}, t) = 0\} \quad (10.7)$$

be defined by the zeros of a  $\mathcal{C}^k$  real valued function  $h$ , where  $k \geq 1$ , that separates the state space into the two regions

$$\mathcal{S}^- = \{\mathbf{x} : h(\mathbf{x}, t) < 0\} \quad \text{and} \quad \mathcal{S}^+ = \{\mathbf{x} : h(\mathbf{x}, t) > 0\}. \quad (10.8)$$

Here, we assume the reference trajectory, with initial point  $\mathbf{x}_0^{\text{ref}}$ , crosses the discontinuity boundary transversally at time  $t_{\text{ref}}$ , i.e.

$$h(\phi_1(\mathbf{x}_0^{\text{ref}}, t_{\text{ref}})) = 0, \quad \text{and} \quad h_{\mathbf{x}}(\phi_1(\mathbf{x}_0^{\text{ref}}, t_{\text{ref}}))\mathbf{f}(\phi_1(\mathbf{x}_0^{\text{ref}}, t_{\text{ref}})) \neq 0, \quad (10.9)$$

where  $\phi_1$  is the flow function prior to reaching  $\Sigma$  with corresponding vector field  $\mathbf{f}_1$ . After the discontinuity the flow function is given by  $\phi_2$  with corresponding vector field  $\mathbf{f}_2$ , and so after a time  $T > t_{\text{ref}}$  the trajectory reaches the point

$$\mathbf{x}_T^{\text{ref}} = \phi_2(\mathbf{j}(\phi_1(\mathbf{x}_0^{\text{ref}}, t_{\text{ref}})), T - t_{\text{ref}}). \quad (10.10)$$

We further assume that the vector fields  $\mathbf{f}_1$  and  $\mathbf{f}_2$  and their corresponding flows are smoothly extendible in a neighbourhood of  $\mathbf{x}_{\text{in}}$  and  $\mathbf{x}_{\text{out}}$ , respectively. Since we are interested in a representation of the flow of the overall system for trajectories with initial conditions  $\mathbf{x}_0 \approx \mathbf{x}_0^{\text{ref}}$  and total time  $T$  we study the mapping

$$\phi(\mathbf{x}_0, T) = \phi_2(\mathbf{j}(\phi_1(\mathbf{x}_0, t)), T - t), \quad (10.11)$$

where  $t = t(\mathbf{x}_0)$  is the time of flight to reach the discontinuity boundary. Note that

$$t(\mathbf{x}_0) = t_{\text{ref}} + t(\phi_1(\mathbf{x}_0, t_{\text{ref}})), \quad (10.12)$$

where  $t(\phi_1(\mathbf{x}_0, t_{\text{ref}}))$  is possibly negative. Since  $t(\mathbf{x}_0) \neq t_{\text{ref}}$  a trajectory starting at  $\mathbf{x}_0$  is topologically distinct from the reference trajectory. In order to account for this we want to construct a ZDM  $\mathbf{D}(\mathbf{x})$  for  $\mathbf{x}$  in a neighbourhood of  $\mathbf{x}_{\text{in}}$  such that

$$\phi(\mathbf{x}_0, T) = \phi_2(\mathbf{D}(\phi_1(\mathbf{x}_0, t_{\text{ref}})), T - t_{\text{ref}}). \quad (10.13)$$

Referring to (10.12), we find that the appropriate  $\mathbf{D}(\mathbf{x})$  is given by

$$\mathbf{D}(\mathbf{x}) = \phi_2(\mathbf{j}(\phi_1(\mathbf{x}, t(\mathbf{x}))), -t(\mathbf{x})). \quad (10.14)$$

The map  $\mathbf{D}$  takes a point in a neighbourhood of  $\mathbf{x}_{\text{in}}$  and maps it to a point in a neighbourhood of  $\mathbf{x}_{\text{out}}$  by moving backwards and forwards by the same amount of time along the trajectories given by  $\phi_1$  and  $\phi_2$  and applying the jump map  $\mathbf{j}$  as shown in Figure 10.2. This setup will be used in Sections 10.4 and 10.5 where we will construct stochastic ZDMs (or SZDMs)  $\tilde{\mathbf{D}}(\mathbf{x})$  for hybrid and piecewise-smooth systems with stochastic boundaries in this manner.

## 10.2.2 Grazing Interactions

In Section 10.6 we will consider an example of an SZDM for a non-transversal grazing boundary interaction, see Figure 10.3. We assume the reference trajectory, with initial point  $\mathbf{x}_0^{\text{ref}}$ , grazes the discontinuity boundary  $\Sigma$  at the point  $\mathbf{x}^*$  at time  $t_1$ , i.e.

$$h(\phi(\mathbf{x}_0^{\text{ref}}, t_{\text{ref}})) = h(\mathbf{x}^*) = 0 \quad \text{and} \quad h_{\mathbf{x}}(\mathbf{x}^*)\mathbf{f}(\mathbf{x}^*) = 0. \quad (10.15)$$

After a time  $T = t_1 + t_2$  the trajectory reaches the point

$$\mathbf{x}_T^{\text{ref}} = \phi(\mathbf{j}(\phi(\mathbf{x}_0^{\text{ref}}, t_1)), t_2) = \phi(\phi(\mathbf{x}_0^{\text{ref}}, t_1), t_2), \quad (10.16)$$

where  $\mathbf{j}(\mathbf{x}^*) = \mathbf{x}^*$  is the identity mapping for grazing points.

Here we will give a brief overview of how the ZDM associated with such a grazing trajectory can be constructed in the deterministic case. We consider a hybrid system such that all dynamics take place in  $\mathcal{S}^+ \cup \Sigma$  with the smooth evolution of the system governed by

$$\dot{\mathbf{x}} = \mathbf{f}(\mathbf{x}), \quad \mathbf{x} \in \mathcal{S}^+, \quad (10.17)$$

which is smoothly extendible into  $\mathcal{S}^-$ . Points on  $\Sigma$  are grouped into incoming trajectories where  $h_{\mathbf{x}}(\mathbf{x})\mathbf{f}(\mathbf{x}) < 0$ , grazing trajectories where  $h_{\mathbf{x}}(\mathbf{x})\mathbf{f}(\mathbf{x}) = 0$  and outgoing trajectories where  $h_{\mathbf{x}}(\mathbf{x})\mathbf{f}(\mathbf{x}) > 0$ . The jump map  $\mathbf{j} : \Sigma \rightarrow \Sigma$  maps points on incoming trajectories to points on outgoing trajectories and is the identity for

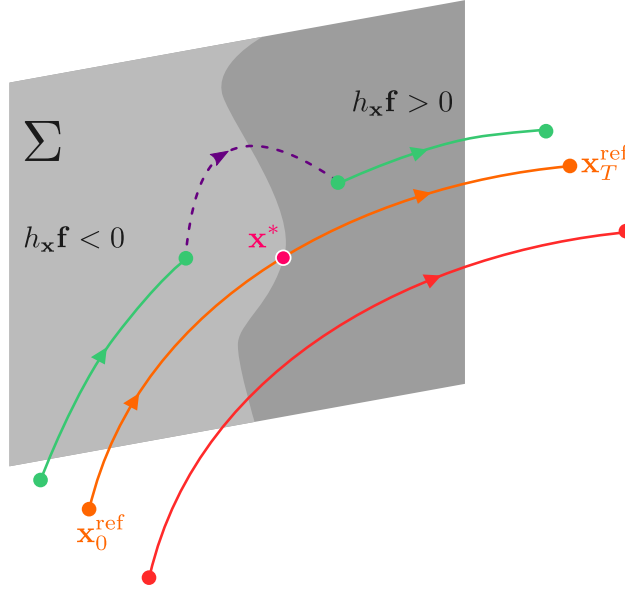


**Figure 10.3:** Schematic of a reference trajectory (orange) which grazes the discontinuity boundary  $\Sigma$  at  $\mathbf{x}^*$  and two nearby trajectories, one which does not impact  $\Sigma$  (red) and one which impacts  $\Sigma$  at low normal velocity (green).

grazing trajectories.

Consider a grazing reference trajectory such as the one shown in Figure 10.3. Taking points  $\mathbf{x}_0$  in a neighbourhood of  $\mathbf{x}_0^{\text{ref}}$  and evolving for time  $T = t_1 + t_2$  we note that trajectories will either intersect  $\Sigma$  in a neighbourhood of  $\mathbf{x}^*$  at a time close to  $t_1$  or not intersect  $\Sigma$  at all. We want to construct a ZDM  $\mathbf{D}(\mathbf{x})$  defined in a neighbourhood of  $\mathbf{x}^*$  such that the local mapping from a neighbourhood of  $\mathbf{x}_0^{\text{ref}}$  to a neighbourhood of  $\mathbf{x}_T^{\text{ref}}$  is given by

$$\phi(\mathbf{D}(\phi(\mathbf{x}, t_1)), t_2). \quad (10.18)$$

In the case of trajectories that do not intersect the boundary and grazing points  $\mathbf{D}$  is trivially the identity. In the case of intersecting trajectories we construct  $\mathbf{D}$  in the manner shown in Figure 10.4. For intersecting points  $\mathbf{x}_0$  in a neighbourhood of  $\mathbf{x}_0^{\text{ref}}$ ,  $\mathbf{x} = \phi(\mathbf{x}_0, t_1)$  is in a neighbourhood of  $\mathbf{x}^*$ . We let  $t_c(\mathbf{x})$  be the (possibly negative) time of flight from  $\mathbf{x}$  to  $\Sigma$ . Then the appropriate ZDM takes intersecting points  $\mathbf{x}$  in a neighbourhood of  $\mathbf{x}^*$  to the boundary at  $\mathbf{x}_1 = \phi(\mathbf{x}, t_c(\mathbf{x}))$ , then the jump map is applied, sending  $\mathbf{x}_1$  to  $\mathbf{x}_2 = \mathbf{j}(\mathbf{x}_1)$ , finally it corrects to zero time by sending  $\mathbf{x}_2$  to

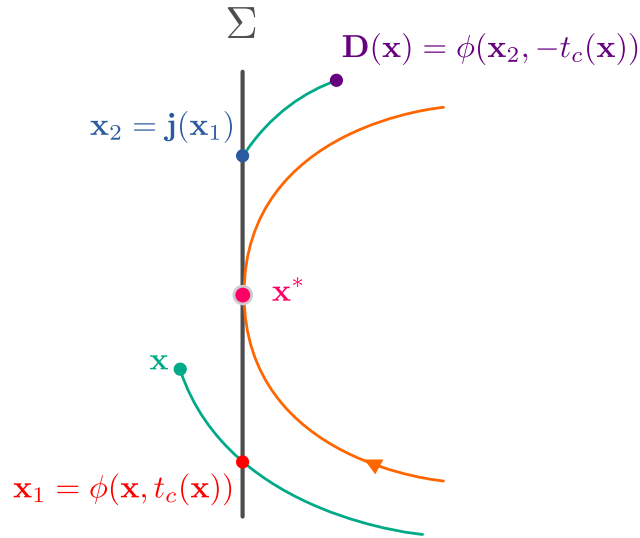


**Figure 10.4:** Deriving the zero-time discontinuity mapping  $\mathbf{D}(\mathbf{x})$  for a grazing trajectory.  $\mathbf{D}$  takes a point  $\mathbf{x}$ , on an impacting trajectory in the neighbourhood of  $\mathbf{x}^*$ , to the point  $\mathbf{x}_1$  on the boundary by flowing for a time  $t_c(\mathbf{x})$ , applies the jump mapping  $\mathbf{j}$  to arrive at  $\mathbf{x}_2$  and finally corrects for zero time by flowing for a time  $-t_c(\mathbf{x})$  to arrive at  $\mathbf{D}(\mathbf{x})$ .

$\mathbf{x}_3 = \phi(\mathbf{x}_2, -t_c(\mathbf{x}))$ . In other words  $\mathbf{D}(\mathbf{x})$  is given by

$$\mathbf{D}(\mathbf{x}) = \phi(\mathbf{j}(\phi(\mathbf{x}, t_c(\mathbf{x}))), -t_c(\mathbf{x})). \quad (10.19)$$

This method of constructing a ZDM for a grazing trajectory will form the basis of our construction of SZDMs for grazing trajectories interacting with stochastic discontinuity boundaries in Section 10.6.

### 10.3 Stochastic Processes

In this section we will introduce a method for constructing stochastic processes  $P(t)$  that may be suitable to describe the noisy component of the position of a stochastically oscillating boundary. We will describe deterministic discontinuity boundaries  $\Sigma$  in state space by the zeros of a real valued function  $h = h(\mathbf{x})$ , and

stochastically oscillating boundaries  $\tilde{\Sigma}$  by the zeros of  $\tilde{h} = \tilde{h}(\mathbf{x}, t) = h(\mathbf{x}) - P(t)$ , i.e.

$$\Sigma = \{\mathbf{x} : h(\mathbf{x}) = 0\} \quad \text{and} \quad \tilde{\Sigma} = \{\mathbf{x} : \tilde{h}(\mathbf{x}, t) = 0\}, \quad (10.20)$$

respectively. In general, we will require the constructed position process  $P(t)$  to be mean reverting with zero mean and to be at least once differentiable. Depending on the SZDM we are constructing we may also require higher-order differentiability.

The processes we construct will be Gaussian and constructed iteratively. They can be thought of as generalised Ornstein-Uhlenbeck processes. An Ornstein-Uhlenbeck Itô process [29] is a process given by

$$d\xi(t) = -\theta\xi(t)dt + \sigma dW_t, \quad \xi(0) = \xi_0, \quad (10.21)$$

where  $\theta, \sigma \in \mathbb{R}$  are positive parameters. This gives that

$$\begin{aligned} \xi(t) &= e^{-\theta t}\xi_0 + \sigma \int_0^t e^{\theta(s-t)} dW_s \\ &\sim N\left(e^{-\theta t}\xi_0, \frac{\sigma^2(1 - e^{-2\theta t})}{2\theta}\right) \\ &\sim N(\mu_\xi(t), \sigma_\xi^2(t)). \end{aligned} \quad (10.22)$$

Ornstein-Uhlenbeck processes have an inherent timescale, making them a good choice for modeling noise in real-world systems, especially noise in mechanical systems such as noise arising from vibrations external to the system under study [30]. All of the examples considered in Section 10.7 will use the processes derived here, however the results hold for any processes that satisfy the necessary mean reversion and differentiability requirements.

Using the Ornstein-Uhlenbeck process (10.21) as our base process  $P_0(t) = \xi(t)$  we construct an  $n$ -time differentiable mean-reverting position process  $P_n(t)$  as

$$\frac{dP_n}{dt}(t) = -\theta_n P_n(t) + \sigma_n P_{n-1}(t), \quad n \geq 1. \quad (10.23)$$

We denote the corresponding velocity and acceleration processes as  $V_n = dP_n/dt$  and  $A_n = d^2P_n/dt^2$ , respectively. We note that  $V_n$  exists for  $n \geq 1$  and  $A_n$  exists for  $n \geq 2$ . For simplicity in the examples presented here we will choose  $\theta_i = \theta$  and  $\sigma_i = \sigma$  for all  $i = 1, 2, \dots, n$ . The distributions of  $P_n$ ,  $V_n$  and  $A_n$  are Gaussian and their associated means, variances and covariances are given in Appendix 10.A.

In this paper we will also consider rugged boundaries, i.e. boundaries with a stochastic small-scale structure defined by a stochastic process on  $\chi(\mathbf{x})$  on  $\mathbb{R}^n$ . In this case the stochastic boundary  $\tilde{\Sigma}$  is given by

$$\tilde{\Sigma} = \{\mathbf{x} : \tilde{h}(\mathbf{x}) = 0\}, \quad (10.24)$$

where  $\tilde{h}(\mathbf{x}) = h(\mathbf{x}) - \chi(\mathbf{x})$ . We note that the Gaussian processes derived in this section may also be used to define distributions  $\chi_i(x_i)$  on the state space component  $x_i$  for  $i = 1, 2, \dots, n$  rather than on time  $t$ . We can then construct a distribution  $\chi(\mathbf{x})$  on  $\mathbb{R}^n$  as

$$\chi(\mathbf{x}) = \sum_{i=1}^n \chi_i(x_i). \quad (10.25)$$

## 10.4 Hybrid Systems

### 10.4.1 Stochastically Oscillating Boundaries

In this section we derive the SZDM for a hybrid system with a stochastically varying boundary given by

$$\tilde{\Sigma} = \{\mathbf{x} : \tilde{h}(\mathbf{x}, t) = 0\} \quad (10.26)$$

where

$$\tilde{h}(\mathbf{x}, t) = h(\mathbf{x}, t) - P(t). \quad (10.27)$$

Leading on from the discussion in Section 10.2.1, we consider a trajectory starting at a point  $\mathbf{x}_0^{\text{ref}}$  that intersects the deterministic boundary  $\Sigma$  after time  $t = t_{\text{ref}}$ ,

i.e.  $h(\phi_1(\mathbf{x}_0^{\text{ref}}, t_{\text{ref}}), t_{\text{ref}}) = 0$ . Our approach is based on the method derived for discontinuous piecewise-smooth systems by the authors in [28]. In order to deal with the fact that the boundary oscillates stochastically we will extend the state space, vector field and jump map to

$$\bar{\mathbf{x}} = (\mathbf{x}, \Delta t_{\text{ref}}, t)^T, \quad \bar{\mathbf{f}} = (\mathbf{f}, 0, 1)^T \quad \text{and} \quad \bar{\mathbf{j}} = (\mathbf{j}, \Delta t_{\text{ref}}, t)^T, \quad (10.28)$$

respectively. Here  $\Delta t_{\text{ref}} = \tilde{t}_{\text{ref}} - t_{\text{ref}}$  is the difference between the time of flight of the reference trajectory to the border in the stochastic system and the deterministic system.

The time-dependent perturbation  $P(t)$  is a small amplitude mean-reverting stochastic process with mean 0, and for example one could consider the position processes introduced in Section 10.3. As a result, the true time of flight to the boundary  $\tilde{t}_{\text{ref}} \approx t_{\text{ref}}$ , where  $t_{\text{ref}}$  is the time of flight in the deterministic system. For  $t \approx t_{\text{ref}}$  and expanding about  $t_{\text{ref}}$  we find that

$$\begin{aligned} \tilde{h}(\phi_1(\mathbf{x}_0^{\text{ref}}, t), t) &= h(\phi_1(\mathbf{x}_0^{\text{ref}}, t), t) - P(t) \\ &= h(\phi_1(\mathbf{x}_0^{\text{ref}}, t_{\text{ref}}), t_{\text{ref}}) - P(t_{\text{ref}}) \\ &\quad + (h_{\mathbf{x}}(\phi_1(\mathbf{x}_0^{\text{ref}}, t_{\text{ref}}), t_{\text{ref}}) \mathbf{f}_1(\phi_1(\mathbf{x}_0^{\text{ref}}, t_{\text{ref}})) \\ &\quad + h_t(\phi_1(\mathbf{x}_0^{\text{ref}}, t_{\text{ref}}), t_{\text{ref}}) - V(t_{\text{ref}})) (t - t_{\text{ref}}) + \mathcal{O}((t - t_{\text{ref}})^2) \\ &\approx (t - t_{\text{ref}}) (h_{\mathbf{x}}(\mathbf{x}_{\text{in}}, t_{\text{ref}}) \mathbf{f}_{\text{in}} + h_t(\mathbf{x}_{\text{in}}, t_{\text{ref}}) - V(t_{\text{ref}})) - P(t_{\text{ref}}), \end{aligned} \quad (10.29)$$

where  $\mathbf{x}_{\text{in}} = \phi_1(\mathbf{x}_0^{\text{ref}}, t_{\text{ref}})$  and  $\mathbf{f}_{\text{in}} = \mathbf{f}_1(\mathbf{x}_{\text{in}})$  and  $V(t) = dP/dt$  is the stochastic component of the discontinuity boundary's velocity. Equation (10.29) implies that  $\Delta t_{\text{ref}}$  is given to first order by

$$\Delta t_{\text{ref}} = \frac{P(t_{\text{ref}})}{h_{\mathbf{x}}(\mathbf{x}_{\text{in}}, t_{\text{ref}}) \mathbf{f}_{\text{in}} + h_t(\mathbf{x}_{\text{in}}, t_{\text{ref}}) - V(t_{\text{ref}}|P(t_{\text{ref}}))}. \quad (10.30)$$

We will also denote  $\mathbf{x}_{\text{out}} = \mathbf{j}(\mathbf{x}_{\text{in}})$  and  $\mathbf{f}_{\text{out}} = \mathbf{f}_2(\mathbf{x}_{\text{out}})$ . We can now think of the realisation of the deterministic trajectory in the stochastic system as

$$\bar{\phi}(\hat{\mathbf{x}}_0^{\text{ref}}, T) = \bar{\phi}((\mathbf{x}_0^{\text{ref}}, 0, 0)^T, T) = (\phi(\mathbf{x}_0^{\text{ref}}, T), 0, T)^T, \quad (10.31)$$

where  $\hat{\mathbf{x}}_0^{\text{ref}} = (\mathbf{x}_0^{\text{ref}}, 0, 0)^T$ . Our approach will be to linearise about this realisation of the deterministic trajectory in the stochastic system. We denote the values associated with the deterministic ZDM as

$$\hat{\mathbf{x}}_{\text{in}} = \bar{\phi}_1(\hat{\mathbf{x}}_0^{\text{ref}}, t_{\text{ref}}), \quad \hat{\mathbf{f}}_{\text{in}} = \bar{\mathbf{f}}_1(\hat{\mathbf{x}}_{\text{in}}), \quad \hat{\mathbf{x}}_{\text{out}} = \bar{\mathbf{j}}(\hat{\mathbf{x}}_{\text{in}}), \quad \hat{\mathbf{f}}_{\text{out}} = \bar{\mathbf{f}}_2(\hat{\mathbf{x}}_{\text{out}}). \quad (10.32)$$

For simplicity, we will drop the bars and refer to  $\mathbf{x}$  and  $\mathbf{f}$  when considering the extended state space, where there is no ambiguity. Following this, we are thus studying the SZDM

$$\phi(\mathbf{x}_0, T) = \phi_2(\mathbf{j}(\phi_1(\mathbf{x}_0, t)), T - t), \quad (10.33)$$

where the random variable  $t = t(\mathbf{x}_0)$  is the time of flight from  $\mathbf{x}_0$  to the boundary. We have that

$$t(\mathbf{x}_0) = \tilde{t}_{\text{ref}} + t(\phi_1(\mathbf{x}_0, t_{\text{ref}})) = t_{\text{ref}} + \Delta t_{\text{ref}} + t(\phi_1(\mathbf{x}_0, \tilde{t}_{\text{ref}})), \quad (10.34)$$

and so we can write (10.33) as

$$\begin{aligned} \phi(\mathbf{x}_0, T) = \phi_2(\phi_2(\phi_2(\mathbf{j}(\phi_1(\phi_1(\phi_1(\mathbf{x}_0, t_{\text{ref}}), \Delta t_{\text{ref}}), t(\phi_1(\mathbf{x}_0, \tilde{t}_{\text{ref}}))))), \\ -t(\phi_1(\mathbf{x}_0, \tilde{t}_{\text{ref}}))), -\Delta t_{\text{ref}}), T - t_{\text{ref}}). \end{aligned} \quad (10.35)$$

This gives that

$$\phi(\mathbf{x}_0, T) = \phi_2(\bar{\mathbf{D}}(\phi_1(\mathbf{x}_0, t_{\text{ref}})), T - t_{\text{ref}}), \quad (10.36)$$

where

$$\widetilde{\mathbf{D}}(\mathbf{x}) = \phi_2(\phi_2(\mathbf{j}(\phi_1(\phi_1(\mathbf{x}, \Delta t_{\text{ref}}), t(\phi_1(\mathbf{x}, \Delta t_{\text{ref}}))), -\Delta t_{\text{ref}}), -t(\phi_1(\mathbf{x}, \Delta t_{\text{ref}}))). \quad (10.37)$$

Setting

$$\tilde{t}(\mathbf{x}) = t(\phi_1(\mathbf{x}, \Delta t_{\text{ref}})) + \Delta t_{\text{ref}}, \quad (10.38)$$

we rewrite (10.37) as

$$\widetilde{\mathbf{D}}(\mathbf{x}) = \phi_2(\mathbf{j}(\phi_1(\mathbf{x}, \tilde{t}(\mathbf{x}))), -\tilde{t}(\mathbf{x})). \quad (10.39)$$

Differentiating  $\widetilde{\mathbf{D}}$  with respect to  $\mathbf{x}$  we find

$$\begin{aligned} \widetilde{\mathbf{D}}_{\mathbf{x}}(\mathbf{x}) &= \phi_{2,\mathbf{x}}(\phi_1(\mathbf{x}, \tilde{t}(\mathbf{x})), -\tilde{t}(\mathbf{x}))\mathbf{j}_{\mathbf{x}}(\phi_{1,\mathbf{x}}(\mathbf{x}, \tilde{t}(\mathbf{x})))\phi_{1,\mathbf{x}}(\mathbf{x}, \tilde{t}(\mathbf{x})) \\ &+ [\phi_{2,\mathbf{x}}(\phi_1(\mathbf{x}, \tilde{t}(\mathbf{x})), -\tilde{t}(\mathbf{x}))\mathbf{j}_{\mathbf{x}}(\phi_{1,\mathbf{x}}(\mathbf{x}, \tilde{t}(\mathbf{x})))\phi_{1,t}(\mathbf{x}, \tilde{t}(\mathbf{x})) \\ &\quad - \phi_{2,t}(\phi_1(\mathbf{x}, \tilde{t}(\mathbf{x})), -\tilde{t}(\mathbf{x}))] \tilde{t}_{\mathbf{x}}(\mathbf{x}). \end{aligned} \quad (10.40)$$

Specifically, at  $\mathbf{x} = \hat{\mathbf{x}}_{\text{in}}$ ,  $\tilde{t}(\mathbf{x}) = \tilde{t}(\hat{\mathbf{x}}_{\text{in}}) = 0$  we find

$$\widetilde{\mathbf{D}}_{\mathbf{x}}(\hat{\mathbf{x}}_{\text{in}}) = \mathbf{j}_{\mathbf{x}}(\hat{\mathbf{x}}_{\text{in}}) + (\mathbf{j}_{\mathbf{x}}(\hat{\mathbf{x}}_{\text{in}})\hat{\mathbf{f}}_{\text{in}} - \hat{\mathbf{f}}_{\text{out}})\tilde{t}_{\mathbf{x}}(\hat{\mathbf{x}}_{\text{in}}). \quad (10.41)$$

It now remains to find an expression for  $\tilde{t}_{\mathbf{x}}(\hat{\mathbf{x}}_{\text{in}})$ . By definition,  $t = \tilde{t}(\mathbf{x})$  is a solution to the equation

$$\tilde{h}(\phi_1(\mathbf{x}, t)) = 0. \quad (10.42)$$

Now, differentiating  $\tilde{h}$  with respect to  $t$  and evaluating at  $(\mathbf{x}, t) = (\hat{\mathbf{x}}_{\text{in}}, t^*(\hat{\mathbf{x}}_{\text{in}})) = (\hat{\mathbf{x}}_{\text{in}}, 0)$ , we obtain

$$\tilde{h}_{\mathbf{x}}(\phi_1(\hat{\mathbf{x}}_{\text{in}}, 0))\phi_{1,t}(\hat{\mathbf{x}}_{\text{in}}, 0) = \tilde{h}_{\mathbf{x}}(\hat{\mathbf{x}}_{\text{in}})\hat{\mathbf{f}}_{\text{in}}. \quad (10.43)$$

By the implicit function theorem it follows that  $\tilde{t}(\mathbf{x})$  is a  $\mathcal{C}^1$  function in a neighbour-

hood of  $\hat{\mathbf{x}}_{\text{in}}$  such that

$$\tilde{t}_{\mathbf{x}}(\hat{\mathbf{x}}_{\text{in}}) = -\frac{\tilde{h}_{\mathbf{x}}(\hat{\mathbf{x}}_{\text{in}})}{\tilde{h}_{\mathbf{x}}(\hat{\mathbf{x}}_{\text{in}})\hat{\mathbf{f}}_{\text{in}}}. \quad (10.44)$$

Projecting back onto the state space  $(\mathbf{x}, \Delta t_{\text{ref}})$  (10.44) becomes

$$\begin{aligned} \tilde{t}_{\mathbf{x}}(\hat{\mathbf{x}}_{\text{in}}) &= -\frac{\tilde{h}_{\mathbf{x}}(\hat{\mathbf{x}}_{\text{in}}, t_{\text{ref}})}{h_{\mathbf{x}}(\hat{\mathbf{x}}_{\text{in}}, t_{\text{ref}})\hat{\mathbf{f}}_{\text{in}} + \hat{h}_t(\mathbf{x}_{\text{in}}, t_{\text{ref}}) - V(t_{\text{ref}}|P(t_{\text{ref}}) = 0)} \\ &= \left( -\frac{h_{\mathbf{x}}(\mathbf{x}_{\text{in}}, t_{\text{ref}})}{h_{\mathbf{x}}(\mathbf{x}_{\text{in}}, t_{\text{ref}})\hat{\mathbf{f}}_{\text{in}} + h_t(\mathbf{x}_{\text{in}}, t_{\text{ref}}) - V(t_{\text{ref}}|P(t_{\text{ref}}) = 0)}, 1 \right) \end{aligned} \quad (10.45)$$

since the second component of  $\tilde{t}_{\mathbf{x}}(\hat{\mathbf{x}}_{\text{in}})$  is

$$\left. \frac{\partial \tilde{t}(\mathbf{x})}{\partial \Delta t_{\text{ref}}} \right|_{\mathbf{x}=\hat{\mathbf{x}}_{\text{in}}} = 1 \quad (10.46)$$

by definition. In (10.45)  $V(t|P(t) = p)$  is the stochastic velocity of the boundary at time  $t$  given its stochastic position. Projecting from the state space given in (10.28) to the state space  $(\mathbf{x}, \Delta t_{\text{ref}})$  we can now write

$$\begin{aligned} \overline{\tilde{\mathbf{D}}}_{\mathbf{x}}(\hat{\mathbf{x}}_{\text{in}}) &= \mathbf{j}_{\mathbf{x}}(\hat{\mathbf{x}}_{\text{in}}, t_{\text{ref}}) + \frac{(\hat{\mathbf{f}}_{\text{out}} - \mathbf{j}_{\mathbf{x}}(\hat{\mathbf{x}}_{\text{in}}, t_{\text{ref}})\hat{\mathbf{f}}_{\text{in}} - \mathbf{j}_t(\hat{\mathbf{x}}_{\text{in}}, t_{\text{ref}}))\tilde{h}_{\mathbf{x}}(\hat{\mathbf{x}}_{\text{in}}, t_{\text{ref}})}{\tilde{h}_{\mathbf{x}}(\hat{\mathbf{x}}_{\text{in}}, t_{\text{ref}})\hat{\mathbf{f}}_{\text{in}} + h_t(\hat{\mathbf{x}}_{\text{in}}, t_{\text{ref}}) - V(t_{\text{ref}}|P(t_{\text{ref}}) = 0)} \\ &= \begin{pmatrix} \overline{\tilde{\mathbf{D}}}_{\mathbf{x}}(\mathbf{x}_{\text{in}}) & \mathbf{j}_{\mathbf{x}}(\mathbf{x}_{\text{in}}, t_{\text{ref}})\mathbf{f}_{\text{in}} + \mathbf{j}_t(\mathbf{x}_{\text{in}}, t_{\text{ref}}) - \mathbf{f}_{\text{out}} \\ 0 & 1 \end{pmatrix}, \end{aligned} \quad (10.47)$$

where

$$\overline{\tilde{\mathbf{D}}}_{\mathbf{x}}(\mathbf{x}_{\text{in}}) = \mathbf{j}_{\mathbf{x}}(\mathbf{x}_{\text{in}}, t_{\text{ref}}) + \frac{(\mathbf{f}_{\text{out}} - \mathbf{j}_{\mathbf{x}}(\mathbf{x}_{\text{in}}, t_{\text{ref}})\mathbf{f}_{\text{in}} - \mathbf{j}_t(\mathbf{x}_{\text{in}}, t_{\text{ref}}))h_{\mathbf{x}}(\mathbf{x}_{\text{in}}, t_{\text{ref}})}{h_{\mathbf{x}}(\mathbf{x}_{\text{in}}, t_{\text{ref}})\mathbf{f}_{\text{in}} + h_t(\mathbf{x}_{\text{in}}, t_{\text{ref}}) - V(t_{\text{ref}}|P(t_{\text{ref}}) = 0)}, \quad (10.48)$$

and find that

$$\bar{\phi}_{\mathbf{x}}(\hat{\mathbf{x}}_0^{\text{ref}}, T) = \bar{\phi}_{2,\mathbf{x}}(\hat{\mathbf{x}}_{\text{out}}, T - t_{\text{ref}})\overline{\tilde{\mathbf{D}}}_{\mathbf{x}}(\hat{\mathbf{x}}_{\text{in}})\bar{\phi}_{1,\mathbf{x}}(\hat{\mathbf{x}}_0^{\text{ref}}, t_{\text{ref}}). \quad (10.49)$$

Here the Jacobians  $\bar{\phi}_{1,\mathbf{x}}(\mathbf{x}, t)$  and  $\bar{\phi}_{2,\mathbf{x}}(\mathbf{x}, t)$  of the flows  $\bar{\phi}_1$  and  $\bar{\phi}_2$  are given by

$$\bar{\phi}_{i,\mathbf{x}} = \begin{pmatrix} \phi_{i,\mathbf{x}} & \mathbf{0} \\ 0 & 1 \end{pmatrix}, \quad i = 1, 2, \quad (10.50)$$

where  $\phi_{i,\mathbf{x}}$  can be found as the solutions of the initial-value problems

$$\dot{\Phi}(\mathbf{x}, t) = \mathbf{f}_{\mathbf{x}}(\phi_i(\mathbf{x}, t))\Phi(\mathbf{x}, t), \quad \Phi(\mathbf{x}, 0) = \mathbf{I}, \quad i = 1, 2. \quad (10.51)$$

The Jacobians  $\phi_{i,\mathbf{x}}$  are entirely smooth and deterministic and the effects of both nonsmoothness and noise are contained within  $\widetilde{\mathbf{D}}_{\mathbf{x}}(\hat{\mathbf{x}}_{\text{in}})$ . The distribution of deviations of a trajectory with an initial condition  $\mathbf{x}_0 \approx \mathbf{x}_0^{\text{ref}}$ , in a small neighbourhood of the reference trajectory based at  $\mathbf{x}_0^{\text{ref}}$  in the original state space, is now given to first order by

$$\bar{\phi}(\bar{\mathbf{x}}_0, T) - \bar{\phi}(\hat{\mathbf{x}}_0^{\text{ref}}, T) \approx \bar{\phi}_{\mathbf{x}}(\hat{\mathbf{x}}_0^{\text{ref}}, T)(\bar{\mathbf{x}}_0 - \hat{\mathbf{x}}_0^{\text{ref}}), \quad (10.52)$$

where  $\bar{\mathbf{x}}_0 = (\mathbf{x}_0, \Delta t_{\text{ref}})^T$  and  $\Delta t_{\text{ref}}$  is the distribution given by (10.30), before projecting back. As a result, in the original state space we find that

$$\phi(\mathbf{x}_0, T) - \phi(\mathbf{x}_0^{\text{ref}}, T) \approx \phi_{\mathbf{x}}(\mathbf{x}_0^{\text{ref}}, T)(\mathbf{x}_0 - \mathbf{x}_0^{\text{ref}}) + \phi_{2,\mathbf{x}}(\mathbf{x}_{\text{out}}, T - t_{\text{ref}})\mathcal{N}(\mathbf{x}_{\text{in}}, t_{\text{ref}})\Delta t_{\text{ref}}, \quad (10.53)$$

where

$$\phi_{\mathbf{x}}(\mathbf{x}_0^{\text{ref}}, T) = \phi_{2,\mathbf{x}}(\mathbf{x}_{\text{out}}, T - t_{\text{ref}})\widetilde{\mathbf{D}}_{\mathbf{x}}(\mathbf{x}_{\text{in}})\phi_{1,\mathbf{x}}(\mathbf{x}_0^{\text{ref}}, t_{\text{ref}}) \quad (10.54)$$

and

$$\mathcal{N}(\mathbf{x}_{\text{in}}, t_{\text{ref}}) = \mathbf{j}_{\mathbf{x}}(\mathbf{x}_{\text{in}}, t_{\text{ref}})\mathbf{f}_{\text{in}} + \mathbf{j}_t(\mathbf{x}_{\text{in}}, t_{\text{ref}}) - \mathbf{f}_{\text{out}}. \quad (10.55)$$

Furthermore, if the jump map  $\mathbf{j}$  itself is a stochastic mapping  $\mathbf{j} = \tilde{\mathbf{j}}$  then we must consider the error introduced by  $\tilde{\mathbf{j}}$  so that (10.53) becomes

$$\begin{aligned} \phi(\mathbf{x}_0, T) - \phi(\mathbf{x}_0^{\text{ref}}, T) &\approx \phi_{\mathbf{x}}(\mathbf{x}_0^{\text{ref}}, T)(\mathbf{x}_0 - \mathbf{x}_0^{\text{ref}}) + \phi_{2,\mathbf{x}}(\mathbf{x}_{\text{out}}, T - t_{\text{ref}})\mathcal{N}(\mathbf{x}_{\text{in}}, t_{\text{ref}})\Delta t_{\text{ref}} \\ &+ \phi_{2,\mathbf{x}}(\mathbf{x}_{\text{out}}, T - t_{\text{ref}})\mathcal{J}(\mathbf{x}_{\text{in}}, t_{\text{ref}}), \end{aligned} \quad (10.56)$$

where

$$\mathcal{J}(\mathbf{x}_{\text{in}}, t_{\text{ref}}) = \tilde{\mathbf{j}}(\mathbf{x}_{\text{in}} | P(t_{\text{ref}}) = 0) - \mathbf{j}(\mathbf{x}_{\text{in}}). \quad (10.57)$$

As an example, in Section 10.7.1 we consider an impacting system where the jump map  $\mathbf{j} = \tilde{\mathbf{j}}$  depends on the stochastic velocity associated with the discontinuity boundary  $V(t) = dP/dt$ . We also note that the inclusion of the  $\tilde{\mathbf{j}}_t$  term in the expression for  $\mathcal{N}$  in this case may impose further conditions on the differentiability of  $P$ . If  $\tilde{\mathbf{j}}$  depends on  $V(t) = dP/dt$  (as is the case in the example presented in Section 10.7.1) we must then be able to calculate  $A(t) = d^2P/dt^2$  and so on.

## 10.4.2 Rugged Boundaries

In this section we will consider hybrid systems with rugged discontinuity boundaries, whose small-scale structure is uncertain. In particular we will consider systems with stochastic discontinuity boundaries described by the zeros of a real-valued function  $\tilde{h}(\mathbf{x}, t)$  of the form

$$\tilde{h}(\mathbf{x}, t) = h(\mathbf{x}, t) - \chi(\mathbf{x}), \quad (10.58)$$

where  $h(\mathbf{x}, t)$  is a deterministic function describing the large-scale structure of the boundary and  $\chi(\mathbf{x})$  is a random process that describes the height of imperfections on the boundary depending on their state-space coordinates.

We consider once again a trajectory starting at a point  $\mathbf{x}_0^{\text{ref}}$  that intersects the deterministic boundary  $\Sigma$  transversally after time  $t = t_{\text{ref}}$ , so that  $h(\phi_1(\mathbf{x}_0^{\text{ref}}, t_{\text{ref}}), t_{\text{ref}}) = 0$ . As in the case of a stochastically oscillating boundary analysed in Section 10.4.1 we linearly approximate the difference between the true hitting time for a given reference trajectory and the deterministic hitting time in the absence of stochastic fluctuations.

Given that  $\chi(\mathbf{x})$  represents small amplitude noise with mean  $\mathbf{0}$ , we have that the true time of flight to the boundary  $\tilde{t}_{\text{ref}} \approx t_{\text{ref}}$ , where  $t_{\text{ref}}$  is the time of flight in the

deterministic system. For  $t \approx t_{\text{ref}}$ , and expanding about  $t_{\text{ref}}$ , we find that

$$\begin{aligned}
 \tilde{h}(\phi_1(\mathbf{x}_0^{\text{ref}}, t), t) &= h(\phi_1(\mathbf{x}_0^{\text{ref}}, t), t) - \chi(\phi_1(\mathbf{x}_0^{\text{ref}}, t)) \\
 &\approx h(\phi_1(\mathbf{x}_0^{\text{ref}}, t_{\text{ref}}), t_{\text{ref}}) - \chi(\phi_1(\mathbf{x}_0^{\text{ref}}, t_{\text{ref}})) \\
 &\quad + (h_{\mathbf{x}}(\phi_1(\mathbf{x}_0^{\text{ref}}, t_{\text{ref}}), t_{\text{ref}})\mathbf{f}_1(\phi_1(\mathbf{x}_0^{\text{ref}}, t_{\text{ref}})) + h_t(\phi_1(\mathbf{x}_0^{\text{ref}}, t_{\text{ref}}), t_{\text{ref}}) \\
 &\quad - \chi_{\mathbf{x}}(\phi_1(\mathbf{x}_0^{\text{ref}}, t_{\text{ref}}))\mathbf{f}_1(\phi_1(\mathbf{x}_0^{\text{ref}}, t_{\text{ref}}))) (t - t_{\text{ref}}) \\
 &= (t - t_{\text{ref}}) (h_{\mathbf{x}}(\mathbf{x}_{\text{in}}, t_{\text{ref}})\mathbf{f}_{\text{in}} + h_t(\mathbf{x}_{\text{in}}, t_{\text{ref}}) - \chi_{\mathbf{x}}(\mathbf{x}_{\text{in}})\mathbf{f}_{\text{in}}) - \chi(\mathbf{x}_{\text{in}}),
 \end{aligned} \tag{10.59}$$

where  $\mathbf{x}_{\text{in}} = \phi_1(\mathbf{x}_0^{\text{ref}}, t_{\text{ref}})$  and  $\mathbf{f}_{\text{in}} = \mathbf{f}_1(\mathbf{x}_{\text{in}})$ . Equation (10.59) implies that  $\Delta t_{\text{ref}} = \tilde{t}_{\text{ref}} - t_{\text{ref}}$  is given to first order by

$$\Delta t_{\text{ref}} \approx \frac{\chi(\mathbf{x}_{\text{in}})}{h_{\mathbf{x}}(\mathbf{x}_{\text{in}}, t_{\text{ref}})\mathbf{f}_{\text{in}} + h_t(\mathbf{x}_{\text{in}}, t_{\text{ref}}) - \chi_{\mathbf{x}}(\mathbf{x}_{\text{in}})\mathbf{f}_{\text{in}}}. \tag{10.60}$$

As we did in Section 10.4.1, we now extend the state space, vector field and jump map to

$$\bar{\mathbf{x}} = (\mathbf{x}, \Delta t_{\text{ref}}, t)^T, \quad \bar{\mathbf{f}} = (\mathbf{f}, 0, 1)^T \quad \text{and} \quad \bar{\mathbf{j}} = (\mathbf{j}, \Delta t_{\text{ref}}, t)^T, \tag{10.61}$$

respectively, and perform the same analysis as before, namely, linearising about the realisation of the deterministic trajectory in the stochastic system. Once again we find that

$$\phi(\mathbf{x}_0, T) - \phi(\mathbf{x}_0^{\text{ref}}, T) \approx \phi_{\mathbf{x}}(\mathbf{x}_0^{\text{ref}}, T)(\mathbf{x}_0 - \mathbf{x}_0^{\text{ref}}) + \phi_{2,\mathbf{x}}(\mathbf{x}_{\text{out}}, T - t_{\text{ref}})\mathcal{N}(\mathbf{x}_{\text{in}}, t_{\text{ref}})\Delta t_{\text{ref}}, \tag{10.62}$$

where

$$\phi_{\mathbf{x}}(\mathbf{x}_0^{\text{ref}}, T) = \phi_{2,\mathbf{x}}(\mathbf{x}_{\text{out}}, T - t_{\text{ref}})\tilde{\mathbf{D}}_{\mathbf{x}}(\mathbf{x}_{\text{in}})\phi_{1,\mathbf{x}}(\mathbf{x}_0^{\text{ref}}, t_{\text{ref}}) \tag{10.63}$$

and

$$\mathcal{N}(\mathbf{x}_{\text{in}}, t_{\text{ref}}) = \mathbf{j}_{\mathbf{x}}(\mathbf{x}_{\text{in}}, t_{\text{ref}})\mathbf{f}_{\text{in}} + \mathbf{j}_t(\mathbf{x}_{\text{in}}, t_{\text{ref}}) - \mathbf{f}_{\text{out}}, \tag{10.64}$$

in the original state space. In this case  $\tilde{\mathbf{D}}_{\mathbf{x}}(\mathbf{x}_{\text{in}})$  is given by

$$\begin{aligned} \tilde{\mathbf{D}}_{\mathbf{x}}(\mathbf{x}_{\text{in}}) &= \mathbf{j}_{\mathbf{x}}(\mathbf{x}_{\text{in}}, t_{\text{ref}}) \\ &+ \frac{(\mathbf{f}_{\text{out}} - \mathbf{j}_{\mathbf{x}}(\mathbf{x}_{\text{in}}, t_{\text{ref}})\mathbf{f}_{\text{in}} - \mathbf{j}_t(\mathbf{x}_{\text{in}}, t_{\text{ref}}))(h_{\mathbf{x}}(\mathbf{x}_{\text{in}}, t_{\text{ref}}) - \chi_{\mathbf{x}}(\mathbf{x}_{\text{in}}|\chi(\mathbf{x}_{\text{in}}) = 0))}{h_{\mathbf{x}}(\mathbf{x}_{\text{in}}, t_{\text{ref}})\mathbf{f}_{\text{in}} + h_t(\mathbf{x}_{\text{in}}, t_{\text{ref}}) - \chi_{\mathbf{x}}(\mathbf{x}_{\text{in}}|\chi(\mathbf{x}_{\text{in}}) = 0)\mathbf{f}_{\text{in}}}. \end{aligned} \quad (10.65)$$

Once again, if the jump map  $\mathbf{j}$  itself is a stochastic mapping  $\mathbf{j} = \tilde{\mathbf{j}}$  then we must consider the error introduced by  $\tilde{\mathbf{j}}$  so that (10.62) becomes

$$\begin{aligned} \phi(\mathbf{x}_0, T) - \phi(\mathbf{x}_0^{\text{ref}}, T) &\approx \phi_{\mathbf{x}}(\mathbf{x}_0^{\text{ref}}, T)(\mathbf{x}_0 - \mathbf{x}_0^{\text{ref}}) + \phi_{2,\mathbf{x}}(\mathbf{x}_{\text{out}}, T - t_{\text{ref}})\mathcal{N}(\mathbf{x}_{\text{in}}, t_{\text{ref}})\Delta t_{\text{ref}} \\ &+ \phi_{2,\mathbf{x}}(\mathbf{x}_{\text{out}}, T - t_{\text{ref}})\mathcal{J}(\mathbf{x}_{\text{in}}, t_{\text{ref}}), \end{aligned} \quad (10.66)$$

where

$$\mathcal{J}(\mathbf{x}_{\text{in}}, t_{\text{ref}}) = \tilde{\mathbf{j}}(\mathbf{x}_{\text{in}}|\chi(\mathbf{x}_{\text{in}}) = 0) - \mathbf{j}(\mathbf{x}_{\text{in}}). \quad (10.67)$$

Here the inclusion of the  $\tilde{\mathbf{j}}_{\mathbf{x}}$  term in the expression for  $\mathcal{N}$  may impose further conditions on the differentiability of  $\chi$ .

We note that in piecewise-smooth systems that are continuous across the boundary, i.e. systems where  $\mathbf{f}_1 = \mathbf{f}_2$  on  $\Sigma$  and  $\mathbf{j}$  is the identity mapping,  $\mathbf{D}_{\mathbf{x}}(\mathbf{x}_{\text{in}})$  collapses to the identity matrix and  $\mathcal{N} = \mathcal{J} = \mathbf{0}$  for both stochastically oscillating and rugged boundaries. This gives that, to first order

$$\phi(\mathbf{x}_0, T) - \phi(\mathbf{x}_0^{\text{ref}}, T) \approx \phi_{2,\mathbf{x}}(\mathbf{x}_{\text{out}}, T - t_{\text{ref}})\phi_{1,\mathbf{x}}(\mathbf{x}_0^{\text{ref}}, t_{\text{ref}})(\mathbf{x}_0 - \mathbf{x}_0^{\text{ref}}), \quad (10.68)$$

which is the same result that we would obtain for the deterministic system. In other words, we find that in piecewise-smooth continuous systems the inclusion of noise on the boundary has no linear effect. In Section 10.5 we will construct higher order approximations for such systems.

## 10.5 Systems with Higher-Order Discontinuities

In this section we will construct SZDMs for piecewise-smooth vector fields with higher-order continuity following the work of Nordmark for deterministic systems [24]. Throughout this section we will use the notation *h.o.t.* for higher-order remainder terms in our derivations of both the deterministic and stochastic ZDMs. For more detail regarding the exact form of these remainder terms refer to [24].

Consider a piecewise-smooth vector field defined by

$$\mathbf{f}(\mathbf{x}) = \begin{cases} \mathbf{f}_1(\mathbf{x}), & h(\mathbf{x}) \geq 0, \\ \mathbf{f}_2(\mathbf{x}), & h(\mathbf{x}) < 0, \end{cases} \quad (10.69)$$

that is  $\mathcal{C}^{n-1}$ , with  $n \geq 1$ , in a neighbourhood of the crossing point  $\mathbf{x}^*$ , where  $h(\mathbf{x})$  is a real-valued analytic function. The discontinuity boundary  $\Sigma$  is therefore defined by the zeros of the function  $h$ , i.e.

$$\Sigma = \{\mathbf{x} : h(\mathbf{x}) = 0\}. \quad (10.70)$$

We assume that there is no real or virtual equilibrium in the neighbourhood of  $\mathbf{x}^*$ , so  $\mathbf{f}_i(\mathbf{x}) \neq \mathbf{0}$  for  $i = 1, 2$  and  $\mathbf{x} \approx \mathbf{x}^*$ . We further assume that the boundary crossing is transversal, i.e.  $h_{\mathbf{x}}(\mathbf{x}^*)\mathbf{f}_1(\mathbf{x}^*) = v < 0$ . Note, here a virtual equilibrium refers to an equilibrium point  $\mathbf{x}_{i,v}^*$  of  $\dot{\mathbf{x}} = \mathbf{f}_i$  such that  $\mathbf{x}_{i,v}^* \in \mathcal{S}_j$  and  $i \neq j$ . A real equilibrium refers to an equilibrium point  $\mathbf{x}_{i,r}^*$  of  $\dot{\mathbf{x}} = \mathbf{f}_i$  such that  $\mathbf{x}_{i,r}^* \in \mathcal{S}_i$ .

Due to  $\mathcal{C}^{n-1}$  continuity all derivatives of order  $k \leq n - 1$  of  $\mathbf{f}_2 - \mathbf{f}_1$  must vanish on the discontinuity boundary  $\Sigma$ . For now, taking  $h = h(\mathbf{x})$  to be one of the coordinates of  $\mathbf{x}$  we can expand  $\mathbf{f}_2 - \mathbf{f}_1$  about  $h = 0$  so that

$$\mathbf{f}_2 - \mathbf{f}_1 = \sum_{k=0}^{\infty} \frac{h^k}{k!} \frac{\partial^k}{\partial h^k} (\mathbf{f}_2 - \mathbf{f}_1)|_{h=0}$$

$$\begin{aligned}
&= \sum_{k=n}^{\infty} \frac{h^k}{k!} \frac{\partial^k}{\partial h^k} (\mathbf{f}_2 - \mathbf{f}_1)|_{h=0} \\
&= h^n \sum_{j=0}^{\infty} \frac{h^j}{(j+n)!} \frac{\partial^{j+n}}{\partial h^{j+n}} (\mathbf{f}_2 - \mathbf{f}_1)|_{h=0} \\
&= h^n g.
\end{aligned} \tag{10.71}$$

This gives that

$$\mathbf{f}_2(\mathbf{x}) = \mathbf{f}_1(\mathbf{x}) + g(\mathbf{x})h(\mathbf{x})^n, \tag{10.72}$$

where  $g(\mathbf{x})$  is analytic in a neighbourhood of the crossing point  $\mathbf{x}^*$ .

By the flow box theorem we can make a coordinate transformation  $\mathbf{y} = \mu(\mathbf{x})$  with inverse  $\mathbf{x} = \gamma(\mathbf{y})$ , where  $\mathbf{y}$  is partitioned as

$$\mathbf{y} = \begin{pmatrix} \mathbf{z} \\ \tau \end{pmatrix} \tag{10.73}$$

such that the vector field  $\mathbf{f}_1(\mathbf{x})$  is transformed into the vector field

$$F_1(\mathbf{y}) = \frac{\partial \mu}{\partial \mathbf{x}}(\gamma(\mathbf{y})) \mathbf{f}_1(\gamma(\mathbf{y})) = \begin{pmatrix} 0 \\ 1 \end{pmatrix} \tag{10.74}$$

in a neighbourhood of  $\mathbf{x}^*$ . The labelling  $\mathbf{z}$  of individual flow lines is arbitrary as is the surface on each line where  $\tau = 0$ . To simplify calculations we will choose the transformation such that the crossing point is transformed to the origin and the discontinuity boundary is given by  $\tau = 0$  so that

$$\mu(\mathbf{x}^*) = \mathbf{0} \quad \text{and} \quad \mu(\Sigma) = \{\mathbf{y} : \tau = 0\}. \tag{10.75}$$

From (10.71)-(10.72) we now have that

$$F_2(\mathbf{y}) = F_1(\mathbf{y}) + G(\mathbf{y})H(\mathbf{y})^n, \tag{10.76}$$

where

$$G(\mathbf{y}) = \frac{\partial \mu}{\partial \mathbf{x}}(\gamma(\mathbf{y}))g(\gamma(\mathbf{y})) \quad \text{and} \quad H(\mathbf{y}) = h(\gamma(\mathbf{x})). \quad (10.77)$$

Since the initial flow under the vector field  $F_1$  crosses the discontinuity boundary transversally near  $\mathbf{y} = \mathbf{0}$  we define the deterministic discontinuity mapping to be

$$\mathbf{D}(\mathbf{y}) = \phi_2(\phi_1(\mathbf{y}, t(\mathbf{y})), -t(\mathbf{y})), \quad (10.78)$$

where  $t(\mathbf{y})$  is the time of flight to the boundary under  $\phi_1$ . The corresponding stochastic mapping is given by

$$\tilde{\mathbf{D}}(\mathbf{y}) = \phi_2(\phi_1(\mathbf{y}, \tilde{t}(\mathbf{y})), -\tilde{t}(\mathbf{y})), \quad (10.79)$$

where  $\tilde{t}(\mathbf{y})$  is the stochastic time of flight to the boundary along flow one. We note that from (10.74) we can easily write

$$\phi_1(\mathbf{y}, t) = \begin{pmatrix} \mathbf{z} \\ \tau + t \end{pmatrix}. \quad (10.80)$$

With (10.76) in mind, close to  $\mathbf{y} = \mathbf{0}$ , we will try to approximate  $\phi_2(\mathbf{y}, t)$  with

$$\hat{\phi}_2(\mathbf{y}, t) = \phi_1(\mathbf{y}, t) + G(0) \int_{\tau}^{\tau+t} (v\rho)^n d\rho, \quad (10.81)$$

where  $(v\rho)^n$  is chosen since we must have that  $H(\mathbf{y}) \approx v\tau$ . Now

$$\begin{aligned} \frac{\partial \hat{\phi}_2}{\partial t}(\mathbf{y}, t) &= \frac{\partial \phi_1}{\partial t}(\mathbf{y}, t) + G(0) \frac{\partial}{\partial t} \left[ \int_{\tau}^{\tau+t} (v\rho)^n d\rho \right] \\ &= F_1 + G(0)[v(\tau + t)]^n \\ &= \begin{pmatrix} 0 \\ 1 \end{pmatrix} + G(0)[v(\tau + t)]^n, \end{aligned} \quad (10.82)$$

while

$$\begin{aligned}
F_2(\hat{\phi}_2(\mathbf{y}, t)) &= F_1(\hat{\phi}_2(\mathbf{y}, t)) + G(\hat{\phi}_2(\mathbf{y}, t))[H(\hat{\phi}_2(\mathbf{y}, t))]^n \\
&= \begin{pmatrix} 0 \\ 1 \end{pmatrix} + G(\hat{\phi}_2(\mathbf{y}, t))[H(\hat{\phi}_2(\mathbf{y}, t))]^n \\
&= \begin{pmatrix} 0 \\ 1 \end{pmatrix} + G(0)[v(\tau + t)]^n + h.o.t.
\end{aligned} \tag{10.83}$$

By Lemma 2 in [24] we now have that

$$\phi_2(\mathbf{y}, t) = \hat{\phi}_2(\mathbf{y}, t) + h.o.t. \tag{10.84}$$

Both the deterministic and the stochastic discontinuity mappings  $\mathbf{D}$  and  $\tilde{\mathbf{D}}$  are of the form  $\phi_2(\phi_1(\mathbf{y}, t), -t)$ , where  $t = t(\mathbf{y})$  and  $t = \tilde{t}(\mathbf{y})$ , respectively. We find that

$$\begin{aligned}
\phi_2(\phi_1(\mathbf{y}, t), -t) &= \phi_1(\phi_1(\mathbf{y}, t), -t) + G(0) \int_{\tau+t}^{\tau+t-t} (v\rho)^n d\rho + h.o.t \\
&= \mathbf{y} + G(0) \int_{\tau+t}^{\tau} (v\rho)^n d\rho + h.o.t.
\end{aligned} \tag{10.85}$$

In the deterministic case

$$t(\mathbf{y}) = -\tau \approx -\frac{H(\mathbf{y})}{v}, \tag{10.86}$$

which gives that the ZDM  $\mathbf{D}(\mathbf{y})$  can be written as

$$\begin{aligned}
\mathbf{D}(\mathbf{y}) &= \mathbf{y} + G(0) \int_0^{\frac{H(\mathbf{y})}{v}} (v\rho)^n d\rho + h.o.t \\
&= \mathbf{y} + G(0) \int_0^1 \left(v \frac{H(\mathbf{y})}{v} s\right)^n \frac{H(\mathbf{y})}{v} ds + h.o.t \\
&= \mathbf{y} + G(0) \frac{H(\mathbf{y})^{n+1}}{v} \int_0^1 s^n ds + h.o.t \\
&= \mathbf{y} + \frac{G(0)H(\mathbf{y})^{n+1}}{(n+1)v} + h.o.t \\
&= \mathbf{y} + \left( \frac{G(0)}{(n+1)v} + h.o.t \right) H(\mathbf{y})^{n+1}
\end{aligned}$$

$$= \mathbf{y} + E(\mathbf{y})H(\mathbf{y})^{n+1}. \quad (10.87)$$

It remains to transform back to the original coordinates. In the deterministic case we find that the ZDM in the original coordinate system  $\mathbf{d}(\mathbf{x})$  is given by

$$\begin{aligned} \mathbf{d}(x) &= \gamma(\mathbf{D}(\mu(\mathbf{x}))) \\ &= \gamma(\mu(\mathbf{x}) + E(\mu(\mathbf{x}))H(\mu(\mathbf{x}))^{n+1}). \end{aligned} \quad (10.88)$$

Expanding  $\gamma(\mathbf{y})$  about  $\mathbf{y} = \mu(\mathbf{x})$  we find that (10.88) becomes

$$\begin{aligned} \mathbf{d}(x) &= \gamma(\mu(\mathbf{x})) + \frac{\partial \gamma}{\partial \mathbf{x}}(\mu(\mathbf{x}))E(\mu(\mathbf{x}))H(\mu(\mathbf{x}))^{n+1} + h.o.t \\ &= \mathbf{x} + \frac{\partial \gamma}{\partial \mathbf{x}}(\mu(\mathbf{x}))E(\mu(\mathbf{x}))h(\mathbf{x})^{n+1} + h.o.t. \end{aligned} \quad (10.89)$$

Further expanding  $\frac{\partial \gamma}{\partial \mathbf{x}}\mu(\mathbf{x})\tilde{E}(\mu(\mathbf{x}))$  about  $\mathbf{x} = \mathbf{x}^*$  we find that (10.89) becomes

$$\begin{aligned} \mathbf{d}(x) &= \mathbf{x} + \left( \frac{\partial \gamma}{\partial \mathbf{x}}(\mu(\mathbf{x}^*))E(\mu(\mathbf{x}^*)) + \mathcal{O}(\mathbf{x} - \mathbf{x}^*) \right) h(\mathbf{x})^{n+1} \\ &= \mathbf{x} + \left( \frac{\partial \gamma}{\partial \mathbf{x}}(\mathbf{0})E(\mathbf{0}) + \mathcal{O}(\mathbf{x} - \mathbf{x}^*) \right) h(\mathbf{x})^{n+1} \\ &= \mathbf{x} + \left( \frac{\partial \gamma}{\partial \mathbf{x}}(\mathbf{0})\frac{G(0)}{(n+1)v} + \mathcal{O}(\mathbf{x} - \mathbf{x}^*) \right) h(\mathbf{x})^{n+1} \\ &= \mathbf{x} + \left( \frac{g(\mathbf{x}^*)}{(n+1)v} + \mathcal{O}(\mathbf{x} - \mathbf{x}^*) \right) h(\mathbf{x})^{n+1} \\ &= \mathbf{x} + e(\mathbf{x})h(\mathbf{x})^{n+1}. \end{aligned} \quad (10.90)$$

Notice that in the stochastic case we must estimate the stochastic time of flight to the boundary  $\tilde{t}(\mathbf{y})$ .

### 10.5.1 Stochastically Oscillating Boundaries

In the case of a stochastically oscillating boundary  $\tilde{\Sigma}$  given by the zeros of  $\tilde{h}(\mathbf{x}, t) = h(\mathbf{x}) - P(t)$  we note that

$$\tilde{H}(\mathbf{y}) = h(\gamma(\mathbf{y})) - P = H(\mathbf{y}) - P \approx v\tau - P. \quad (10.91)$$

Now,  $\tilde{t}(\mathbf{y})$  is given by  $\tilde{H}(\phi_1(\mathbf{y}, \tilde{t}(\mathbf{y}))) = 0$  and thus

$$\tilde{t}(\mathbf{y}) \approx \frac{P - H(\mathbf{y})}{v - V}, \quad (10.92)$$

where  $V = d/dt(P)$ . We now find that

$$\begin{aligned} \tilde{\mathbf{D}}(\mathbf{y}) &= \mathbf{y} + G(0) \int_{\frac{Pv - H(\mathbf{y})V}{v(v-V)}}^{\frac{H(\mathbf{y})}{v}} (v\rho)^n d\rho + h.o.t \\ &= \mathbf{y} + G(0) \int_0^{\frac{H(\mathbf{y})}{v}} (v\rho)^n d\rho + G(0) \int_{\frac{Pv - H(\mathbf{y})V}{v(v-V)}}^0 (v\rho)^n d\rho + h.o.t \\ &= \mathbf{y} + G(0) \int_0^{\frac{H(\mathbf{y})}{v}} (v\rho)^n d\rho - G(0) \int_0^{\frac{Pv - H(\mathbf{y})V}{v(v-V)}} (v\rho)^n d\rho + h.o.t \\ &= \mathbf{y} + \frac{G(0)}{v} \left( (H(\mathbf{y}))^{n+1} - \left( \frac{Pv - H(\mathbf{y})V}{v - V} \right)^{n+1} \right) \int_0^1 s^n ds + h.o.t \\ &= \mathbf{y} + \frac{G(0)}{(n+1)v} \left( (H(\mathbf{y}))^{n+1} - \left( \frac{Pv - H(\mathbf{y})V}{v - V} \right)^{n+1} \right) + h.o.t \\ &= \mathbf{y} + \left( \frac{G(0)}{(n+1)v} + h.o.t \right) \left( H(\mathbf{y})^{n+1} - \left( \frac{Pv - H(\mathbf{y})V}{v - V} \right)^{n+1} \right) \\ &= \mathbf{y} + \tilde{E}(\mathbf{y}) \left( H(\mathbf{y})^{n+1} - \left( \frac{Pv - H(\mathbf{y})V}{v - V} \right)^{n+1} \right). \end{aligned} \quad (10.93)$$

Transforming back to the original co-ordinates in this case we find that

$$\tilde{\mathbf{d}}(x) = \gamma(\tilde{\mathbf{D}}(\mu(\mathbf{x})))$$

$$\begin{aligned}
&= \gamma(\mu(\mathbf{x}) + \tilde{E}(\mu(\mathbf{x}))) \left( H(\mu(\mathbf{x}))^{n+1} - \left( \frac{Pv - H(\mu(\mathbf{x}))V}{v - V} \right)^{n+1} \right) \\
&= \gamma(\mu(\mathbf{x})) + \frac{\partial \gamma}{\partial \mathbf{x}}(\mu(\mathbf{x})) \tilde{E}(\mu(\mathbf{x})) \left( h(\mathbf{x})^{n+1} - \left( \frac{Pv - h(\mathbf{x})V}{v - V} \right)^{n+1} \right) + h.o.t \\
&= \mathbf{x} + \left( \frac{\partial \gamma}{\partial \mathbf{x}}(\mu(\mathbf{x}^*)) \tilde{E}(\mu(\mathbf{x}^*)) + \mathcal{O}(\mathbf{x} - \mathbf{x}^*) \right) \left( h(\mathbf{x})^{n+1} - \left( \frac{Pv - h(\mathbf{x})V}{v - V} \right)^{n+1} \right) \\
&= \mathbf{x} + \left( \frac{\partial \gamma}{\partial \mathbf{x}}(\mathbf{0}) \tilde{E}(\mathbf{0}) + \mathcal{O}(\mathbf{x} - \mathbf{x}^*) \right) \left( h(\mathbf{x})^{n+1} - \left( \frac{Pv - h(\mathbf{x})V}{v - V} \right)^{n+1} \right) \\
&= \mathbf{x} + \left( \frac{\partial \gamma}{\partial \mathbf{x}}(\mathbf{0}) \frac{G(0)}{(n+1)v} + \mathcal{O}(\mathbf{x} - \mathbf{x}^*) \right) \left( h(\mathbf{x})^{n+1} - \left( \frac{Pv - h(\mathbf{x})V}{v - V} \right)^{n+1} \right) \\
&= \mathbf{x} + \left( \frac{g(\mathbf{x}^*)}{(n+1)v} + \mathcal{O}(\mathbf{x} - \mathbf{x}^*) \right) \left( h(\mathbf{x})^{n+1} - \left( \frac{Pv - h(\mathbf{x})V}{v - V} \right)^{n+1} \right) \\
&= \mathbf{x} + \tilde{e}(\mathbf{x}) \left( h(\mathbf{x})^{n+1} - \left( \frac{Pv - h(\mathbf{x})V}{v - V} \right)^{n+1} \right). \tag{10.94}
\end{aligned}$$

## 10.5.2 Rugged Boundaries

In the case of a rugged boundary  $\tilde{\Sigma}$  given by the zeros of  $\tilde{h}(\mathbf{x}) = h(\mathbf{x}) - \chi(\mathbf{x})$  we note that

$$\tilde{H}(\mathbf{y}) = h(\gamma(\mathbf{y})) - \chi(\gamma(\mathbf{y})) = H(\mathbf{y}) - \chi(\gamma(\mathbf{y})) \approx v\tau - \chi(\gamma(\mathbf{y})) = v\tau - \chi(\mathbf{x}). \tag{10.95}$$

Now  $\tilde{t}(\mathbf{y})$  is given by  $\tilde{H}(\phi_1(\mathbf{y}, \tilde{t}(\mathbf{y}))) = 0$  and thus

$$\tilde{t}(\mathbf{y}) \approx \frac{\chi(\gamma(\mathbf{y})) - H(\mathbf{y})}{v - \chi_{\mathbf{x}}(\gamma(\mathbf{y}))\gamma_{\mathbf{x}}(\mathbf{y})F_1(\mathbf{y})} = \frac{\chi(\mathbf{x}) - H(\mathbf{y})}{v - \chi_{\mathbf{x}}(\mathbf{x})\mathbf{f}_1(\mathbf{x})}. \tag{10.96}$$

Following the same approach as in the case of stochastic oscillations (10.93), we find that

$$\tilde{\mathbf{D}}(\mathbf{y}) = \mathbf{y} + \frac{G(0)}{(n+1)v} \left( (H(\mathbf{y}))^{n+1} - \left( \frac{\chi(\mathbf{x})v - H(\mathbf{y})\chi_{\mathbf{x}}(\mathbf{x})\mathbf{f}_1(\mathbf{x})}{v - \chi_{\mathbf{x}}(\mathbf{x})\mathbf{f}_1(\mathbf{x})} \right)^{n+1} \right) + h.o.t$$

$$\begin{aligned}
&= \mathbf{y} + \left( \frac{G(0)}{(n+1)v} + h.o.t \right) \left( H(\mathbf{y})^{n+1} - \left( \frac{\chi(\mathbf{x})v - H(\mathbf{y})\chi_{\mathbf{x}}(\mathbf{x})\mathbf{f}_1(\mathbf{x})}{v - \chi_{\mathbf{x}}(\mathbf{x})\mathbf{f}_1(\mathbf{x})} \right)^{n+1} \right) \\
&= \mathbf{y} + \tilde{E}(\mathbf{y}) \left( H(\mathbf{y})^{n+1} - \left( \frac{\chi(\mathbf{x})v - H(\mathbf{y})\chi_{\mathbf{x}}(\mathbf{x})\mathbf{f}_1(\mathbf{x})}{v - \chi_{\mathbf{x}}(\mathbf{x})\mathbf{f}_1(\mathbf{x})} \right)^{n+1} \right). \quad (10.97)
\end{aligned}$$

Transforming back to the original co-ordinates in this case we find that

$$\begin{aligned}
\tilde{\mathbf{d}}(x) &= \gamma(\tilde{\mathbf{D}}(\mu(\mathbf{x}))) \\
&= \gamma(\mu(\mathbf{x}) + \tilde{E}(\mu(\mathbf{x}))) \left( H(\mu(\mathbf{x}))^{n+1} - \left( \frac{\chi(\mathbf{x})v - H(\mu(\mathbf{x}))\chi_{\mathbf{x}}(\mathbf{x})\mathbf{f}_1(\mathbf{x})}{v - \chi_{\mathbf{x}}(\mathbf{x})\mathbf{f}_1(\mathbf{x})} \right)^{n+1} \right) \\
&= \gamma(\mu(\mathbf{x})) + \frac{\partial \gamma}{\partial \mathbf{x}}(\mu(\mathbf{x}))\tilde{E}(\mu(\mathbf{x})) \\
&\quad \times \left( h(\mathbf{x})^{n+1} - \left( \frac{\chi(\mathbf{x})v - h(\mathbf{x})\chi_{\mathbf{x}}(\mathbf{x})\mathbf{f}_1(\mathbf{x})}{v - \chi_{\mathbf{x}}(\mathbf{x})\mathbf{f}_1(\mathbf{x})} \right)^{n+1} \right) + h.o.t \\
&= \mathbf{x} + \left( \frac{\partial \gamma}{\partial \mathbf{x}}(\mu(\mathbf{x}^*))\tilde{E}(\mu(\mathbf{x}^*)) + \mathcal{O}(\mathbf{x} - \mathbf{x}^*) \right) \\
&\quad \times \left( h(\mathbf{x})^{n+1} - \left( \frac{\chi(\mathbf{x})v - h(\mathbf{x})\chi_{\mathbf{x}}(\mathbf{x})\mathbf{f}_1(\mathbf{x})}{v - \chi_{\mathbf{x}}(\mathbf{x})\mathbf{f}_1(\mathbf{x})} \right)^{n+1} \right) \\
&= \mathbf{x} + \left( \frac{\partial \gamma}{\partial \mathbf{x}}(\mathbf{0})\tilde{E}(\mathbf{0}) + \mathcal{O}(\mathbf{x} - \mathbf{x}^*) \right) \\
&\quad \times \left( h(\mathbf{x})^{n+1} - \left( \frac{\chi(\mathbf{x})v - h(\mathbf{x})\chi_{\mathbf{x}}(\mathbf{x})\mathbf{f}_1(\mathbf{x})}{v - \chi_{\mathbf{x}}(\mathbf{x})\mathbf{f}_1(\mathbf{x})} \right)^{n+1} \right) \\
&= \mathbf{x} + \left( \frac{\partial \gamma}{\partial \mathbf{x}}(\mathbf{0})\frac{G(0)}{(n+1)v} + \mathcal{O}(\mathbf{x} - \mathbf{x}^*) \right) \\
&\quad \times \left( h(\mathbf{x})^{n+1} - \left( \frac{\chi(\mathbf{x})v - h(\mathbf{x})\chi_{\mathbf{x}}(\mathbf{x})\mathbf{f}_1(\mathbf{x})}{v - \chi_{\mathbf{x}}(\mathbf{x})\mathbf{f}_1(\mathbf{x})} \right)^{n+1} \right) \\
&= \mathbf{x} + \left( \frac{g(\mathbf{x}^*)}{(n+1)v} + \mathcal{O}(\mathbf{x} - \mathbf{x}^*) \right) \\
&\quad \times \left( h(\mathbf{x})^{n+1} - \left( \frac{\chi(\mathbf{x})v - h(\mathbf{x})\chi_{\mathbf{x}}(\mathbf{x})\mathbf{f}_1(\mathbf{x})}{v - \chi_{\mathbf{x}}(\mathbf{x})\mathbf{f}_1(\mathbf{x})} \right)^{n+1} \right) \\
&= \mathbf{x} + \tilde{e}(\mathbf{x}) \left( h(\mathbf{x})^{n+1} - \left( \frac{\chi(\mathbf{x})v - h(\mathbf{x})\chi_{\mathbf{x}}(\mathbf{x})\mathbf{f}_1(\mathbf{x})}{v - \chi_{\mathbf{x}}(\mathbf{x})\mathbf{f}_1(\mathbf{x})} \right)^{n+1} \right). \quad (10.98)
\end{aligned}$$

## 10.6 Grazing

The results of Section 10.4 and Section 10.5 apply only to systems with transversal boundary interactions. In this section we will consider an example of a system where the reference trajectory grazes the boundary in the deterministic system, i.e.  $h_{\mathbf{x}}(\mathbf{x})\mathbf{f}(\mathbf{x}) = 0$  at the boundary intersection. We will follow the method of constructing grazing ZDMs described in Section 10.2.2. In particular, we consider the impact oscillator with many degrees of freedom studied by Fredriksson and Nordmark [31] in the deterministic setting, and generalise their method of constructing a ZDM to the stochastic case.

SZDMs associated with grazing interactions with stochastic boundaries have been considered previously by Simpson and Kuske [26]. In their work Simpson and Kuske considered a three-dimensional piecewise-smooth system with Ornstein-Uhlenbeck noise (10.21) on the boundary and used the simplifying assumption that the stochastic process remains constant while the trajectory is close to the grazing point. Our work differs in the fact that we consider a hybrid system in  $n$ -dimensions and drop the assumption of the stochastic process remaining constant while the trajectory is close to the grazing point. We will, however, assume that a trajectory cannot have multiple interactions with the discontinuity boundary in quick succession as it passes near a single deterministic grazing point. In addition [26] showed that noise in the impacting dynamics rather than the position of the boundary corresponds to parametric noise in the discontinuity mapping. The same authors along with Hogan have also shown that additive white noise in the piecewise-smooth flow corresponds to additive white noise in the square root map [25]. The effects of additive noise on multistability in the one-dimensional square root map were investigated by the authors of the current work in some depth in [32, 33].

First, as motivation we will outline the method for constructing the deterministic

ZDM. Let the smooth evolution in the system be governed by

$$\dot{\mathbf{x}} = \mathbf{f}(\mathbf{x}), \quad (10.99)$$

with formal solution  $\phi(\mathbf{x}, t)$ . We assume throughout that  $\mathbf{x} = (\mathbf{u}, \mathbf{v})^T$  is partitioned into a set of generalised coordinates  $\mathbf{u}$  and velocities  $\mathbf{v}$ . We let the impacting boundary  $\Sigma$  be defined by the zeros of the function  $h = h(\mathbf{x})$ , i.e.

$$\Sigma = \{\mathbf{x} : h(\mathbf{x}) = 0\}. \quad (10.100)$$

Non-impacting dynamics take place in the region where  $h(\mathbf{x}) > 0$ . We then define  $\Pi(\mathbf{x}, t)$  to be the function

$$\Pi(\mathbf{x}, t) = h(\phi(\mathbf{x}, t)), \quad (10.101)$$

which can be seen as the distance a trajectory starting at  $\mathbf{x}$  is from the discontinuity boundary  $\Sigma$  as a function of time  $t$ . On  $\Sigma$  we then define a function  $v(\mathbf{x})$  as

$$v(\mathbf{x}) = \frac{\partial \Pi}{\partial t}(\mathbf{x}, 0), \quad \mathbf{x} \in \Sigma, \quad (10.102)$$

to distinguish between incoming and outgoing trajectories. This allows us to divide  $\Sigma$  into 3 sets

$$\Sigma^- = \{\mathbf{x} \in \Sigma : v(\mathbf{x}) < 0\}, \quad (10.103)$$

$$\Sigma^0 = \{\mathbf{x} \in \Sigma : v(\mathbf{x}) = 0\}, \quad (10.104)$$

$$\Sigma^+ = \{\mathbf{x} \in \Sigma : v(\mathbf{x}) > 0\}. \quad (10.105)$$

Consider now a grazing trajectory starting at  $O_1$  that impacts at  $O_* \in \Sigma$  after time  $t_1$  such that  $v(O_*) = 0$ , i.e.  $O_* \in \Sigma^0$  and  $a(O_*) = A_g > 0$ , where

$$a(\mathbf{x}) = \frac{\partial^2 \Pi}{\partial t^2}(\mathbf{x}, 0), \quad \mathbf{x} \in \Sigma. \quad (10.106)$$

We then consider an impact mapping

$$\mathbf{j}: \Sigma^- \rightarrow \Sigma^+ \quad (10.107)$$

and note that points in a neighbourhood of the grazing trajectory starting at  $O_1$  either impact at low velocity or do not impact. In particular, we will consider impact maps that are of the form

$$\mathbf{j}(\mathbf{x}) = \mathbf{x} + \Delta\mathbf{x} \approx \mathbf{x} - v(\mathbf{x})\xi, \quad (10.108)$$

where  $\xi = (\mathbf{0}, \xi_v)^T$  is zero in the position coordinates and given by  $\xi_v$  in the velocity coordinates.

From here on we will assume that local coordinates have been introduced to make the grazing point  $O_*$  correspond to  $\mathbf{x}^* = \mathbf{0}$ . Taking a point  $\mathbf{x}$  in the neighbourhood  $\mathbf{x}^*$  it is clear that  $\Pi$  will have a local minimum for some small time  $\tau = \tau(\mathbf{x})$ . We then introduce the function  $\psi$  by

$$\psi(\mathbf{x}) = \Pi(\mathbf{x}, \tau(\mathbf{x})). \quad (10.109)$$

In the deterministic system we now have that impacting points are given by  $\psi(\mathbf{x}) \leq 0$ . For such impacting points  $\mathbf{x}$  we can now find the time of flight  $t_c(\mathbf{x})$  from  $\mathbf{x}$  to the boundary by expanding  $\Pi(\mathbf{x}, t)$  about  $t = \tau(x)$ , which gives

$$t_c(\mathbf{x}) \approx \tau(\mathbf{x}) - \sqrt{-\psi(\mathbf{x})2/A_g}. \quad (10.110)$$

We also find that

$$v = \Pi_t(\mathbf{x}, t_c(\mathbf{x})) \approx (t_c(\mathbf{x}) - \tau(\mathbf{x}))A_g \approx -\sqrt{-\psi(\mathbf{x})2A_g} \quad (10.111)$$

and so

$$\Delta \mathbf{x} \approx \sqrt{-\psi(\mathbf{x})2A_g\xi}. \quad (10.112)$$

Approximating  $\phi(\mathbf{x}, t_c)$  and  $\phi(\mathbf{x}, -t_c)$  by linearising about  $\mathbf{x}^*$  we find the grazing ZDM is given by

$$\mathbf{D}(\mathbf{x}) = \phi(\mathbf{j}(\phi(\mathbf{x}, t_c(\mathbf{x}))), -t_c(\mathbf{x})) \approx \mathbf{x} + \sqrt{-\psi(\mathbf{x})2A_g\xi}. \quad (10.113)$$

In what follows, in Sections 10.6.1 and 10.6.2 we will extend this method to systems where the position and structure of the boundary, respectively, have a stochastic component.

### 10.6.1 Stochastic Oscillations

In this section we will apply stochastic oscillations to the boundary by considering the noisy boundary

$$\tilde{\Sigma} = \{\mathbf{x} : \tilde{h}(\mathbf{x}, t) = 0\}, \quad (10.114)$$

where

$$\tilde{h}(\mathbf{x}, t) = h(\mathbf{x}) - P(t). \quad (10.115)$$

We can then consider the function

$$\tilde{\Pi}(\mathbf{x}, t) = h(\phi(\mathbf{x}, t)) - P(t), \quad (10.116)$$

which describes the distance to the noisy boundary as a function of time and initial condition. In this case we will consider stochastic impact maps that are of the form

$$\tilde{\mathbf{j}}(\mathbf{x}, t) = \mathbf{x} + \tilde{\Delta}\mathbf{x} \approx \mathbf{x} - \tilde{v}(\mathbf{x})\xi, \quad (10.117)$$

We will now consider a trajectory with initial condition  $\mathbf{x}_0$  in a neighbourhood of  $O_1$ . After time  $t_1$  it will be at some point  $\mathbf{x} = \phi(\mathbf{x}_0, t_1)$  in a neighbourhood of the

deterministic grazing point  $O_*$ . We want to find the stochastic time of flight from  $\mathbf{x}$  to the boundary  $\tilde{t}_c$  by expanding  $\tilde{\Pi}(\mathbf{x}, t)$  about  $\tau(\mathbf{x})$ , so that

$$\begin{aligned}\tilde{\Pi}(\mathbf{x}, t) &= \tilde{\Pi}(\mathbf{x}, \tau(\mathbf{x})) + (t - \tau(\mathbf{x})) \frac{\partial \tilde{\Pi}}{\partial t}(\mathbf{x}, \tau(\mathbf{x})) + \frac{(t - \tau(\mathbf{x}))^2}{2} \frac{\partial^2 \tilde{\Pi}}{\partial t^2}(\mathbf{x}, \tau(\mathbf{x})) + \dots \\ &= \psi(\mathbf{x}) - P(\kappa(\mathbf{x})) + (t - \tau(\mathbf{x}))(-V(\kappa(\mathbf{x}))) \\ &\quad + \frac{(t - \tau(\mathbf{x}))^2}{2}(A_g - A(\kappa(\mathbf{x}))) + \dots,\end{aligned}\quad (10.118)$$

where  $\kappa(\mathbf{x}) = t_1 + \tau(\mathbf{x})$ ,  $V = dP/dt$  and  $A = dV/dt$ . Setting  $\tilde{\Pi}(\mathbf{x}, \tilde{t}_c) = 0$  we find that

$$\psi(\mathbf{x}) - P - (\tilde{t}_c - \tau(\mathbf{x}))V + \frac{(\tilde{t}_c - \tau(\mathbf{x}))^2}{2}(A_g - A) \approx 0, \quad (10.119)$$

where the stochastic variables associated with the boundary  $P, V$  and  $A$  are evaluated at time  $\kappa(\mathbf{x}) = t_1 + \tau(\mathbf{x})$  when  $\Pi$  reaches its minimum. This gives that  $\tilde{t}_c$  can be approximated as

$$\tilde{t}_c = \tau(\mathbf{x}) + \frac{V}{A_g - A} - \sqrt{\left(-\psi(\mathbf{x}) + P + V\tau(\mathbf{x}) + \frac{V^2}{2(A_g - A)}\right) \frac{2}{A_g - A}}, \quad (10.120)$$

where we have taken the minus sign of the two possible solutions of (10.119) in order to find the first intersection with the boundary.

From (10.118) we find that

$$\begin{aligned}\tilde{v}(\mathbf{x}) = \frac{\partial \tilde{\Pi}}{\partial t}(\mathbf{x}, \tilde{t}_c) &\approx -V + (\tilde{t}_c - \tau(\mathbf{x}))(A_g - A) \\ &= \sqrt{\left(-\psi(\mathbf{x}) + P + V\tau(\mathbf{x}) + \frac{V^2}{2(A_g - A)}\right) 2(A_g - A)}.\end{aligned}\quad (10.121)$$

We then have that

$$\tilde{\Delta \mathbf{x}} \approx \sqrt{\left(-\psi(\mathbf{x}) + P + V\tau(\mathbf{x}) + \frac{V^2}{2(A_g - A)}\right) 2(A_g - A)} \xi, \quad (10.122)$$

and so, approximating  $\phi(\mathbf{x}, t)$  by linearising about the grazing point, the SZDM  $\tilde{\mathbf{D}}$  is given by

$$\begin{aligned}\tilde{\mathbf{D}}(\mathbf{x}) &= \phi(\tilde{\mathbf{j}}(\phi(\mathbf{x}, \tilde{t}_c(\mathbf{x}))), -\tilde{t}_c(\mathbf{x})) \\ &\approx \mathbf{x} + \sqrt{\left(-\psi(\mathbf{x}) + P + V\tau(\mathbf{x}) + \frac{V^2}{2(A_g - A)}\right) 2(A_g - A)\xi},\end{aligned}\quad (10.123)$$

if

$$-\psi(\mathbf{x}) + P + V\tau(\mathbf{x}) + \frac{V^2}{2(A_g - A)} \geq 0 \quad (10.124)$$

and the identity mapping otherwise. In practice we do not evaluate  $\psi$  or  $\tau$  directly. Instead we estimate them by linearisation. We find that  $\psi(\mathbf{x}) \approx \eta\mathbf{x}$ , where

$$\eta = \frac{\partial h}{\partial \mathbf{x}}(\mathbf{x}^*), \quad (10.125)$$

and by linearising  $\Pi_t(\mathbf{x}, t)$  about  $t = 0$  we also find that

$$\tau(\mathbf{x}) \approx -\frac{\Pi_t(\mathbf{x}, 0)}{\Pi_{tt}(\mathbf{x}, 0)}. \quad (10.126)$$

Next we let

$$L = \phi_{\mathbf{x}}(\mathbf{x}^*, T) \quad (10.127)$$

be the Jacobian of the grazing periodic orbit that grazes at  $\mathbf{x}^*$ . Then we can investigate the stability of the grazing orbit by examining the mapping

$$\mathbf{x}_{i+1} = \begin{cases} \sqrt{\Upsilon(\mathbf{x}_i) 2(A_g - A_i)} L\xi, & \text{if } \Upsilon(\mathbf{x}_i) \geq 0, \\ L\mathbf{x}_i, & \text{otherwise,} \end{cases} \quad (10.128)$$

where

$$\Upsilon(\mathbf{x}_i) = -\eta\mathbf{x}_i + P_i - V_i \frac{\Pi_t(\mathbf{x}_i, 0)}{\Pi_{tt}(\mathbf{x}_i, 0)} + \frac{V_i^2}{2(A_g - A_i)} \quad (10.129)$$

and  $P_i, V_i, A_i$  are respectively the stochastic position, velocity and acceleration of the boundary evaluated at the end of each period of length  $T$ /iterate  $i$ .

## 10.6.2 Rugged Boundaries

Next we will consider a rugged boundary  $\tilde{\Sigma}$  with stochastic imperfections such that

$$\tilde{\Sigma} = \{\mathbf{x} : \tilde{h}(\mathbf{x}) = 0\}, \quad (10.130)$$

where

$$\tilde{h}(\mathbf{x}) = h(\mathbf{x}) - \chi(\mathbf{x}). \quad (10.131)$$

In the case of an impact oscillator these imperfections could be caused by instantaneous damage/wear caused by repeated impacts. Following the derivation in the case of a stochastically oscillating boundary in Section 10.6.1 we find that the SZDM  $\tilde{\mathbf{D}}$  is given by

$$\tilde{\mathbf{D}}(\mathbf{x}) = \phi(\tilde{\mathbf{j}}(\phi(\mathbf{x}, \tilde{t}_c(\mathbf{x}))), -\tilde{t}_c(\mathbf{x})) \approx \mathbf{x} + \tilde{\Delta}\mathbf{x}, \quad (10.132)$$

where

$$\tilde{\Delta}\mathbf{x} = \sqrt{\left(-\psi(\mathbf{x}) + \chi + \chi_{\mathbf{x}}\mathbf{f}\tau(\mathbf{x}) + \frac{(\chi_{\mathbf{x}}\mathbf{f})^2}{2(A_g - (\chi_{\mathbf{x}}\mathbf{f})_{\mathbf{x}}\mathbf{f})}\right) 2(A_g - (\chi_{\mathbf{x}}\mathbf{f})_{\mathbf{x}}\mathbf{f})\xi} \quad (10.133)$$

and  $\chi$ ,  $\chi_{\mathbf{x}}$ ,  $(\chi_{\mathbf{x}}\mathbf{f})_{\mathbf{x}}$ ,  $\mathbf{f}$  are all evaluated at  $\phi(\mathbf{x}, \tau(\mathbf{x}))$  if

$$-\psi(\mathbf{x}) + \chi + \chi_{\mathbf{x}}\mathbf{f}\tau(\mathbf{x}) + \frac{(\chi_{\mathbf{x}}\mathbf{f})^2}{2(A_g - (\chi_{\mathbf{x}}\mathbf{f})_{\mathbf{x}}\mathbf{f})} \geq 0 \quad (10.134)$$

and the identity mapping otherwise. Linearising we find that  $\psi(\mathbf{x}) \approx \eta\mathbf{x}$  where

$$\eta = \frac{\partial h}{\partial \mathbf{x}}(\mathbf{x}^*). \quad (10.135)$$

Also, by linearising  $\Pi_t(\mathbf{x}, t)$  about  $t = 0$  we find that

$$\tau(\mathbf{x}) \approx -\frac{\Pi_t(\mathbf{x}, 0)}{\Pi_{tt}(\mathbf{x}, 0)} \quad (10.136)$$

and so we can approximate  $\phi(\mathbf{x}, \tau(\mathbf{x}))$  by

$$\phi(\mathbf{x}, \tau(\mathbf{x})) \approx \phi\left(\mathbf{x}, -\frac{\Pi_t(\mathbf{x}, 0)}{\Pi_{tt}(\mathbf{x}, 0)}\right) \approx \mathbf{x} - \mathbf{f}(\mathbf{x}) \frac{\Pi_t(\mathbf{x}, 0)}{\Pi_{tt}(\mathbf{x}, 0)} + \frac{\mathbf{g}(\mathbf{x})}{2} \left(\frac{\Pi_t(\mathbf{x}, 0)}{\Pi_{tt}(\mathbf{x}, 0)}\right)^2. \quad (10.137)$$

Once again, letting

$$L = \phi_{\mathbf{x}}(\mathbf{x}^*, T) \quad (10.138)$$

be the Jacobian of the grazing periodic orbit that grazes at  $\mathbf{x}^*$  we can investigate the stability of the grazing orbit by examining the mapping

$$\mathbf{x}_{i+1} = \begin{cases} \sqrt{\Theta(\mathbf{x}_i) 2(A_g - (\chi_{\mathbf{x}}^i \mathbf{f}^i)_{\mathbf{x}} \mathbf{f}^i)} L \xi, & \text{if } \Theta(\mathbf{x}_i) \geq 0, \\ L \mathbf{x}_i, & \text{otherwise,} \end{cases} \quad (10.139)$$

where

$$\Theta(\mathbf{x}_i) = -\eta \mathbf{x}_i + \chi^i + \chi_{\mathbf{x}}^i \mathbf{f}^i \frac{\Pi_t(\mathbf{x}_i, 0)}{\Pi_{tt}(\mathbf{x}_i, 0)} + \frac{(\chi_{\mathbf{x}}^i \mathbf{f}^i)^2}{2(A_g - (\chi_{\mathbf{x}}^i \mathbf{f}^i)_{\mathbf{x}} \mathbf{f}^i)}, \quad (10.140)$$

$\chi_i$  is the appropriate random imperfection evaluated at the end of each period  $T$ /iterate  $i$  and

$$\mathbf{f}^i = \mathbf{f}\left(\mathbf{x}_i - \mathbf{f}(\mathbf{x}_i) \frac{\Pi_t(\mathbf{x}_i, 0)}{\Pi_{tt}(\mathbf{x}_i, 0)} + \frac{\mathbf{g}(\mathbf{x}_i)}{2} \left(\frac{\Pi_t(\mathbf{x}_i, 0)}{\Pi_{tt}(\mathbf{x}_i, 0)}\right)^2\right) \quad (10.141)$$

is the appropriate vector field where  $\mathbf{g} = \dot{\mathbf{f}}$ .

## 10.7 Numerical Examples

In this section we present some simple numerical examples to illustrate the use of the SZDMs derived in Sections 10.4-10.5. In all cases we use the generalised Ornstein-Uhlenbeck processes derived in Section 10.3 to describe the noise in the system. For the sake of brevity we will consider stochastically oscillating boundaries rather than rugged boundaries in most examples although the results in both cases

are similar.

### 10.7.1 Hybrid Systems with Stochastically Oscillating Boundaries

Here we analyse an example of a transversal boundary intersection in a hybrid system using the SZDMs derived in Section 10.4. In particular we consider a simple one-dimensional impact type hybrid system that describes a ball bouncing on an oscillating surface

$$\mathbf{x} = (u, v)^T, \quad \dot{\mathbf{x}} = \mathbf{f} = (v, g)^T \quad (10.142)$$

where  $u$  is the height of the ball,  $v$  is its velocity and  $g < 0$  is acceleration due to gravity. The deterministic discontinuity boundary in this system is an oscillating surface with frequency  $\omega$  and amplitude  $\gamma$ . In other words the stochastic boundary  $\tilde{\Sigma}$  is given by the zeros of the function

$$\tilde{h}(\mathbf{x}, t) = u - \gamma \sin(\omega t) - P(t). \quad (10.143)$$

The jump map  $\tilde{\mathbf{j}}$  does not change the height of the ball  $u$  but it reverses and attenuates the ball's normal velocity to the floor by a factor  $0 \leq r \leq 1$  such that

$$\tilde{\mathbf{j}}(\mathbf{x}) = (u, -rv + (r + 1)(\gamma\omega \cos(\omega t) + V(t)))^T, \quad (10.144)$$

where  $V(t) = dP/dt$ . In this case we will need  $P$  to be at least twice differentiable due to the presence of  $V(t)$  in the expression of  $\tilde{\mathbf{j}}$ . As a result we will take  $P(t) = P_n(t)$  with  $n = 2$  as given in Section 10.3 for our numerical examples. In this case we have

$$\tilde{\mathbf{j}}_{\mathbf{x}} = \begin{pmatrix} 1 & 0 \\ 0 & -r \end{pmatrix}, \quad \tilde{\mathbf{j}}_t = \begin{pmatrix} 0 \\ (r + 1)[- \gamma\omega^2 \sin(\omega t) + A(t)] \end{pmatrix}, \quad (10.145)$$

where  $A(t) = d^2P/dt^2$  is the stochastic acceleration of the floor. We also find that

$$h_{\mathbf{x}} = (1, 0), \quad h_t = -\gamma\omega \cos(\omega t) \quad (10.146)$$

and

$$\phi(\mathbf{x}, t) = \begin{pmatrix} u + vt + \frac{1}{2}gt^2 \\ v + gt \end{pmatrix}, \quad \phi_{\mathbf{x}}(\mathbf{x}, t) = \begin{pmatrix} 1 & t \\ 0 & 1 \end{pmatrix}. \quad (10.147)$$

Referring to Section 10.4 we find that

$$\tilde{\mathbf{D}}_{\mathbf{x}}(\mathbf{x}_{\text{in}}) = \begin{pmatrix} \frac{v_{\text{out}} - \gamma\omega \cos(\omega t_{\text{ref}}) - V(t_{\text{ref}}|P=0)}{v_{\text{in}} - \gamma\omega \cos(\omega t_{\text{ref}}) - V(t_{\text{ref}}|P=0)} & 0 \\ \frac{(r+1)(g + \gamma\omega^2 \sin(\omega t_{\text{ref}}) - A(t_{\text{ref}}|P=0))}{v_{\text{in}} - \gamma\omega \cos(\omega t_{\text{ref}}) - V(t_{\text{ref}}|P=0)} & -r \end{pmatrix}, \quad (10.148)$$

$$\mathcal{N}(\mathbf{x}_{\text{in}}, t_{\text{ref}}) = \begin{pmatrix} v_{\text{in}} - v_{\text{out}} \\ (r+1)(A(t_{\text{ref}}|P=0) - \gamma\omega^2 \sin(\omega t_{\text{ref}}) - g) \end{pmatrix}, \quad (10.149)$$

where  $v_{\text{in}}$  and  $v_{\text{out}}$  are the incoming and outgoing velocities, respectively, and

$$\mathcal{J}(\mathbf{x}_{\text{in}}, t_{\text{ref}}) = \begin{pmatrix} 0 \\ (r+1)V(t_{\text{ref}}|P=0) \end{pmatrix}. \quad (10.150)$$

In the absence of noise this system has a large family of periodic orbits of period  $T = \frac{2n\pi}{\omega}$ , where  $n \in \mathbb{N}$ , which interact exactly once with the discontinuity boundary each period [34]. These can be identified with their outgoing velocities from the boundary

$$v_{\text{out}} = -\frac{\pi n g}{\omega} \quad (10.151)$$

and the velocity of the floor at impact

$$\gamma\omega \cos(\omega t') = \frac{\pi n g}{\omega} \left( \frac{r-1}{r+1} \right). \quad (10.152)$$

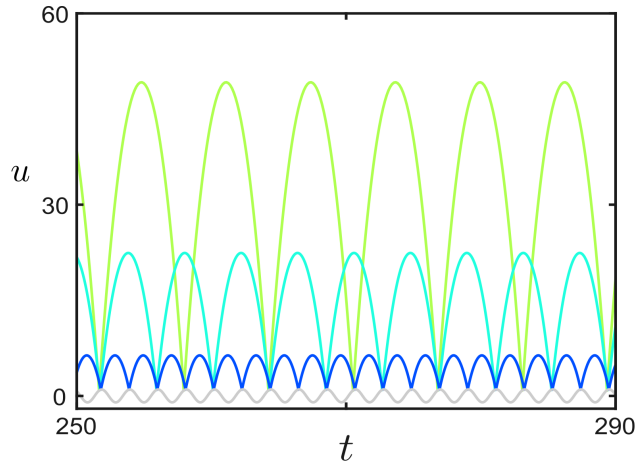


**Figure 10.5:** The dynamics of a bouncing ball in a stable periodic orbit with period  $\frac{2n\pi}{\omega}$  with one impact per period for  $n = 1, 2, 3$ . The height of the oscillating floor about  $u = 0$  is shown in grey and the periodic orbits are shown in colour with lighter colour corresponding to higher  $n$ . Here  $g = -9.8$ ,  $\gamma = 1$  and  $\omega = 3$ .

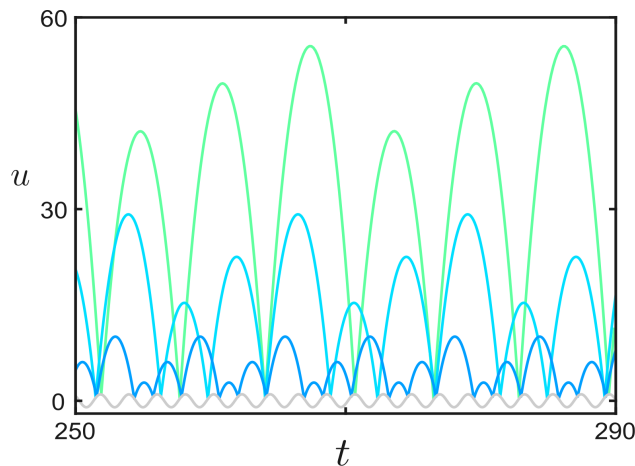


**Figure 10.6:** The dynamics of a bouncing ball in a stable periodic orbit with period  $\frac{6n\pi}{\omega}$  with three impacts per period for  $n = 1, 2, 3$ . The height of the oscillating floor about  $u = 0$  is shown in grey and the periodic orbits are shown in colour with lighter colour corresponding to higher  $n$ . Here  $g = -9.8$ ,  $\gamma = 1$  and  $\omega = 3$ .

In other words, the initial conditions for these periodic orbits are given by

$$\mathbf{x}_0 = \mathbf{x}_{\text{out}} = \begin{pmatrix} \gamma \sqrt{1 - \left( \frac{\pi n g}{\gamma \omega^2} \frac{r-1}{r+1} \right)^2} \\ -\frac{\pi n g}{\omega} \end{pmatrix} \quad (10.153)$$

and the periodic orbits exist provided

$$\left| \frac{\pi n g}{\gamma \omega^2} \left( \frac{r-1}{r+1} \right) \right| < 1. \quad (10.154)$$

In the deterministic case the eigenvalues  $\lambda_{1,2}$  of

$$\mathbf{D}_{\mathbf{x}}(\mathbf{x}_{\text{in}})\phi_{\mathbf{x}}(\mathbf{x}_{\text{out}}, T) = \begin{pmatrix} -r & 0 \\ \eta & -r \end{pmatrix} \begin{pmatrix} 1 & T \\ 0 & 1 \end{pmatrix} = \begin{pmatrix} -r & -rT \\ \eta & \eta T - r \end{pmatrix}, \quad (10.155)$$

where

$$\eta = \frac{(r+1)^2(g + \gamma\omega^2 \sin(\omega t_{\text{ref}}))}{2v_{\text{in}}} = \frac{(r+1)^2(g + \omega^2 u_{\text{in}})}{2v_{\text{in}}}, \quad (10.156)$$

determine the stability of the periodic orbit. These eigenvalues are less than 1 in magnitude and therefore the periodic orbit is stable provided

$$-\gamma\omega^2 \sin(\gamma t') > 2g \frac{r^2 + 1}{(r+1)^2}, \quad (10.157)$$

where  $\gamma\omega^2 \sin(\gamma t')$  is the acceleration of the floor at impact, or equivalently if

$$u_{\text{in}} < -2g \frac{r^2 + 1}{\omega^2 (r+1)^2}. \quad (10.158)$$

The eigenvalues  $\lambda_{1,2}$  are complex with magnitude  $|\lambda_{1,2}| = r$  if

$$-\gamma\omega^2 \sin(\gamma t') \in \left( g, g \left[ \frac{r-1}{r+1} \right]^2 \right) \quad (10.159)$$

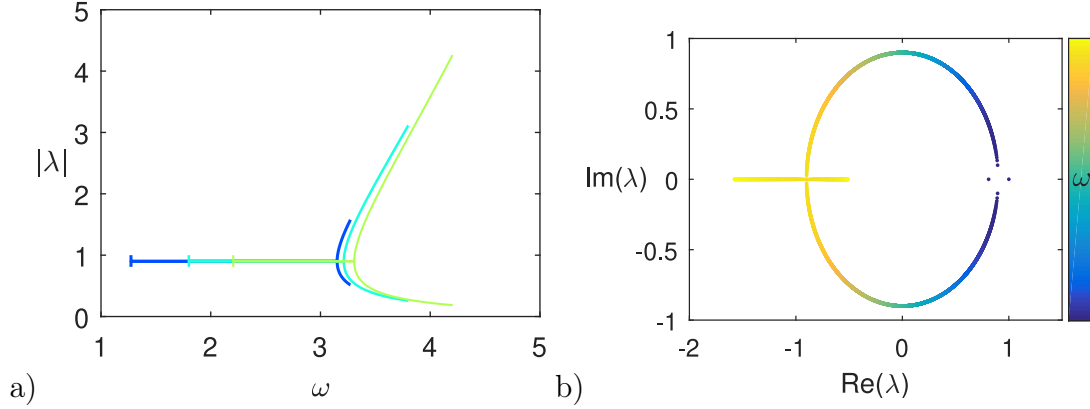


**Figure 10.7:** a) The magnitude of the eigenvalues of the periodic orbits ( $n = 1, 2, 3$ ) shown in Figure 10.5 as  $\omega$  increases. Here lighter colours correspond to higher  $n$ . b) Representative figure of the positions of the eigenvalues of the periodic orbit in the complex plane for  $n = 1$  coloured according to  $\omega$ . Here  $g = -9.8$  and  $\gamma = 1$ .

or equivalently if

$$u_{\text{in}} \in \left( -\frac{g}{\omega^2} \left[ \frac{r-1}{r+1} \right]^2, -\frac{g}{\omega^2} \right) \quad (10.160)$$

and real elsewhere. In particular, it is possible for this system to have multiple coexisting periodic attractors. For example, when  $g = -9.8$ ,  $\gamma = 1$  and  $\omega = 3$  the periodic orbits with period  $\frac{2n\pi}{\omega}$  that impact once per period exist and are stable for  $n = 1, 2, 3, 4$  and four associated periodic attractors with period  $\frac{6n\pi}{\omega}$  that impact three times per period are also present. As an example, the dynamics of a bouncing balls in period  $\frac{2n\pi}{\omega}$  and period  $\frac{6n\pi}{\omega}$  orbits are plotted in Figures 10.5 and 10.6 for  $n = 1, 2, 3$ , respectively.

The basins of attraction of the system's periodic attractors for these parameter values are plotted in  $(v_{\text{out}}, \tau)$ -space in Figure 10.8, where  $\tau$  is the time of impact mod  $\frac{2\pi}{\omega}$ . We note that the basins have a complicated intermingled structure that indicates that this system and its attractors have the potential to be highly sensitive to the addition of noise to the motion of the oscillating floor. As a result it would be interesting to study the effects of boundary noise on these periodic attractors. An in-depth study is beyond the scope of this paper, here we will simply demonstrate the use of the SZDM derived in Section 10.4.

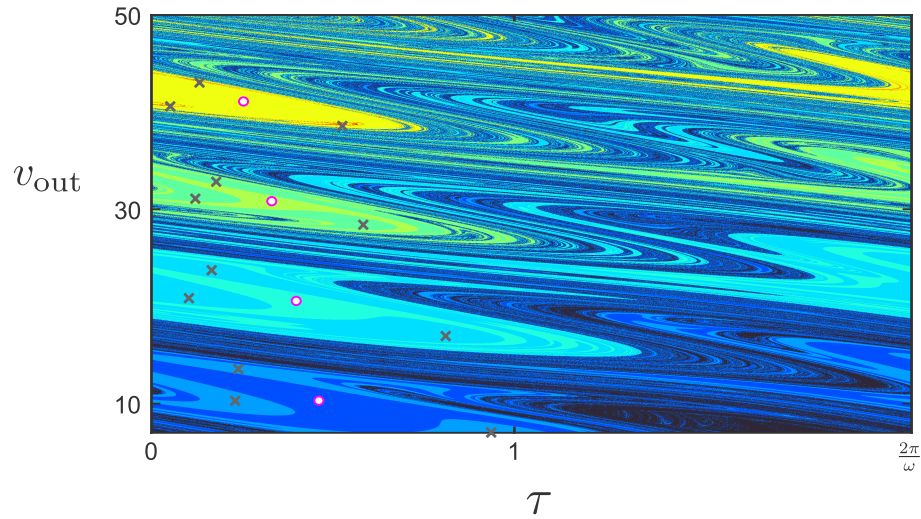


**Figure 10.8:** The basins of attraction of the bouncing ball system (10.143)-(10.144) in  $(v_{\text{out}}, \tau)$ -space when  $g = -9.8$ ,  $\gamma = 1$  and  $\omega = 3$ . Pink circles indicate orbits with one impact per period, grey xs indicate orbits with three impacts per period. Areas coloured black are absorbed by attractors outside the plotted region.

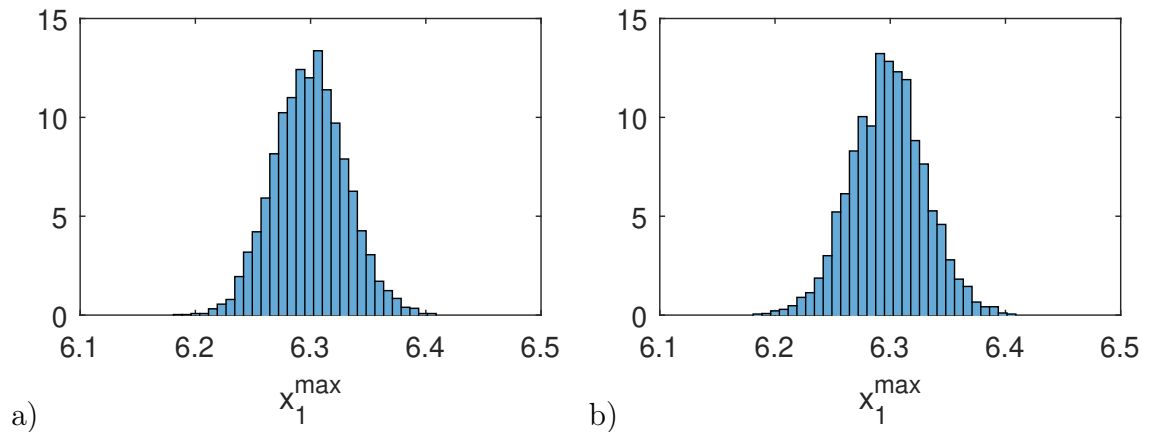


**Figure 10.9:** Histograms of the probability density function (pdf) of the maximum height attained by the bouncing ball between its 50<sup>th</sup> and 51<sup>st</sup> impacts given by a) a full simulation of the system b) linear approximation. Here  $g = -9.8$ ,  $\gamma = 1$ ,  $\omega = 3$ ,  $n = 1$ ,  $r = 0.8$ ,  $\theta = 50$ , and  $\sigma = 2$ . A sample of size  $N = 5000$  was used in both cases with initial conditions given by (10.153). The Kolmogorov-Smirnov test statistic measure of the distance between the two distributions is  $D_{KS} = 0.0228$ .

We do this by comparing the full system and the linearised system about the periodic orbit of period  $T = 2\pi/\omega$  given by (10.153). In particular we will present results for the case where the deterministic parameters are given by  $\gamma = 1$ ,  $\omega = 3$ , and  $r = 0.8$ , while the stochastic parameters are given by  $\theta = 50$  and  $\sigma = 0.2$ . First, taking an initial condition away from the discontinuity boundary and on the periodic attractor, we simulate the full system numerically. We consider a sample size of  $N = 5000$  and use an Euler-Maruyama scheme [35] with a fixed timestep of  $10^{-7}$  for the stochastic component of the boundary. We then consider the distribution of  $u$  on the Poincaré section given by  $\dot{u} = v = 0$  between the ball's 50<sup>th</sup> and 51<sup>st</sup> bounces, in other words the maximum height attained by the ball on this interval. We then compare this with the distribution given by the linearisation (10.56) projected onto the same Poincaré section. We find that the linearisation gives a good approximation to the full system and plot the results in Figure 10.9. In particular, as a measure of the difference between the two distributions, we have calculated the Kolmogorv-Smirnov test statistic to be  $D_{KS} = 0.0228$  using MATLAB<sup>®</sup>'s inbuilt `kstest2` function.

### 10.7.2 Hybrid Systems with Rugged Boundaries

We will now briefly present a 2-dimensional version of the bouncing ball example considered in Section 10.7.1. We will also replace the stochastically oscillating boundary with a sinusoidally oscillating discontinuity boundary that is rugged with stochastic imperfections. Non-impacting dynamics of the ball in 2-dimensional space are given by

$$\mathbf{x} = (u_1, v_1, u_2, v_2)^T, \quad \dot{\mathbf{x}} = \mathbf{f} = (v_1, g, v_2, 0)^T, \quad (10.161)$$

where  $(u_1, v_1)^T$ ,  $(u_2, v_2)^T$  are the position and velocity of the ball in the vertical and horizontal directions, respectively, and  $g$  is acceleration due to gravity. The oscillating boundary with stochastic imperfections in the horizontal or  $u_2$  direction

$\tilde{\Sigma}$  is given by the zeros of the function

$$\tilde{h}(\mathbf{x}, t) = u_1 - \gamma \sin(\omega t) - \chi(u_2). \quad (10.162)$$

The jump map  $\mathbf{j}$  does not change the position of the ball  $(u_1, u_2)^T$ , but it reverses and attenuates the ball's normal velocity to the floor by a factor  $0 \leq r \leq 1$  such that

$$\mathbf{j}(\mathbf{x}) = \mathbf{x} - \left( \frac{r+1}{1 + \chi'(u_2)^2} \right) (v_1 - \gamma\omega \cos(\omega t) - \chi'(u_2)v_2) \begin{pmatrix} 0 \\ 1 \\ 0 \\ -\chi'(u_2) \end{pmatrix}. \quad (10.163)$$

In the deterministic system, choosing the initial velocity in the horizontal direction  $v_2$  to be zero, the behaviour of this system reduces to the one-dimensional deterministic system studied in Section 10.7.1. As an example we will consider the effect of stochastic boundary imperfections  $\chi(u_2)$  on the behaviour of the deterministic periodic orbit with initial conditions given by (10.153) in the vertical direction  $(u_1, v_1)^T$ , and  $(0, 0)^T$  in the horizontal direction  $(u_2, v_2)^T$ . In this case we find that

$$\phi(\mathbf{x}, t) = \begin{pmatrix} u_1 + v_1 t + \frac{1}{2} g t^2 \\ v_1 + g t \\ u_2 + v_2 t \\ v_2 t \end{pmatrix}, \quad \phi_{\mathbf{x}}(\mathbf{x}, t) = \begin{pmatrix} 1 & t & 0 & 0 \\ 0 & 1 & 0 & 0 \\ 0 & 0 & 1 & t \\ 0 & 0 & 0 & 1 \end{pmatrix}, \quad (10.164)$$

$$\tilde{\mathbf{D}}_{\mathbf{x}}(\mathbf{x}_{\text{in}}) = [\mathcal{D}_{ij}], \quad i, j \in \{1, 2, 3, 4\}, \quad (10.165)$$

$$\mathcal{D}_{11} = \frac{v_1^{\text{out}} - \zeta}{v_1^{\text{in}} - \zeta}, \quad \mathcal{D}_{12} = \mathcal{D}_{14} = \mathcal{D}_{31} = \mathcal{D}_{32} = \mathcal{D}_{34} = 0,$$

$$\mathcal{D}_{12} = \frac{(v_1^{\text{out}} - v_1^{\text{in}})\chi'}{v_1^{\text{in}} - \zeta}, \quad \mathcal{D}_{21} = \frac{(r+1)(g + \omega^2 u_1^{\text{in}})}{(1 + (\chi')^2)(v_1^{\text{in}} - \zeta)}, \quad \mathcal{D}_{22} = \frac{-r + (\chi')^2}{1 + (\chi')^2},$$

$$\begin{aligned}
\mathcal{D}_{23} &= \frac{(r+1)\chi'}{1+(\chi')^2} \left( \frac{2\chi''}{1+(\chi')^2} + \frac{g+\omega^2 u_1^{\text{in}}}{v_1^{\text{in}}-\zeta} \right), & \mathcal{D}_{24} = \mathcal{D}_{42} &= \frac{(r+1)\chi'}{1+(\chi')^2}, \\
\mathcal{D}_{33} &= 1, & \mathcal{D}_{41} &= -\frac{(r+1)(g+\omega^2 u_1^{\text{in}})\chi'}{(1+(\chi')^2)(v_1^{\text{in}}-\zeta)}, & \mathcal{D}_{44} &= -\frac{(r+1)(\chi')^2}{1+(\chi')^2}, \\
\mathcal{D}_{43} &= \frac{r+1}{1+(\chi')^2} \left( \frac{(1-(\chi')^2)\chi''}{1+(\chi')^2} + \frac{(g+\omega^2 u_1^{\text{in}})(\chi')^2}{v_1^{\text{in}}-\zeta} \right), & & & & & (10.166)
\end{aligned}$$

$$\mathcal{N}(\mathbf{x}_{\text{in}}, t_{\text{ref}}) = \begin{pmatrix} v_1^{\text{in}} - v_1^{\text{out}} \\ -\frac{r+1}{1+(\chi')^2} (\omega^2 u_1^{\text{in}} + g) \\ 0 \\ \frac{(r+1)\chi'}{1+(\chi')^2} (\omega^2 u_1^{\text{in}} + g) \end{pmatrix} \quad (10.167)$$

and

$$\mathcal{J}(\mathbf{x}_{\text{in}}, t_{\text{ref}}) = \chi' \left( \frac{r+1}{1+(\chi')^2} \right) (v_1^{\text{in}} - \zeta) \begin{pmatrix} 0 \\ \chi' \\ 0 \\ 1 \end{pmatrix}, \quad (10.168)$$

where  $\zeta = \gamma\omega \cos(\omega t_{\text{ref}})$ ,  $\chi' = \chi'(0|\chi = 0)$  and  $\chi'' = \chi''(0|\chi = 0)$ .

In Figure 10.10 we plot the distribution of maximum height achieved by the ball  $u_1^{\text{max}}$  after a single bounce and its corresponding horizontal position  $u_2$  given by full numerical simulation of the system and by the linearisation (10.66). Once again we find that the linearisation gives a good approximation to the dynamics of the full system. We have calculated the generalised 2-dimensional K-S test statistic, derived by Fasano and Franceschini [36] and implemented using the MATLAB<sup>®</sup> routine `kstest2d.m` [37], to be  $D_{KS} = 0.0171$ .

### 10.7.3 Continuous Systems

In this section we consider the example of the *Chua circuit* with stochastically oscillating discontinuity boundaries using the SZDMs derived in Section 10.5. Previously the authors have investigated the effects of boundary noise on periodic attractors in

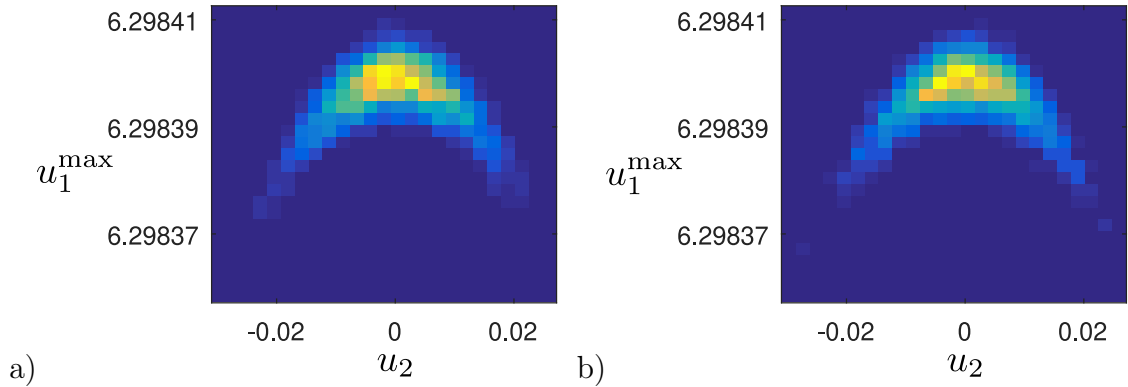


**Figure 10.10:** Heatmaps of the distribution of the maximum height attained by the bouncing ball and its corresponding horizontal position after one bounce on the rugged surface given by a) full simulation of the system b) linear approximation. Here  $g = -9.8$ ,  $\gamma = 1$ ,  $\omega = 3$ ,  $n = 1$ ,  $r = 0.8$ ,  $\theta = 300$ , and  $\sigma = 2$ . A sample of size  $N = 5000$  was used in both cases with initial conditions on the periodic given by (10.153) and  $(u_2, v_2)^T = (0, 0)^T$ . The generalised 2-dimensional K-S test statistic between the two sample distributions is  $D_{KS} = 0.0171$ .

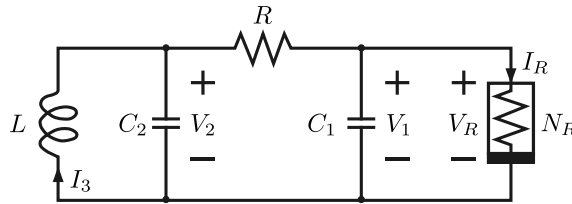


**Figure 10.11:** Circuit diagram of the Chua circuit. The circuit consists of four linear elements (a linear inductor  $L$  with internal resistance  $R_0$ , a linear resistor  $R$  and two capacitors  $C_1$  and  $C_2$ ) and a nonlinear resistor  $N_R$ , called the Chua diode.

a discontinuous variant the Chua circuit in some detail in [28].

The Chua circuit is a nonlinear circuit that was created with the aim of being the simplest autonomous circuit capable of generating chaos [38, 39]. It was the first physical system for which the presence of chaos was shown experimentally, numerically and mathematically [40]. The circuit, shown in Figure 10.11, contains four linear elements and one nonlinear resistor known as a *Chua diode*. It can be

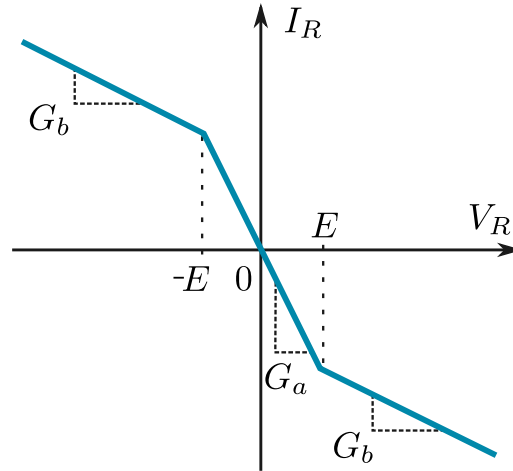


**Figure 10.12:** Typical voltage-current response of the Chua diode ( $N_R$  in Figure 10.11). The voltage-current response is piecewise-linear and symmetric.

described by the nondimensionalised ODE system

$$\begin{aligned}\frac{dx}{dt} &= \alpha(y - x - g(x)), \\ \frac{dy}{dt} &= x - y + z, \\ \frac{dz}{dt} &= -(\beta y + \gamma z),\end{aligned}\tag{10.169}$$

where

$$g(x) = m_1 x + \frac{1}{2}(m_0 - m_1)(|x + 1| - |x - 1|)\tag{10.170}$$

describes the piecewise-linear nature of the voltage-current response of the Chua diode shown in Figure 10.12. We note that the vector field given by (10.169) - (10.170) is  $\mathcal{C}^0$  and so trajectories that cross the discontinuity boundaries can be analysed using the ZDMs described in Section 10.5 first derived by Nordmark in [24].

We let  $\Sigma^-$  and  $\Sigma^+$  denote the two discontinuity boundaries given by  $x = -1$  and  $x = 1$ , respectively. We will denote the regions given by  $x < -1$ ,  $|x| \leq 1$  and  $x > 1$ , as  $S^-$ ,  $S^0$  and  $S^+$  with corresponding vector fields  $\mathbf{f}^-$ ,  $\mathbf{f}^0$  and  $\mathbf{f}^+$ , respectively. The

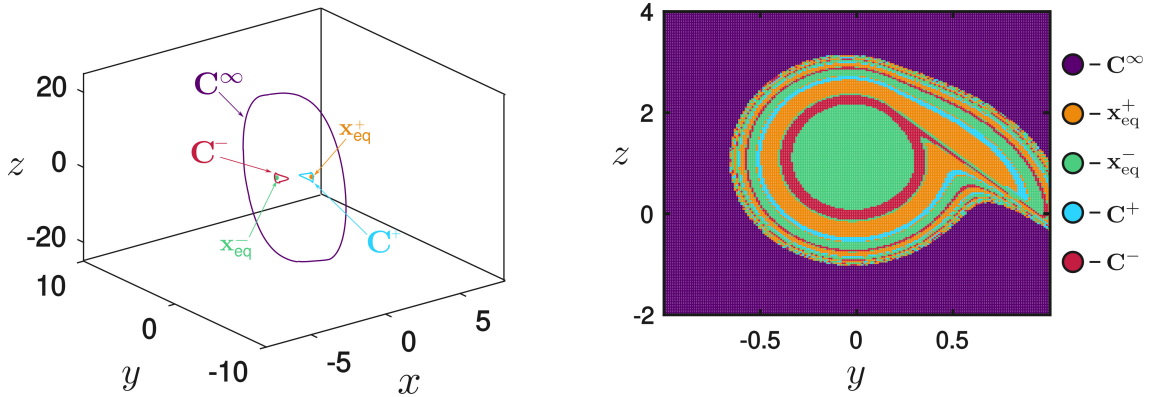


**Figure 10.13:** Five coexisting attractors when  $\alpha = 8.4$ ,  $\beta = 12$ ,  $\gamma = -0.005$ ,  $m_0 = -1.2$  and  $m_1 = 0.05$  in the system (10.169) (left) and their corresponding basins of attraction projected onto the boundary  $\Sigma^-$  (right).

system (10.169)-(10.170) has up to three equilibrium points, namely

$$\begin{aligned}
 \mathbf{x}_{\text{eq}}^0 &= (0, 0, 0)^T, \\
 \mathbf{x}_{\text{eq}}^- &= \frac{m_0 - m_1}{\gamma m_1 + \beta m_1 + \beta} (\gamma + \beta, \gamma, -\beta)^T, \\
 \mathbf{x}_{\text{eq}}^+ &= -\mathbf{x}_{\text{eq}}^-.
 \end{aligned} \tag{10.171}$$

Of these equilibrium points  $\mathbf{x}_{\text{eq}}^0$  always exists, while  $\mathbf{x}_{\text{eq}}^-$  and  $\mathbf{x}_{\text{eq}}^+$  only exist provided  $\mathbf{x}_{\text{eq}}^- \in S^-$  and  $\mathbf{x}_{\text{eq}}^+ \in S^+$ .

When  $\alpha = 8.4$ ,  $\beta = 12$ ,  $\gamma = -0.005$ ,  $m_0 = -1.2$  and  $m_1 \in (0.02, 0.14765)$  the system (10.169)-(10.170) has five coexisting attractors as shown in Figure 10.13 [28, 41]. These attractors are the equilibrium points  $\mathbf{x}_{\text{eq}}^-$  and  $\mathbf{x}_{\text{eq}}^+$  given in (10.171) and three periodic attractors. Two of the periodic attractors are small symmetric period-1 periodic orbits,  $C^-$  and  $C^+$  that cross  $\Sigma^-$  and  $\Sigma^+$  twice, respectively. The third periodic attractor is a large period-1 orbit  $C^\infty$ , that crosses both  $\Sigma^-$  and  $\Sigma^+$  twice. The three periodic attractors,  $C^-$ ,  $C^+$  and  $C^\infty$ , are hidden attractors as if we choose initial conditions in the vicinity of any equilibrium point of the system (10.169)-(10.170) (stable or unstable), we will reach one of the stable equilibrium points.

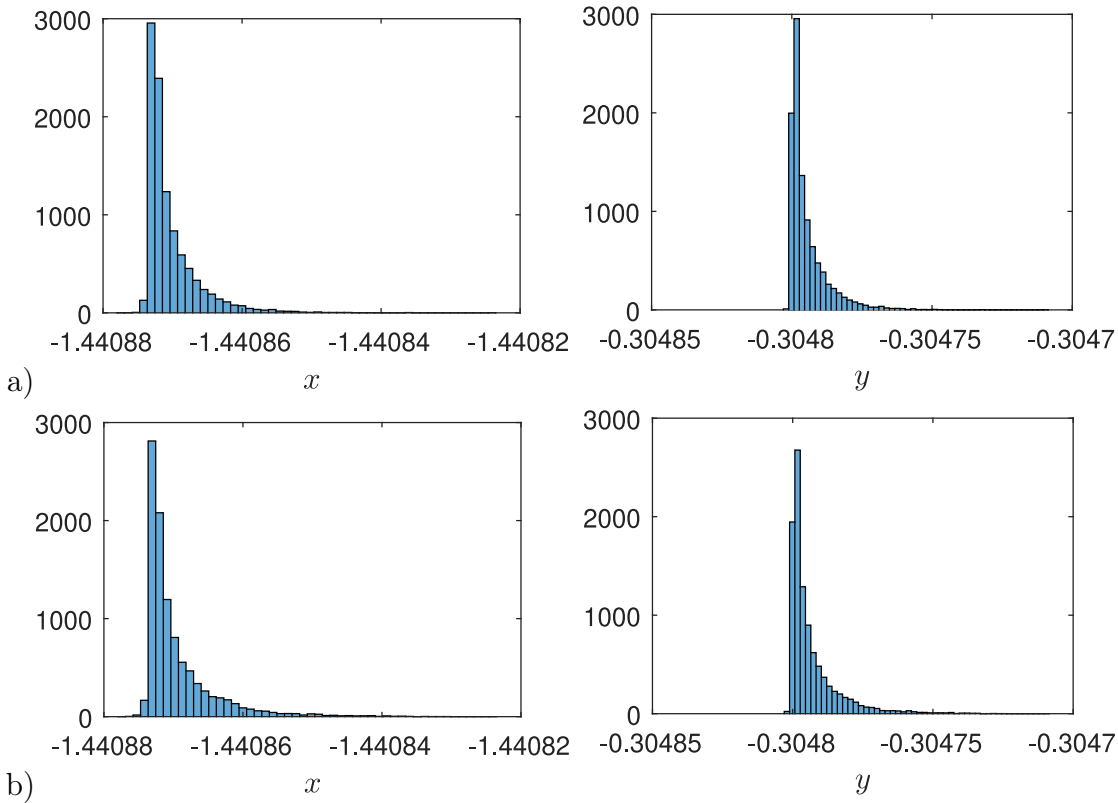


**Figure 10.14:** Histograms of the distributions of  $x$  and  $y$  co-ordinates of trajectories with initial conditions  $\mathbf{x}_0^{\text{ref}} = (x_0^{\text{ref}}, y_0^{\text{ref}}, z_0^{\text{ref}})^T \in \mathbf{C}^-$ , such that  $\mathbf{x}_0^{\text{ref}} \in S^-$  and  $\dot{x} = 0$ , on their first return to the Poincaré section given by  $z = z_0^{\text{ref}}$ . Here  $\alpha = 8.4$ ,  $\beta = 12$ ,  $\gamma = -0.005$ ,  $m_0 = -1.2$ ,  $m_1 = 0.145$ ,  $\sigma = 1$  and  $\theta = 50$ . The results of full numerical-simulation are shown in a) and the approximations obtained by using the SZDM (10.94) in place of boundary interactions are shown in b). In both cases the sample size used was  $N = 10000$ . The 2-dimensional generalised K-S statistic between the two sample distributions is  $D_{KS} = 0.0526$ .

The smaller symmetric periodic attractors  $\mathbf{C}^-$  and  $\mathbf{C}^+$  are born in a saddle-node bifurcation as the parameter  $m_1$  decreases through  $m_1 \approx 0.14765$ . We will focus on the effects of stochastic oscillations applied to the system's two discontinuity boundaries on these two attractors, and how the methods derived in Section 10.5 can be used to estimate these effects. As the attractors are symmetric it suffices to restrict our attention to  $\mathbf{C}^-$ . In [28] we have used similar methods to predict the destruction of the corresponding periodic attractor in a discontinuous variant of the Chua circuit.

We describe the stochastically oscillating discontinuity boundaries  $\tilde{\Sigma}^\pm$  in the noisy system by the zeros of

$$\tilde{h}^\pm(\mathbf{x}, t) = x - (\pm 1) - P^\pm(t), \quad (10.172)$$

respectively. In particular, in our numerical examples we will take  $P^\pm(t)$  to be once-differentiable stochastic processes  $P^\pm(t) \sim P_1(t)$  as defined in Section 10.3. In our examples we consider trajectories with initial conditions  $\mathbf{x}_0^{\text{ref}} = (x_0^{\text{ref}}, y_0^{\text{ref}}, z_0^{\text{ref}})^T$  on the deterministic periodic orbit  $\mathbf{C}^-$ , such that  $\mathbf{x}_0^{\text{ref}} \in S^-$  and  $\dot{x} = 0$ . We compare the distributions of the  $x$  and  $y$  coordinates of these trajectories on their first return to the Poincaré section given by  $z = z_0^{\text{ref}}$  given by full numerical simulation of the system, using an Euler-Maruyama scheme with a fixed timestep of  $7 \times 10^{-7}$  for the stochastic component of the boundary, to the estimate given by using the SZDM (10.94) in place of the two boundary crossings. We plot the results in Figure 10.14 and find that the SZDMs give a very good approximation to the full dynamics of the system. The 2-dimensional generalised K-S statistic between the two sample distributions calculated using `kstest2d.m` [37] is given by  $D_{KS} = 0.0526$ .

We note that when  $\mathbf{x} = \mathbf{x}^*$ , as is the case in the first boundary intersection in the example considered in this section, the estimate of the error introduced by noise on the boundary  $\tilde{\epsilon}$  given by (10.94) corresponds exactly with the heuristic second-order approximation proposed in [28]. In other words, we find that

$$\begin{aligned} \tilde{\epsilon} &= \frac{g(\mathbf{x}^*)}{2h_{\mathbf{x}}(\mathbf{x}^*)\mathbf{f}^-(\mathbf{x}^*)} \left( h(\mathbf{x}^*)^2 - \left( \frac{P(t_{\text{ref}})h_{\mathbf{x}}(\mathbf{x}^*)\mathbf{f}^-(\mathbf{x}^*) - h(\mathbf{x}^*)V(t_{\text{ref}})}{h_{\mathbf{x}}(\mathbf{x}^*)\mathbf{f}^-(\mathbf{x}^*) - V(t_{\text{ref}})} \right)^2 \right) \\ &= -\frac{g(\mathbf{x}^*)(h_{\mathbf{x}}(\mathbf{x}^*)\mathbf{f}^-(\mathbf{x}^*))^2}{2h_{\mathbf{x}}(\mathbf{x}^*)\mathbf{f}^-(\mathbf{x}^*)} \left( \frac{P(t_{\text{ref}})}{h_{\mathbf{x}}(\mathbf{x}^*)\mathbf{f}^-(\mathbf{x}^*) - V(t_{\text{ref}})} \right)^2 \\ &= -\frac{\partial}{\partial h}(\mathbf{f}^0 - \mathbf{f}^-)|_{\mathbf{x}=\mathbf{x}^*} h_{\mathbf{x}}(\mathbf{x}^*)\mathbf{f}^-(\mathbf{x}^*) \frac{1}{2} \left( \frac{P(t_{\text{ref}})}{h_{\mathbf{x}}(\mathbf{x}^*)\mathbf{f}^-(\mathbf{x}^*) - V(t_{\text{ref}})} \right)^2 \\ &= \frac{\partial}{\partial h}(\mathbf{f}^- - \mathbf{f}^0)|_{\mathbf{x}=\mathbf{x}^*} \frac{\partial h(\phi(\mathbf{x}, t))}{\partial t} \Big|_{(\mathbf{x}, t)=(\mathbf{x}^*, 0)} \frac{\Delta t_{\text{ref}}^2}{2} \\ &= \frac{\partial}{\partial t}(\mathbf{f}^- - \mathbf{f}^0)|_{\mathbf{x}=\mathbf{x}^*} \frac{\Delta t_{\text{ref}}^2}{2}. \end{aligned} \quad (10.173)$$

### 10.7.4 Grazing

Next we consider a classic example of a grazing nonsmooth system, a one-degree-of-freedom impact oscillator as shown in Figure 10.15. We describe the motion of a body in one spatial dimension by the position  $u(t)$  and velocity  $v(t) = \dot{u}(t)$  of its centre of mass. We then write  $\mathbf{x} = (u, v)^T$ . The non-impacting dynamics of the system are given by

$$\ddot{u}(t) + 2\mu\dot{u}(t) + ku(t) = \gamma \cos(\omega(t + \tau)), \quad (10.174)$$

where  $\mu > 0$  is the damping coefficient,  $k > 0$  is the stiffness coefficient and  $\gamma \cos(\omega(t + \tau))$  represents the external periodic sinusoidal forcing of the system with amplitude  $\gamma$  and initial phase  $\tau$ . We will rewrite (10.174) as

$$\begin{aligned} \dot{u} &= v, \\ \dot{v} &= \gamma \cos(\omega(t + \tau)) - ku - 2\mu v, \end{aligned} \quad (10.175)$$

and assume that the oscillator is free to move in the region where  $u > \alpha$  for some constant  $\alpha$ . We thus have that there is a discontinuity boundary  $\Sigma$  in the system given by the zeros of  $h(\mathbf{x}) = u - \alpha$ , which represents some rigid obstacle. When the oscillator impacts the rigid obstacle we apply the impact mapping

$$\mathbf{j}(\mathbf{x}) = \mathbf{j}((u, v)^T) = (u, -rv)^T, \quad (10.176)$$

where  $0 < r < 1$  is the coefficient of restitution that gives the energy lost during impact.

Provided  $\mu \neq 0$ , this system has a periodic attractor of period  $\frac{2\pi}{\omega}$  in free-flight [42].

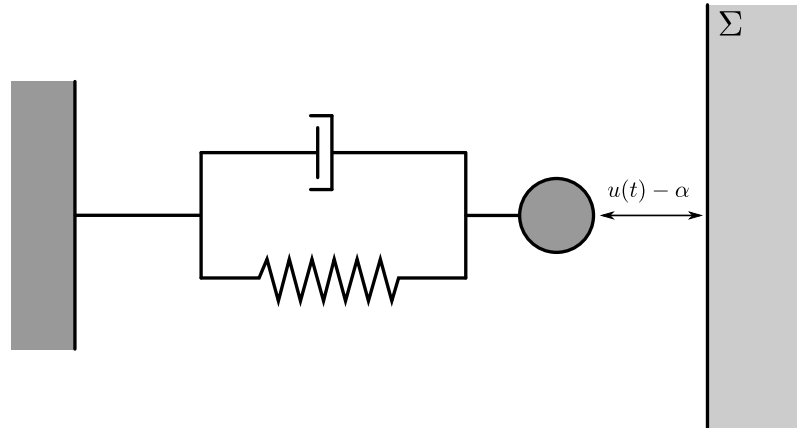


**Figure 10.15:** A one-degree-of-freedom impact oscillator. The position of the impacting surface is indicated by  $\Sigma$  and  $u(t) - \alpha$  is the distance between the oscillator and  $\Sigma$ .

This periodic orbit is given by

$$u(t) = \vartheta \cos(\omega(t + \tau)) + \beta \sin(\omega(t + \tau)), \quad (10.177)$$

where  $\vartheta$  and  $\beta$  are the constants given by

$$\vartheta = \frac{\gamma(k - \omega^2)}{(k - \omega^2)^2 + (2\mu\omega)^2}, \quad \beta = \frac{2\gamma\mu\omega}{(k - \omega^2)^2 + (2\mu\omega)^2}. \quad (10.178)$$

Increasing  $\alpha$  from  $-\infty$ , this periodic orbit grazes the boundary when

$$\alpha = \alpha_g = -\frac{\gamma}{\sqrt{(k - \omega^2)^2 + (2\mu\omega)^2}}, \quad (10.179)$$

as shown in Figure 10.16.

We will consider the effect of a stochastically oscillating boundary on trajectories in the neighbourhood of the grazing periodic orbit (10.177) shown in Figure 10.16. In the stochastic model we will describe the stochastically oscillating boundary  $\tilde{\Sigma}$  by the zeros of the function

$$\tilde{h}(\mathbf{x}, t) = u - \alpha_g - P(t), \quad (10.180)$$

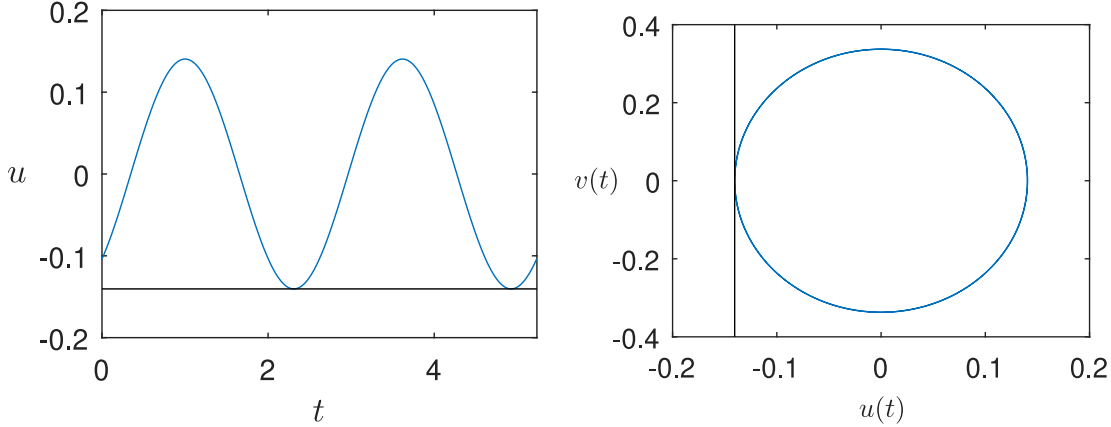


**Figure 10.16:** Grazing orbit in the system (10.175), with  $\omega = 2.4$ ,  $\mu = 1$ ,  $k = 1/2$ ,  $\gamma = 1$ ,  $\tau = 0$  and  $\alpha = \alpha_g = -\frac{\gamma}{\sqrt{(k-\omega^2)^2+(2\mu\omega)^2}}$ . In both cases the position of the discontinuity boundary  $\Sigma = \{(u, v)^T : u = \alpha_g\}$  is indicated by the black line.

where  $P(t)$  is a twice differentiable stochastic process. In our numerical examples we have chosen  $P(t) = P_2(t)$  as defined in Section 10.3. The stochastic impact mapping  $\tilde{\mathbf{j}}$  reverses the oscillator's normal velocity to the boundary and attenuates it by a factor of  $0 < r < 1$ , such that

$$\tilde{\mathbf{j}}(\mathbf{x}, t) = \mathbf{j}((u, v)^T) = (u, -rv + (r+1)V(t))^T, \quad (10.181)$$

where  $V(t) = dP/dt$  is the stochastic velocity associated with the boundary at the time of impact.

In particular, we will consider the distribution of  $u$  projected on to the Poincaré section  $\mathcal{P} = \{(u, v) : u > 0, v = 0\}$  after one passage close to the discontinuity boundary, i.e. the distribution of the maximum amplitude achieved by the oscillator after one potential low-velocity impact. We compare the results of full numerical simulations to the estimate given by using the SZDM (10.123) in place of boundary interactions. The numerical simulations use an Euler-Maruyama scheme with a fixed timestep and assume a maximum of one low-velocity impact per passage close to the

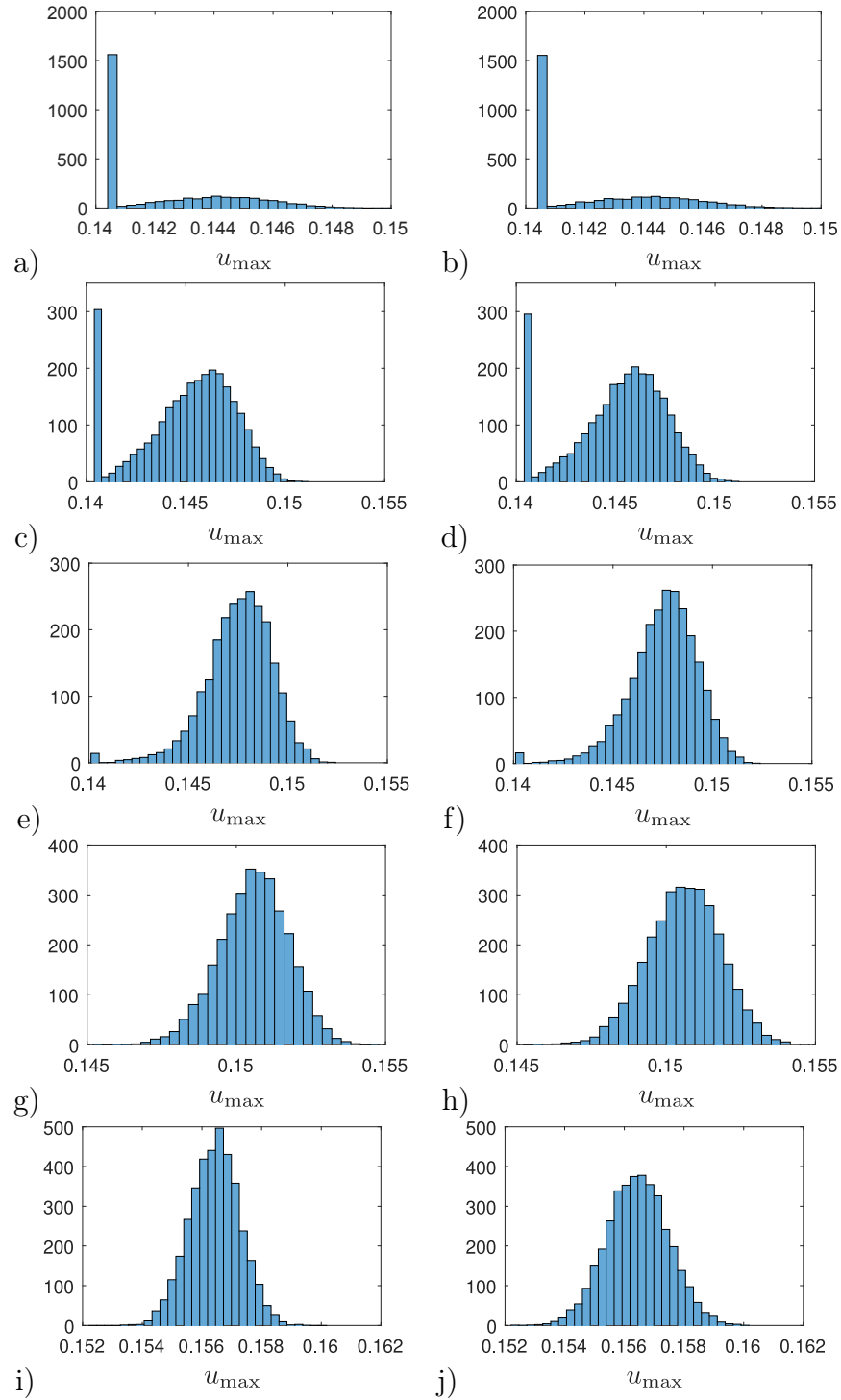


**Figure 10.17:** Pdf of the maximum amplitude attained by the impact oscillator given by a), c), e), g), i) full simulation of the system and b), d), f), h), j) approximation using the SZDM (10.123). Here  $\omega = 2.4$ ,  $\mu = 1$ ,  $k = 1/2$ ,  $\gamma = 1$ ,  $r = 0.8$ ,  $\theta = 50$ ,  $\sigma = 1$ , the sample size  $N = 10000$  and initial conditions are given by (10.183). In a), b)  $\varepsilon = 0$ ,  $D_{KS} = 0.0048$ , c), d)  $\varepsilon = 0.00005$ ,  $D_{KS} = 0.0159$ , e), f)  $\varepsilon = 0.0001$ ,  $D_{KS} = 0.0120$ , g), h)  $\varepsilon = 0.0002$ ,  $D_{KS} = 0.0197$  and i), j)  $\varepsilon = 0.0005$ ,  $D_{KS} = 0.0618$ .

grazing point. Referring to the SZDM (10.123) in this case we have that

$$\begin{aligned} \eta &= (1, 0), \quad \xi = (0, r + 1)^T, \quad A_g = -\omega^2 \alpha_g, \\ \Pi_t(\mathbf{x}, 0) &= \eta \mathbf{f}(\mathbf{x}), \quad \Pi_{tt}(\mathbf{x}, 0) = (0, 1) \mathbf{f}(\mathbf{x}). \end{aligned} \quad (10.182)$$

For our examples we take a sample of  $N = 10000$  trajectories with initial conditions

$$\begin{pmatrix} u(0) \\ v(0) \end{pmatrix} = \begin{pmatrix} \vartheta \cos(\omega\tau) + \beta \sin(\omega\tau) - \epsilon \\ \beta\omega \cos(\omega\tau) - \vartheta\omega \sin(\omega\tau) \end{pmatrix} \quad (10.183)$$

close the grazing periodic orbit of the deterministic system (10.177). We note that the initial conditions (10.183) lie exactly on the periodic orbit when  $\epsilon = 0$ . We present results for a sample of values of  $\epsilon$  in Figure 10.17. We focus on the cases where  $\epsilon \geq 0$  as when  $\epsilon < 0$  the majority of trajectories do not interact with the grazing boundary at all, making the SZDM redundant. We see that in the cases considered the SZDM gives an excellent approximation to the dynamics of the full system, with the estimates growing slightly less accurate for larger  $\epsilon$ , as one would expect. We find that the K-S test statistic for the two sample distributions when  $\epsilon = 0$  is  $D_{KS}(0) = 0.0048$ , this grows as  $\epsilon$  increases with  $D_{KS}(0.0005) = 0.0618$ . Not only does the SZDM accurately predict the distribution of impacting trajectories, it also gives a good approximation of the proportion of trajectories which do not impact with the boundary (in the left-most bar of Figure 10.17 a)-f)).

## 10.8 Summary and Discussion

This paper concerns the effects of boundary noise on discontinuity mappings in piecewise-smooth vector fields and hybrid dynamical systems. In particular, we have derived stochastic zero-time discontinuity mappings for systems with stochastically oscillating boundaries and systems with boundaries with stochastic imperfections.

In Section 10.3 we introduced a method for constructing generalised  $n$ -time differentiable Ornstein-Uhlenbeck processes. These processes are mean-reverting with mean zero and so are examples of processes that are suitable to describe both stochastic oscillations and stochastic imperfections applied to a deterministic boundary. In general Ornstein-Uhlenbeck processes have an inherent timescale and are often used to describe noise in real-world mechanical systems [30]. We later used these processes to model the noise in the numerical examples presented in Section 10.7.

Section 10.4 generalised the results of [28] to hybrid systems with transversal boundary crossings and further to the case of piecewise-smooth vector fields and hybrid systems with *rugged* boundaries. We also discussed how the form of the jump map  $\mathbf{j}$  on the boundary may impose conditions on the form of the stochastic process that can be used. In Section 10.6 we considered an example of a grazing trajectory in a hybrid system describing an impact oscillator with many degrees of freedom. In both the case of a stochastically oscillating boundary and a rugged boundary with small-scale stochastic imperfections showed that the derived SZDM has a noise term under the square-root and a noise term in the switching condition. These results are similar to those of Simpson and Kuske [26] who considered grazing in a three-dimensional piecewise-smooth system with Ornstein-Uhlenbeck noise on the boundary and the simplifying assumption that the noise process is constant while the trajectory is close to the grazing point.

Section 10.5 considered the case of transversal crossings in piecewise-smooth-continuous vector fields with stochastically oscillating boundaries, generalising the work of Nordmark [24] to stochastic systems. Finally section 10.7 presented some numerical examples, validating the results of Sections 10.4-10.5. In all cases we found that the SZDMs derived in this paper provided good approximations to numerical simulations of the full system.

It should be noted that the perturbations  $P(t)$  and  $\chi(\mathbf{x})$ , which describe the small oscillations and small imperfections of the discontinuity boundaries in this paper,

respectively, do not need to be stochastic processes in order for our analysis to hold. As long as the perturbations considered are of small amplitude about the original boundary, the discontinuity mappings derived in Sections 10.4-10.6 are valid. However, in the case of a deterministic perturbation in most cases it may be more simple to calculate the deterministic zero-time discontinuity mapping of the true system, considering the perturbation as an intrinsic part of the discontinuity boundary rather than treating it separately. It is for this reason that we believe that these results are most useful when analysing systems with noisy boundaries.

In future it remains to generalise our results to systems that have stochastic discontinuity boundaries which are both rugged, with small scale imperfections, and randomly oscillating. We would also like to consider the effects of noise on codimension-2 or higher crossings i.e. crossings at intersections of two or more discontinuity boundaries, by constructing appropriate SZDMs.

## Funding

EJS is supported by an Irish Research Council Postgraduate Scholarship, Award Number GOIPG/2015/3500.

## Declarations of Interest

None.

# Bibliography

- [1] S. Foale and S. R. Bishop, “Bifurcations in impact oscillations,” *Nonlinear dynamics*, vol. 6, no. 3, pp. 285–299, 1994.
- [2] Y. Yoshitake and A. Sueoka, “Forced self-excited vibration with dry friction,” in *Applied nonlinear dynamics and chaos of mechanical systems with discontinuities*, pp. 237–259, World Scientific, 2000.
- [3] A. B. Nordmark, “Non-periodic motion caused by grazing incidence in an impact oscillator,” *Journal of Sound and Vibration*, vol. 145, no. 2, pp. 279–297, 1991.
- [4] M. di Bernardo, P. Kowalczyk, and A. B. Nordmark, “Sliding bifurcations: a novel mechanism for the sudden onset of chaos in dry friction oscillators,” *International journal of Bifurcation and chaos*, vol. 13, no. 10, pp. 2935–2948, 2003.
- [5] A. B. Nordmark, H. Dankowicz, and A. R. Champneys, “Discontinuity-induced bifurcations in systems with impacts and friction: discontinuities in the impact law,” *International journal of non-linear mechanics*, vol. 44, no. 10, pp. 1011–1023, 2009.
- [6] H. Dankowicz, P. T. Piiroinen, and A. B. Nordmark, “Low-velocity impacts of quasiperiodic oscillations,” *Chaos, Solitons & Fractals*, vol. 14, no. 2, pp. 241–255, 2002.

- [7] M. di Bernardo, F. Garefalo, L. Glielmo, and F. Vasca, “Switchings, bifurcations, and chaos in DC/DC converters,” *IEEE Transactions on Circuits and Systems I: Fundamental Theory and Applications*, vol. 45, no. 2, pp. 133–141, 1998.
- [8] E. Fossas and G. Olivar, “Study of chaos in the buck converter,” *IEEE Transactions on Circuits and Systems I: Fundamental Theory and Applications*, vol. 43, no. 1, pp. 13–25, 1996.
- [9] D. Amrani and D. P. Atherton, “Designing autonomous relay systems with chaotic motion,” in *Decision and Control, 1989., Proceedings of the 28th IEEE Conference on*, pp. 512–517, IEEE, 1989.
- [10] M. di Bernardo, K. H. Johansson, and F. Vasca, “Self-oscillations and sliding in relay feedback systems: Symmetry and bifurcations,” *International Journal of Bifurcation and chaos*, vol. 11, no. 04, pp. 1121–1140, 2001.
- [11] C. P. Fall, E. S. Marland, J. M. Wagner, and J. J. Tyson, eds., *Computational cell biology*, vol. 20 of *Interdisciplinary Applied Mathematics*. Springer-Verlag, New York, 2002.
- [12] K. Hill, D. S. Abbot, and M. Silber, “Analysis of an arctic sea ice loss model in the limit of a discontinuous albedo,” *SIAM Journal on Applied Dynamical Systems*, vol. 15, no. 2, pp. 1163–1192, 2016.
- [13] J. G. Donohue and P. T. Piiroinen, “Mathematical modelling of seasonal migration with applications to climate change,” *Ecological modelling*, vol. 299, pp. 79–94, 2015.
- [14] J. Leifeld, “Non-smooth homoclinic bifurcation in a conceptual climate model,” *European Journal of Applied Mathematics*, pp. 1–14, 2018.
- [15] P. Kowalczyk and P. Glendinning, “Boundary-equilibrium bifurcations in piecewise-smooth slow-fast systems,” *Chaos: An Interdisciplinary Journal of Nonlinear Science*, vol. 21, no. 2, p. 023126, 2011.

- 
- [16] E. Santor, L. Suchanek, *et al.*, “Unconventional monetary policies: evolving practices, their effects and potential costs,” *Bank of Canada Review*, vol. 2013, no. Spring, pp. 1–15, 2013.
- [17] J. A. Amador, G. Olivar, and F. Angulo, “Smooth and Filippov models of sustainable development: Bifurcations and numerical computations,” *Differential Equations and Dynamical Systems*, vol. 21, no. 1-2, pp. 173–184, 2013.
- [18] M. di Bernardo, C. J. Budd, A. R. Champneys, P. Kowalczyk, A. B. Nordmark, G. O. Tost, and P. T. Piiroinen, “Bifurcations in nonsmooth dynamical systems,” *SIAM review*, vol. 50, no. 4, pp. 629–701, 2008.
- [19] R. I. Leine and H. Nijmeijer, *Dynamics and bifurcations of non-smooth mechanical systems*, vol. 18. Springer Science & Business Media, 2013.
- [20] Z. T. Zhusubaliyev and E. Mosekilde, *Bifurcations and chaos in piecewise-smooth dynamical systems*. World Scientific, 2003.
- [21] M. di Bernardo, M. I. Feigin, S. J. Hogan, and M. E. Homer, “Local analysis of c-bifurcations in n-dimensional piecewise-smooth dynamical systems,” *Chaos, Solitons and Fractals: the interdisciplinary journal of Nonlinear Science, and Nonequilibrium and Complex Phenomena*, vol. 11, no. 10, pp. 1881–1908, 1999.
- [22] M. di Bernardo, C. J. Budd, A. R. Champneys, and P. Kowalczyk, *Piecewise-smooth dynamical systems: theory and applications*, vol. 163. Springer Science & Business Media, 2008.
- [23] T. S. Parker and L. O. Chua, “Efficient solution of the variational equation for piecewise-linear differential equations,” *International journal of circuit theory and applications*, vol. 14, no. 4, pp. 305–314, 1986.
- [24] A. B. Nordmark, “Discontinuity mappings for vector fields with higher order continuity,” *Dynamical systems*, vol. 17, no. 4, pp. 359–376, 2002.

- [25] D. J. W. Simpson, S. J. Hogan, and R. Kuske, “Stochastic regular grazing bifurcations,” *SIAM Journal on Applied Dynamical Systems*, vol. 12, no. 2, pp. 533–559, 2013.
- [26] D. J. W. Simpson and R. Kuske, “The influence of localized randomness on regular grazing bifurcations with applications to impacting dynamics,” *Journal of Vibration and Control*, p. 1077546316642054, 2016.
- [27] D. J. W. Simpson and R. Kuske, “Stochastic perturbations of periodic orbits with sliding,” *Journal of Nonlinear Science*, vol. 25, no. 4, pp. 967–1014, 2015.
- [28] E. J. Staunton and P. T. Piiroinen, “Estimating the dynamics of systems with noisy boundaries,” *To appear in Nonlinear Analysis: Hybrid Systems*, vol. 36, May 2020.
- [29] B. Øksendal, *Stochastic differential equations: an introduction with applications*. Springer Science & Business Media, 2013.
- [30] P. Hänggi and P. Jung, “Colored noise in dynamical systems,” *Advances in chemical physics*, vol. 89, pp. 239–326, 1995.
- [31] M. H. Fredriksson and A. B. Nordmark, “Bifurcations caused by grazing incidence in many degrees of freedom impact oscillators,” in *Proceedings of the Royal Society of London A: Mathematical, Physical and Engineering Sciences*, vol. 453, pp. 1261–1276, The Royal Society, 1997.
- [32] E. J. Staunton and P. T. Piiroinen, “Noise and multistability in the square root map,” *Physica D: Nonlinear Phenomena*, vol. 380, pp. 31–44, 2018.
- [33] E. J. Staunton and P. T. Piiroinen, “Noise-induced multistability in the square root map,” *Nonlinear Dynamics*, vol. 95, no. 1, pp. 769–782, 2019.
- [34] P. J. Holmes, “The dynamics of repeated impacts with a sinusoidally vibrating table,” *Journal of Sound and Vibration*, vol. 84, no. 2, pp. 173–189, 1982.

- [35] P. E. Kloeden and E. Platen, *Numerical solution of stochastic differential equations*, vol. 23. Springer Science & Business Media, 2013.
- [36] G. Fasano and A. Franceschini, “A multidimensional version of the Kolmogorov–Smirnov test,” *Monthly Notices of the Royal Astronomical Society*, vol. 225, no. 1, pp. 155–170, 1987.
- [37] B. Lau, “multdist GitHub repository.” <https://github.com/brian-lau/multdist>, Commit: 868acf6b7bca1fe65451ced4acad9a59ee77cca5, Accessed 9 September 2019, 2013.
- [38] T. Matsumoto, “A chaotic attractor from Chua’s circuit,” *IEEE Transactions on Circuits and Systems*, vol. 31, no. 12, pp. 1055–1058, 1984.
- [39] L. O. Chua, “The genesis of Chua’s circuit,” *International Journal of Electronics Communication*, vol. 46, no. 4, pp. 250–257, 1992.
- [40] L. O. Chua, M. Komuro, and T. Matsumoto, “The double scroll family,” *IEEE transactions on circuits and systems*, vol. 33, no. 11, pp. 1072–1118, 1986.
- [41] N. V. Stankevich, N. V. Kuznetsov, G. A. Leonov, and L. O. Chua, “Scenario of the birth of hidden attractors in the Chua circuit,” *International Journal of Bifurcation and Chaos*, vol. 27, no. 12, p. 1730038, 2017.
- [42] N. Humphries and P. T. Piiroinen, “A discontinuity-geometry view of the relationship between saddle–node and grazing bifurcations,” *Physica D: Nonlinear Phenomena*, vol. 241, no. 22, pp. 1911–1918, 2012.

## 10.A Appendix: Generalised Ornstein-Uhlenbeck Processes

In Section 10.3, using the Ornstein-Uhlenbeck process (10.21) as our base process  $P_0(t) = \xi(t)$  we constructed an  $n$ -time differentiable mean-reverting position processes  $P_n(t)$  as

$$\frac{dP_n}{dt}(t) = -\theta P_n(t) + \sigma P_{n-1}(t), \quad n \geq 1 \quad (10.184)$$

and denoted the corresponding velocity and acceleration processes as  $V_n = dP_n/dt$  and  $A_n = d^2P_n/dt^2$ , respectively. We then find that  $P_n$  is given by

$$\begin{aligned} P_n(t) &= e^{-\theta t} \left( \sum_{i=0}^{n-1} \frac{(\sigma t)^i}{i!} P_{n-i}(0) + \frac{(\sigma t)^n}{n!} \xi_0 \right) + \frac{\sigma^{n+1}}{n!} \int_0^t e^{\theta(s-t)} (t-s)^n dW_s \\ &= \mu_{P_n}(t) + \frac{\sigma^{n+1}}{n!} \int_0^t e^{\theta(s-t)} (t-s)^n dW_s \\ &\sim N(\mu_{P_n}(t), \sigma_{P_n}^2(t)), \end{aligned} \quad (10.185)$$

where

$$\begin{aligned} \sigma_{P_n}^2(t) &= \left( \frac{\sigma^{n+1}}{n!} \right)^2 \int_0^t e^{2\theta(s-t)} (s-t)^{2n} ds \\ &= \left( \frac{\sigma^{n+1}}{n!} \right)^2 \left( \frac{2n!}{(2\theta)^{2n+1}} - \frac{e^{-2\theta t}}{2\theta} \sum_{i=0}^{2n} \frac{2n!}{(2n-i)!} \frac{t^{2n-i}}{(2\theta)^i} \right). \end{aligned} \quad (10.186)$$

We also find that the corresponding velocity and acceleration processes  $V_n$  and  $A_n$  are given by

$$\begin{aligned} V_n(t) &= -\theta \mu_{P_n}(t) + \sigma \mu_{P_{n-1}}(t) + \sigma^{n+1} \int_0^t e^{\theta(s-t)} \left( \frac{(t-s)^{n-1}}{(n-1)!} - \theta \frac{(t-s)^n}{n!} \right) dW_s \\ &= \mu_{V_n}(t) + \sigma^{n+1} \int_0^t e^{\theta(s-t)} \left( \frac{(t-s)^{n-1}}{(n-1)!} - \theta \frac{(t-s)^n}{n!} \right) dW_s \\ &\sim N(\mu_{V_n}(t), \sigma_{V_n}^2(t)), \end{aligned} \quad (10.187)$$

where

$$\begin{aligned}
\sigma_{V_n}^2(t) &= \sigma^{2(n+1)} \int_0^t e^{2\theta(s-t)} \left( \frac{(t-s)^{n-1}}{(n-1)!} - \theta \frac{(t-s)^n}{n!} \right)^2 ds \\
&= \theta^2 \sigma_{P_n}^2(t) + \sigma^2 \sigma_{P_{n-1}}^2(t) \\
&\quad + 2\theta\sigma \frac{\sigma^{2n+1}n}{(n!)^2} \left( \frac{e^{-2\theta t}}{2\theta} \sum_{i=0}^{2n-1} \frac{(2n-1)!}{(2n-1-i)!} \frac{t^{2n-1-i}}{(2\theta)^i} - \frac{(2n-1)!}{(2\theta)^{2n}} \right) \\
&= \theta^2 \sigma_{P_n}^2(t) + \sigma^2 \sigma_{P_{n-1}}^2(t) - 2\theta\sigma \text{Cov}(P_n(t), P_{n-1}(t)) \tag{10.188}
\end{aligned}$$

and

$$\begin{aligned}
A_n(t) &= \theta^2 \mu_{P_n}(t) - 2\theta\sigma \mu_{P_{n-1}}(t) + \sigma^2 \mu_{P_{n-2}}(t) \\
&\quad + \sigma^{n+1} \int_0^t e^{\theta(s-t)} (t-s)^{n-2} \left( \theta^2 \frac{(s-t)^2}{n!} + 2\theta \frac{s-t}{(n-1)!} + \frac{1}{(n-2)!} \right) dW_s \\
&\sim N(\mu_{A_n}(t), \sigma_{A_n}^2(t)), \tag{10.189}
\end{aligned}$$

where

$$\begin{aligned}
\sigma_{A_n}^2(t) &= \theta^4 \sigma_{P_n}^2(t) + \left( 4 + 2 \frac{n-1}{n} \right) \theta^2 \sigma^2 \sigma_{P_{n-1}}^2(t) + \sigma^4 \sigma_{P_{n-2}}^2(t) \\
&\quad - 4\theta^3 \sigma \text{Cov}(P_n(t), P_{n-1}(t)) - 4\theta\sigma^3 \text{Cov}(P_{n-1}(t), P_{n-2}(t)). \tag{10.190}
\end{aligned}$$

We note that (10.188) implies that

$$\text{Cov}(P_n(t), P_{n-1}(t)) = \frac{\sigma^{2n+1}n}{(n!)^2} \left( \frac{(2n-1)!}{(2\theta)^{2n}} - \frac{e^{-2\theta t}}{2\theta} \sum_{i=0}^{2n-1} \frac{(2n-1)!}{(2n-1-i)!} \frac{t^{2n-1-i}}{(2\theta)^i} \right), \tag{10.191}$$

while (10.190) implies that

$$\text{Cov}(P_n(t), P_{n-2}(t)) = \left( \frac{n-1}{n} \right) \sigma_{P_{n-1}}^2(t). \tag{10.192}$$

We can now calculate the covariances associated with the position process as

$$\begin{aligned}\text{Cov}(P_n(t), V_n(t)) &= -\theta\sigma_{P_n}^2(t) + \sigma\text{Cov}(P_n(t), P_{n-1}(t)), \\ \text{Cov}(P_n(t), A_n(t)) &= \theta^2\sigma_{P_n}^2(t) + \sigma^2\left(\frac{n-1}{n}\right)\sigma_{P_{n-1}}^2(t) \\ &\quad - 2\theta\sigma\text{Cov}(P_n(t), P_{n-1}(t)), \\ \text{Cov}(V_n(t), A_n(t)) &= 3\theta^2\sigma\text{Cov}(P_n(t), P_{n-1}(t)) + \sigma^3\text{Cov}(P_{n-1}(t), P_{n-2}(t)) \\ &\quad - (\theta^3\sigma_{P_n}^2(t) + \left(2 + \frac{n-1}{n}\right)\theta\sigma^2\sigma_{P_{n-1}}^2(t)).\end{aligned}\quad (10.193)$$